NORTHWESTERN UNIVERSITY

Chemical Trends in Complex Electronic Structures of Thermoelectric Semiconductors

A DISSERTATION

SUBMITTED TO THE GRADUATE SCHOOL
IN PARTIAL FULFILLMENT OF THE REQUIREMENTS

for the degree

DOCTOR OF PHILOSOPHY

Materials Science & Engineering

By

Madison K. Brod

EVANSTON, ILLINOIS

June 2023

Abstract

Thermoelectric devices convert between temperature gradients and electricity, implying numerous applications, such as powering exploratory space vehicles, industrial waste-heat recovery, and solid-state refrigeration. Thermoelectric devices consist of doped p-type and n-type semiconductor legs, and the overall device efficiency depends on the transport properties of these semiconductor materials. High-performing thermoelectric materials require a high Seebeck coefficient and high electrical conductivity, but these can be conflicting requirements—increasing the doping level increases the electrical conductivity but decreases the Seebeck coefficient. However, electronic band engineering in $\boldsymbol{k}$-space, or reciprocal space, can partially decouple these properties and yield materials that have a high Seebeck coefficient and electrical conductivity. Specifically, it is beneficial to engineer bands that have complex Fermi surfaces, characterized by high valley (band) degeneracy, carrier pocket anisotropy, and/or low-dimensional transport. The goal of this dissertation is to understand the chemical origins of complex Fermi surfaces by studying the $\boldsymbol{k}$-dependence of atomic-orbital interactions in various thermoelectric semiconductors. The motivation behind this work is to use this understanding of complex electronic structures to predict chemical trends in band structure behavior, and therefore, predict alloying design strategies for engineering better thermoelectric materials. In this thesis, the tight-binding method, also known as the Linear Combination of Atomic Orbitals, is used in conjunction with density-functional theory, to gain chemical insights into the origins of complex electronic structures in a variety of technologically-relevant thermoelectric material systems, including IV-VI semiconductors, transition-metal-based half-Heusler semiconductors, and Zintl-phase Mg_3Sb_2.

Acknowledgements

I certainly would not have been able to make it to this point alone, and I am immensely grateful to all of the people who have supported me throughout my studies. Jeff, thank you for sharing your genuine curiosity and passion for science. I appreciate how much trust and freedom you have given me to explore my interests and different approaches to tackling research questions. Because of your mentorship, I have learned to look a problems from new, creative perspectives. It is abundantly clear that you are invested in the growth and success of your students above all else, and I definitely would not be the person or scientist I am today without you as an advisor. I also want to thank my other committee members, Dr. Mercouri Kanatzidis, Dr. James Rondinelli, and Dr. Chris Wolverton, for your valuable feedback and guidance.

Next, I'd like to thank the Applied Physics and Applied Math (APAM) department, my professors, and my advisor, Dr. Simon Billinge, at Columbia University in New York, where I completed the first-year of my PhD studies. I learned a tremendous amount while I was there, and the knowledge I gained has proved invaluable in completing my thesis. I also appreciate the support I received from the department and faculty in continuing my PhD at Northwestern.

My experience at Northwestern would not have been the same without the support of my labmates, past and present, in the Snyder group. I want to thank Dr. Maxwell Dylla and Dr. Shashwat Anand, who were valuable mentors upon the start of my PhD and inspired much of my work on half-Heuslers and Mg_3Sb_2. Shash, thank you for your continued collaboration, encouragement and support throughout my entire PhD. I also want to thank Michael Toriyama, who has been by my side in the Snyder from first-year courses to co-authoring papers together. Your scientific insights and collaborations have been incredibly valuable to me, and I have learned a great deal from working together and from our discussions in the office. Finally, to the other current Snyder group members, Leah Borgsmiller, Duncan Zavanelli, Adetoye Adekoya, Muath Al-Malki, and Patrick Ding, you all inspire and impress me with your work, and I wish you all the very best in completing your studies.

I have also been fortunate enough to work with several collaborators outside of Northwestern, and I want to thank all my co-authors, in addition to the co-PIs and members of the DMREF and TECCA collaborations. I have learned so much from collaborating on papers and sharing research at meetings.

I also want to thank all my MSE (and non-MSE) friends outside of lab who remind me that there is life beyond thermoelectrics. To my book-club friends, thanks for giving me a reason to read something other than textbooks and journal articles. I am also incredibly thankful for the support and friendship of Stephanie Ribet. Steph, thank you so much for making me feel so welcome when I started at Northwestern. Your hard work and love of science has been a source of inspiration, and your friendship has meant so much to me through the ups and downs of grad school.

Finally, I would not have been able to reach this point without the support of my family. I cannot thank my parents, Bruce and Jennifer, enough for all their unconditional love and support. You have given me everything I could have ever wanted or needed to succeed. Mom, I don't know how I would have made it through college and graduate school without our phone calls, where you remind me that everything will be okay and that you believe in me. Dad, thank you for showing me the importance of not only hard work, but also standing up for your values in the process. To my older brother, Eric, thank you for your endless support and for always knowing how to make me (and everyone else) laugh. If there were a PhD degree in Philadelphia sports, you would definitely have it. And to my fiancé, David, I can't thank you enough for all your support these past few years. On good days and bad, I always feel at peace knowing that I get to go home to you.

This thesis is dedicated to Mom, Dad, Eric, and David.

Notation Conventions and Abbreviations

Physical Constants

- Boltzmann constant: $k_B = 1.38 \times 10^{-23}$ J/K
- Planck's constant: $h = 6.63 \times 10^{-34}$ J·s
- Reduced Planck's constant: $\hbar = 1.05 \times 10^{-34}$ J·s
- Electron rest mass: $m_e = 9.11 \times 10^{-31}$ kg
- Electron charge: $e = 1.60 \times 10^{-19}$ C

List of Symbols

- T: Absolute Temperature
- ZT: Thermoelectric Figure-of-Merit (device)
- zT: Thermoelectric Figure-of-Merit (material)
- B: Thermoelectric Quality Factor
- σ: Electrical conductivity
- κ : Thermal conductivity (lattice: κ_L, electronic: κ_e)
- L: Lorenz number
- E_F: Electron chemical potential (Fermi level) or Fermi energy[1]
- η: Reduced electron chemical potential
- α: Seebeck coefficient
- m^* : Effective mass (inertial: m_I^*, density-of-states: m_{DOS}^*, band: m_b^*, conductivity: m_c^*, Seebeck: m_S^*)
- N_V: Valley (band) degeneracy
- n (or p for holes): Carrier concentration
- μ: Mobility (weighted: μ_w, parameter: μ_0)

[1] In this dissertation, we distinguish between the Fermi *level* and the Fermi *energy*, though both are denoted by E_F. The Fermi level is the electron chemical potential (also denoted μ), which is the energy at which the probability of electron occupation is 1/2. In an intrinsic (undoped) semiconductor, the Fermi level lies in the middle of the band gap. The Fermi energy is only defined for zero Kelvin, and refers to the energy of the highest filled electron state. In an intrinsic semiconductor, the Fermi energy is located at the valence band maximum.

- τ: Carrier relaxation time
- f: Fermi-Dirac distribution function
- F_j: Fermi integral of jth order

Frequently Used Abbreviations

- Tight-binding (TB)
- Linear Combination of Atomic Orbitals (LCAO)
- Density-of-states (DOS)
- half-Heusler (hH)
- Density Functional Theory (DFT)
- Crystal orbital Hamilton population (COHP)
- Perdew–Burke-Ernzerhof (PBE)
- Spin-orbit coupling (SOC)
- Valence band (VB)
- Conduction band (CB)
- Valence band maximum (VBM)
- Conduction band minimum (CBM)
- Brillouin zone (BZ)

Contents

List of Figures

List of Tables

Introduction

1.1 Thermoelectric Devices

Thermoelectric devices are solid-state heat engines that possess the unique ability to directly convert between temperature gradients and electricity through the flow of charge carriers (electrons and holes), implying important applications in sustainable power generation and solid-state cooling [7]. Thermoelectric devices are comprised of a number of thermoelectric modules that contain p-type and n-type semiconductor legs that are electrically in series and thermally in parallel [8]. In the power-generation mode, a temperature gradient is applied across the devices, which generates a voltage and induces the flow of charge carriers from the cool side to the hot side, producing an electric current. Conversely, when an external voltage is applied to the device, the flow of charge carriers, and hence heat, is directed such that one side of the device is cooled [7, 8].

NASA has been successfully employing Radioisotope Thermoelectric Generators (RTGs) to power deep-space missions since the middle of the 20th century [9], and RTGs have been used to power the Voyager, Cassini, Curiosity Rover, and Perseverance Rover missions [10]. However, with the current climate crisis, there is a growing need to develop technology that can reduce greenhouse gas emissions, pushing the field of thermoelectrics to focus more attention on terrestrial applications. One potential application is industrial-scale waste-heat recovery. According to one analysis [11], 80% of industrial waste heat is released as heated gas (373–573 K). Using thermoelectrics to convert this waste heat into electricity can improve overall energy efficiencies and mitigate the deleterious en-

vironmental impacts of alternative waste-heat management strategies [12]. Similarly, waste-heat recovery in automobiles could be a potential route to improving fuel-efficiency, and hence, reducing harmful carbon emissions. Automotive internal combustion engines typically have efficiencies ranging between 25% and 40%, and much of the unused energy is rejected as waste-heat, which could be captured and used by thermoelectric generators [13, 14].

Additionally, thermoelectric cooling provides a means to reduce the environmental impact of carbon emissions and harmful refrigerants [15]. Over 25% of the electricity consumed in the United States is used for heating, ventilation, and air-conditioning (HVAC). Much of this energy is wasted because most HVAC systems are designed to heat or cool entire buildings or cars. Thermoelectric coolers and heat pumps can provide the technology required for distributed HVAC, which provides heating and cooling locally, where necessary, and has the potential to greatly reduce HVAC energy requirements [15].

The performance of a thermoelectric device for both power generation and cooling is determined by its dimensionless figure-of-merit ZT. For power generation, the relationship between the device ZT and efficiency, η, is given in Equation 1.1, where T_c and T_h are the absolute temperatures of the cold side and hot side, respectively, of the device, and $\bar{T}$ is the average temperature across the device. The term $(T_h - T_c)/T_h$ is the Carnot efficiency, or the thermodynamic efficiency limit. As ZT approaches infinity, the device efficiency approaches this Carnot limit.

$$\eta = \frac{T_h - T_c}{T_h} \left(\frac{\sqrt{1 + Z\bar{T}} - 1}{\sqrt{1 + Z\bar{T}} + \frac{T_c}{T_h}} \right) \tag{1.1}$$

For thermoelectric refrigerators, the coefficient of performance (COP), denoted ϕ, also depends on ZT and the temperature gradient (Equation 1.2). The COP is defined as the heat removed divided by the electrical power consumed, and the term, $T_c/(T_h - T_c)$ is the Carnot COP (thermodynamic limit) [16]. For thermoelectric coolers/heat pumps to be competitive with vapor-compression cooling systems, $ZT > 2$ is required, while $ZT > 6$ is would be required to cool to cryogenic temperatures [16]. However, the best thermoelectric cooling systems to-date are yet to reliably reach values

of $ZT = 1$, indicating the need for better mid- to low-temperature thermoelectric materials [17].

$$\phi = \frac{T_c}{T_h - T_c}\left(\frac{\sqrt{1+Z\bar{T}} - T_h/T_c}{\sqrt{1+Z\bar{T}}+1}\right) \tag{1.2}$$

1.2 Optimizing Thermoelectric Performance

In the previous section, we described the device figure-of-merit, ZT, as a means to determine the efficiency of a thermoelectric device for power generation or cooling. However, the focus of this dissertation is on engineering the *materials* that comprise the n-type and p-type legs themselves, so we require a means to quantify the performance of thermoelectric materials. To describe the performance of a thermoelectric material, we employ the material figure-of-merit zT, given by Equation 1.3, where T is the absolute temperature, σ is the electrical conductivity, α is the Seebeck coefficient, κ_e is the electronic contribution to the thermal conductivity, and κ_L is the lattice (phonon) contribution to the thermal conductivity [8, 18]. The term $\alpha^2\sigma$ term in the numerator is referred to as the power factor. The electronic contribution to the thermal conductivity can be written as $\kappa_e = L\sigma T$, where L is the Lorenz number, so $\kappa_L = \kappa - L\sigma T$.

$$zT = \frac{\alpha^2\sigma T}{\kappa_e + \kappa_L} \tag{1.3}$$

Thus, designing high-performing thermoelectric materials is a complex optimization problem that requires increasing the Seebeck coefficient and electrical conductivity, while minimizing the thermal conductivity. Unfortunately, these properties have competing behaviors, as increasing the electrical conductivity often reduces the Seebeck coefficient and increases the electronic contribution to the thermal conductivity. Therefore, the thermoelectric quality factor, B, is introduced as a means to decouple competing effects and elucidate strategies to optimize thermoelectric performance.

1.2.1 Thermoelectric Quality Factor

The material properties that comprise zT are functions of the reduced Fermi level, η (also called the reduced chemical potential) (Figure 1.1a). The reduced Fermi level is given by $\eta = E_F/k_BT$, where E_F is the Fermi level (electron chemical potential), and the reduced Fermi level depends on the doping level (i.e., carrier concentration), such that η increases monotonically with increasing carrier concentration. The exact relationship between η and carrier concentration (n or p) depends on the nature (shape) of the band structure. The Seebeck coefficient (magnitude) decreases with increasing η, while the total thermal conductivity and the electrical conductivity both increase with η. Because of these competing effects, the zT reaches a maximum value at an optimal carrier concentration, or reduced Fermi level. The maximum zT that a thermoelectric material can achieve when it is optimally doped is determined by its dimensionless thermoelectric quality factor, B, which is independent of doping (Equation 1.4). As B increases, the peak zT that can be achieved when the material is optimally doped also increases (Figure 1.1b) [18, 19].

$$B \propto \frac{N_V}{m_I^* \kappa_L} \tag{1.4}$$

The quality factor, which is derived in Chapter 2, is proportional to the valley (band) degeneracy (N_V) and inversely related to the lattice thermal conductivity (κ_L) and to the inertial effective mass (m_I^*). While a reduction in the lattice thermal conductivity is crucial for optimizing thermoelectric performance [20–27], this dissertation centers on optimizing the electronic transport properties of thermoelectrics, namely by increasing N_V and decreasing m_I^*. The valley degeneracy describes the number of carrier pockets (Fermi surface pockets) contributing to transport at a given Fermi level, while the inertial effective mass determines the velocity, and hence, mobility of the charge carrier and is inversely related to the curvature of the electronic dispersion near the band edge (valence band edge for holes and conduction band edge for electrons). Low inertial effective masses are beneficial because they lead to higher electrical conductivity, σ, and high valley degeneracy is

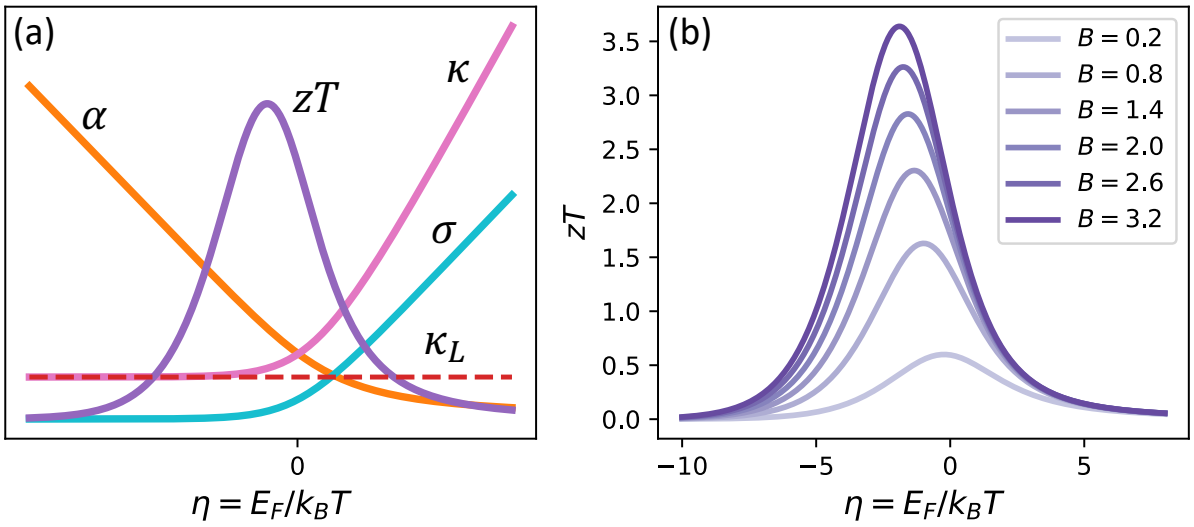

Figure 1.1: (a) The thermoelectric figure-of-merit, zT, depends on the Seebeck coefficient, α, the electrical conductivity, σ, and the (total) thermal conductivity, κ, which all have different dependencies on the reduced Fermi level, η, such that the zT reaches a peak value at an optimal value of η, which is a function of doping level. (b) The thermoelectric quality factor, B, determines the maximum zT that can be achieved in a material as a function of doping level (or η). As B increases, the maximum zT increases. κ_L is the lattice thermal conductivity, and E_F is the Fermi level. Figure reproduced with permission from M. K. Brod, S. Guo, Y. Zhang and G. J. Snyder. *MRS Bulletin*, 47, 573–583 (2022). Copyright 2022 by the Author(s), under exclusive License to the Materials Research Society.

beneficial because of the trade-off between electrical conductivity and the Seebeck coefficient with respect to the reduced chemical potential, η, and hence, carrier concentration (see Figure 1.1). The electrical conductivity increases with η specifically because of the associated increase in carrier concentration ($\sigma \propto n$), while the relationship between α and η is not actually related to the carrier concentration itself (its dependence on the carrier concentration is a consequence of its dependence on η). Thus, high valley degeneracy partially resolves the trade-off between α and σ with respect to η, in that it allows for higher carrier concentrations (increased σ) without increasing η (α is not reduced).

1.2.2 Electronic Band Engineering

Electronic band engineering in reciprocal-space ($\boldsymbol{k}$-space) is a popular and highly effective approach for enhancing the electronic components (i.e., N_V and m_I^*) of the thermoelectric quality factor, B [8, 28–35]. Specifically, it is desirable to engineer bands that have high curvature (low inertial effective mass) and multiple carrier pockets near the band edge (high valley degeneracy), assuming minimal inter-valley scattering [36].

A large portion of this dissertation focuses on achieving high valley degeneracy, which can be achieved in two ways. The first is to have band extrema (valence band maximums (VBMs) or conduction band minimums (CBMs)) at lower symmetry points in the Brillouin zone (BZ) of higher-symmetry crystals. In other words, it is better to have band extrema at $\boldsymbol{k}$-vectors that are located on as few symmetry operators (e.g., mirror planes, glide planes, rotation axes, inversion centers, etc.) as possible. When a point is located on a symmetry operator, that symmetry operation maps the point back onto itself, so no additional copies of that point are generated. However, if a point is located off that symmetry operator, the symmetry operation generates copies of that point. For instance, a four-fold rotation axis would create three additional copies (four total) and a mirror plane would create one additional copy (see Figure 1.2). Therefore, when a point in the BZ has lower symmetry (located on fewer symmetry operators) and the crystal itself has higher symmetry,

there are more symmetrically equivalent copies of this point inside the BZ. The Γ-point ($\boldsymbol{k} = 0$) is the highest-symmetry point, located at the center of the BZ, and it always has a degeneracy of $N_V = 1$ associated with it. Thus, it is generally desirable to have band extrema located *off* the Γ-point.

The second way to increase valley degeneracy is to have multiple VBMs (p-type) or CBMs (n-type) converged in energy at the same or different $\boldsymbol{k}$-point. Due to inter-band scattering, it is generally more beneficial to have bands converged at distant $\boldsymbol{k}$-points, rather than the same $\boldsymbol{k}$-points [36]. Band convergence can be achieved through numerous routes, such as alloying, strain, temperature, and symmetry distortions, and it has proven effective in numerous thermoelectric systems, such as IV-VI semiconductors [29, 37–39], half-Heuslers [31, 40], Bi_3Te_2 [41], Mg_2(Si, Ge, Sn) [42, 43], and $CoSb_3$ skutterudites [44].

In addition to high valley degeneracy, Fermi surfaces characterized by carrier pocket anisotropy, non-parabolicity, and low-dimensional-like transport (in bulk 3D crystals) are also predicted to be beneficial for thermoelectric performance [34, 45, 46]. Band structures with these types of non-ellipsoidal carrier pockets behave like bands that have very high valley degeneracy in that higher carrier concentrations can be achieved at given η, yielding higher power factor [34,47]. Fermi surfaces characterized by high valley degeneracy and non-parabolic, anisotropic, and/or low-dimensional carrier pockets can be generalized as complex Fermi surfaces. The degree of high valley degeneracy, and/or carrier pocket anisotropy can be described by a single value known as the Fermi surface complexity factor, $N_V^* K^*$, where N_V^* is the effective valley degeneracy and K^* describes the effective anisotropy of the carrier pockets [34]. In general, we want to engineer *complex Fermi surfaces*, for optimal thermoelectric performance.

1.3 Dissertation Overview

The primary objective of this dissertation is to explore the chemistry behind high valley degeneracy and, more generally, complex Fermi surfaces in an array of thermoelectric materials in order to

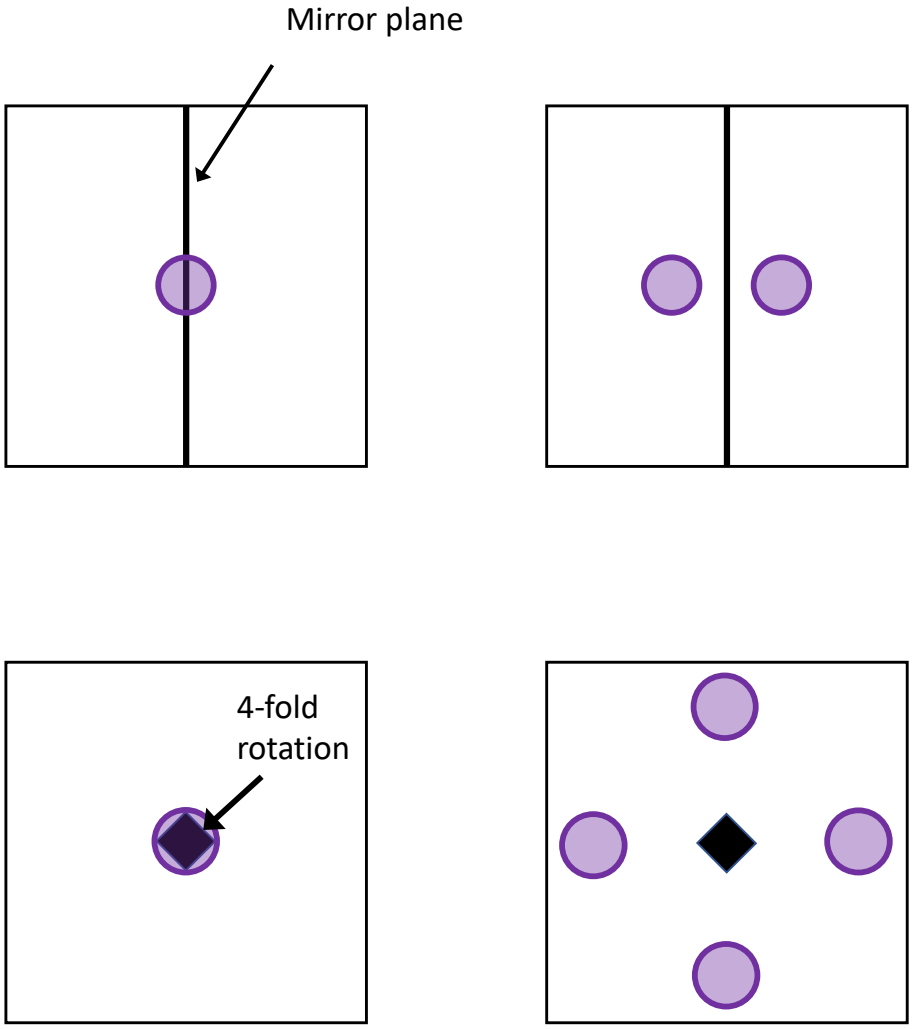

Figure 1.2: Illustration of how the symmetry of a point influences its degeneracy, using a mirror plane and four-fold rotation axis as examples. When the point is located on top of a symmetry operator, no additional copies of that point are made. However, when the point is located off the symmetry operator, then copies of that point are made in accordance with the symmetry operation.

understand and predict chemical trends in thermoelectric performance. This dissertation aims to explore not only *how* to modify band structures in $\boldsymbol{k}$-space, but also *why* band structures behave and change the way they do. We employ the tight-binding (TB) method, or Linear Combination of Atomic Orbitals (LCAO), as the overarching orbital-chemistry framework for understanding the behavior of complex electronic structures. Additional methods include DFT, crystal orbital Hamilton population (COHP) calculations, and group theory. The DFT calculations are performed using the Vienna ab intio Simulation Package (VASP) [48–50] using the Perdew-Burke-Ernzerhof (PBE) [51] exchange-correlation functional. All of the DFT-based COHP calculations were performed using the Local-Orbital Basis Suite Towards Electronic-Structure Reconstruction (LOBSTER) software [52–54]. The first part of Chapter 2 gives an introduction to thermoelectric transport and a derivation of the thermoelectric quality factor. In the second part of Chapter 2, an overview of the TB method as a means to interpret and engineer electronic band structures is provided.

In Chapter 3, we develop a TB framework that describes the valence band (VB) structure of IV-VI rock salt semiconductor materials like PbTe. Then, we use this framework to explain the chemical origins of high valley degeneracy in PbTe, one of the best-performing thermoelectric materials, by analyzing the symmetry of the VB crystal orbitals and deriving analytical expressions that describe the VB energy throughout reciprocal space. Next, in Chapter 4, we extend the TB model developed in Chapter 4 to understand how the complexity of the VB Fermi surface in PbTe (and other IV-VI rock salt compounds) can be further enhanced by converging the energies of the VB edge at multiple different $\boldsymbol{k}$-points. We then identify three basic types of Fermi surface geometries that may arise in this materials system with different levels of convergence, and we introduce and discuss transport models for these different types of Fermi surfaces to evaluate the their relative predicted performances. Chapters 3 and 4 are based on work published in *Chemistry of Materials* 32, 22, 9771–9779 (2020) [55] and *Journal of Materials Chemistry A*, 9, 12119-12139 (2021) [47].

In Chapter 5, we return to the IV-VI semiconductor framework introduced in Chapters 3-4, but this time applied to GeTe, which undergoes a cubic to rhombohedral transformation at lower

temperature. The change in crystal structure in accompanied by a change in the electronic structure, which affects the valley degeneracy and Fermi surface complexity. Thus, in this chapter, we go beyond the cubic (rock salt) system in order to better understand how and *why* the rhombohedral distortion influences the electronic structure, specifically the valence band degeneracy. Here, we show that a simple atomic-orbital framework based on the TB model can explain changes to the band structure upon the cubic to rhombohedral transformation.

Chapter 6 explores chemical trends in the band structures of transition-metal based half-Heusler (hH) semiconductors to explain how to engineer high valley degeneracy for both n-type and p-type hH compounds. We show that the techniques to achieve high N_V are quite similar between the n-type and p-type versions because similar atomic orbitals dictate the behavior of both the valence and conduction band edges. Furthermore, we identify and explain how different orbital interactions influence the band energies using COHP calculations, group theory, and TB. We show that recognizing avoided crossings (also known as anti-crossings) is crucial for fully understanding the chemistry of the band edges in hH compounds.

Finally, in 7, we explore the origins of the low-symmetry, highly degenerate CBM in Mg_3Sb_2, a high-performing mid-to-low temperature n-type thermoelectric material. The chemical origins of this low-symmetry CBM are important for understanding alloying strategies that tune the electron mobility and carrier pocket anisotropy. While prior studies focused on Mg–Mg interactions, we show that Mg–Sb interactions can explain the low-symmetry CBM in addition to changes in electronic properties upon alloying. The importance of Mg–Sb interactions are shown using DFT, COHP, and TB calculations.

Theoretical Background

2.1 Derivation of Quality Factor

In this section we derive the thermoelectric quality factor, B, for a band structure characterized by parabolic bands, acoustic-phonon scattering (deformation potential scattering), and minimal intervalley scattering [18, 19, 36, 56–60]. We employ the reduced variables, $\varepsilon = E/k_BT$ and $\eta = E_F/k_BT$, where E is the energy below (p-type) or above (n-type) the band edge (transport edge) and η is the reduced Fermi level (E_F).

To derive the thermoelectric quality factor, B, we use the effective mass (m^*) model, also known as the single parabolic band (SPB) model, to describe thermoelectric transport properties [18,56–58]. For this derivation, we assume that the electrons are free-electron-like and form spherical, parabolic bands ($E = \frac{\hbar^2|k|^2}{2m^*}$), with a density of states (DOS), g, given below. Note that the effective mass that is used to define the DOS is given the label, m^*_{DOS}.

$$g(E) = \frac{\sqrt{2}(m^*_{DOS})^{3/2}}{\pi^2\hbar^3}E^{1/2} \tag{2.1}$$

We define an energy-dependent transport function, $\sigma_E(E)$, given by Equation 2.2. We assume that the particles move with an average squared velocity, $\langle v^2\rangle$, and that on average each particle encounters a scattering event after a characteristic relaxation time, τ.

$$\sigma_E(E) = e^2\langle v(E)^2\rangle\tau(E)g(E) \tag{2.2}$$

Because the group velocity, v_g, of the carriers is given by the slope of the electronic dispersion ($v_g = \partial E/\partial k$), the velocity is simply $v(E) = \sqrt{2E/m^*}$ for a spherical band. Moreover, because we assume isotropy, we can replaced $\langle v^2\rangle$ with $v^2/3$. We can also use the assumption that scattering time is inversely related to the DOS (from Fermi's golden rule), which is is proportional to $E^{1/2}$ (Equation 2.1). Therefore, we assume that τ is of the form $\tau = \tau_0\varepsilon^{-1/2}$. Then, we can write the scattering constant as $\tau_0 = m^*\mu_0/e$ (Drude model), where μ_0 is the carrier mobility parameter.

Substituting in our energy-dependent expressions for v^2, τ, and g, we can obtain an analytical form of our transport function, σ_E, which is proportional to the energy from the transport edge.

$$\sigma_E(E) = \frac{e\mu_0(2m^*_{DOS})^{3/2}(k_BT)^{1/2}}{3\pi^2\hbar^3}E \tag{2.3}$$

All three electronic components of the zT (α, σ, and κ_e) equations can be written as convolutions of the electronic transport function and various selection functions, which are related to the Fermi-Dirac distribution, f, and the Fermi level, E_F.

$$\sigma = \int \sigma_E(E)\frac{-\partial f}{\partial E}dE \tag{2.4}$$

$$\alpha = \frac{1}{\sigma e}\int \sigma_E(E)\left(\frac{E-E_F}{T}\right)\frac{-\partial f}{\partial E}dE \tag{2.5}$$

$$\kappa_e = \frac{1}{e^2}\int \sigma_E(E)\left(\frac{(E-E_F)^2}{T}\right)\frac{-\partial f}{\partial E}dE - \alpha^2\sigma T \tag{2.6}$$

In order to simply the above expressions, we employ Fermi integrals of the form, $F_j(\eta)$.

$$F_j(\eta) = \int_0^\infty \frac{\varepsilon^j d\varepsilon}{1 + e^{\varepsilon - \eta}} \tag{2.7}$$

By substituting Equation 2.3 into Equation 2.4, substituting $\varepsilon k_B T$ for E, and making use of the integral, I_n, defined in below (derived using integration by parts) [61], we can rewrite the energy-dependent expression of σ for a parabolic band, assuming scattering inversely related to the DOS ($n = 1$ in Equation 2.8).

$$I_n = -\int_0^\infty x^n \frac{\partial f}{\partial x} dx = nF_{n-1}(\eta) \tag{2.8}$$

$$\sigma = \frac{e\mu_0 (2m^*_{DOS} k_B T)^{3/2}}{3\pi^2 \hbar^3} F_0(\eta) \tag{2.9}$$

We condense the pre-factor (energy-independent terms) of Equation 2.9 into the term σ_{E_0}, such that $\sigma = \sigma_{E_0} F_0(\eta)$. This gives us the following expression for σ_{E_0}.

$$\begin{aligned} \sigma_{E_0} &= \frac{e\mu_0 (2m^*_{DOS} k_B T)^{3/2}}{3\pi^2 \hbar^3} \\ &= \frac{e(2m_e k_B T)^{3/2}}{3\pi^2 \hbar^3} \mu_0 \left(\frac{m^*_{DOS}}{m_e} \right)^{3/2} \\ &= \frac{e(2m_e k_B T)^{3/2}}{3\pi^2 \hbar^3} \mu_w \end{aligned} \tag{2.10}$$

Here, we define the weighted mobility, $\mu_w = \mu_0 (m^*_{DOS}/m_e)^{3/2}$, where m^*_{DOS} can be related to the valley (or band) degeneracy, N_V, such that, $m^*_{DOS} = m^*_b N_V^{2/3}$. The parameter, m^*_b, is the DOS effective mass of a single band, and is referred to as the band effective mass. While we began this derivation assuming spherical bands, we can extend it to general ellipsoidal bands ($E(\boldsymbol{k}) = \frac{\hbar^2 k_x^2}{2m^*_x} + \frac{\hbar^2 k_y^2}{2m^*_y} + \frac{\hbar^2 k_z^2}{2m^*_z}$, where m^*_x, m^*_y, and m^*_z are the inertial effective masses along the Cartesian axes), by defining the band effective mass, such that $m^*_b = (m^*_x m^*_y m^*_z)^{1/3}$.

Next, we can obtain an expression for the Seebeck coefficient and show that it is only a function

of η, given that the shape of the dispersion is known (in this case spherical).

$$\alpha(\eta) = \frac{k_B}{e}\left(\frac{2F_1(\eta)}{F_0(\eta)} - \eta\right) \tag{2.11}$$

Then, using Equations 2.6, 2.9, 2.11, and the relationship, $\kappa_e = L\sigma T$, we can obtain an expression for the Lorenz number, L, using Fermi integrals.

$$L(\eta) = \frac{k_B^2}{e^2}\left(\frac{3F_0(\eta)F_2(\eta) - F_1^2(\eta)}{F_0^2(\eta)}\right) \tag{2.12}$$

Like α, L is a function of only the reduced chemical potential, η. Finally, we can re-express the zT equation such that all of the η-independent terms are condensed into a single dimensionless, doping-independent parameter, the thermoelectric quality factor, B [18].

$$\begin{aligned} zT = \frac{\alpha^2\sigma T}{\kappa_L + \kappa_e} &= \frac{\alpha^2}{\frac{\kappa_L}{\sigma T} + L} \\ &= \frac{\alpha^2(\eta)}{\frac{\kappa_L}{T\sigma_{E_0}F_0(\eta)} + L(\eta)} \qquad = \frac{\alpha^2(\eta)}{\frac{(k_B/e)^2}{BF_0(\eta)} + L(\eta)} \end{aligned} \tag{2.13}$$

$$B = \left(\frac{k_B}{e}\right)^2 \frac{\sigma_{E_0}}{\kappa_L} T \tag{2.14}$$

Clearly, the quality factor is proportional to the electronic transport function coefficient, σ_{E_0}, and inversely related to the lattice thermal conductivity. By comparing Equations 2.10 and 2.14, it can be seen that the quality factor is proportional to the weighted mobility.

Furthermore, an expression for the carrier mobility parameter, μ_0, can be derived—assuming that acoustic-phonon scattering is the dominant scattering mechanism—using the deformation potential model [59,60]. The mobility parameter for acoustic-phonon scattering is derived from Fermi's Golden Rule (Equation 2.15), which states that the scattering rate $(1/\tau)$ of an electron with energy, E, and occupying state $\boldsymbol{k}$ to a state $\boldsymbol{k'}$, is related to the density of states and the relevant matrix

element ($M_{k',k}$) for the perturbation Hamiltonian, $\hat{\boldsymbol{H}}'$.

$$\frac{1}{\tau(\boldsymbol{k})} = \frac{2\pi}{\hbar} g(E) |M_{k',k}|^2 \tag{2.15}$$

Then, assuming $|M_{k',k}|^2$, which is related to the deformation potential and elastic constants, is independent of $\boldsymbol{k}$, it can be shown [59] that the mobility parameter for the SPB model is given by

$$\mu_0 = \frac{\pi e \hbar^4 C_l}{\sqrt{2} m_I^* (m_b^* k_B T)^{3/2} \Xi^2}. \tag{2.16}$$

In the above equation, Ξ is the deformation potential, C_l is the longitudinal elastic constant, and m_I^* is the inertial effective mass, which is related to the band curvature. In the expression for the weighted mobility, the $1/(m_b^*)^{3/2}$ term in the denominator (from Equation 2.16) cancels with the $(m_b^*)^{3/2}$ term in the numerator. Thus, the weighted mobility, and hence, quality factor is proportional to the valley degeneracy and inversely related to the inertial effective mass (Equation 1.4).

While this derivation of quality factor is based on the assumption that we are dealing with spherical—or more generally, ellipsoidal—parabolic bands, this quality-factor analysis can be extended to describe transport in more complex, non-ellipsoidal bands (using the Fermi surface complexity factor, $N_V^* K^*$, for example) [34].

2.2 Tight-Binding Model

The tight-binding (TB) method is a computationally inexpensive approach to approximate the electronic structures of molecules and crystalline solids using a basis set consisting of recognizable atomic orbitals (s, p, d, etc.). The TB method is often referred to as the Linear Combination of Atomic Orbitals (LCAO) because it asserts that electronic states in molecules or crystalline materials come from molecular or crystal wavefunctions that are linear superpositions of atomic-orbital

wavefunctions. This approximation is based upon the assumption that the electrons are "tightly bound" by the nucleus, so it is generally most effective in reproducing valence band structures, and more limited in reproducing bands deeper higher into the conduction band. That being said, even in cases where the TB model is limited in its ability to reproduce the conduction band structure, it can still be helpful in understanding the bonding and symmetry of the conduction band states, especially near the conduction band edge.

In this section, we first describe the TB method for determining the molecular orbital energy levels in a diatomic molecule. Then, we describe how to use the TB method to determine the electronic dispersion relationship for a crystalline material. In both the molecular and crystalline cases, the procedure involves determining the form of the molecular or crystalline wavefunctions and Hamiltonian operators and subsequently using Schrodinger's equation to solve for the energy levels. Finally, we explain how the TB method can be used predict and explain band behavior using simple atomic orbital pictures. Details on the TB model and methods used in this section can be found in Refs. 62, 63, 64, 6, and 65.

2.2.1 Tight-Binding Model of a Diatomic Molecule

In this section, we derive the energy levels of a diatomic molecule, based on the steps outlined in Refs. 6 and 63. First, we must write the molecular wavefunction for the diatomic molecule (ψ_m) as a linear combination, or superposition, of the two atomic orbital wavefunctions (ϕ_1 and ϕ_2),

$$\psi_m(\boldsymbol{r}) = c_1\phi_1(\boldsymbol{r}) + c_2\phi_2(\boldsymbol{r}) \tag{2.17}$$

where c_1 and c_2 are coefficients. The coefficients relate to how much each type of orbital contributes to the wavefunction, and we often refer to these contributions as describing the "character" of the energy state. For instance, if $|c_1|^2 > |c_2|^2$ for a given state, we would say that it has more orbital 1 character than orbital 2 character. We assume that the atomic-orbital wavefunctions are

orthonormal, such that

$$\langle \phi_i | \phi_j \rangle = \begin{cases} 1, & \text{if } i = j \\ 0, & \text{otherwise.} \end{cases} \tag{2.18}$$

The energy levels (ε_n) and molecular orbital wavefunctions ($\psi_{m,n}$) are the eigenvalues and eigenvectors (of index n), respectively, given by the time-independent Schrodinger equation,

$$\hat{\boldsymbol{H}} \psi_{m,n}(\boldsymbol{r}) = \varepsilon_n \psi_{m,n}(\boldsymbol{r}), \tag{2.19}$$

where $\hat{\boldsymbol{H}}$ is the Hamiltonian operator, which is an Hermitian operator defined by matrix elements of the form H_{ij}, such that

$$H_{ij} = \langle \phi_i | \, \hat{\boldsymbol{H}} \, | \phi_j \rangle \, . \tag{2.20}$$

The Hamiltonian for a generic diatomic molecule is given by

$$\hat{\boldsymbol{H}} = \begin{pmatrix} E_1 & H_{12} \\ H_{21} & E_2 \end{pmatrix} = \begin{pmatrix} E_1 & V \\ V & E_2 \end{pmatrix}, \tag{2.21}$$

where $H_{12} = H_{21} = V$, and V is the hopping integral, which describes the interaction strength between the two orbitals and depends largely on the interatomic separation and the amount of orbital overlap. E_1 and E_2 are the atomic-orbital energies, or on-site energies.

A schematic of a molecular orbital diagram for a diatomic molecule is given in Figure 2.1, showing the on-site energies, bonding and anti-bonding molecular orbital states (ε_- and ε_+), and bond energy b, which is defined later. From Equation 2.19, the energy levels ($\varepsilon_\pm$) and the coefficients $(c_1, c_2)_\pm$ of the molecular wavefunctions ($\psi_{m,\pm}$) can be found by solving for the eigenvalues and eigenvectors, respectively, of the Hamiltonian matrix, $\hat{\boldsymbol{H}}$.

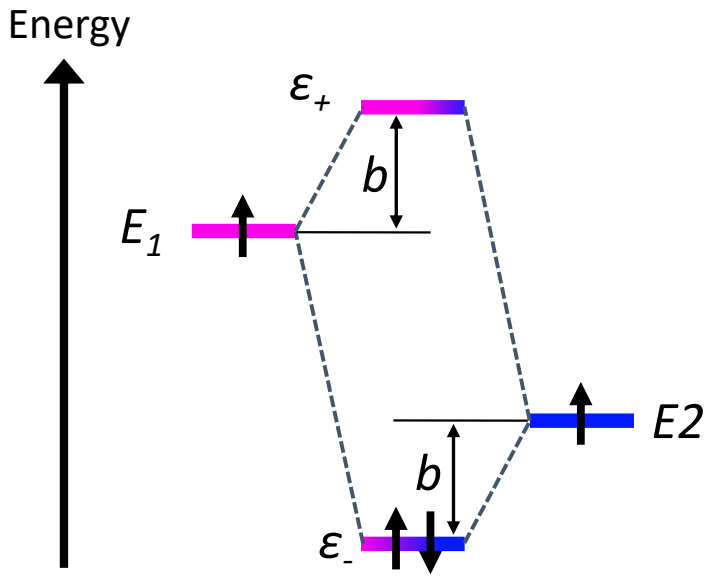

Figure 2.1: Molecular orbital bonding diagram for a diatomic molecule formed from the interaction between orbital 1 (shown with magenta coloring), with on-site energy E_1, and orbital 2 (shown with blue coloring), with on-site energy E_2. The bonding molecular orbital has an energy ε_- and the anti-bonding molecular orbital has an energy ε_+. The bond energy is given by b, and the colors (magenta and blue) are used to qualitatively represent the relative contribution of each atomic orbital to each molecular orbital. The bonding molecular orbital has more blue coloring to indicate that it has more orbital 2 character, and the anti-bonding molecular orbital has more magenta coloring to indicate that it has more orbital 1 character.

$$\varepsilon_{\pm} = \frac{E_1 + E_2}{2} \pm \frac{1}{2}\sqrt{(E_1 - E_2)^2 + 4V^2} \tag{2.22}$$

$$(c_1, c_2)_{\pm} = C_N \left(\frac{E_1 - E_2 \pm \sqrt{(E_1 - E_2)^2 + 4V^2}}{2V}, 1 \right) \tag{2.23}$$

Here, we use a plus sign (+) to denote the anti-bonding (higher energy) state and a minus sign (−) to denote the bonding (lower energy) state. C_N is a normalization coefficient that ensures the modulus of each eigenvector is equal to one. We can simplify the expression for the energy levels and wavefunction coefficients by defining a parameter, A, which describes half of the energy separation between the atomic orbitals ($A = \frac{1}{2}(E_1 - E_2)$) and a parameter, $\bar{E}$, which describes the average on-site energy ($\bar{E} = \frac{1}{2}(E_1 + E_2)$). Note that here we are assuming that $E_1 \geq E_2$.

$$\varepsilon_{\pm} = \bar{E} \pm \sqrt{A^2 + V^2} \tag{2.24}$$

$$(c_1, c_2)_{\pm} = C_N \left(\frac{A \pm \sqrt{A^2 + V^2}}{V}, 1 \right) \tag{2.25}$$

From Equation 2.25, it can be shown that if $E_1 = E_2$ ($A = 0$), the coefficients will be given by $(c_1, c_2)_+ = \frac{1}{\sqrt{2}}(|V|/V, 1)$ and $(c_1, c_2)_- = \frac{1}{\sqrt{2}}(-|V|/V, 1)$, which simplifies to $(c_1, c_2)_{\pm} = \frac{1}{\sqrt{2}}(\pm 1, 1)$ if $V > 0$, and $(c_1, c_2)_{\pm} = \frac{1}{\sqrt{2}}(\mp 1, 1)$, if $V < 0$. This means that for the case of a homopolar diatomic molecule, the bonding and anti-bonding states both have an equal contribution from each atomic orbital. Also, when $V < 0$, the orbitals are bonding when c_1 and c_2 have the same sign and anti-bonding when they have opposite signs (and vice-versa for $V > 0$). When $A > 0$, it can be shown that $|c_1|^2 < |c_2|^2$ for the bonding (−) molecular orbital and that $|c_1|^2 > |c_2|^2$ for the anti-bonding (+) molecular orbital. This means that the contribution from the higher-energy atomic orbital (orbital 1) is greater than the contribution of the lower-energy atomic orbital (orbital 2) in the anti-bonding molecular orbital state, and the contribution from the lower-energy atomic

orbital is greater in the bonding molecular orbital. Moreover, if $|V|$ decreases and/or A increases, the asymmetry in the atomic-orbital contributions to each molecular-orbital state increases, such that the anti-bonding state will have even more orbital 1 character, and the bonding state will have even more orbital 2 character. In the limit where $|V|$ approaches zero, the coefficients for the higher-energy state are given by $(c_1, c_2) = (1, 0)$ and the coefficients for the lower-energy state are $(c_1, c_2) = (0, 1)$, with the corresponding energies being E_1 and E_2, respectively.

We can also define a bond energy, b, which describes the energy difference between the on-site energies and the molecular orbital energies ($b = \varepsilon_+ - E_1 = E_2 - \varepsilon_-$), as shown in Figure 2.1 [66]. It can be shown that the bond energy is given by

$$b = \sqrt{V^2 + A^2} - A. \tag{2.26}$$

Thus, the bond energy increases with $|V|$ and decreases with A, which indicates that the bonding strength in the diatomic molecule increases with stronger orbital interactions and smaller energy separations between the interacting orbitals. For the case of a homopolar diatomic molecule ($E_1 = E_2$), the energy levels are simply given by $\varepsilon_\pm = E_1 \pm V$, and the bond energy is simply $b = |V|$.

2.2.2 Tight-Binding Model of a Crystalline Solid

To move from molecular-orbital energy levels in isolated molecules to electronic dispersions in crystalline solids, we must the TB method to approximate electronic wavefunctions in periodic, crystalline materials. Any electron wavefunction in a periodic crystal must obey Bloch's theorem (Equation 2.27), which states that the wavefunction at a location $\boldsymbol{r} + \boldsymbol{R}$, where $\mathbf{R}$ is any lattice translation vector (in real space), must be equal to the wavefunction at $\boldsymbol{r}$ times a Bloch phase factor of the form $e^{-i\boldsymbol{k}\cdot\boldsymbol{R}}$ [67].

$$\psi(\boldsymbol{r} + \boldsymbol{R}) = e^{-i\boldsymbol{k}\cdot\boldsymbol{R}}\psi(\boldsymbol{r}) \tag{2.27}$$

Functions that satisfy Bloch's theorem must be linear combinations of Bloch functions, defined as

$$\psi(\boldsymbol{r}) = e^{-i\boldsymbol{k}\cdot\boldsymbol{r}}u(\boldsymbol{r}), \tag{2.28}$$

where $u(\boldsymbol{r})$ obeys the periodicity of the lattice, such that $u(\boldsymbol{r}+\boldsymbol{R}) = u(\boldsymbol{r})$.

Now, using the LCAO approach, we can write out the expression for the crystal wavefunction (ψ_c), which is a function of $\boldsymbol{k}$ and $\boldsymbol{r}$, as a linear combination of atomic-orbitals wavefunctions in their Bloch form (ϕ_α), where α denotes a specific atomic orbital. The number of electronic bands will be equal to the number of elements in 2.29 (i.e., the number of c_α coefficients).

$$\psi_c(\boldsymbol{k},\boldsymbol{r}) = \sum_\alpha c_\alpha(\boldsymbol{k})\phi_\alpha(\boldsymbol{k},\boldsymbol{r}) \tag{2.29}$$

$$\phi_\alpha(\boldsymbol{k},\boldsymbol{r}) = \frac{1}{\sqrt{N}}\sum_j^N e^{-i\boldsymbol{k}\cdot\boldsymbol{R_j}}a_\alpha(\boldsymbol{r}-\boldsymbol{R_j}) \tag{2.30}$$

In the above equation, N represents the number of lattice sites in the crystal, $a_\alpha(\boldsymbol{r})$ is the function (constrained by the periodicity of the lattice) associated with the atomic orbital labelled α, and $\boldsymbol{R_j}$ are lattice translations. The proof that Equation 2.30 obeys Bloch's theorem is as follows (from Ref. 67):

$$\begin{aligned}
\phi_\alpha(\boldsymbol{k},\boldsymbol{r}+\boldsymbol{R}) &= \frac{1}{\sqrt{N}}\sum_j^N e^{-i\boldsymbol{k}\cdot\boldsymbol{R_j}}a_\alpha(\boldsymbol{r}-\boldsymbol{R_j}+\boldsymbol{R}) \\
&= \frac{1}{\sqrt{N}}e^{-i\boldsymbol{k}\cdot\boldsymbol{R}}\sum_j^N e^{-i\boldsymbol{k}\cdot(\boldsymbol{R_j}-\boldsymbol{R})}a_\alpha(\boldsymbol{r}-(\boldsymbol{R_j}-\boldsymbol{R})) \\
&= \frac{1}{\sqrt{N}}e^{-i\boldsymbol{k}\cdot\boldsymbol{R}}\sum_l^N e^{-i\boldsymbol{k}\cdot\boldsymbol{R_l}}a_\alpha(\boldsymbol{R_l}) \\
&= e^{-i\boldsymbol{k}\cdot\boldsymbol{R}}\phi_\alpha(\boldsymbol{k},\boldsymbol{r})
\end{aligned} \tag{2.31}$$

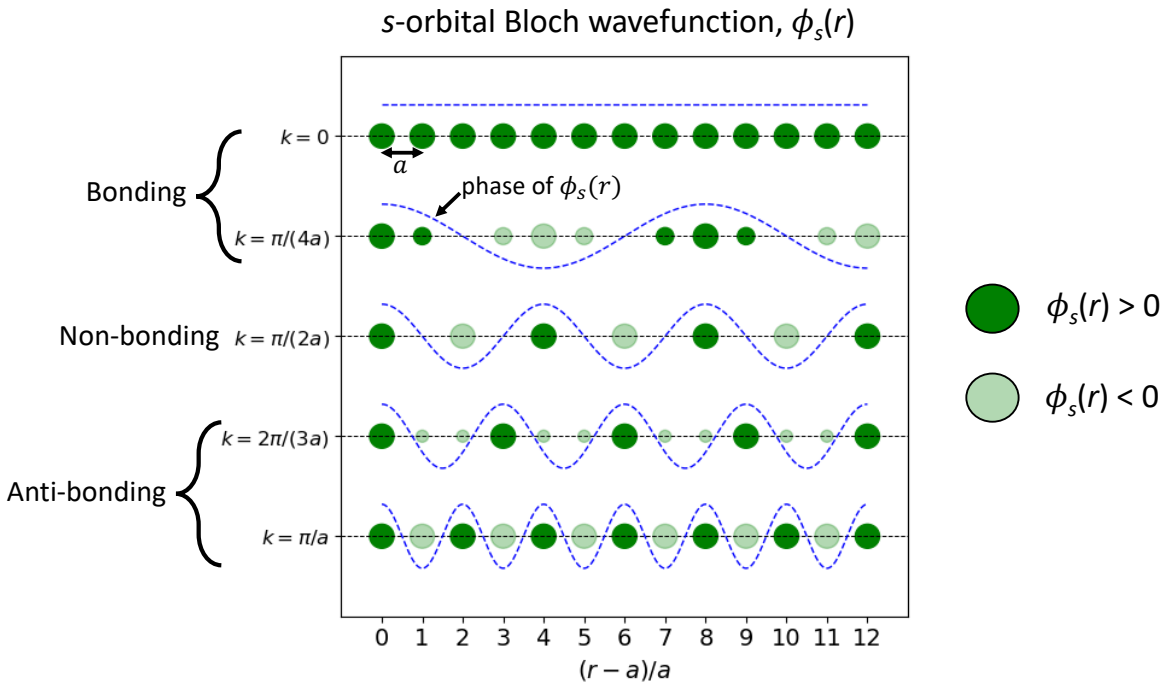

Figure 2.2: Schematic representation of 1D s-orbital Bloch functions (at position, r) for different values of k in a periodic 1D lattice (defined by a lattice constant, a) comprised of one s-orbital per unit cell. The blue dashed line represents the real-part of the wavefunction phase, while the wavefunction itself is represented using the green circles, which represent the spherically symmetric s-orbitals. The shading of the s-orbitals (dark green versus light green) represents the sign of the phase (positive versus negative), while the size of the circles represents the amplitude. Interactions between neighboring orbitals that have phases with the same sign are bonding, while interactions between neighboring orbitals that have opposite-signed phases are anti-bonding.

Again, we assume that the atomic-orbital basis is orthonormal, and must therefore satisfy the following expression:

$$\langle \phi_i(\boldsymbol{r}) | \phi_j(\boldsymbol{r} + \boldsymbol{R}) \rangle = \begin{cases} 1, & \text{if } i = j \text{ and } \boldsymbol{R} = 0 \\ 0, & \text{otherwise.} \end{cases} \tag{2.32}$$

A real-space visualization of a 1D s-orbital Bloch wavefunction for different values of k is shown in Figure 2.2. In this example, all of the lattice vectors $\boldsymbol{R_j}$ are of the form $n_j a$, where n_j is an integer, and a is the lattice constant of the infinite 1D chain of s-orbitals.

To determine the energy levels (ε_n) and wavefunctions ($\psi_{c,n}$) of the crystal at a certain $\boldsymbol{k}$-point,

we must solve Schrodinger's equation (Equation 2.33) at that $\boldsymbol{k}$-point.

$$\hat{\boldsymbol{H}}(\boldsymbol{k})\psi_{c,n}(\boldsymbol{k}) = \varepsilon_n(\boldsymbol{k})\psi_{c,n}(\boldsymbol{k}). \tag{2.33}$$

This means finding the eigenvalues and eigenvectors of the Hamiltonian operator, $\hat{\boldsymbol{H}}$, given by the matrix elements,

$$H_{\alpha\beta}(\boldsymbol{k}) = \langle \phi_\alpha(\boldsymbol{k})| \, \hat{\boldsymbol{H}}(\boldsymbol{k}) \, |\phi_\beta(\boldsymbol{k})\rangle \,, \tag{2.34}$$

where α and β label two different atomic orbital types belonging to the atomic-orbital basis set. As shown in Ref. 63, these Hamiltonian matrix elements can be constructed by summing over all of the terms, $V^{(j)}_{\alpha,\beta} e^{-i\boldsymbol{k}\cdot\boldsymbol{r}_j^{(\boldsymbol{\alpha}\rightarrow\boldsymbol{\beta})}}$, where $V^{(j)}_{\alpha,\beta}$ is a Slater-Koster matrix element [65] between orbitals α (located at a position j_1) and β (located at a position j_2), and $\boldsymbol{r}_{\boldsymbol{j}}^{(\boldsymbol{\alpha}\rightarrow\boldsymbol{\beta})}$ are the real-space vectors between each α-β neighbor pair, such that $\boldsymbol{r}_{\boldsymbol{j}}^{(\boldsymbol{\alpha}\rightarrow\boldsymbol{\beta})} = \boldsymbol{r}_{\boldsymbol{j_2}} - \boldsymbol{r}_{\boldsymbol{j_1}}$.

$$H_{\alpha\beta}(\boldsymbol{k}) = \sum_j V^{(j)}_{\alpha,\beta} e^{-i\boldsymbol{k}\cdot\boldsymbol{r}_j^{(\boldsymbol{\alpha}\rightarrow\boldsymbol{\beta})}} \tag{2.35}$$

$$V^{(j)}_{\alpha,\beta} = \langle a_\alpha(\boldsymbol{r}_{\boldsymbol{j_1}})| \, \hat{\boldsymbol{H}} \, |a_\beta(\boldsymbol{r}_{\boldsymbol{j_2}})\rangle \tag{2.36}$$

The matrix elements defined in Equation 2.36 can be parameterized using the methods outlined in Ref. 65 and are known as Slater-Koster matrix elements. We construct these parameterized matrix elements using a set of fundamental hopping parameters of the form $V_{ll'm}$, where l and l' describe basic atomic orbital types (s, p, d, etc.), and m represents the bonding type (σ, π, δ, etc.). Illustrations of these fundamental interaction types are given in Figure 2.3. Interaction types that are in-phase, or bonding, are described by values of $V_{ll'm}$ that are less than zero, while interaction types that are out-of-phase, or anti-bonding, are characterized by values of $V_{ll'm}$ that are greater than zero. In this dissertation, we assert that $V_{ss\sigma} < 0$, $V_{sp\sigma} > 0$, $V_{pp\sigma} > 0$, and $V_{pp\pi} < 0$. Moreover,

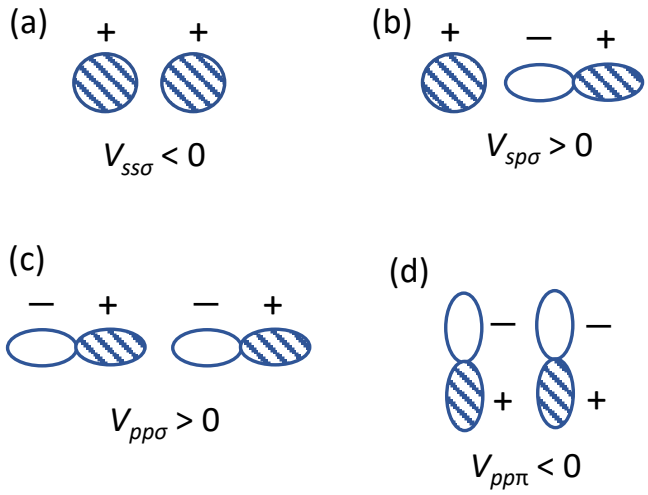

Figure 2.3: Sketch of fundamental interaction parameters between s and p orbitals, such the shading (versus no shading) represents the phase (+ or −) of the atomic orbitals. In-phase interactions are bonding, while out-of-phase interactions are anti-bonding. The convention of the interaction parameters ($V_{ll'm}$) is such that (a) $V_{ss\sigma} < 0$, (b)$V_{sp\sigma} > 0$, (c) $V_{pp\sigma} > 0$, and (d) $V_{pp\pi} < 0$.

the magnitude of $V_{ll'm}$ describes the strength of the interaction and depends mainly on interatomic distance and the amount of overlap between the orbitals.

Examples of the Slater-Koster matrix elements between s and p orbitals are given in Table 2.1 [6, 65].

Table 2.1: Expressions for Slater-Koster matrix elements, where l, m, and n, are the direction cosines of the vector between the atomic-orbital states described.

Matrix element	Expression
$V_{s,s}$	$V_{ss\sigma}$
V_{s,p_x}	$lV_{sp\sigma}$
V_{s,p_y}	$mV_{sp\sigma}$
V_{s,p_z}	$nV_{sp\sigma}$
V_{p_x,p_x}	$l^2V_{pp\sigma} + (1-l^2)V_{pp\pi}$
V_{p_y,p_y}	$m^2V_{pp\sigma} + (1-m^2)V_{pp\pi}$
V_{p_z,p_z}	$n^2V_{pp\sigma} + (1-n^2)V_{pp\pi}$
V_{p_x,p_y}	$lmV_{pp\sigma} - lmV_{pp\pi}$
V_{p_x,p_z}	$lnV_{pp\sigma} - lnV_{pp\pi}$
V_{p_y,p_z}	$mnV_{pp\sigma} - mnV_{pp\pi}$

Finally, when $\alpha = \beta$ and $j_1 = j_2$ (i.e., the same orbital on the same lattice site), $V_{\alpha\alpha} = E_\alpha$, where E_α is the on-site energy of the α atomic orbital.

2.2.3 Crystal Orbital Hamilton Population from Tight-Binding

In this section, we show a brief derivation of the crystal orbital Hamilton population (COHP) [52] using the TB, or LCAO, framework. The derivation follows from that provided in Ref. 68.

Assuming that our crystal wavefunction (ψ_c) is given by a superposition of atomic-orbital Bloch wavefunctions (Equation 2.29), the energy levels at each $\boldsymbol{k}$-point ($\varepsilon_n(\boldsymbol{k})$) are given by

$$\begin{aligned}
\varepsilon_n(\boldsymbol{k}) &= \langle \psi_{c,n}(\boldsymbol{k}) | \, \hat{\boldsymbol{H}}(\boldsymbol{k}) \, | \psi_{c,n}(\boldsymbol{k}) \rangle \\
&= \sum_{\alpha,\beta} c_\alpha^{n*}(\boldsymbol{k}) c_\beta^n(\boldsymbol{k}) H_{\alpha\beta}(\boldsymbol{k}) \\
&= \sum_\alpha |c_\alpha^n(\boldsymbol{k})|^2 H_{\alpha\alpha}(\boldsymbol{k}) + 2 \sum_{\alpha<\beta} Re(c_\alpha^{n*}(\boldsymbol{k}) c_\beta^n(\boldsymbol{k}) H_{\alpha\beta}(\boldsymbol{k}))
\end{aligned} \tag{2.37}$$

where $\psi_{c,n}$ are the eigenfunctions (wavefunctions) for the nth band at a given $\boldsymbol{k}$-point, and c_α^{n*} is the complex conjugate of c_α^n. The final expression from Equation 2.37 can be divided into two terms, the local term (first term) and the non-local term (second term). If we assume that only nearest-neighbor interactions are important (which is not always the case), then we can make the approximation $H_{\alpha\alpha} \simeq E_\alpha$. Thus, the local term simply yields the on-site energies weighted by their relative contributions to the nth band at a specific $\boldsymbol{k}$-point.

The second term is defined as the COHP (Equation 2.38) for a given band at a given $\boldsymbol{k}$-point (band-resolved, $\boldsymbol{k}$-resolved COHP), and it describes the interactions between atomic orbitals on different lattice sites. In order to obtain the partial COHP (pCOHP) between two orbitals, we simply only sum over the relevant terms to describe that interaction.

$$\mathrm{COHP}_n(\boldsymbol{k}) = 2 \sum_{\alpha<\beta} Re(c_\alpha^{n*}(\boldsymbol{k}) c_\beta^n(\boldsymbol{k}) H_{\alpha\beta}(\boldsymbol{k})) \tag{2.38}$$

2.2.4 Understanding Band Behavior from Tight-Binding

Tight-binding is a powerful tool for understanding band behavior in terms of simple atomic orbital pictures [62, 66]. This section contains a brief introduction into how tight-binding can help us understand the behavior of electronic bands, such as location of the band extrema and the band widths.

One-Band Model

Consider an infinite 1D chain of a single atomic orbital type with a lattice constant, a. If we consider only nearest-neighbor interactions, the 1D crystal orbital wavefunction is given by $\psi_c = \phi_\alpha$ (see equation 2.30), and we can show that our Hamiltonian is given by $H = E_{at} + V(e^{-ika} + e^{iak}) = E_{at} + 2V\cos(ka)$, where E_{at} is the on-site energy and V is the Slater-Koster matrix element for the interaction. It is trivial to see that the eigenvalue of this solution $\varepsilon = E_{at} + 2V\cos(ka)$.

Here, we focus on two features of this simple band structure: how the band "runs" from $k = 0$ (Γ) and the band width. The direction that the band runs from $k = 0$ depends on the sign of V, and the band width depends on the magnitude of V. If $V < 0$, the band will reach a minimum of $-2|V|$ at Γ and a maximum of $2|V|$ at $k = \pm\frac{\pi}{a}$, the 1D Brillouin zone edge. Conversely, if $V > 0$, the band will reach the maximum at Γ and a minimum at the Brillouin zone edge. The band width, W, is defined as the difference in energy between the highest and lowest energy in the band, and it is trivial to see that, in this TB framework, the band width is given by $W = 4|V|$. Thus, increasing the interaction strength between the orbitals increases the band width.

This simple one-band model can guide us in predicting the difference between a band derived from s versus p orbitals. The bonding between s-orbitals is given by a negative-valued matrix element, $V_{ss\sigma}$, while σ-bonding between p-orbitals is given by a positive-valued matrix element, $V_{pp\sigma}$. Therefore, the band dispersion for the s-band is given by, $\varepsilon_s = E_s - 2|V_{ss\sigma}|\cos(ka)$, and the dispersion for the p-band is given by $\varepsilon_p = E_p + 2|V_{pp\sigma}|\cos(ka)$. Therefore, the s-orbital band

runs up in energy from $k = 0$, or Γ, and the σ-bonding p-orbital band runs down in energy from Γ (Figure 2.4). Also, while a 1D chain of σ-bonding p-orbitals runs down in energy from Γ, a chain of π-bonding p-orbitals runs up in energy because $V_{pp\pi} < 0$ (Figure 2.3). However, because p–p σ-bonding interactions are much stronger than the π-bonding interactions [6], we expect p-orbital bands to run down in energy from Γ, when both types of interactions are present. Moreover, as shown in Figure 2.4, when the strength of the interaction increases, the band width increases regardless of the orbital type.

This s- and p-orbital behavior can also be understood visually with simple atomic orbital sketches of the s- and p-orbital phases at different values of k (see Figure 2.4). The magnitude of the wave-vector, $|k|$, describes the spatial frequency, so it represents how frequently in real-space the phases of the orbitals change sign. Essentially, we can say that the sign of the orbital flips when r satisfies $e^{-ikr} = -1$ or $kr = n\pi$ ($n = \pm1, \pm3, \pm5$, etc.).[1] For instance, when $k = 0$, the phases of the orbitals never change ($kr = 0$) sign so all of the s-orbitals are in-phase (bonding) with both of their nearest-neighbors, while the p-orbitals are out-of-phase (anti-bonding) with both of their nearest-neighbors. At $k = \pm\frac{\pi}{2a}$, the phases change sign with a frequency of once for every two lattice translations ($2a$). Therefore, each orbital is bonding with one of its neighbors but anti-bonding with its other neighbor, making it a net non-bonding state. Finally, at the 1D Brillouin zone edge ($k = \frac{\pi}{a}$), the phase changes with a frequency of one time for every one lattice translation, so now every s-orbital is out-of-phase (anti-bonding) and every p-orbital is in-phase (bonding).

Clearly, the signs of the fundamental interaction parameters ($V_{ll'm}$) are not arbitrary or trivial, as they have a profound influence on the band dispersion. The sign of the parameter is directly to related to whether the orbitals are in-phase ($V < 0$) or out-of-phase ($V > 0$) at Γ. We can show that orbitals that are symmetric along the bonding axis (e.g., s-orbitals and π-bonding p-orbitals) must always be in-phase at $k = 0$ and that orbitals that are anti-symmetric (e.g., σ-bonding p-orbitals) along the bonding axis must always be out-of-phase at Γ. The atomic orbital Bloch functions (ϕ_α) at the Γ-point are of the form, $\phi_\alpha(r, k = 0) = \frac{1}{\sqrt{N}} \sum_j^N a_\alpha(r + n_j a)$ ($n_j = -1, -2, 0, 1, 2,$ etc),

[1] In higher dimensions (i.e., 2D or 3D) this condition generalizes to $e^{-i\boldsymbol{k}\cdot\boldsymbol{r}} = -1$ or $\boldsymbol{k} \cdot \boldsymbol{r} = n\pi$.

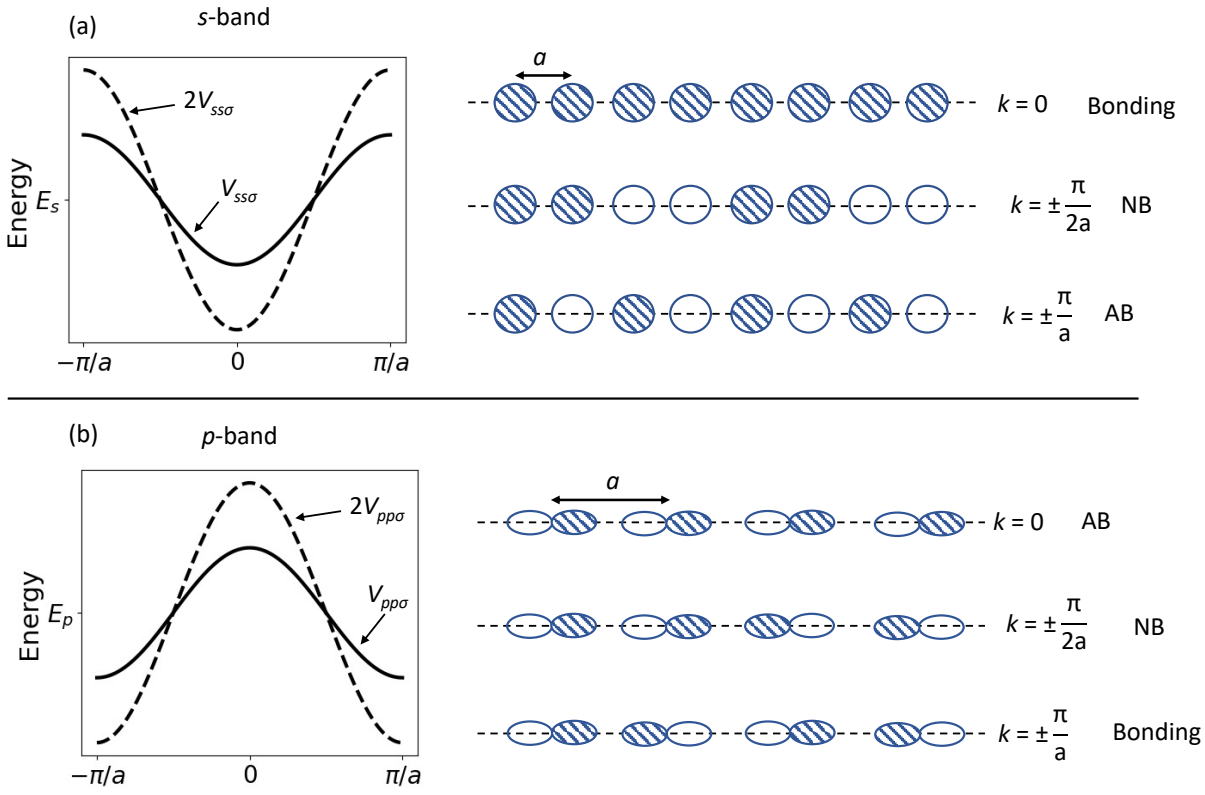

Figure 2.4: Tight-binding band structure and corresponding wavefunction ($\psi_c(k)$) sketches (periodic boundary conditions) for 1D chains of (a) s-orbitals and (b) σ-bonding p-orbitals. The dashed-line band structures are calculated for the case where the interaction parameters are $2V_{ss\sigma}$ or $2V_{pp\sigma}$, which are twice the magnitude of that used to calculate the solid-line bands ($V_{ss\sigma}$ or $V_{pp\sigma}$) . The s-orbital chain is in an entirely bonding configuration at $k = 0$, while it in a completely antibonding (AB) configuration at $k = \pm\pi/a$. Conversely, the σ-bonding p-orbital chain is completely antibonding (AB) at $k = 0$ and completely bonding at $k = \pm\pi/a$. Both are non-bonding (NB) at $k = \pm\pi/2a$. The shading in the orbital sketches represents the phase, such that in-phase overlaps are bonding and out-of-phase interactions are antibonding.

where $a_\alpha(r + n_j a) = a_\alpha(r)$ for all n_j. Thus, at the Γ-point, all of the orbitals separated by any lattice spacing $n_j a$ must have identical phases to each other, which means that atomic orbitals with symmetric phases are in-phase with both their nearest-neighbors, while atomic-orbitals that are anti-symmetric are out-of-phase with both nearest-neighbors. *To generalize, a band from a 1D chain of atomic orbitals (with one atomic orbital per unit cell) runs up in energy from* Γ *when the orbital is symmetric about the bonding axis, and it runs down in energy when the orbital is anti-symmetric about the bonding axis.*

Two-Band Model

Now, consider an infinite 1D lattice with a two-orbital basis, $\{\alpha, \beta\}$. The orbitals of the same type (α or β) are separated by distance, na ($n = \pm1, \pm2, \pm3$, etc.), and the α and β orbitals are separated by a distance of $\frac{na}{2}$ ($n = \pm1, \pm3, \pm5$, etc.). The 1D crystal wavefunction for this system is given by, $\psi_c = c_\alpha\phi_\alpha + c_\beta\phi_\beta$, and, assuming that interactions beyond nearest-neighbors are negligible, the Hamiltonian operator for this system is given by

$$\hat{\boldsymbol{H}} = \begin{pmatrix} \langle\phi_\alpha|\,\hat{\boldsymbol{H}}\,|\phi_\alpha\rangle & \langle\phi_\alpha|\,\hat{\boldsymbol{H}}\,|\phi_\beta\rangle \\ \langle\phi_\beta|\,\hat{\boldsymbol{H}}\,|\phi_\alpha\rangle & \langle\phi_\beta|\,\hat{\boldsymbol{H}}\,|\phi_\beta\rangle \end{pmatrix} = \begin{pmatrix} E_\alpha & V_{\alpha\beta} \\ V^*_{\alpha\beta} & E_\beta \end{pmatrix}. \tag{2.39}$$

Then, it can be shown that the energy of the energy levels (eigenvalues) as a function of k are given by the following expression (notice the form is analogous to Equation 2.22):

$$\varepsilon_\pm(k) = \frac{1}{2}(E_\alpha + E_\beta) \pm \frac{1}{2}\sqrt{(E_\alpha - E_\beta)^2 + 4|V_{\alpha\beta}(k)|^2} \tag{2.40}$$

Consider, for example, a 1D lattice where α is an M-s orbital and β is an X-s orbital, and $E_{M-s} > E_{X-s}$. It can be shown that the hopping integral $V_{\alpha\beta}$ is given by $V_{\alpha\beta}(k) = 2V_{ss\sigma}\cos(ka/2)$. The band structure and wavefunctions for each band is shown in Figure 2.5. The lower-energy band runs up in energy from Γ ($k = 0$), while the higher-energy band runs down in energy from Γ. At

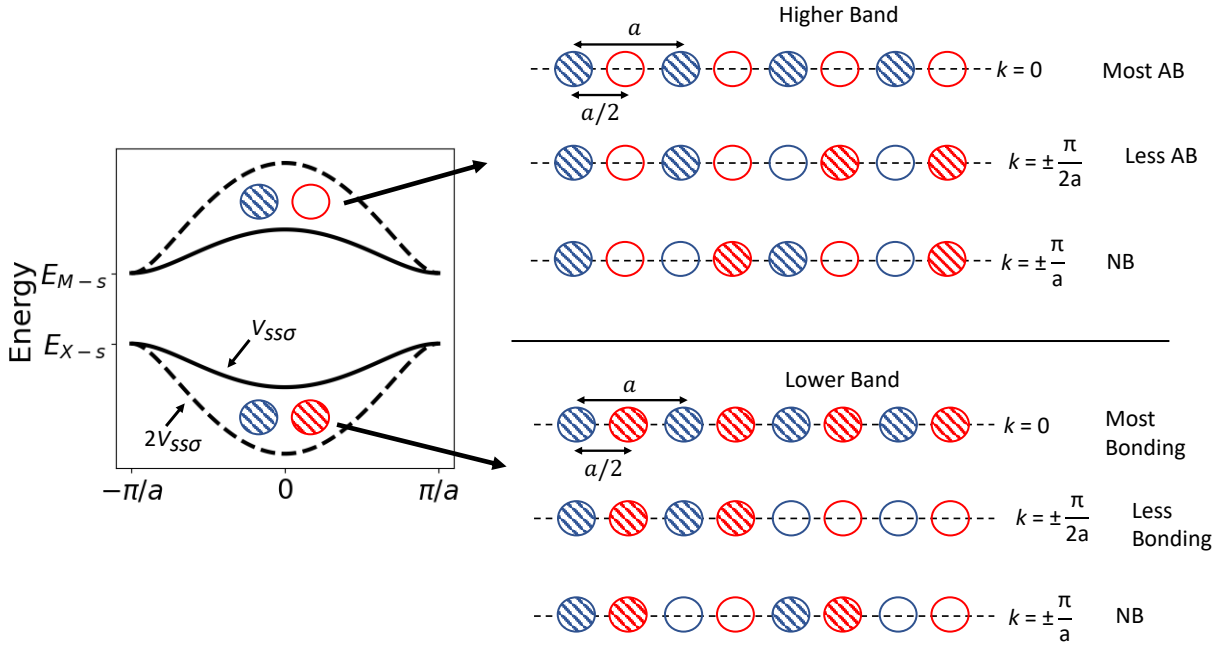

Figure 2.5: Tight-binding band structure and wavefunction ($\psi_c(k)$) sketches (with periodic boundaries) of a 1D chain of M-s and X-s orbitals. The dashed-line band structure is calculated for an interaction parameter $2V_{ss\sigma}$, while solid-line band structure is calculated using $V_{ss\sigma}$. The wavefunction for the top band is entirely anti-bonding (AB) at Γ and becomes non-bonding (NB) at $k = \pm\pi/a$. The wavefunction of the lower-band is entirely bonding at Γ and non-bonding (NB) at $k = \pm\pi/a$. The shading of the orbitals represents the phase ($\pm$), and the different colors (red versus blue) represent different atoms (M or X). Note that the size of the orbitals *does not* represent the relative magnitude of the atomic-orbital wavefunctions—all the orbitals are made to be the same size such that they only represent the symmetry of the phases ($\pm$).

first this may seem counter-intuitive based on the previous section because a single s-orbital band runs up in energy from Γ. However, when considering a lattice with two or more atomic sites in the basis, it is necessary to look at the symmetry of the crystal orbital units, rather than of the atomic orbitals alone [69].

Each band stems from a different crystal orbital unit ($a_c(r)$), which is one unit cell of the crystal orbital wavefunction at the Γ-point. Then, when $k \neq 0$, the wavefunction for that band is given by the linear combination of these crystal orbital functions ($a_c(r - n_j a)$) multiplied by the Bloch phase factors ($e^{-ikn_j a}$), where $n_j a$ is an integer number of lattice translations. Therefore, a band with a symmetric crystal orbital (along the bonding axis) will behave like the s-band (as described in the previous) section and increase in energy away from Γ. In this case, the lower-energy band comes

from a crystal orbital described by M-s and X-s orbitals that are the same phase (bonding), such that the *phase* (sign) of this crystal orbital unit is symmetric. Therefore, the lower energy band runs up in energy from Γ to the Brillouin zone edge. On the other hand, the higher-energy band comes from a crystal orbital described by the two out-of-phase (anti-bonding) s-orbitals. Thus, the crystal orbital phase is anti-symmetric with respect to the bonding axis, so this band behaves like a p-orbital band despite coming from s-orbitals. As a result, the band-gap for this two-band system is at $\pm\pi/a$. Moreover, increasing the s-s interaction strength increases the band width of each band (Figure 2.5).

The location of the bandgap in the 1D two-band model depends on the nature of the two orbitals. As we just showed, two s-orbitals leads to a bandgap at the Brillouin zone edge. For different orbital interactions, we can predict how the bands will run and the location of the bandgap, based on the symmetry of the bonding and anti-bonding crystal orbital units (Figure 2.6). Like the infinite 1D chain of two different atomic s-orbitals, a chain of two different σ-bonding p-orbitals gives a lower band with a symmetric crystal orbital and higher band with an anti-symmetric crystal orbital, so the bands should behave in an analogous manner to those in Figure 2.5. The same will be true for π-bonding p-orbitals. On the other hand, when the lattice contains one s- and one p-orbital, the bonding band (lower band) has an anti-symmetric crystal orbital and runs down in energy, while the anti-bonding band has a symmetric crystal orbital and runs up in energy from Γ. Hence, the bandgap for the *sp* system is at Γ rather than the Brillouin zone edge.

If we were to consider the next-nearest-neighbor interactions in these simple 1D systems, the behavior of the bands would change because the interactions of the orbitals with their periodic images would become important. Interactions of atomic-orbitals with their periodic images favors the band behavior predicted from the single-orbital lattices discussed in the previous section. That is, interactions between s-orbital periodic images would give the band more of a tendency to run up in energy from Γ, and interactions between p-orbital periodic images would have the opposite effect of favoring a decrease in energy form Γ.

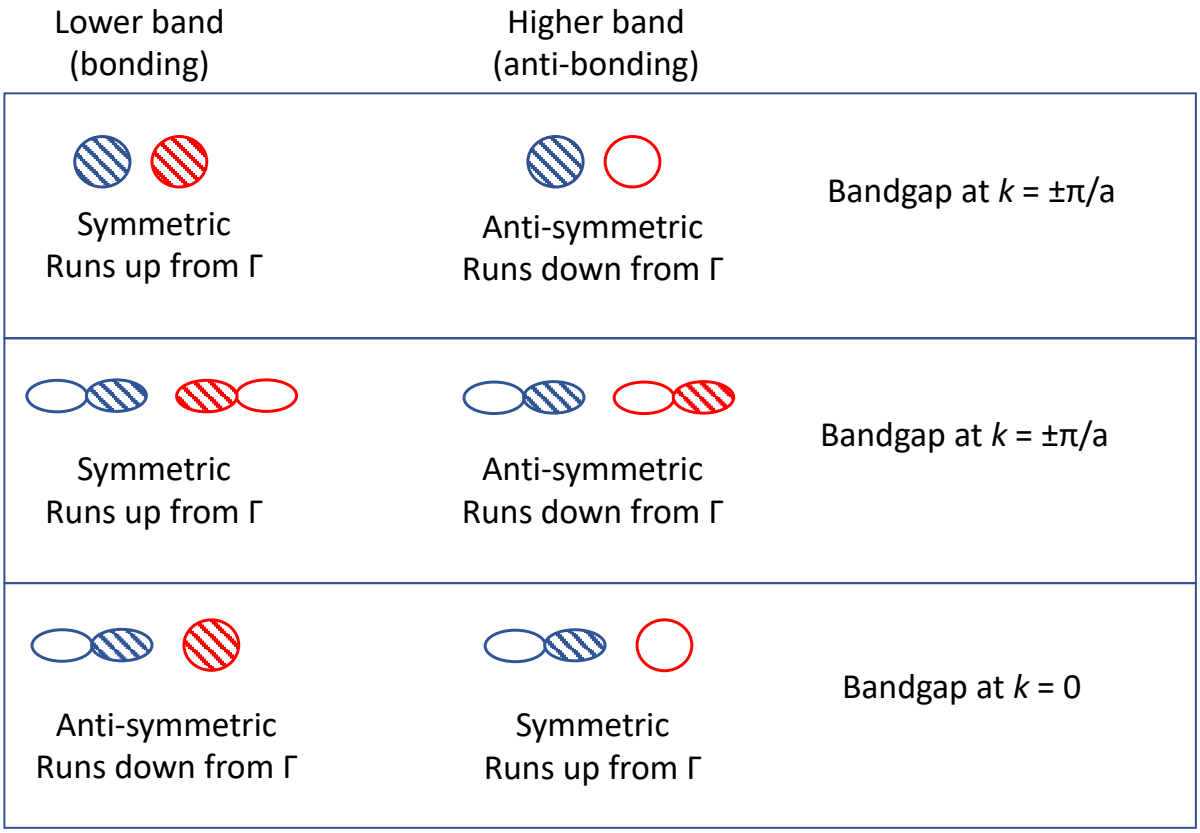

Figure 2.6: Sketches of the Γ-point crystal orbital units for 1D crystals with two-atomic-orbital bases. When the orbitals are both s-orbitals or both p-orbitals, the crystal orbital of the lower band is symmetric and its band runs up in energy from $k = 0$, and the crystal orbital of the higher band is anti-symmetric and its band runs down in energy from $k = 0$. When one orbital is a p-orbital and the other is an s-orbital, the lower band has an anti-symmetric crystal orbital and runs down in energy, while higher band has a symmetric crystal orbital and runs up in energy.

The relative importance of nearest-neighbor and next-nearest-neighbor interactions depends on the energy separation of the nearest-neighbor orbitals. If the energy difference between the two different orbitals in a unit cell is sufficiently large, the nearest-neighbor interaction will be very weak relative to the interaction between the periodic images of the same orbital (which have the same energy), despite the smaller interatomic separation (see Equation 2.26). This would cause the bands to behave more like the bands from a lattice that contains only that orbital. For instance, in our 1D *s*-*p* example, if $E_s >> E_p$, such that the *s*-*p* interactions is negligible compared to the *s*-*s* and *p*-*p* interactions. As a result, the higher-energy band would behave like a *s*-orbital band and run up from Γ, and the lower-energy band would behave like an *p*-orbital band and run down in energy from Γ. However, if $E_s > E_p$, but the *s*-*p* interactions are not negligible, then the higher band—which would have more *s* than *p* character—would be favored to run down from both the *s*-*p* nearest-neighbor and *s*-*s* next-nearest neighbor interactions. Moreover, the lower band—which would have more *p* character—would be favored to run down in energy by both the *s*-*p* and next-nearest neighbor *p*-*p* interactions. Therefore, the curvature/bandwidth of both bands would be higher with the nearest neighbor *and* next-nearest neighbor interactions than from only nearest-neighbor interactions (Figure 2.7).

While the band structures in real 3D materials are far more complicated and need more scrutiny to fully understand, the 1D examples given in this section can be used as starting points help decipher and understand the chemical origins of complex electronic structures. In Chapter 3, we will employ a very similar framework to that described in this section to understand the valence band structure of PbTe and IV-VI semiconductors in general.

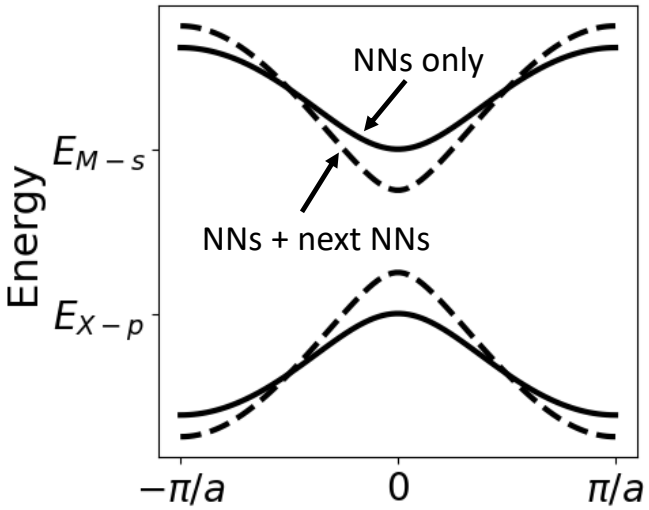

Figure 2.7: Tight-binding band structure corresponding to a 1D lattice consisting of an M-s and X-p orbital separated by a distance of $a/2$, where a is the lattice constant. The solid lines represent the bandstructure when only nearest-neighbor (NN) interactions (s-p interactions) are included, while the dashed line represents the band structure when NN and next NN interactions (s-s and p-p) are included.

Chemical Origins of High Valley Degeneracy in p-Type PbTe

3.1 Introduction

Rock salt PbTe (Figure 3.1) has long been considered one of the highest performing thermoelectric materials, reaching $zT > 1$ when optimally doped [29, 70–73]. PbTe and the similar SnTe and GeTe based alloys have been employed as a power source for NASA space missions since the 1960's [28, 74]. Much of the exceptional thermoelectric performance of PbTe can be attributed to its favorable electronic band structure, particularly the high valley degeneracy of the conduction band (CB) and valence band (VB) edges. In this chapter, we focus specifically on the VB structure of PbTe, but this work can be applied directly to the other lead chalcogenide or IV-VI semiconductor (PbS, PbSe, SnTe, GeTe, etc.) VB structures.

The high VB degeneracy in PbTe stems from the fact that its VBM is located at the L-point in the face-centered cubic (FCC) Bravais lattice Brillouin zone (BZ),[1] which has a degeneracy of $N_V = 4$ [29, 35, 72, 73, 75, 76], and inter-valley scattering is symmetry-forbidden at the L-point [36, 77, 78]. There are also lower-energy VB maxima located along the ΓK (Σ) line ($N_V = 12$), the ΓX (Δ) line ($N_V = 6$), and at the W-point ($N_V = 6$), which lead to promise for even higher valley degeneracy if and when these band extrema are converged (Figure 3.2). The second valence band along the Σ symmetry line ($N_V = 12$) is found ∼0.1-0.2 eV below the L band at low temperature [28, 29, 75, 77,

[1] See Table A.1 in Appendix A for description of the Brillouin zone of the FCC lattice type.

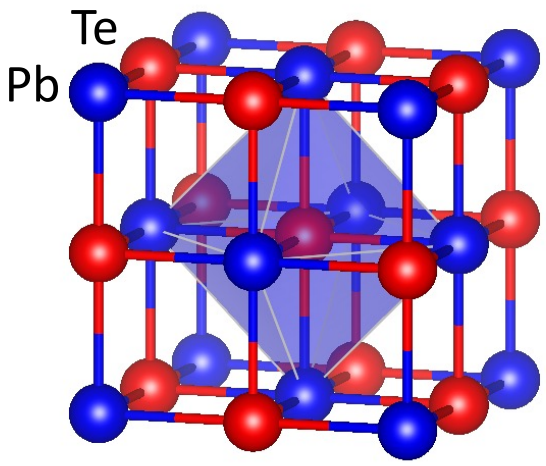

Figure 3.1: Crystal structure of rock salt PbTe, showing the conventional cubic unit cell. The Te atoms are octahedrally coordinated by Pb atoms (coordination octahedron shown in blue), and the Pb atoms are octahedrally coordinated by Te atoms.

79–81]. It is known that as temperature increases, the energy of the L band decreases relative to that of the Σ band, causing the bands to approach each other in energy (when the L maximum is higher) [29, 35, 80–82]. The two bands converge at $T \sim 700$ K, resulting in an exceptionally high (nominal) valley degeneracy of $N_V \sim 16$ and significantly enhanced thermoelectric performance. [29, 35, 35, 71–73, 83].

Based on the band-structure orbital projections shown in Figure 3.2, we can broadly break down the PbTe band structure into the Te-s, Pb-s, Te-p, and Pb-p bands, or groups of bands (see Figure 3.3 for corresponding density of states sketch), to better understand the chemical origins of the band structure. The s-bands are the two singly degenerate bands deep inside the VB, with the Te-s band below the Pb-s band. The next group of three bands closest to the VB edge (triply degenerate at Γ) are mainly Te-p states, while the next set of triply degenerate (at Γ) bands, which comprise the conduction band edge, come from the Pb-p orbitals. Of course, there is hybridization between all of these orbitals, which causes mixing of orbital character throughout the BZ. In this Chapter, we

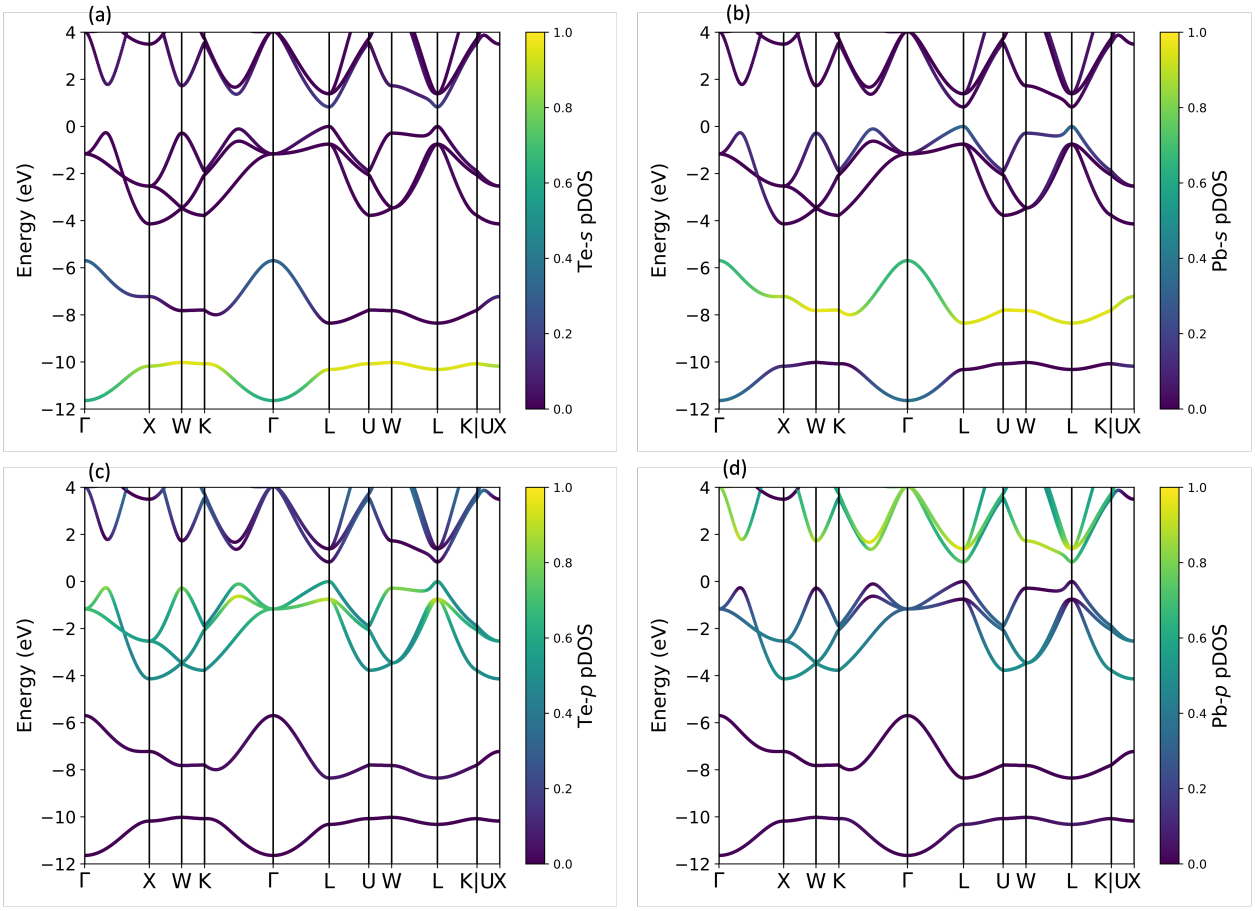

Figure 3.2: Electronic band structure of PbTe with the normalized band-resolved projected density of states (pDOS) for the (a) Te-s, (b) Pb-s, (c) Te-p and (d) Pb-p orbitals. Band structure calculated using DFT with the PBE functional without spin-orbit coupling.

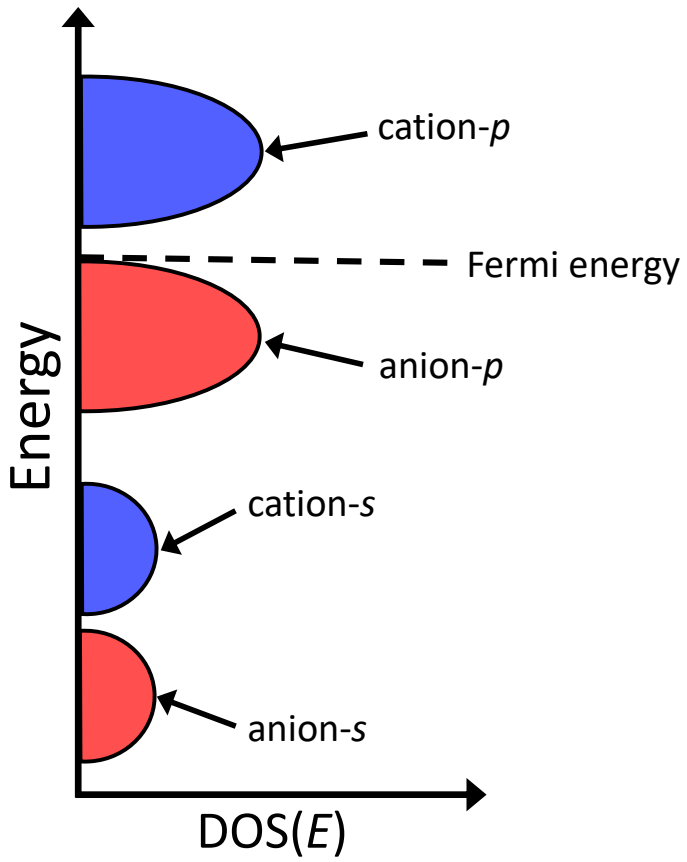

Figure 3.3: Sketch of the projected density of states (pDOS) in a IV-VI rock salt compound like PbTe. Red coloring represents the anion, while blue coloring represents the cation.

are mainly interested the highest VB, which comes from primarily Te-p, with a smaller contribution from the Pb-s states near the top of the band. Typically, VBs that are dominated by p-orbital-like states have a VBM at the high-symmetry Γ-point ($N_V = 1$) because p-orbitals tend to be most anti-bonding with their periodic images at Γ and become more less anti-bonding (or more bonding) away from Γ [62, 66, 84] (see Figure 2.4). However, because the highest VB in PbTe runs up in energy from Γ it must have s-orbital-like symmetry despite containing largely p-orbital character.

In prior work, the filled Pb-s orbitals have been pointed to as the primary reason for the VBM of PbTe being located at the L-point [66, 85, 86]. Ref. 66 claims that the lone-pair s-orbitals from the Pb make the highest VB behave like an s-orbital band. While these lone-pair s-orbitals certainly

contribute significantly to the behavior of the VB states, these explanations overlook the importance of the p-orbitals in dictating the shape of the VB edge. In this chapter, we employ the tight-binding (TB) method to describe a more complete VB picture that explains the L VBM— in addition to the Σ, Δ, and W VBMs— that includes the bonding between the nearest and next-nearest neighbor p-orbitals. We show that the TB wavefunction that describes the VB edge has s-like symmetry and that this s-like symmetry does not even require (but may include) the presence of atomic-s states. In fact, the s-orbitals are not requisite for the VB to increase in energy from Γ to L (and to the Σ, Δ and W VBMs), though it is required for the L VBM to exceed the energy of the Σ, Δ, and W VBMs.

3.2 Tight-Binding Band Structure

We build a simple TB model for a toy IV-VI rock salt compounds in order to understand the chemical origins of the VB behavior in PbTe. Details on how to construct the PbTe TB Hamiltonian are given in Appendix B, and this Hamiltonian construction can be directly generalized to describe the other IV-VI rock salt semiconductor compounds.

One important advantage of the TB method for calculating (approximate) band structures is the flexibility in constructing toy models. In this section, we perform TB computational thought experiments that would not be tractable using more sophisticated electronic structure calculation methods like DFT. These thought experiments involve adding/removing and varying certain interactions in order to rapidly visualize which interactions lead to which (qualitative) features in the band structure. The TB hopping (interaction) parameters for the toy IV-VI rock salt system used in both this chapter and Chapter 4, unless specified otherwise, are summarized in Table 3.1. These parameters give the values for the cases where their respective interactions are completely "turned on". Here, we use Pb as the cation and Te as the anion for the sake of discussion, but these can be replaced with any other group-IV cation and group-VI anion, respectively. In this chapter and in Chapter 4, the hopping parameters for the Pb–s–Te-p (cation-s–anion-p) interaction is denoted by

Table 3.1: Tight-binding hopping parameters for a toy IV-VI rock salt semiconductor. All interactions mentioned describe the shortest-distance interactions of that type, so cation–anion interactions are nearest-neighbor interactions (6 nearest-neighbors) and anion–anion interactions are next-nearest-neighbor interactions (12 next-nearest-neighbors).

Matrix element	Description	Value (eV)
$V_{sp\sigma}$	cation-s–anion-p σ-bonding	0.8
$V_{pp\sigma}$	cation-p–anion-p σ-bonding	1.0
$V_{pp\pi}$	cation-p–anion-p π-bonding	-(1/8)$V_{pp\sigma}$
$V_{pp\sigma,an}$	anion-p–anion-p σ-bonding	0.15
$V_{pp\pi,an}$	anion-p–anion-p π-bonding	-(1/8)$V_{pp\sigma,an}$
$E_{an-p} - E_{cat-s}$	cation-s–anion-p on-site energy separation	5
$E_{cat-p} - E_{an-p}$	cation-p–anion-p on-site energy separation	2

$V_{sp\sigma}$, and the hopping parameters for the Pb–p–Te-p (cation-p–anion-p) σ- and π-interactions are denoted by $V_{pp\sigma}$ and $V_{pp\pi}$, respectively. The next-nearest neighbor anion-p–anion-p interactions are denoted by $V_{pp\sigma,an}$ and $V_{pp\pi,an}$ ($V_{pp\sigma,Te}$ and $V_{pp\pi,Te}$ for the PbTe case).

First, we calculate TB band structures that include (1) the Pb-s–Te-p and Pb–p–Te-p interactions, (2) only Pb-s–Te-p interactions, and (3) only Pb-p–Te-p band structures (Figure 3.4). The TB model with both cation-s–anion-p and cation-p–anion-p interactions (Figure 3.4a) yields the L-point VBM, and the Σ, Δ and W VB pockets are lower in energy with the Σ band higher in energy than the Δ and W bands (Δ and W are nearly equal). When only cation-s–anion-p interactions are included (Figure 3.4b), we only get dispersion in one band, the band that corresponds to the highest VB (when all important interactions are included). This band reaches a maximum at L, with secondary maxima at W and along Σ and Δ, and the energy at the Σ maximum is higher than the Δ and W maxima. Finally, if only cation-p–anion-p interactions are included, the VB edge still runs up from Γ to L, but the energy of the L, W, Δ, and Σ VBMs are all equal (Figure 3.4c).

The thought experiment depicted in Figure 3.4, shows that the Pb-s orbitals are not necessary for the VB edge to run up in energy from Γ to L, but they are necessary for the L VBM to exceed the energies of the other competing VBMs at W and along Σ and Δ. Because the highest VB still increases in energy from Γ to L without the lone-pair s-orbitals, the hypothesis presented in

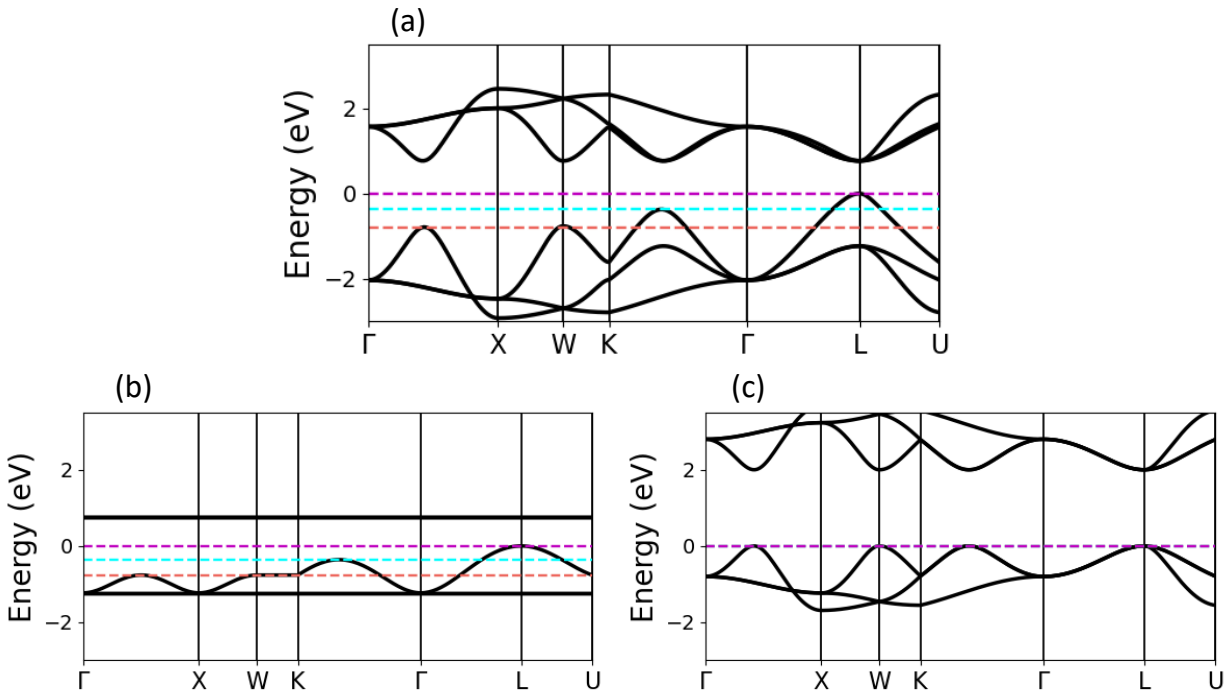

Figure 3.4: Tight-binding (TB) band structures for PbTe toy models calculated using (a) Pb-s–Te-p and Pb–p–Te-p interactions, (b) only Pb-s–Te-p interactions, and (c) only Pb–p–Te-p interactions. The magenta, cyan, and orange horizontal lines are visual guides that show the energy of the L, Σ, and Δ VBMs, respectively. The TB hopping parameters are given by $V_{sp\sigma} = 0.8$ eV, $V_{pp\sigma} = 1$ eV, and $V_{pp\pi} = -1/8$ eV (see Table 3.1).

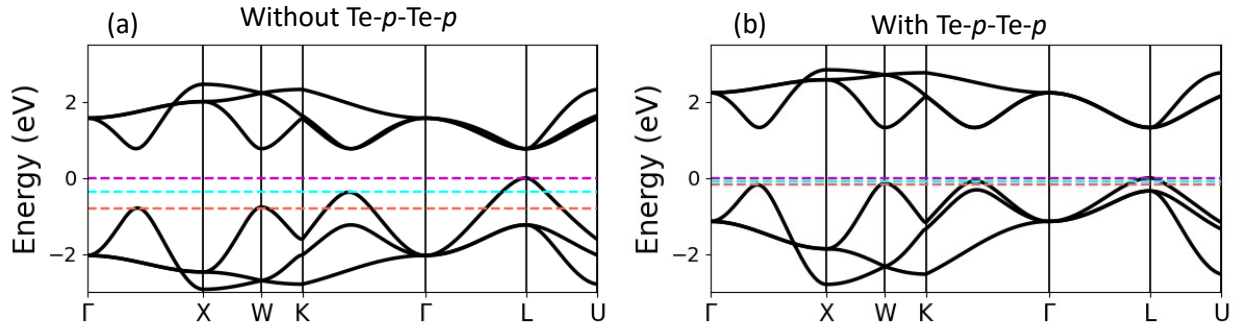

Figure 3.5: Tight-binding (TB) band structures for PbTe toy models calculated using (a) Pb-s–Te-p and Pb–p–Te-p interactions and (b) using Pb-s–Te-p, Pb–p–Te-p, and Te-p–Te-p interactions. The magenta, cyan, and orange horizontal lines are visual guides that show the energy of the L, Σ, and Δ VBMs, respectively. The TB hopping parameters are given by $V_{sp\sigma} = 0.8$ eV, $V_{pp\sigma} = 1$ eV, $V_{pp\pi} = -1/8$ eV, $V_{pp\sigma,Te} = 0.15eV$, and $V_{pp\pi,Te} = -V_{pp\sigma,Te}/8$ eV (see Table 3.1).

Ref. 66 claiming that the s-orbitals give the VB the symmetry needed to run up from Γ is not entirely correct. The symmetry needed for the band to run up in energy is satisfied from both the hybridization between the cation-p and anion-p orbitals and the hybridization between the cation-s and anion-p orbitals.

While the nearest-neighbor interactions between the Te-p orbitals that dominate the VB edge and the Pb-s and Pb-p orbitals qualitatively reproduce the shape of the VB edge, the next-nearest neighbor Te-p–Te-p interactions provide some further insight into the VB structure in PbTe and similar IV-VI rock salt semiconductors. Numerically, we can investigate the effect of these next-nearest neighbor anion-p interactions by comparing the TB electronic structure of the toy IV-VI rock salt model with and without these interactions (Figure 3.5). Including the anion-p–anion-p interactions decreases the difference in energy between the L, Σ, Δ, and W VBMs and increases the bandgap energy.

3.3 Analytical Tight-Binding Solutions

Analytical solutions for our toy IV-VI rock salt TB model can be determined by setting up and solving for the eigenvalues of Hamiltonian matrices that that describe the interactions between

certain pairs of orbitals.

3.3.1 Cation-s–Anion-p Interaction

First, we write out the Hamiltonian that describes only the Pb-s–Te-p interactions (the Hamiltonian and its constituent hopping integrals are a function of $\mathbf{k}$).

$$\bar{\boldsymbol{H}}_{Pb-s,Te-p} = \begin{pmatrix} E_{Pb-s} & H_{Pb-s,Te-p_x} & H_{Pb-s,Te-p_y} & H_{Pb-s,Te-p_z} \\ H^*_{Pb-s,Te-p_x} & E_{Pb-p} & 0 & 0 \\ H^*_{Pb-s,Te-p_y} & 0 & E_{Pb-p} & 0 \\ H^*_{Pb-s,Te-p_z} & 0 & 0 & E_{Pb-p} \end{pmatrix} \tag{3.1}$$

The hopping integrals as a function of $\boldsymbol{k}$ in Equation 3.1 can be simplified by choosing specific paths along the FCC Brillouin zone. Here, we will give the solutions along ΓL (Λ), ΓK (Σ), and ΓX (Δ). Along $\Lambda = \frac{\pi}{a}(l,l,l)$, the hopping integrals are given by $H_{Pb-s,Te-p_x} = H_{Pb-s,Te-p_y} = H_{Pb-s,Te-p_z} = -2iV_{sp\sigma}\sin(l\pi/2)$, where l varies from 0 at Γ to 1 at L. This shows that the Pb-s–Te-p interaction is zero at Γ, which can also be shown using group theory [4]. Along $\Sigma = \frac{3\pi}{2a}(0,s,s)$, the hopping integrals are given by $H_{Pb-s,Te-p_x} = 0$, and $H_{Pb-s,Te-p_y} = H_{Pb-s,Te-p_z} = -2iV_{sp\sigma}\sin(3s\pi/4)$, where s varies from 0 at Γ to 1 at K. Finally, along $\Delta = \frac{2\pi}{a}(0,0,d)$, we have $H_{Pb-s,Te-p_x} = H_{Pb-s,Te-p_y} = 0$ and $H_{Pb-s,Te-p_z} = -2iV_{sp\sigma}\sin(d\pi)$, where d varies from 0 at Γ to 1 at X.

If we solve for the eigenvalues along these three BZ paths, we obtain solutions for the VB energy of the form,

$$E_{VB,sp} = \frac{1}{2}(E_{Pb-s} + E_{Te-p}) + \frac{1}{2}\sqrt{(E_{Te-p} - E_{Pb-s})^2 + 4(xV_{sp\sigma})^2}. \tag{3.2}$$

Notice that Equation 3.2 has the same form as the anti-bonding TB eigenvalue solutions for the diatomic molecule described by Equation 2.22 in Chapter 2, where $V_{sp} = xV_{sp\sigma}$ is like the diatomic

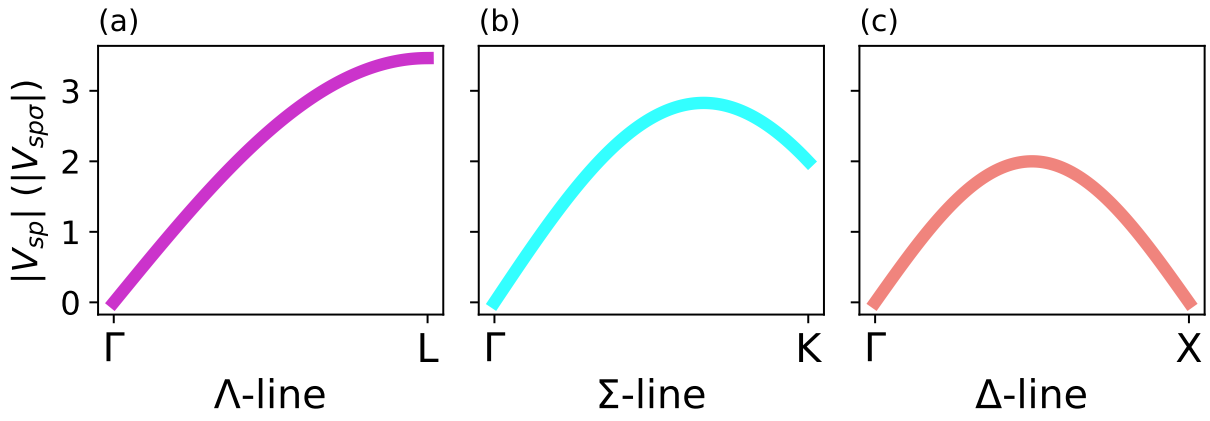

Figure 3.6: $\boldsymbol{k}$-dependent strength of the cation-s–anion-p tight-binding (TB) hopping integral (based on the diatomic molecule model) ($|V_{sp}|$) corresponding to the highest valence band along the (a) Λ (ΓL)-line, (b) Σ (ΓK)-line, and (c) Δ (ΓX)-line of the FCC Brillouin zone for the IV-VI rock salt TB model. The values are shown in terms of the cation-s–anion-p hopping parameter, $V_{sp\sigma}$.

hopping parameter, V. For the Λ, Σ, and Δ paths, the value of x is given by $x = (6/\sqrt{3})\sin(l\pi/2)$, $x = (4/\sqrt{2})\sin(3s\pi/4)$, and $x = 2\sin(d\pi)$, respectively. The corresponding $\boldsymbol{k}$-dependent values of $|V_{sp}|$, which represents the $\boldsymbol{k}$-dependent hopping strength, are plotted in Figure 3.6. The value of x, and hence $|V_{sp}|$, reaches a maximum along Λ at $l = 1$, a maximum along Σ at $s = 2/3$, and a maximum along Δ at $d = 1/2$. In this chapter we define the points at $s = 2/3$ and $d = 1/2$ as Σ′ and Δ′, respectively. That is $\Sigma' = \frac{\pi}{a}(0, 1, 1)$ and $\Delta' = \frac{\pi}{a}(0, 0, 1)$. Then, we can write the values of $V_{sp} = xV_{sp\sigma}$ for the local maxima along Λ, Σ and Δ, as $V_{sp}(L) = 6V_{sp\sigma}/\sqrt{3}$, $V_{sp}(\Sigma') = 4V_{sp\sigma}/\sqrt{2}$, and $V_{sp}(\Delta') = 2V_{sp\sigma}$. Also, it can be shown that $V_{sp}(W) = V_{sp}(\Delta')$. Clearly, based on Equation 3.2, and the values of $|V_{sp}|$ for each local VB, the cation-s–anion-p antibonding strength is strongest at L, followed by Σ′ then Δ′ and W, which is evident in both Figures 3.4b and 3.6.

The bonding analogues of Equation 3.2 (plus sign in front of the square-root term is replaced with a minus sign) describes the s-p bonding states that are found in the (predominantly) cation-s band deeper into the VB (see Figures 3.2 and 3.3).

Table 3.2: TB Hamiltonian matrix elements for nearest-neighbor Pb-p–Te-p interactions along Λ, Σ, and Δ lines in FCC Brillouin zone. We use $H_{x,x}$ as shorthand for $H_{Pb-p_x,Te-p_x}$, etc.

H_{ij}	Λ	Σ	Δ
$H_{x,x}$	$(2V_{pp\sigma}+4V_{pp\pi})\cos(l\pi/2)$	$2V_{pp\sigma}+4V_{pp\pi}\cos(3s\pi/4)$	$2V_{pp\sigma}+V_{pp\pi}[2+2\cos(d\pi)]$
$H_{y,y}$	$(2V_{pp\sigma}+4V_{pp\pi})\cos(l\pi/2)$	$2(V_{pp\sigma}+V_{pp\pi})\cos(3s\pi/4)+2V_{pp\pi}$	$2V_{pp\sigma}+V_{pp\pi}[2+2\cos(d\pi)]$
$H_{z,z}$	$(2V_{pp\sigma}+4V_{pp\pi})\cos(l\pi/2)$	$2(V_{pp\sigma}+V_{pp\pi})\cos(3s\pi/4)+2V_{pp\pi}$	$2V_{pp\sigma}\cos(d\pi)+4V_{pp\pi}$

3.3.2 Cation-p–Anion-p Interaction

Next, we look at the effect of the cation-p–anion-p interactions. The Hamiltonian describing these interactions is given as follows:

$$\bar{\boldsymbol{H}}_{Pb-p,Te-p}=\begin{pmatrix} E_{Pb-p} & 0 & 0 & H_{Pb-p_x,Te-p_x} & 0 & 0 \\ \cdot & E_{Pb-p} & 0 & 0 & H_{Pb-p_y,Te-p_y} & 0 \\ \cdot & \cdot & E_{Pb-p} & 0 & 0 & H_{Pb-p_z,Te-p_z} \\ \cdot & \cdot & \cdot & E_{Te-p} & 0 & 0 \\ \cdot & \cdot & \cdot & \cdot & E_{Te-p} & 0 \\ \cdot & \cdot & \cdot & \cdot & \cdot & E_{Te-p} \end{pmatrix}. \quad (3.3)$$

We only give the upper diagonal elements, but we can use the fact that the Hamiltonian is Hermitian ($H_{ij}=H_{ji}^{*}$) to fill in the lower diagonal elements. Along the Λ, Σ, and Δ direction, the Hamiltonian elements are give in Table 3.2.

When we solve for the eigenvalues to Equation 3.3, the highest VB is triply degenerate along Λ, doubly degenerate along Σ, and singly degenerate along Δ (see Figure 3.4c). Note that when the cation-s–anion-p interaction is included, the highest VB is singly degenerate. The energy the highest VB(s) along the Λ, Σ, and Δ paths based on only the Pb-p–Te-p interactions can also be written in a form similar to Equation 2.22, where $V=V_{pp}$ (see Equation 3.4). The $\boldsymbol{k}$-dependent values of V_{pp} are listed below, and E_1 and E_2 (from Equation 2.22) are given by E_{Pb-p} and E_{Te-p}, respectively.

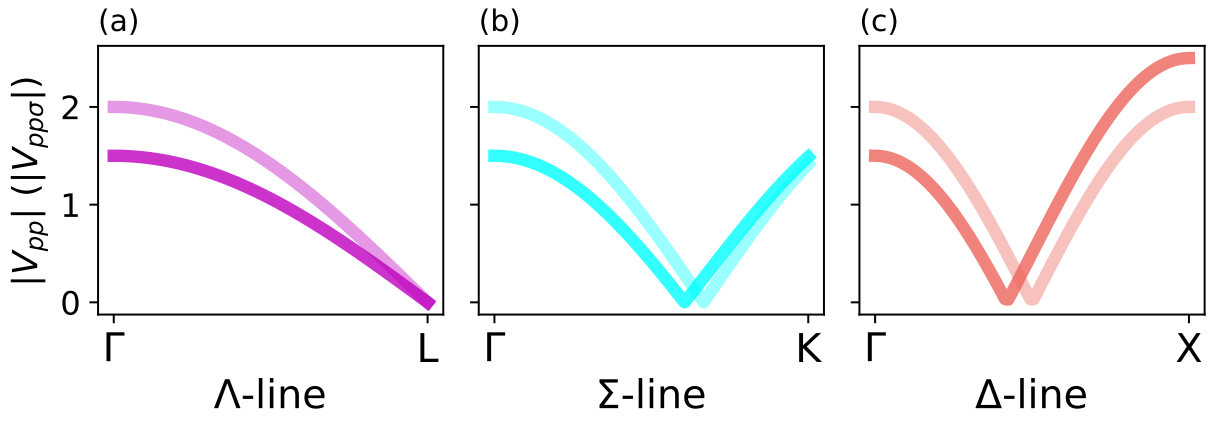

Figure 3.7: $\boldsymbol{k}$-dependent strength of the cation-p–anion-p tight-binding (TB) hopping integral (based on a diatomic molecule model), $|V_{pp}|$, for the highest valence band along the (a) Λ (ΓL)-line, (b) Σ (ΓK)-line, and (c) Δ (ΓX)-line of the FCC Brillouin zone for the IV-VI rock salt TB model. The values are shown in terms of the cation-s–anion-p hopping parameter, $V_{pp\sigma}$. The fainter lines in (a)-(c) represent the case where $V_{pp\pi} = 0$, and the darker lines represent the cases where $V_{pp\pi} = -(1/8)V_{pp\sigma}$.

- Λ: $V_{pp}(l) = (2V_{pp\sigma} + 4V_{pp\pi})\cos(l\pi/2)$
- Σ: $V_{pp}(s) = 2(V_{pp\sigma} + V_{pp\pi})\cos(3s\pi/4) + 2V_{pp\pi}$
- Δ: $V_{pp}(d) = 2V_{pp\sigma}\cos(d\pi) + 4V_{pp\pi}$

The strength of the cation-p–anion-p interaction parameter, $|V_{pp}|$ along each path is plotted in Figure 3.7.

When considering the cation-p–anion-p interactions, the VB edge is the *bonding* (lower-energy) solution of Equation 2.22.

$$E_{VB,pp} = \frac{1}{2}(E_{Pb-p} + E_{Te-p}) - \frac{1}{2}\sqrt{(E_{Pb-p} - E_{Te-p})^2 + 4(V_{pp})^2}. \tag{3.4}$$

At Γ, the cation-p–anion-p hopping parameter is given by $V_{pp}(\Gamma) = 2V_{pp\sigma} + 4V_{pp\pi}$. Recall, that $V_{pp\sigma} > 0$, while $V_{pp\pi} < 0$, so given that the p-orbitals are σ-bonding at Γ, then they must be π-anti-bonding at Γ. Because we can assume that the σ-bonding interaction is at least two times as strong

as the π-bonding interaction [63], p-orbitals must be in a net-bonding state at Γ. Along the Λ-line, the magnitude of the interaction decreases from Γ to L, such that it is zero at the L-point. This explains why the highest VB (and the two other anion-p VBs below that) runs up in energy from Γ to L when only the cation-p–anion-p interactions are considered. It can also be shown that at the W-point, the highest VB is singly degenerate and the cation-p–anion-p hopping parameter at this point equals zero. As seen in Figures 3.4c and 3.7b-c, there are also points along Σ and Δ where the net interaction between the Pb-p and Te-p orbitals is zero, leading to additional VBMs that are equal in energy to the VBM at L (when only Pb-p–Te-p interactions are present). In contrast to the case where only Pb-s–Te-p interactions are present, the maxima along Σ and Δ for the case where Pb-p–Te-p interactions are considered are not necessarily at the exact Δ' and Σ' points. The exact location of the maxima depends on the ratio of $V_{pp\sigma}$ to $V_{pp\pi}$ (see Figure 3.7b-c). Along Δ, the maximum occurs at the value of d that satisfies, $d\pi = \arccos(-2V_{pp\pi}/V_{pp\sigma})$, and along Σ, the maximum occurs at the value of s that satisfies $s\pi = (4/3)\arccos\left(-V_{pp\pi}/(V_{pp\sigma} + V_{pp\pi})\right)$. In the toy model we use to create Figure 3.4 and 3.5, we assume that $V_{pp\pi} = -(1/8)V_{pp\sigma}$. This assumption gives a value of $d = 0.42$, and $s = 0.61$. However, if we were to set $V_{pp\pi} = 0$, then $d = 1/2$ and $s = 2/3$.

The antibonding analogues to the VB cation-p–anion-p bonding states are found in the CB, which is why the shape of the CB edge somewhat mirrors that of the VB edge.

3.3.3 Anion-p–Anion-p Interaction

We can think of the Te-p–Te-p interactions as adjusting the *effective* on-site energy of the Te-p orbitals when estimating the energies of the local VBMs using Equation 3.2. Note that this effective on-site energy does not apply to all of the Te-p VBs and should only be applied to the highest (singly degenerate) VB at the specified $\boldsymbol{k}$-points. We denote this effective on-site energy as E'_{Te-p}. We skip the details of the derivation here, but by setting up a 3×3 Hamiltonian that only describes the Te-p–Te-p interactions (see Te-p–Te-p matrix elements in Appendix B), we can show

that the adjusted on-site energies at L, W, Δ', and Σ' are as follows:

$$E'_{Te-p}(L) = E_{Te-p} + 4V_{pp\pi,Te} - 4V_{pp\sigma,Te} \tag{3.5}$$

$$E'_{Te-p}(\Sigma') = E_{Te-p} + 2V_{pp\pi,Te} - 2V_{pp\sigma,Te} \tag{3.6}$$

$$E'_{Te-p}(\Delta') = E_{Te-p} + 4V_{pp\pi,Te} \tag{3.7}$$

$$E'_{Te-p}(W) = E_{Te-p} - 4V_{pp\pi,Te} \tag{3.8}$$

Because $V_{pp\sigma,Te} > 0$ and $V_{pp\sigma,Te} < 0$, the anion-p–anion-p interaction lowers the energy of the highest VB at L, Σ' and Δ', and slightly increases the energy at W.

Using these adjusted, or effective, on-site anion-p energies, the VB edges at the different VB pockets (L, Σ, Δ, and W) can be approximated using these effective on-site energies substituted into E_{Te-p} in Equation 3.2.

3.3.4 Summary of Interactions

In summary, the L, W, Σ, and Δ VBMs are all Pb-s–Te-p antibonding states and Pb-p–Te-p non-bonding (or nearly non-bonding for the Δ and Σ VBMs) states. Away from these VBMs, the band becomes less Pb-s–Te-p anti-bonding and more Pb-p–Te-p bonding, which results in these VBMs or local VBMs. The Pb-s–Te-p anti-bonding strength is greatest at the L point, followed by Σ', then Δ' and W. The weaker next-nearest neighbor Te-p-Te-p interactions are also relevant when studying the VB behavior of PbTe. These interactions push down the VB edge in the L, Σ, and Δ VBMs, with the interaction being strongest at L, followed by Σ' then Δ'. This interaction is slightly

anti-bonding at W.

3.4 Atomic-Orbital Pictures

The results of the numerical and analytical results can be explained using simple molecular-orbital-like bonding diagrams (at specific $\boldsymbol{k}$-points) and atomic-orbital sketches that represent the TB wavefunctions that describe the various VB edges. As discussed in the previous section, at different $\boldsymbol{k}$-points, different orbital interactions are present, and the strengths of these interactions vary with $\boldsymbol{k}$. For instance, at the Γ-point, the cation-p–anion-p and cation-s–anion-s interactions are present but the nearest-neighbor s–p interactions are not present, while at the L point, the converse is true (Figure 3.8). The VBM and CBM at the L-point are described by cation-s–anion-p and cation-p–anion-s anti-bonding states, respectively (Figure 3.8b).

3.4.1 Crystal Orbitals with s-Like-Symmetry

In Chapter 2, we showed that bands that have s-like-symmetry run up in energy from Γ to the BZ edge, while bands that have p-like-symmetry (and σ-bonding dominates) run down in energy from Γ to the BZ edge. Therefore, it may initially seem counter-intuitive for the VBM in PbTe and in other IV-VI rock salt semiconductors to be located at the L-point, as the VB edge comes primarily from anion-p states. Ref. 66 offers the explanation that the filled Pb-s states, which are also present in the VB edge, themselves make the highest VB behave like an s-band—simply because s-orbitals are present. While the Pb-s orbitals are important, this explanation has two pitfalls. The first is that the percentage of Te-p character in the highest VB is greater than the percent Pb-s character, even at L (Figure 3.2). Therefore, there is no reason that the Pb-s-orbital interactions should be more important than the Te-p-orbital interactions. Second, our toy TB model shows that the highest VB runs up in energy from Γ to the BZ zone edge with only the Pb-p–Te-p interactions (no Pb-s orbitals).

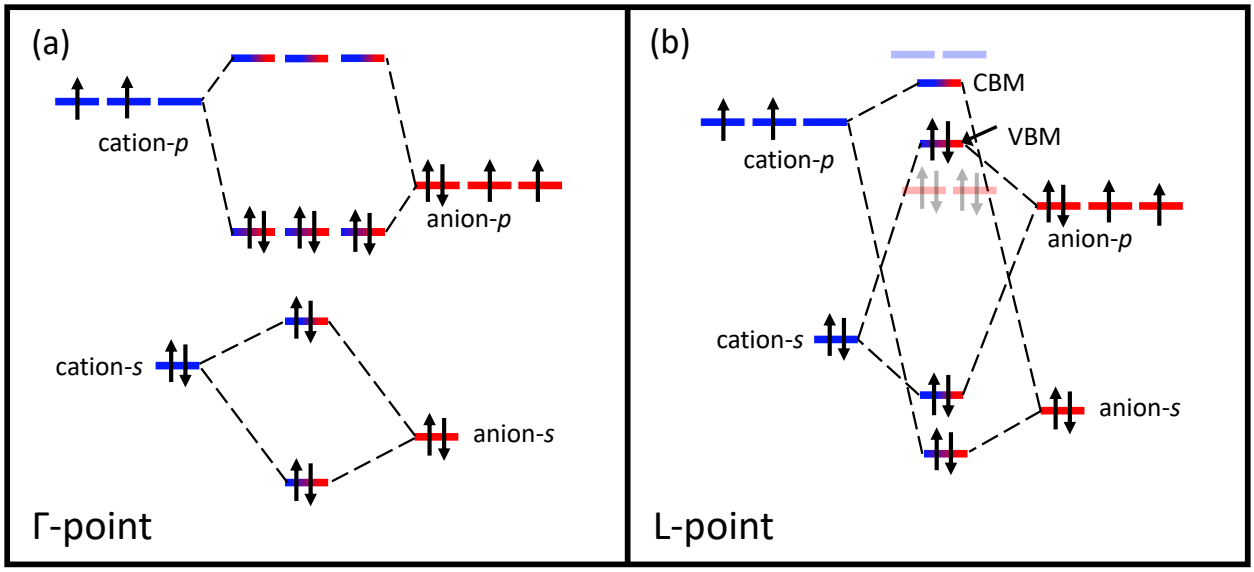

Figure 3.8: Sketches of molecular-orbital-like diagrams showing the nearest-neighbor bonding interactions in IV-VI rock salt semiconductors at the Γ-point and at the L-point. (a) At the Γ-point, interactions between the cation-s and anion-s orbitals and between the cation-p and anion-p orbitals are present. The valence band (VB) edge at Γ comes from the cation-p–anion-p bonding states and the conduction band (CB) edge comes from the cation-p–anion-p antibonding states. (b) At the L-point, cation-s–anion-p and cation-p–anion-s interactions are present, and the valence band maximum (VBM) and conduction band minimum (CBM) come from cation-s–anion-p and cation-p–anion-s anti-bonding states, respectively. The final energies of the molecular orbitals in (b) are modified due to next-nearest-neighbor interactions (e.g., cation-p–cation-p and anion-p–anion-p next-nearest-neighbor interactions push the nearest-neighbor s-p anti-bonding states in (b) down in energy and the non-bonding p-states up in energy).

Here, we show that the highest VB state can be described by Pb-s–Te-p and Pb-p-Te-p *crystal* orbitals [69] that have s-like symmetry. The crystal orbitals describe superpositions of the atomic orbitals within a single repeat unit (primitive unit cell) of the crystal. Like atomic orbitals, we can construct Bloch functions from these crystal orbital units in order to understand band behavior (Figure 3.9). For simplicity, we show 1D linear interpretations of the Bloch wavefunctions, such that they can be easily compared to Figures 2.4 and 2.5 in Chapter 2. Note that these sketches are only intended to show the symmetry and phases of the orbitals, not the relative orbital contributions. In fact, the Te-p orbitals have the greatest contribution to the VB edge, but the contribution varies in $\boldsymbol{k}$-space. The Pb-s/Te-p crystal orbital unit representing the highest VB is constructed from a Te-p orbital in an anti-bonding configuration with a near-neighbor Pb-s orbital (Figure 3.9a). The overall symmetry of the *phase* (shown using dark versus light shading for negative of positive phase) of this unit is symmetric with respect to the σ-bonding axis, giving it s-like-symmetry. Therefore, at the Γ-point, where all of these crystal orbitals are aligned with no phase change, the interactions between the crystal orbital units are all bonding. However, because the interaction within the crystal orbital units is always anti-bonding, the bonding and anti-bonding interactions cancel out from symmetry making this state at Γ net non-bonding. On the other hand, at L, each crystal orbital unit is out-of-phase with its neighboring crystal orbital unit, so the crystal orbital wavefunction at L is completely anti-bonding.

The Pb-p/Te-p crystal orbital unit that describes the highest VB is constructed from an in-phase (bonding) Pb-p–Te-p interaction that also has s-like (symmetric) phase symmetry with respect to the σ-bonding axis (Figure 3.9b). Thus, at Γ the interaction between the crystal orbital units is bonding, and at L the interaction between the units is anti-bonding. Because the interaction within the unit is bonding, the Γ-point Bloch function is an entirely bonding state, while the L-point Bloch function is non-bonding. Overall, the TB crystal orbital transitions from being a Pb-p–Te-p bonding state at Γ to a Pb-s–Te-p anti-bonding state at L, resulting in a band that runs up in energy from Γ. Moreover, the 1D interpretation of the L-point in Figure 3.9 can be generalized to represent the Bloch function corresponding to the VB pockets at Σ', Δ', and W. The difference in bonding

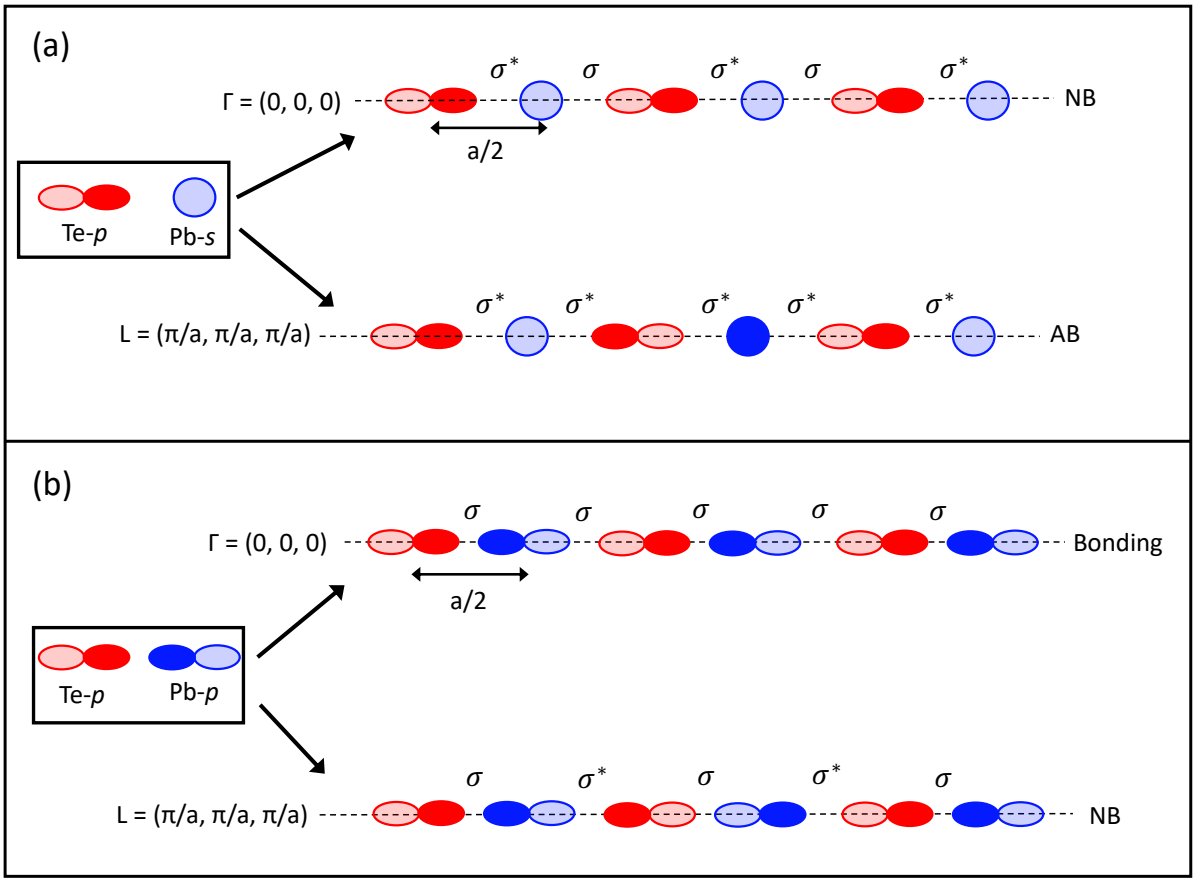

Figure 3.9: Sketch of linear (1D) *representations* of the crystal orbital units and corresponding Bloch functions at Γ and L in the highest valence band in PbTe. (a) The Te-p/Pb-s crystal orbital unit is described by a Te-p orbital and Pb-s orbital in an anti-bonding (AB) configuration. The Γ-point Bloch function for this unit is non-bonding (NB), as the nearest neighbor bonds alternate between being anti-bonding and bonding, cancelling out to give zero net-bonding. The L-point Bloch function is entirely anti-bonding (AB). (b) The Te-p/Pb-p crystal orbital unit is described by a Pb-p–Te-p bonding interaction. The Γ-point Bloch function is bonding, while the L-point Bloch function is non-bonding (NB). Dark versus light shading is used to represent the orbital phases (positive or negative), such that overlaps between orbitals of the same phase are bonding (σ) and overlaps between orbitals of opposite phases are anti-bonding (σ^*). Note that the size of the orbitals *does not* represent the orbital contributions/characters. The orbitals are all shown using the same size, such that only the symmetry of the phase is represented by these sketches. The 1D L-point representation also corresponds to the 1D representations of the W-point, Σ'-point, and Δ'-point VB edges.

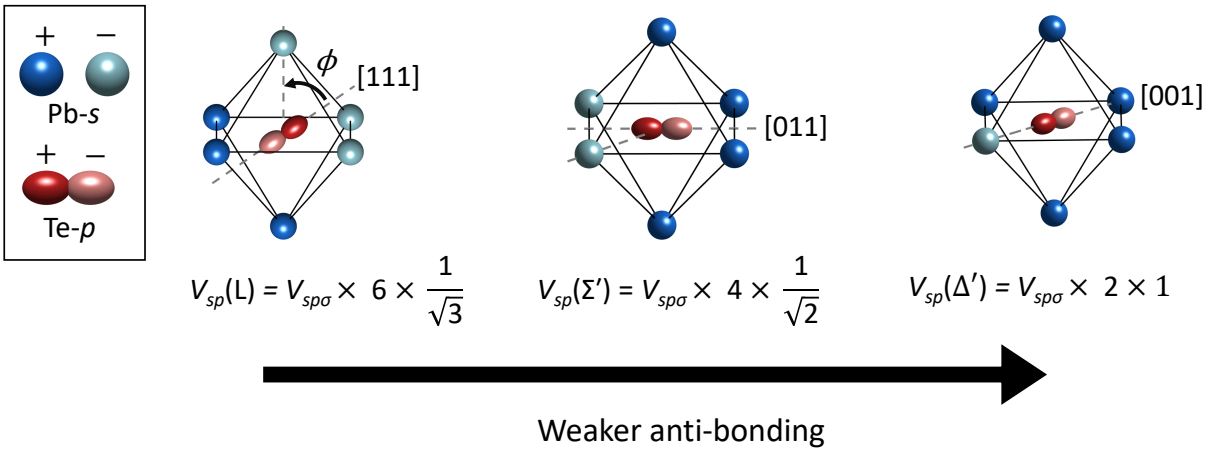

Figure 3.10: 3D sketches of the tight-binding wavefunctions in the highest valence band of PbTe at the L-point, Σ'-point, and Δ'-point. At the L-point, the Te-p orbital is aligned along the [111] direction, at $\Sigma' = \frac{\pi}{a}(0,1,1)$ it is aligned along the [011] direction, and at $\Delta' = \frac{\pi}{a}(0,0,1)$ it is aligned along [001]. The overall s-p interaction strength (hopping integral), given by $V_{sp}(\boldsymbol{k})$, decreases from L to Σ' to Δ'. The shading indicates the orbital phases (positive or negative), and the relative phases of the Pb-s orbitals were assigned using the 3D Bloch functions.

(anti-bonding) between the competing VBMs is elucidated by considering the 3D atomic-orbital interpretation of the VB wavefunctions.

3.4.2 3D Valence Band s-p Anti-bonding Pictures

While simple 1D sketches of the Bloch functions are sufficient to understand why the highest VB increases in energy from Γ to L, W, the Σ maximum, and the Δ maximum, to understand the relative energies of the four different local VBMs (L, Σ, Δ, and W), 3D sketches are needed. For these sketches, we show a single Te-p orbital octahedrally coordinated by its six nearest-neighbor Pb-s orbitals (see Figure 3.1), whose phases are given by the 3D Bloch functions for each $\boldsymbol{k}$-point (Figure 3.10). The vector describing the direction of the p-orbital is determined by the $\boldsymbol{k}$-point. At the L-point, the Te-p orbital is oriented along a <111> direction, along Σ, it is oriented along a <011> direction, and along Δ, it is oriented along a <001> direction.

These simple VB eigenfunction sketches can be used to obtain the same analytical solutions for the VBM (from s-p interactions) given in the prior section. Specifically, we can reproduce the

values of $V_{sp}(\boldsymbol{k})$ (found by analytically solving part of the TB Hamiltonian) for L, Σ', and Δ' using the geometry and symmetry of the sketches in Figure 3.10. As given in Table 2.1 of Chapter 2, the Slater-Koster matrix element for an s-p interaction is $lV_{sp\sigma}$, where l is the direction cosine (projected along the direction of the p-orbital) of the vector between the p-orbital and s-orbital sites. We can use a similar formalism to describe the anti-bonding nature of the VB edge states, but instead of using the Cartesian basis of p-orbitals (p_x, p_y, and p_z), we use the p-orbital that describes the VB eigenstates at the various local VBMs. Formally, we can write the s-p anti-bonding strength for the L, Σ', and Δ' VBMs using Equation 3.9, where i sums over each nearest-neighbor and ϕ_i is the angle between the p-orbital direction and the vector between the neighbor pairs (see Figure 3.10).

$$V_{sp}(\boldsymbol{k}) = V_{sp\sigma} \sum_{i}^{6} \cos(\phi_i(\boldsymbol{k})) \tag{3.9}$$

It is important to note that this equation can only be used at $\boldsymbol{k}$-points where the s-orbitals are in a *phase* that is completely (maximally) bonding, anti-bonding, or non-bonding with the p-orbital. If we apply Equation 3.9 at the L-point, we get $V_{sp}(L) = 6V_{sp\sigma} \times 1/\sqrt{3}$. At the Σ'-point, we get $V_{sp}(\Sigma') = 4V_{sp\sigma} \times 1/\sqrt{2} + 2V_{sp\sigma} \times 0 = 4V_{sp\sigma}/\sqrt{2}$. Finally, at Δ', we get $V_{sp\sigma}(\Delta') = 2V_{sp\sigma} \times 1 + 4V_{sp\sigma} \times 0 = 2V_{sp\sigma}$.

This atomic-orbital picture framework is not limited to understanding cubic IV-VI semiconductors. We use the same equation and similar eigenstate sketches to understand how the band structure in GeTe changes with respect to its cubic (rock salt) to rhombohedral phase transition in Chapter 5.

3.5 Computational Methods

The first-principles DFT calculations to obtain the PbTe band structure (and corresponding orbital characters) were performed using the Vienna ab initio Simulation Package (VASP), employing projector augmented wave (PAW) pseudopotentials and the PBE functional, derived from the gen-

eralized gradient approximation (GGA). [48–51, 87, 88]. A plane-wave cutoff energy of 450 eV was used for each calculation. The structural degrees of freedom were relaxed—until the forces on atoms were less than 0.01 eV/nm—using a Γ-centered [89] $\boldsymbol{k}$-point mesh of size $13 \times 13 \times 13$. The electronic structure calculations were performed using a Γ-centered $\boldsymbol{k}$-point mesh of size $20 \times 20 \times 20$.

3.6 Conclusion

The high valley degeneracy in the VBs of PbTe is partially due to its four-fold-degenerate L-point VBM, and it can be increased further when the L band is converged with the twelve-fold-degenerate Σ band. Theoretically, band convergence can be enhanced even more if the Δ and W VB pockets are also converged at the VB edge, though this type of convergence is not as well documented in the literature. In this chapter, we have developed a simple and intuitive orbital-chemistry framework to aid in the understanding of high band degeneracy in PbTe and IV-VI rock salt semiconductors.

First, we use a toy TB model to show that the highest VB increases in energy from Γ to the VB edges (L, W, Σ, and Δ) with cation-s–anion-p and/*or* cation-p–anion-p interactions included in the model. Simple 1D orbital sketches show that a crystal orbitals unit constructed from cation-s-anion-p anti-bonding interactions and from cation-p–anion-p bonding interactions have the s-like symmetry expected from a wavefunction that describes a band that increases in energy away from the Γ-point. The highest VB has cation-p–anion-p bonding character at Γ, but the cation-p–anion-p bonding strength decreases away from Γ, such that it is non-bonding at L. The VBM at L is a cation-s–anion-p anti-bonding state, while this cation-s–anion-p interaction is forbidden at Γ. The other local VBMs at W and along Σ and Δ can also be described as largely cation-s–anion-p anti-bonding states and cation-p–anion-p non-bonding (or nearly non-bonding) states. The s-p interaction is strongest at L, followed by Σ, then Δ and W. The difference in s-p anti-bonding strength can be understood using 3D sketches of the s-p wavefunctions describing these VBMs. Anion-p–anion-p next-nearest neighbor interactions also influence the shape of the VB. These interactions (in the highest VB) are bonding in nature at L, Σ, and Δ, with the bonding interaction being stronger at L,

followed by Σ, then Δ. At the W-point, the anion-p–anion-p interactions are slightly anti-bonding.

In addition to providing insight into band engineering of PbTe, the framework described in this chapter has been used to understand the chemical origins of band inversion in the crystalline topological insulator, SnTe [90]. In the next chapter, we build upon this framework to understand and develop strategies for achieving high band convergence and complex Fermi surface topologies.

Band Convergence and Low-Dimensional Band Topology in IV-VI Rock Salt Semiconductors

4.1 Introduction

In Chapter 3, we developed a tight-binding (TB) framework of the valence band (VB) structure in IV-VI rock salt semiconductors. In this chapter, we extent upon this framework to yield insights for designing complex Fermi surfaces for better thermoelectric performance in PbTe and other IV-VI semiconductors.

Convergence of the VB extrema, specifically between L and Σ has been shown to improve the thermoelectric performance of p-type PbTe and other IV-VI semiconductor materials [29, 30, 35, 38, 72, 73, 75, 91–95]. At low temperature, the Σ VB ($N_V = 12$) is found below the L band ($N_V = 4$) [28, 29, 75, 79–81, 96], but as temperature increases, the energy of the L band decreases relative to that of the Σ band, causing the bands to approach each other until the Σ band overtakes the L band at $\sim$ 700K [29,35,80–82]. Through experiment, alloying is well-known to be an effective method for tuning the relative energies of the L and Σ bands [97]. For instance, alloying PbTe with PbSe, decreases the energy of the secondary VBM along Σ relative to the primary VBM at L [29]. By contrast, cation-site alloying with impurities, such as Cd, Mg, Sr, Mn, Na, and Hg—all of which introduce s^0 states above the VB edge—decreases the energy of the L-band relative to the Σ band [28, 71, 73, 75, 85, 95, 97–100].

In this chapter, we use the TB framework from the previous chapter to elucidate the chemi-

cal origins of band convergence in order to explain these alloying strategies. Additionally, while discussion of band convergence has typically been limited to the L and Σ bands, in this chapter, we discuss convergence with the Δ and W bands, which can further improve band degeneracy and Fermi surface complexity [34]. Higher convergence of band edge extrema may lead to interesting variations (beyond simply increasing the nominal valley degeneracy) in the Fermi surface, leading to unique low-dimensional-like transport in 3D *bulk* materials. In general, increasing the band convergence favors lower-dimensional Fermi surfaces in IV-VI semiconductors, and reducing the band dimensionality in thermoelectric materials may improve performance [45, 101, 102].

Traditionally, low-dimensional behavior is achieved by designing nano-scale materials that confine electronic transport in at least one dimension [103–105]. While low-dimensional materials were initially thought to enhance thermoelectric performance [103, 104], when multiple bands contribute to transport, quantum confinement from low-dimensionality can actually *reduce* thermoelectric performance by breaking degeneracy [106, 107]. However, low-dimensional transport has been reported in 3D materials that have lower dimensional Fermi surfaces, and associated gains in thermoelectric performance are predicted [45,69,101,108]. Thus, engineering low-dimensional bands in 3D materials provides a novel pathway to achieve the efficiency gains associated with low-dimensionality without the challenges and costs associated with synthesizing nano-scale material or the loss in thermoelectric power from degeneracy-breaking quantum confinement effects seen in true low-dimensional materials [45, 101].

While transport in these materials does occur in all three dimensions (as dictated by the symmetry of the bulk crystal), the density of states (DOS) has the same energy dependence as true low-dimensional materials, such as nano-wires and nano-scale thin-films (see Figure 4.1). Fermi surfaces that yield 3D-type transport are ellipsoidal and expand in all three dimensions with an increase Fermi energy, so the DOS is proportional to the square-root of energy. Fermi surfaces with 2D-type transport are cylindrical, and therefore, only expand in two dimensions with increasing Fermi energy. The corresponding DOS is independent of energy. Finally, Fermi surfaces with 1D-

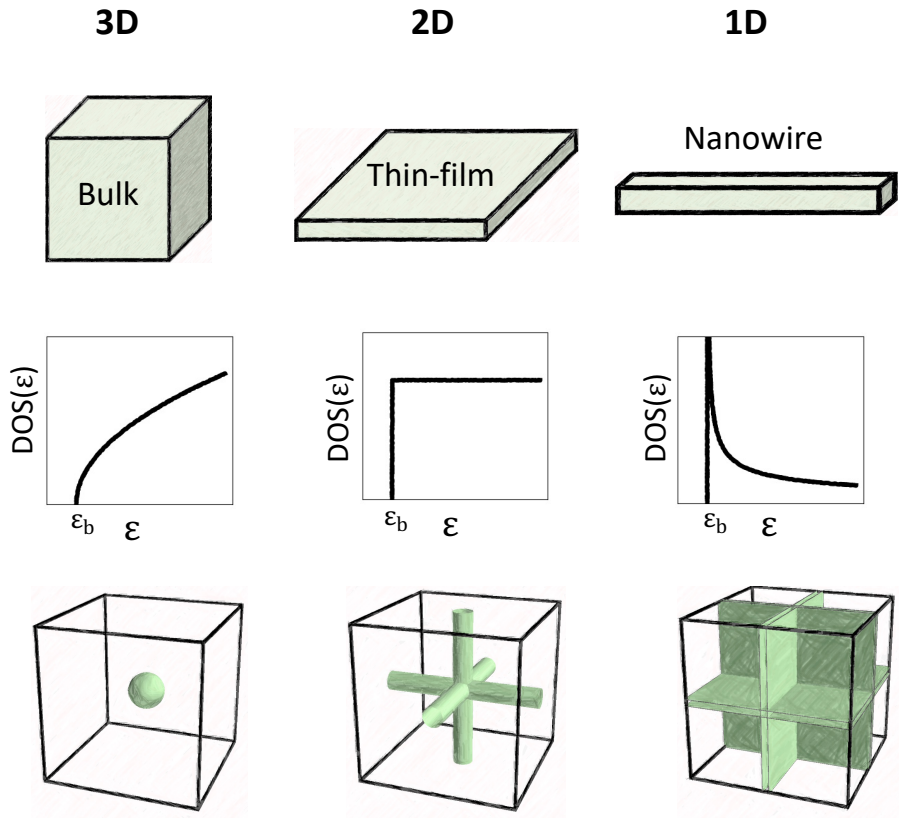

Figure 4.1: Low-dimensional Fermi surfaces in bulk 3D materials have density of states (DOS) with energy (ε) dependencies that correspond to those in true low-dimensional materials, such as thin-films and nanowires. The top row depicts sketches of true 3D, 2D, and 1D materials. The middle row contains sketches of the corresponding DOS for these materials, assuming parabolic bands in the dispersive direction(s). The bottom row shows sketches of Fermi surfaces in cubic bulk 3D materials that have DOSs with energy dependencies corresponding to 3D-type transport (DOS $\propto \sqrt{\varepsilon}$), 2D transport (DOS independent of energy), and 1D transport (DOS $\propto 1/\sqrt{\varepsilon}$). In the DOS sketches, ε_b denotes the band edge.

type transport resemble sheets and expand in one dimension as the Fermi energy moves deeper into the band. The DOS for these bands is inversely related to the square-root of energy.

In Ref. 45, first-principles calculations show that PbTe, PbSe, PbS, and SnTe with sufficient carrier concentrations exhibit a 2D VB Fermi surface topology consisting of 12 tubes, or "threads", connecting the L-points and intersecting the 12 Σ VB pockets. Higher power factors are predicted for the tubes than the ellipsoids [45]. Here, we use the toy IV-VI rock salt TB model to show that the lower-dimensional Fermi surfaces could emerge closer to the band edge (accessible at lower carrier

concentrations/electron chemical potentials) if the various VB pockets are more converged. We also describe the chemical origins of this transition from the 3D ellipsoidal Fermi surface to the 2D topology (tubes/threads), along with an additional theoretical transition to a topology characteristic of 1D transport. By varying the relative convergence of the VB extrema using "chemical knobs" within the TB model, we see a topological evolution in the Fermi surface from 3D, to 2D, to 1D. Using an effective mass model, we show that the lower-dimensional Fermi surfaces have higher Fermi surface complexity factors (quantification of Fermi surface complexity [34]) and may lead to higher Seebeck coefficients and power factors, although the extent of the benefits depend on the scattering assumption.

4.2 Identifying Chemical Knobs for Tuning Convergence

4.2.1 Insights from Tight-Binding Model

The first step to developing an orbital-chemistry framework for band convergence is to write out analytical TB expressions that describe the energy difference between the L and Σ VB extrema ($E_{L\Sigma}$) and between the L and Δ VB extrema ($E_{L\Delta}$) (see Figure 4.2). The notation for the TB parameters adopted in this chapter is the same as that used in Chapter 3. For the most part, we neglect spin-orbit coupling (SOC) effects, in order to understand the effects of the simple atomic-orbital interactions themselves. Discussion on the potential influences of SOC can be round in Ref. 47. The overall chemical *trends* in VB are not significantly impacted by SOC, though SOC does have a significant impact on the bandgap energy, and this effect becomes less important as Pb and Te are replaced with lighter elements [109, 110].

Using Equation 3.2 for the L, Σ, and Δ VB extrema, in addition to Equations 3.5-3.7, we can write out analytical expressions that *approximate* the values of $E_{L\Sigma}$ and $E_{L\Delta}$, where we let $A_{sp} = \frac{1}{2}(E_{Te-p} - E_{Pb-s})$. We plot these solutions alongside the numerical solutions to the TB model (see Chapter 3 for parameters) with respect to $V_{sp\sigma}$, $V_{pp\sigma,Te}$ ($V_{pp\pi,Te} = -\frac{1}{8}V_{pp\sigma,Te}$), and A_{sp}

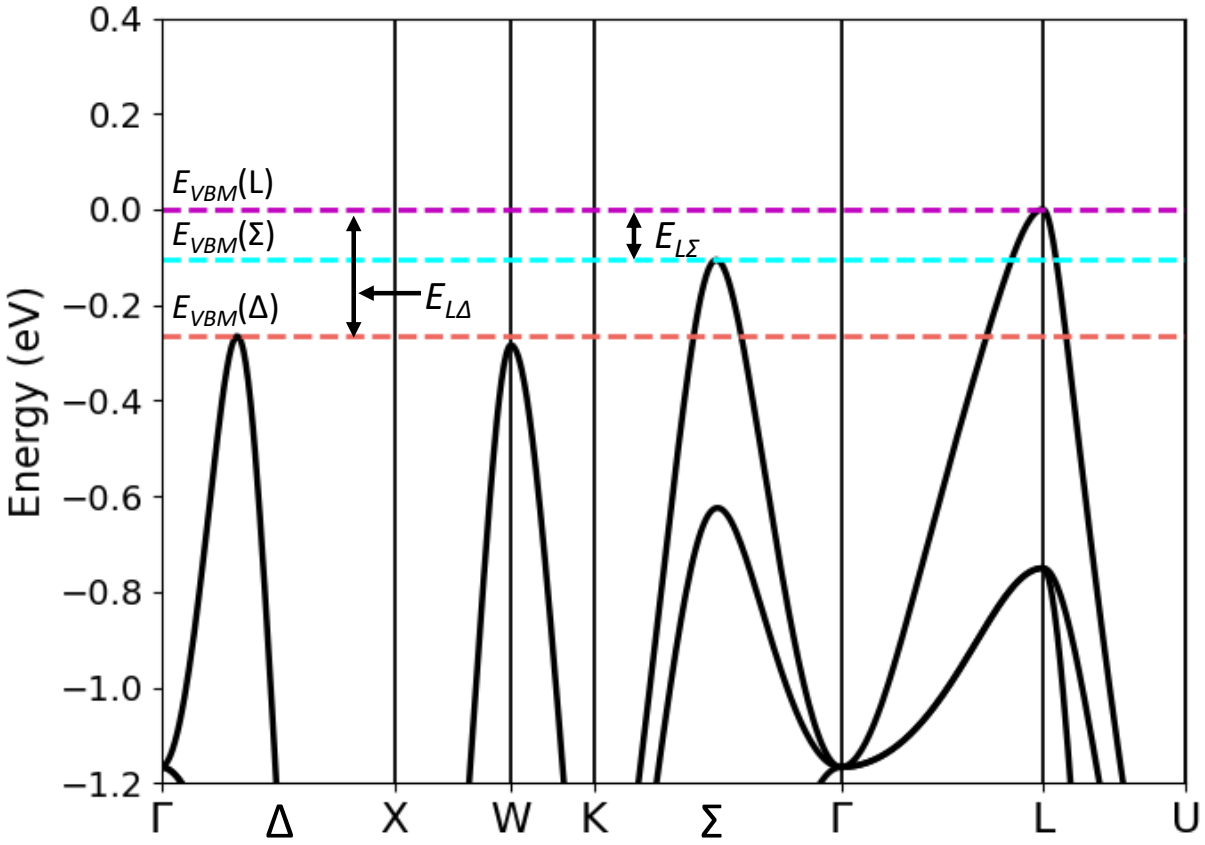

Figure 4.2: DFT-calculated (using the PBE functional without spin-orbit coupling) electronic structure of PbTe, showing the valence band edge. The energy of the L, Σ, and Δ valence band extrema are shown using the magenta, cyan, and coral dotted lines, respectively. The energy differences between the L and Σ bands ($E_{L\Sigma}$) and L and Δ bands ($E_{L\Delta}$) are labeled.

(Figure 4.3).[1] The analytical solutions are determined assuming that the Σ and Δ VBMs occur exactly at the points, $\Delta' = \frac{\pi}{a}(0,0,1)$ and $\Sigma' = \frac{\pi}{a}(0,1,1)$ while the numerical TB solutions use the true locations of these maximums, which deviate from these values. Clearly, both $E_{L\Sigma}$ and $E_{L\Delta}$ increase as $V_{sp\sigma}$ increases and as $V_{pp\sigma,Te}$ and A_{sp} decrease. Additionally, when convergence between L and Σ and between L and Δ increase, Σ and Δ also converge.

$$E_{L\Sigma} \approx V_{pp\pi,Te} - V_{pp\sigma,Te} + \frac{1}{2}\sqrt{(2A_{sp} + 4V_{pp\pi,Te} - 4V_{pp\sigma,Te})^2 + 48V_{sp\sigma}^2} - \frac{1}{2}\sqrt{(2A_{sp} + 2V_{pp\pi,Te} - 2V_{pp\sigma,Te})^2 + 32V_{sp\sigma}^2} \quad (4.1)$$

$$E_{L\Delta} \approx -2V_{pp\sigma,Te} + \frac{1}{2}\sqrt{(2A_{sp} + 4V_{pp\pi,Te} - 4V_{pp\sigma,Te})^2 + 48V_{sp\sigma}^2} - \frac{1}{2}\sqrt{(2A_{sp} + 4V_{pp\pi,Te})^2 + 16V_{sp\sigma}^2} \quad (4.2)$$

The trends with respect to $V_{sp\sigma}$ and A_{sp} are directly related to the fact that the different VB extrema have differing dependencies on the cation-s–anion-p interaction. As discussed in Chapter 3, the local VB maximums in PbTe and similar IV-VI rock salt semiconductors are primarily cation-s–anion-p anti-bonding states. Because the s–p interaction is strongest at L, followed by Σ, then Δ and W, the VBM is located at L, while the other VB maximums are lower in energy. Therefore, when this interaction is weakened, either by reducing the interaction parameter ($V_{sp\sigma}$) or by increasing the energy separation between the orbitals ($2A_{sp}$) [66], it reduces the difference in energy between the different anti-bonding states at different $\boldsymbol{k}$-points (Figure 4.3a,c). Moreover, the next-nearest-neighbor anion-p–anion-p interactions have an influence on the energy of the VBMs. In the L, Σ, and Δ VBMs, this interaction is bonding in nature, and lowers the energy of these bands, while in

[1] Like in Chapter 3, we use Pb as the cation and Te as the anion for the sake of discussion, but Pb can be generalized to a group-IV cation (Ge, Sn Pb), and Te can be generalized to any group-VI anion (S, Se, Te).

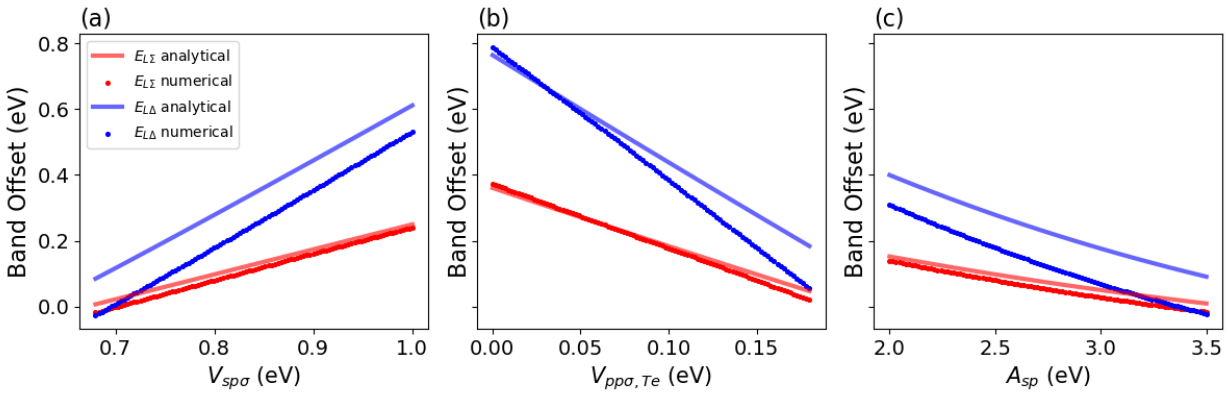

Figure 4.3: Tight-binding (TB)-calculated band convergence between L, Σ, and Δ valence bands with respect to (a) the cation-s–anion-p interaction strength ($V_{sp\sigma}$), (b) the anion-p-anion-p interaction strength ($V_{pp\sigma,Te}$) and (c) the energy separation between the cation-s and anion-p orbitals ($2A_{sp}$). The solid lines are calculated using the analytical approximations given in Equations 4.1-4.2, and the circles represent values calculated numerically using the TB model. The values of the TB parameters when they are held constant are $V_{sp\sigma} = 0.8$ eV, $V_{pp\sigma,Te} = 0.15$ eV, $2A_{sp} = 5$ eV, $V_{pp\sigma} = 1$ eV, and $V_{pp\pi} = -1/8$ eV. $V_{pp\pi,Te}$ is constrained, such that $V_{pp\pi,Te} = -\frac{1}{8}V_{pp\sigma,Te}$ (see Table 3.1).

the W VBM, it is *slightly* anti-bonding. Because the bonding interaction is stronger in the L band, followed by Σ, then Δ, increasing the interaction strength causes the L band to decrease relative to the Σ, Δ and W bands, while the Σ band decreases relative to the Δ band, and the Δ band decreases relative to the W band, enhancing the overall band convergence (Figure 4.3b).

4.2.2 Design Strategies for Valence Band Convergence

The theoretical insights from the TB model can be used to inform and explain real design strategies for achieving band convergence in PbTe and other IV-VI rock salt materials. As discussed in the previous section, the TB routes for achieving convergence involve tuning the values that influence the cation-s–anion-p nearest-neighbor and anion-p–anion-p next-nearest-neighbor interactions.[2] Because the cation-s–anion-p interaction dominates over the next-nearest neighbor anion-p

[2]While the cation-p–anion-p interactions do not play a significant role in controlling band convergence—the VB maxima are non-bonding or nearly non-bonding with respect to this interaction—these s–p interactions should influence the curvature of the VB (and CB) edges. Increasing the strength of this interaction (i.e., decreasing the energy separation between the p-orbitals or increasing the hopping parameter between the orbitals) should increase the curvature. The increase in curvature should then yield a lower inertial effective mass and higher carrier mobility [111]. While we do not investigate this relationship in detail, it is an interesting topic for study.

interactions, we focus on strategies that target the strength of the *s*-*p* coupling at the VB edges. The *s*-*p* interaction strength depends on both $V_{sp\sigma}$ and A_{sp}, so methods to enhance convergence should target, or effectively target, one or both of these parameters. Note that when we describe strategies to enhance convergence, we are assuming that the VBM is at L, rather than along Σ. However, at higher temperatures or certain compositions, Σ may overtake L and become the VBM [29], and in those cases, the opposite strategies should be employed to enhance convergence. We are also assuming that there is no change to the crystal structure—these effects are discussed in Chapter 5.

The value of $V_{sp\sigma}$ can be directly reduced by increasing the lattice constant, as the magnitude of any interaction (hopping) parameter decrease with interatomic distance [63, 64]. This can be achieved through an increase in temperature (thermal expansion) [112], decreasing hydrostatic pressure, or tuning alloying concentrations to increase the lattice constant. Because temperature and pressure do not change the composition of the compounds, they have been shown to consistently tune band convergence in the predicted direction based on the change in lattice constant and corresponding change in $V_{sp\sigma}$ [29,86,109]. This trend in $V_{sp\sigma}$ and convergence with respect to lattice constant is evident in Figure 4.4, which shows that the convergence between the L, Σ, and Δ bands increases with lattice constant—up until the point where the Σ and Δ overtake the L band—and that both the contribution of the cation-*s* orbital at L and the difference between the contribution at L and in the Σ and Δ bands decreases with lattice constant. The percent contribution of the cation-*s* orbital in the VB edges acts as a proxy for the strength of the *s*-*p* coupling [113], so these trends show that the *s*-*p* coupling (described by $V_{sp\sigma}$), and hence *differences* in *s*-*p* coupling between the different VB pockets, decreases with increasing lattice constant. Clearly, increasing the lattice constant decreases the energy separation between the L VBM and the other local VBMs, and this trend can be directly linked to a decrease in cation-*s*–anion-*p* coupling with increasing lattice constant.

When chemical substitutions that change the composition alter the lattice constant, the trend with respect to *s*-*p* interaction strength and subsequent change in convergence is less straightforward.

For instance, substitutions on the anion-site with a more electronegative species (e.g., substituting Te with Se or S or substituting Se with S) [6] decreases the lattice constant [86, 112] but also decreases the on-site energy of the anion-p orbitals, which reduces the values of A_{sp} [64]. Because the decrease in lattice constant and decrease in s-p energy splitting both increase the strength of the s–p coupling, there is a consistent trend indicating that substituting Te or Se with a more electronegative chalcogen decreases VB convergence [29, 86, 109, 112]. Furthermore, when replacing Pb with Sn, both the decrease in A_{sp} (Sn is more electropositive than Pb [3]) and the decrease in lattice constant should lead to a decrease in convergence, which is in fact the case [114–116].[3] On the other hand, when the cation-site is replaced with a more electropositive cation species that increases the lattice constant (e.g., substituting Ge with Sn) [6], we would expect a decrease in convergence due to a decrease in A_{sp},[4], but an increase in convergence from the larger unit-cell volume. That is, replacing Ge with Sn should lead to a decrease in convergence from Sn being more electropositive than Ge (smaller A_{sp}), but should lead to an increase in convergence from the lattice constant of SnTe being larger than that of GeTe [116]. In this case, the effect of reducing the s-p energy splitting evidently wins out, as it is known from first-principles calculations that the convergence between band edges at low temperature is greater in GeTe than in SnTe [38, 91, 119–122].

It is worthwhile to point out that SnTe exhibits band inversion at the L-point (when SOC is considered), making it a topological crystalline insulator, so the cation-s–anion-p anti-bonding state actually constitutes the CBM at L, while the cation-p-anion-s anti-bonding state constitutes the L-point VBM [90, 114, 115, 119]. Therefore, in SnTe with band inversion, Equation 4.1 and 4.2 do not hold. In pure SnTe with band inversion, the differences in band-edge energy are even greater

[3] The PBE electronic band structures of rock salt GeTe, PbTe, and SnTe, in addition to other IV-VI semiconductors without SOC can be found on the Materials Project database: https://materialsproject.org/materials. The interactive band structure plots allow users to see the relative energy of the different VB pockets relative to the VBM at the L-point.

[4] While the electronegativity generally decreases down a group on the periodic table, Pb represents an exception in the chalcogen series, as it is more electronegative than both Sn and Ge. This somewhat anomalous electronegativity trend is attributed to relativistic effects—which decrease the energy of the valence electrons by contracting the s and p electron shells—from the large size of Pb [116–118]. This electronegativity trend actually contradicts the atomic on-site energies given in Ref. 63, which indicates that the Pb-s and Pb-p energies are higher than those of Sn and Ge.

than the differences that would be calculated using the actual VBM energies, because the L-point cation-s–anion p anti-bonding state is higher in energy than the L-point VBM (a cation-p–anion-s anti-bonding state). That being said, when we consider alloying SnTe with IV-VI rock salt materials that do not exhibit band inversion (and the alloy also does not exhibit band inversion), then the differences between the cation-s–anion-p anti-bonding states at L, Σ, Δ, and W are the relevant factors in determining trends in band convergence with respect to alloying.

The difference in the VB offsets between PbTe and (cubic) GeTe are more difficult to explain using $V_{sp\sigma}$ and A_{sp}. Based on both electronegativity and equilibrium lattice constants ($a_{\mathrm{GeTe}} = 6.02$ Å, $a_{\mathrm{PeTe}} = 6.56$ Å), we would expect GeTe to have a *less* converged VB structure because it has a smaller lattice constant and should have a smaller value of A_{sp}. However, cubic GeTe is more converged than PbTe, showing that this intuition is not sufficient. As seen in Figure 4.4a, the difference in energy between the L VBM and Δ and Σ VBs is larger in PbTe than in GeTe when the lattice constants are equal.[5] Additionally, at the equilibrium lattice constants, GeTe is more converged than PbTe, despite GeTe having a smaller lattice constant. The fact that the L–Σ and L–Δ offsets are greater in PbTe than GeTe for the same lattice constant indicates that chemically, GeTe intrinsically favors having smaller offsets, independent of lattice constant effects.

Based on Figure 4.4b-c, the s-p coupling does not decisively explain these differences in VB offsets. The difference in cation-s contribution between the L and Σ bands and L and Δ bands are very similar between the two materials (Figure 4.4b). Based only on the cation-s contributions in the L-point VBM, PbTe exhibits greater s-p coupling than GeTe, given that they have the same lattice constant, but equilibrium GeTe exhibits greater s–p coupling than equilibrium PbTe (Figure 4.4c). The former observation is not consistent with Pb being more electronegative than Ge and the latter is inconsistent with the band offsets being larger in PbTe than GeTe. The first contradiction may be from the Ge-s orbitals being lower in energy than Pb-s orbitals, despite what the Pauling electronegativity values [3] would suggest. In fact, according to Ref. 63, this is the case, and Ge-s

[5]The methods used to calculate the DFT energy levels are the same as those described in Chapter 4. For the strain calculations, the lattice constants are set manually and not by structural relaxations.

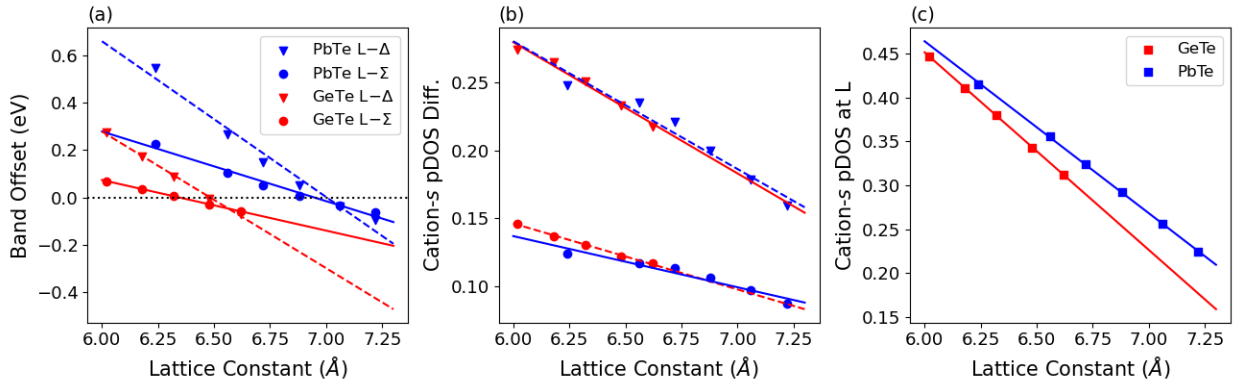

Figure 4.4: Comparison of DFT-calculated (no SOC) valence band (VB) offsets and $\boldsymbol{k}$-resolved, band-resolved projected density of states (pDOS) values for the cation-s orbitals as a function of lattice constant between GeTe and PbTe. (a) Difference in energy between L and Σ VBs (circles) and between L and Δ VBs (inverted triangles) for GeTe (red) and PbTe (blue). Lines of best fit are shown with solid lines (L−Σ) or dashed lines (L−Δ). (b) Difference in the (normalized) pDOS of cation-s between L and Σ VBs and between L and Δ VBs for GeTe and PbTe (same label key as (a)). (c) Normalized cation-s pDOS in the L-point VBM as a function of lattice constant for GeTe and PbTe.

orbitals are lower in energy than Pb-s orbitals. The second contradiction *may* be due to relatively stronger Te-p–Te-p interactions in GeTe than in PbTe, which would lower the energy of the L VBM relative to the Σ and Δ bands. However, this hypothesis still needs to be confirmed, and other unexplored explanations may be possible.

Finally, one of the most popular and effective strategies for enhancing band convergence in the IV-VI rock salt thermoelectrics, alloying/doping on the cation-site with elements that introduce unfilled s^0-orbitals *above* the VBM, can be explained as *effectively* decreasing the s-p coupling strength. These unfilled cation-s^0-orbitals interact with the anion-p states in the VB with the same relative strength (between different VB pockets) as the filled cation-s^2–anion-p interactions, but because these unfilled cation-s orbitals are above the VB edge, they push the VB edges *down* in energy. That is, the VB edges contain unfilled cation-s^0–anion-p *bonding* states, analogous to the filled cation-s^2–anion-p anti-bonding states. This interaction directly counteracts the filled cation-s^2–anion-p anti-bonding interaction in the VB edges, and it is strongest in the L VB, followed by Σ VB, then Δ and W VBs, so it leads to an effective decrease in $V_{sp\sigma}$, and therefore, increase in convergence. Additionally, increasing the content of the s^0-cations decreases the content of the

s^2-cations, which simply reduces the number of s^2-orbitals that can interact with the anion-p VB states.

The impact of cation-s^0 states on the VB structure can be qualitatively modeled using the TB method in conjunction with the virtual crystal approximation (VCA). The VCA is a computationally inexpensive method to model alloy systems that is simple to implement. Within the VCA, the alloying site is treated as a weighted average of the its constituents. If we consider the alloy, $A_{1-x}B_xC$, the VCA potential describing the electronic structure of the alloy can be written as a linear combination, or weighted average, of the potential of the compounds, AC and BC [123–126].

This VCA methodology can be translated to understanding cation-site substitutions (with different on-site energies) by adding an an additional TB basis element for the cation-s^0 state. Consider the alloy, $M1_xM2_{1-x}X$, where $M1$ is a cation that introduces unfilled s^0 states above the VB edge (Na, Mn, Mg, Cd, Hg, etc.), $M2$ is a group-IV cation (Ge, Sn, Pb), and X is a group-VI anion (S, Se, Te). To implement the VCA in this case, we simply modify the Hamiltonian such that we weight the hopping parameter for the $M1$-s^0–X-p interaction by x and weight the hopping parameter for the $M2$-s^2–X-p interaction by $1-x$. Additionally, we weight the $M2$-p–X-p interactions by $1-x$, and we assume that the $M1$ atom only introduces s^0 states and no other orbital states. Results for this model are depicted in Figure 4.5. Clearly, increasing the $M1$ content within this TB model causes both $E_{L\Sigma}$ and $E_{L\Delta}$ to decrease such that the VB structure is more converged. Moreover, this effect is still present when we do not consider the $M1$-s^2–X-p interactions at all but still weight the $M1$–X interactions by $1-x$ (treating $M1$ as a vacancy), but the effect is weaker, especially at larger x.

4.3 Low-Dimensional Fermi Surface Topology

When more and more VB pockets are converged in energy near the band edge in PbTe (and similar IV-VI compounds), the result is not merely an increase in the nominal number of carrier pockets to increase N_V. Rather, the result is a more fundamental change to the *nature* of the Fermi surface

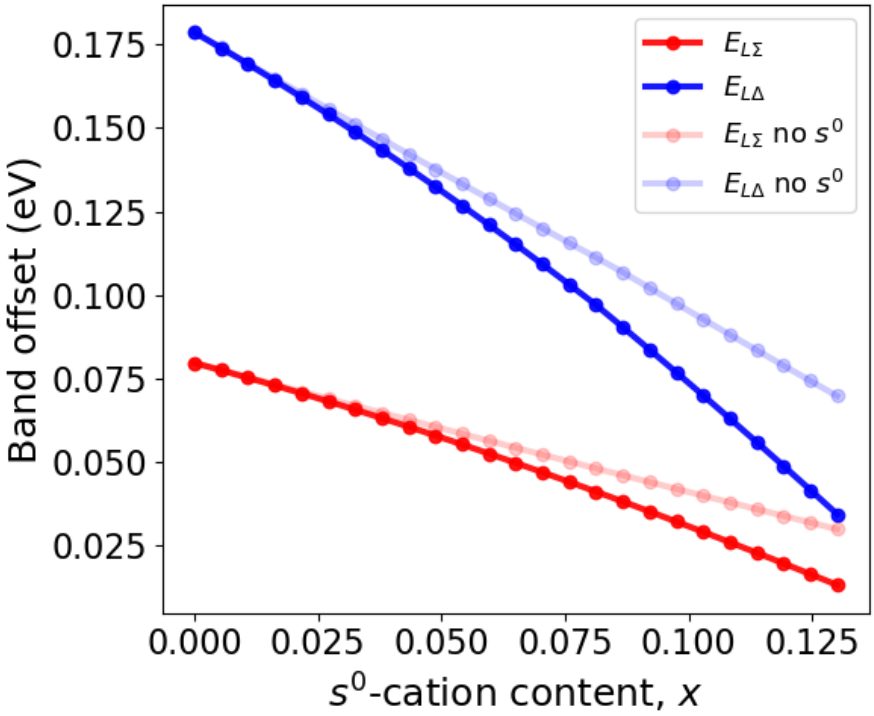

Figure 4.5: Numerical tight-binding (TB) values of valence band (VB) offsets between the L and Σ VBs ($E_{L\Sigma}$) and between the L and Δ VBs ($E_{L\Delta}$) as a function of x in $M1_xM2_{1-x}X$, where $M1$ is a cation that introduces unfilled s^0 states above the VB edge (Na, Mn, Mg, Cd, Hg, etc.), $M2$ is a group-IV cation (Ge, Sn, Pb), and X is a group-VI anion (S, Se, Te). The darker lines represent values calculated with the $M1$-s^0–X-p and $M2$-s^2–X-p interactions included, while the fainter lines represent values calculated where only the $M2$-s^2–X-p interaction is considered (s^0-cation ($M1$) acts as a cation vacancy). The same s-p hopping parameter, $V_{sp\sigma}$, is used for both s-p interactions, and the on-site energy of $M1$-s^0 is set to be 2.5 eV above the X-p on-site energy. The other TB parameters are the same as those used to calculate Figure 4.3 (see Table 3.1). The $M2$-p–X-p interaction is also included in all calculations. Note that only the effects of the cation-s-orbital contents are being considered in this model— we do not regard the effects of introducing other $M1$ orbitals.

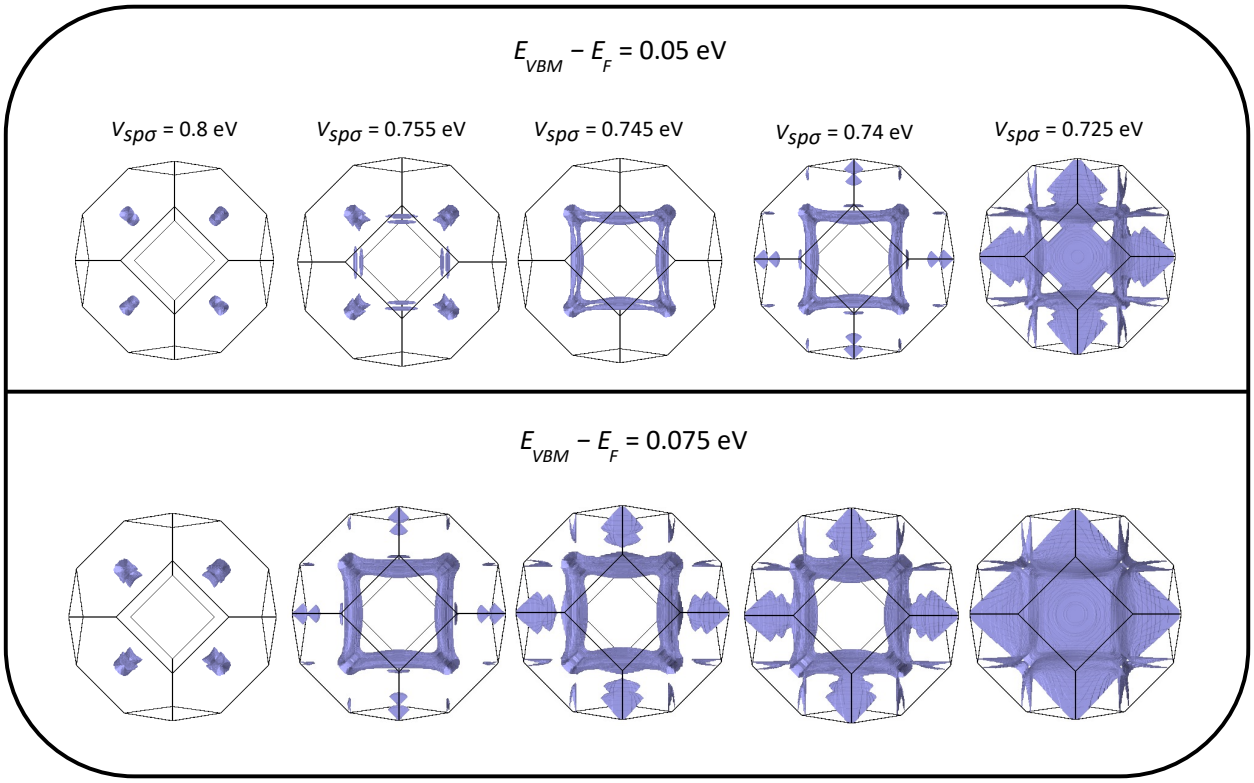

Figure 4.6: Valence band (VB) Fermi surface evolution from tight-binding (TB) band structures of a toy IV-VI rock salt semiconductor, where the cation-s–anion-p hopping parameter, $V_{sp\sigma}$, is varied. The top panel shows TB Fermi surfaces when the Fermi energy is set to be 0.05 eV below the VBM, and the bottom panel shows Fermi surfaces with the same $V_{sp\sigma}$ values for a Fermi energy 0.075 eV below the VBM. All the TB parameters aside from $V_{sp\sigma}$ are given by the values listed in Table 3.1.

topology, such that complex and non-ellipsoidal Fermi surface geometries emerge, leading to low-dimensional-like (1D-like or 2D-like) transport in 3D materials.

4.3.1 Description of Fermi Surfaces

The VB Fermi surfaces calculated using the TB model for the toy IV-VI rock salt system provide a picture of a theoretical evolution of Fermi surface geometries as certain parameters are varied. Here, we present an evolution based on varying the cation-s–anion-p hopping parameter, $V_{sp\sigma}$ (Figure 4.6). However, a similar type of evolution would be expected from increasing the strength of the anion-p–anion-p interactions or increasing the energy separation between the cation-s and anion-p orbitals.

At higher values of $V_{sp\sigma}$ the Fermi surface near the band edge is characterized by four ellipsoidal pockets that start to form "prongs" slightly deeper into the VB edge.[6] Then, as $V_{sp\sigma}$ is reduced, the twelve Σ pockets emerge, and if $V_{sp\sigma}$ is reduced further or the Fermi energy is moved deeper below the VBM, the Fermi surface extends continuously between the L-points, through the twelve Σ pockets, such that the Fermi surface is characterized by twelve tubes that roughly outline a cube (like the IV-VI rock salt Fermi surfaces depicted in Ref. 45). Additionally, at slightly lower values of $V_{sp\sigma}$ or (Fermi energies), pockets at the W-points begin to emerge and eventually connect to the tubes. Finally, at even lower values of $V_{sp\sigma}$ the Δ pockets begin to form and coalesce with the tubes, such that Fermi surface "sheets" are formed. While the exact nature of the evolution depends on the other TB parameters, the Fermi surfaces depicted in Figure 4.6 give an general sense of the types of Fermi surface geometries that can be (theoretically) achieved in IV-VI rock salt semiconductors.

We can simplify the features of these Fermi surfaces into three types of idealized shapes: ellipsoids spheres, cylinders, and sheets (Figure 4.7). Specifically, the Fermi surface types include four spheres (radius $|\boldsymbol{k_{3D}}|$), twelve cylinders (radius $|\boldsymbol{k_{2D}}|$, length $2\pi/a$), and six intersecting sheets (thickness $2|\boldsymbol{k_{1D}}|$, side length $2\sqrt{2}\pi/a$). We distinguish these three different Fermi surface based on the energy-dependence of their DOS expressions, as described in Figure 4.1. The spherical Fermi surface has a 3D-like DOS, the cylindrical Fermi surface has a 2D-like DOS, and the sheet-like Fermi surface has a 1D-like DOS. Using these simplified Fermi surfaces geometries, we can develop transport models to describe them, following a similar approach to that used in Chapter 2 to derive the thermoelectric quality factor, B.

4.3.2 Thermoelectric Transport Predictions

To develop transport models for the three Fermi surface types described in the previous section, we start with the generic electronic dispersion for a free-electron-like band (Equation 4.3), following the assumptions in the single parabolic band (SPB) model [18,56]. We also assume acoustic-phonon

[6] This pronged, or corrugated, type of Fermi surface is very similar to that described in Ref. 46 to describe the GeTe and SnTe Fermi surfaces.

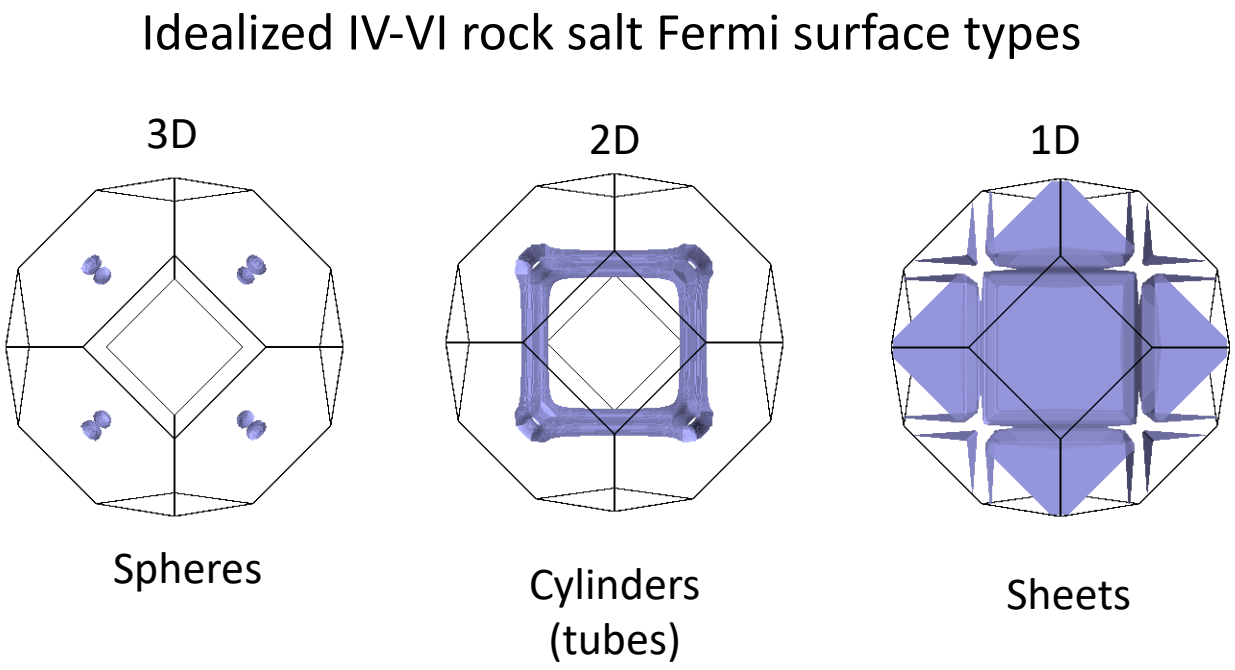

Figure 4.7: Idealized IV-VI rock salt valence band (VB) Fermi surfaces types. Each type of Fermi surface is distinguished by the energy dependence of its density of states (DOS), and the dimensionality of transport that coincides with this DOS. The 3D-type Fermi surface (left) consists of four spheres (eight half-spheres), with radius $|\boldsymbol{k_{3D}}|$. The 2D-like Fermi surface (center) consists of twelve cylinders with radius $|\boldsymbol{k_{2D}}|$ and length $\frac{2\pi}{a}$, where a is the unit cell lattice constant. The 1D-like Fermi surface (right) can be approximated as six intersecting sheets (neglecting the overlapping areas) with side lengths $\frac{2\sqrt{2}\pi}{a}$ and thickness $2|\boldsymbol{k_{1D}}|$.

scattering, which means that the scattering rate should be approximately proportional to the DOS (from Fermi's Golden Rule).

$$E(\boldsymbol{k}) = \frac{\hbar^2 k_x^2}{2m_x^*} + \frac{\hbar^2 k_y^2}{2m_y^*} + \frac{\hbar^2 k_z^2}{2m_z^*} \tag{4.3}$$

In the above equation, k_x, k_y, and k_z are the Cartesian components of the $\boldsymbol{k}$-vector, and m_x^*, m_y^*, and m_z^* are the inertial effective masses along the three Cartesian directions. For a spherical Fermi surface pocket, the inertial effective mass will be isotropic ($m_x^* = m_y^* = m_z^*$), so the dispersion can be simplified (Equation 4.4).

$$E(\boldsymbol{k}) = \frac{\hbar^2 (k_x^2 + k_y^2 + k_z^2)}{2m_I^*} = \frac{\hbar^2 |\boldsymbol{k_{3D}}|^2}{2m_I^*} \tag{4.4}$$

For a (perfectly) cylindrical Fermi surface pocket, the curvature is zero (i.e., the band is flat), in one of the three directions. The inertial effective mass is inversely related to the curvature, so the effective mass for this direction would approach infinity, making the term, $\frac{\hbar^2 k_i^2}{2m_i^*}$ —where i is the direction with zero curvature— approach zero. Therefore, the cylindrical dispersion is given by the expression in Equation 4.5, where we assume (arbitrarily) that the cylinder is oriented along the z-axis.

$$E(\boldsymbol{k}) = \frac{\hbar^2 (k_x^2 + k_y^2)}{2m_I^*} = \frac{\hbar^2 |\boldsymbol{k_{2D}}|^2}{2m_I^*} \tag{4.5}$$

Finally, for the sheet-like Fermi surface, the bands have zero curvature in two of the three directions, giving the following electronic dispersion, assuming (arbitrarily) that the sheet is oriented in the y-z plane:

$$E(\boldsymbol{k}) = \frac{\hbar^2 k_x^2}{2m_I^*} = \frac{\hbar^2 |\boldsymbol{k_{1D}}|^2}{2m_I^*}. \tag{4.6}$$

The velocity of the charge carrier in a given direction is related to the partial derivative of the dispersion relationship [67, 69].

$$v_i(\mathbf{k}) = \frac{1}{\hbar}\frac{\partial E(\mathbf{k})}{\partial k_i} = \frac{\hbar k_i}{m_i} \tag{4.7}$$

In Equation 4.7, v_i is the carrier velocity along the i–direction, where $i = x, y$, or z. The velocity in a given direction is inversely proportional to the respective effective mass. Therefore, when there is virtually zero dispersion in a given direction (flat band), then the effective mass in that direction approaches infinity, and the velocity approaches zero. Consequently, the carrier transport is effectively zero in that direction and limited to the other direction(s). That is, in the 3D-like Fermi surface (spheres) transport occurs in all three dimensions from each Fermi surface pocket, while for the 2D-like (cylindrical) Fermi surface, each cylinder will contribute to transport in only two dimension, as the dispersion is flat in the third direction. Moreover, for the 1D-like Fermi surface (sheets), each sheet only contributes to transport in one of the three directions. Even though each individual cylinder (or sheet) only contribute to transport in two (or one) directions, *the overall transport is still isotropic* for this cubic system because the contributions of each cylinder (or sheet) can be added, and there are three cylinders (two sheets) in each direction [69]. Thus, the contributions to transport are equal in all three directions.

The expressions for the scattering time, τ, Seebeck coefficient, α, quality factor, B, Lorenz number L, figure of merit, zT, and DOS, g, for 1D-, 2D-, and 3D-type bands are given in Appendix D.13 (see Chapter 2 for background on thermoelectric transport). Because we assume acoustic-phonon scattering ($\tau \propto 1/g$) the expression for α, L, and zT are identical for 1D, 2D, and 3D in terms of B and the reduced Fermi Level (this is not the case for all scattering assumptions), η, where $\eta = E_F/k_BT$, and E_F is the Fermi energy. They are given in Equations 4.8-4.10.

$$\alpha(\eta) = \left(\frac{k_B}{e}\right)\left[\frac{2F_1(\eta)}{F_0(\eta)} - \eta\right] \tag{4.8}$$

$$L(\eta) = \left(\frac{k_B}{e}\right)^2 \left[\frac{3F_2(\eta)F_0(\eta) - 4F_1^2(\eta)}{F_0^2(\eta)}\right] \tag{4.9}$$

$$zT(\eta, B) = \frac{\alpha^2(\eta)}{\frac{(k_B/e)^2}{BF_0(\eta)} + L(\eta)} \tag{4.10}$$

$F_j(\eta)$ is the Fermi-Dirac integral, which is defined in Equation 2.7.

Although α is the same for all three dimensions *for a given value of* η, the reduced chemical potential is a function of the hole concentration, p, which is given by $p = \int_0^\infty g(E)f(E)dE$, where f is the Fermi-Dirac distribution. Because the DOS is different for each dimension, the relationship between p and η changes with dimensionality, as seen in Equations 4.11-4.13. Here, p_{1D}, p_{2D}, p_{3D} represent the number of holes per unit volume of the material corresponding to the idealized 1D, 2D, and 3D Fermi surface types, respectively, and m_b^* is the band effective mass (or the DOS effective mass for a single band).

$$p_{1D} = \frac{12(2m_b^* k_B T)^{1/2}}{a^2 \pi \hbar} F_{-\frac{1}{2}}(\eta) \tag{4.11}$$

$$p_{2D} = \frac{12 m_b^* k_B T}{a \pi \hbar^2} F_0(\eta) \tag{4.12}$$

$$p_{3D} = \frac{2(2m_b^* k_B T)^{3/2}}{\pi^2 \hbar^3} F_{\frac{1}{2}}(\eta) \tag{4.13}$$

Using Equations 4.11-4.13 and Equation 4.8, we can calculate the Pisarenko relationship at 300K (α versus p) for each dimension as seen in Figure 4.8a. The lattice parameter is taken to be $a = 6.46$ Å, and the band effective mass is taken to be $m_b^* = 0.2m_e$ [45]. For a given p, the Seebeck coefficient increases as the dimensionality of the bands is reduced, and this increase in thermopower is due to the higher hole concentration for a given value of η. Moreover, using the expressions for

the electrical conductivity, σ, and Lorenz number, L derived in Appendix C for the three Fermi surface geometries, we plot estimates for the power factor ($\alpha^2\sigma$) and zT for each type of Fermi surface. Here, we assume (solely for the sake of comparison between Fermi surface types) that the lattice thermal conductivity is given by $\kappa_L = 5$ W/mK.

Furthermore, because the scattering time, and hence, mobility should be inversely related to the DOS of a given carrier pocket (from acoustic-phonon scattering assumption based on Fermi's golden rule) [59, 60, 127], we scale the value of the carrier mobility parameter, μ_0, by the DOS of each type of carrier pocket, such that the mobility is decreased when the DOS is larger. To start, we try a mobility approximation that uses the DOS of a *single* sphere, cylinder, or sheet, and does not include the degeneracy of each type of carrier pocket (Equations 4.14-4.16]). We introduce a variable, ε, which is the reduced energy ($\varepsilon = E/k_BT$).

$$g_{sphere}(E) = \frac{\sqrt{2}(m_b^*)^{3/2}}{\pi^2\hbar^3}E^{1/2} = \frac{\sqrt{2}(m_b^*)^{3/2}}{\pi^2\hbar^3}(k_BT)^{1/2}\varepsilon^{1/2} \tag{4.14}$$

$$g_{cylinder}(E) = \frac{m_b^*}{a\pi\hbar^2} \tag{4.15}$$

$$g_{sheet}(E) = \frac{2(2m_b^*)^{1/2}}{a^2\pi\hbar}E^{-1/2} = \frac{2(2m_b^*)^{1/2}}{a^2\pi\hbar}(k_BT)^{-1/2}\varepsilon^{-1/2} \tag{4.16}$$

Thus, if we assume that $\mu_0 = \mu_{0_{3D}}$ for the spherical Fermi surface pockets, then the mobility parameter for the cylindrical Fermi surface pockets can be *roughly estimated* to be $\mu_{0_{2D}} = \mu_{0_{3D}}\sqrt{2}a(m_b^*k_BT)^{1/2}/(\pi\hbar)$, and the mobility parameter for the sheet-like Fermi surface pockets can be approximated as $\mu_{0_{1D}} = \mu_{0_{3D}}a^2(m_b^*k_BT)/(2\pi\hbar^2)$. Thus, $\mu_{0_{2D}} \sim (1/10)\mu_{0_{3D}}$ and $\mu_{0_{1D}} \sim (1/200)\mu_{0_{3D}}$. For this example, we take the mobility of the spherical pockets to be $\mu_{0_{3D}} = 1000$ cm^{2}V/s. The energy-dependence of the DOS is already taken care of in the derivation of α, σ, and L as a function of carrier concentration (see Appendix C for more details).

Using these scattering-rate assumptions, we predict an improvement to the peak power factor (Figure 4.8b) and zT (Figure 4.8c) as the Fermi surface evolves from the 3D-like geometry (spheres) to the 2D-like geometry (cylinders), and from the spheres to the 1D-like Fermi surface (sheets), but a decrease in peak power factor and zT from the cylinders to the sheets. The predicted improvement in the 2D and 1D cases (from the 3D case) is the result of higher carrier concentrations closer to the band edge (lower η), allowing for the Seebeck coefficient and electrical conductivity to be simultaneously enhanced. However, in the 1D case, the increased carrier concentration near the band edge is counteracted by the higher scattering rate, such that the overall power factor and zT is reduced relative to the 2D case. Additionally, the power factor and zT peak at higher carrier concentrations as the Fermi surface evolves from the 3D to the 2D to the 1D case (9×10^{18} cm^{-3}, 2×10^{20} cm^{-3}, and 4×10^{21} cm^{-3}, respectively).

In the last, assumption, we assume that scattering occurs at equal rates on the entire surface of a cylinder or sheet but not *between* cylinders and sheets. Another assumption we can try, is to assert that there is complete scattering between the states closest to one of the four L-points, and no scattering between states that are closest to different L-points. That is, we use the DOS that corresponds to 1/4 of the *total* DOS for the four spheres, twelve cylinders, or six sheets. The mobility parameters for the 1D and 2D bands (relative to that for the 3D bands) for this assumption are $\mu_{0_{1D}} = \mu_{0_{3D}} a^2 (m_b^* k_B T)/(3\pi\hbar^2)$ and $\mu_{0_{2D}} = \mu_{0_{3D}} \sqrt{2} a (m_b^* k_B T)^{1/2}/(3\pi\hbar)$. This assumptions leads to equivalent maximum values of power factor (Figure 4.8d) and zT (Figure 4.8d) for all three cases (the Seebeck coefficient is still highest in the 1D case and lowest in the 3D case for a given η). These results indicate that all the benefits of having a higher hole concentration are completely cancelled out by the increase in electron-phonon scattering from the higher DOS. The optimal carrier concentrations for this assumption are 9×10^{18} cm^{-3}, 3×10^{20} cm^{-3}, and 5×10^{21} cm^{-3} for the 3D, 2D, and 1D cases, respectively.

The scattering assumptions based on the simple scaling of the mobility by the DOS for each Fermi surface type assumes that the electron-phonon scattering rate is independent on the initial

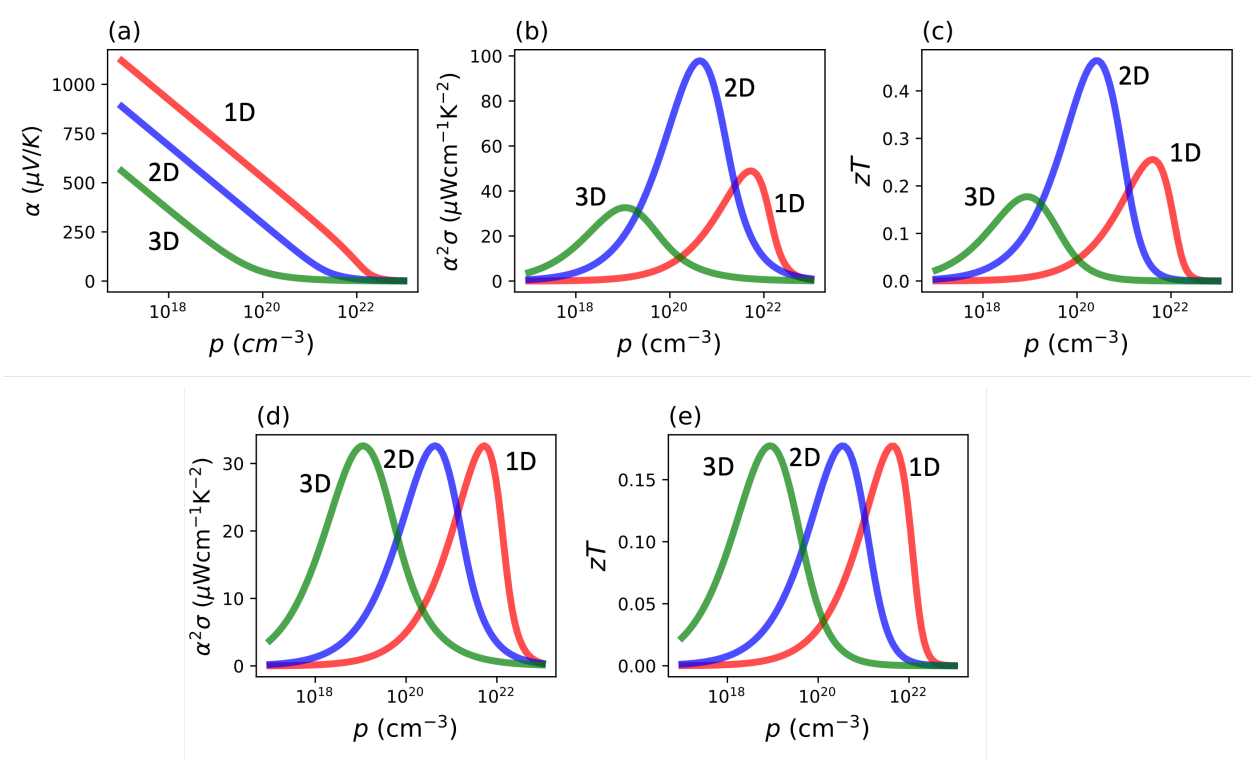

Figure 4.8: Seebeck coefficient (α), power factor ($\alpha^2\sigma$), and zT as a function of hole concentration (p) at 300K for different scattering assumptions (based on acoustic-phonon scattering) for the 3D- (green), 2D- (blue), and 1D-like (red) Fermi surfaces in IV-VI rock salt compounds. (a) The Seebeck coefficient is highest in the 1D Fermi surface, followed by the 2D then 3D Fermi surface geometries. (b) Power factor and (c) zT as a function of carrier concentration, assuming that the scattering rate is proportional to the density of states of a single sphere, cylinder, or sheet. (d) Power factor and (e) zT, assuming that the scattering rate is proportional to the density of states corresponding to one of the four L-points (1/4 of the total DOS for 4 spheres, 12 cylinders, or 6 sheets).

and final $\boldsymbol{k}$-vectors and the distance between the $\boldsymbol{k}$-vectors on the iso-energy Fermi surface. However, in general, electron-phonon scattering between $\boldsymbol{k}$-points is less likely in more distant $\boldsymbol{k}$-points [36]. Also, this simplified DOS scaling of the scattering time is not entirely consistent with real behavior seen in in IV-VI compounds because it would mean that there would be no benefit from having Σ-pockets contributing to the transport in PbTe, as the benefits from the extra carriers introduced by the Σ pockets would be completely cancelled out by an increase in electron-phonon scattering. The Σ-pockets do, in fact, enhance the performance of PbTe [29, 78], so this DOS scaling likely presents an over-correction to the mobility.

Therefore, it is beneficial to look at the other extreme: the constant scattering time approximation. This assumption asserts that the scattering time τ is independent of energy and has no dependence on the DOS [57, 128]. The Pisarenko relationship, power factor, and zT following this assumption are shown in Figure 4.9. We assume $\mu_0 = 1000$ cm^{2}V/s fall all three Fermi surface geometries. Clearly, the constant scattering time approximation predicts a dramatic increase in the power factor and zT upon a reduction in the transport dimensionality, in accordance with Ref. 45. Again, the enhancement is due to the large increase in charge carriers for a given value of η. While the constant scattering time approximation is not a good model for thermoelectric transport, as it completely neglects the DOS dependence electron-phonon scattering, it provides a kind of upper limit on the potential for performance gains in low-dimensional bands in bulk 3D materials. Thus, if the DOS-scaling is an over-correction, and the constant τ approximation is an under-correction, then the real effects of low-dimensional-type transport may lie in between, suggesting the possibility of more modest gains in thermoelectric performance from the 2D- and 1D-type Fermi surfaces. To more accurately understand the effects of Fermi surface geometry and dimensionality, numerical calculations of the $\boldsymbol{k}$-dependent scattering matrix elements (see Equation 2.15) would need to carried out [78].

Another metric that can be used to compare the potential performance of the different Fermi surface types—but is less (directly) dependent on scattering time approximations—is the Fermi

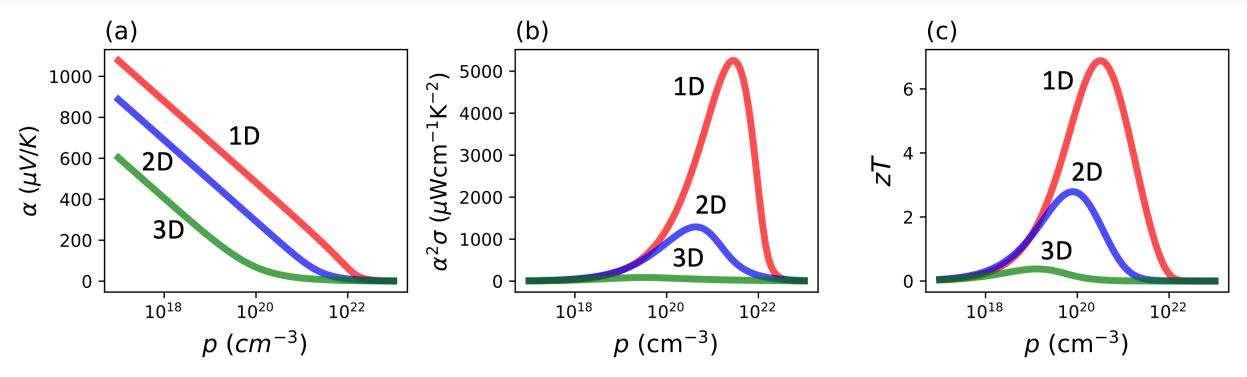

Figure 4.9: (a) Seebeck coefficient (α), (b) power factor ($\alpha^2\sigma$), and (c) zT as a function of hole concentration (p) at 300K calculated using the constant scattering time approximation for the 3D- (green), 2D- (blue), and 1D-like (red) Fermi surfaces in IV-VI rock salt compounds.

surface complexity factor, $N_V^* K^*$, which quantifies how complex a Fermi surface is based on its *effective* degeneracy (N_V^*) and *effective* anisotropy factor (K^*) [34]. Note that the anisotropy factor refers to the anisotropy of the Fermi surface pocket(s), and not the overall conductivity. In the cubic rock salt materials, the conductivity tensor is isotropic, even with anisotropic carrier pockets. Higher complexity factors strongly correlate with maximum power factors ($\alpha^2\sigma$) and better performing thermoelectric materials. The complexity factor depends on both the the conductivity effective mass (m_c^*) and the Seebeck effective mass (m_S^*) which is simply the DOS effective mass that is extracted from Seebeck versus carrier concentration data using Equation 4.8.

$$N_V^* K^* = \left(\frac{m_S^*}{m_c^*}\right)^{3/2} \tag{4.17}$$

The conductivity effective mass can be determined from the inertial effective masses, using the following relationship: $m_c^* = 3/(\frac{1}{m_x^*} + \frac{1}{m_y^*} + \frac{1}{m_z^*})$. It is not difficult to show that the conductivity effective mass values are , $m_c^* = m_b^*$, $m_c^* = 2m_b^*$, and $m_c^* = 3m_b^*$ (m_b^* as used in Equations 4.11-4.16) for the 3D-, 2D- and 1D-type Fermi surfaces, respectively. Recall that in this example, we assume that m_b^* is constant at a value of $0.2m_e$. The Seebeck versus carrier concentration values used to determine the Seebeck effective mass are those given in Figure 4.8a, which is calculated assuming electron-phonon scattering. The values of the Seebeck effective mass, m_S^*, and complexity factor,

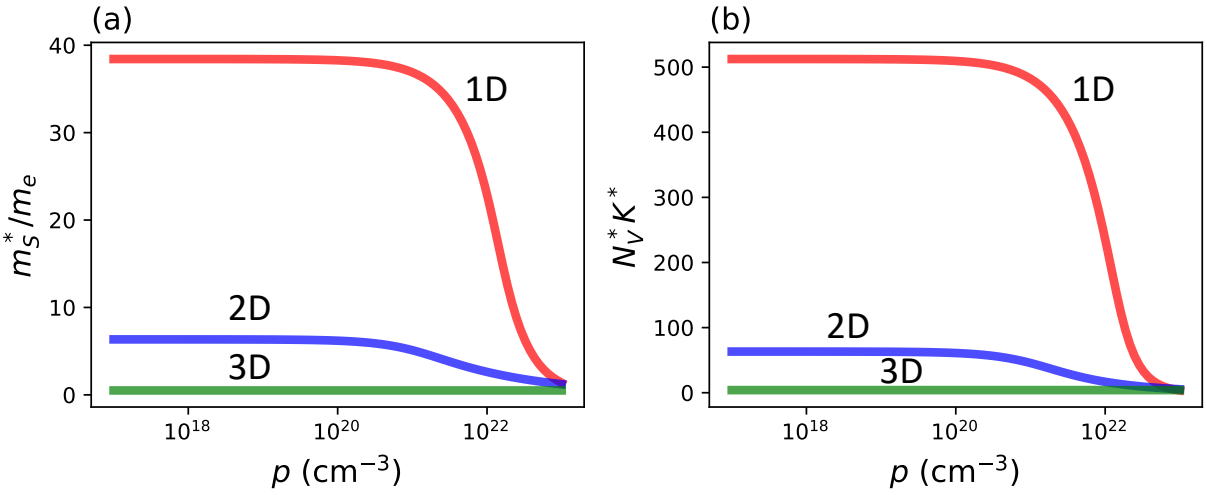

Figure 4.10: Comparison of Seebeck effective mass and Fermi surface complexity factors for idealized IV-VI rock salt Fermi surfaces with 3D- (green), 2D- (blue), and 1D-like (red) transport—described by spheres, cylinders, and sheets, respectively. (a) Seebeck effective mass (m_S^*) versus carrier concentration (p) relationships calculated using an acoustic-phonon scattering assumption with the Seebeck versus carrier concentration data in Figure 4.8a. (b) Fermi surface complexity factor, $N_V^*K^*$, for each type of Fermi surface using conductivity effective masses (m_c^*) of $0.2m_e$, $0.4m_e$, and $0.6m_e$, for the 3D-, 2D-, and 1D-type Fermi surfaces, respectively. All calculations were done at $T = 300$K.

$N_V^*K^*$, are shown in Figure 4.10.

Clearly, the Fermi surface complexity factor is increases substantially as the bands become more converged and the Fermi surface geometries evolve from spheres to cylinders to sheets. The complexity factor for the 3D case (spheres) is constant at $N_V^*K^* = 4$. The complexity factors for the 2D (cylinders) and 1D (sheets) cases are not constant with hole concentration, p, but they peak (and plateau before decreasing) at values of $N_V^*K^* \sim 60$ and $N_V^*K^* \sim 500$. Based on this metric alone, we would expect significant improvement in a material that has a Fermi surface more closely resembling the 1D-like sheets and more modest improvement in a Fermi surface resembling the cylinders, relative to the ellipsoidal or spherical Fermi surface. However, the complexity factor does not capture the scattering effects on the conductivity, so more detailed analysis of scattering rates must still be performed to truly understand the benefits, or lack thereof, associated with low-dimensional Fermi surfaces in 3D bulk materials. In fact, in Ref. 108, a computational analysis

of various types of band structures is performed using a more detailed treatment of deformation-potential scattering, polar-optical scattering, and ionized impurity scattering, and it was found that, regardless of the scattering assumption, that 1D-type bidirectional bands (sheets) are the ideal Fermi surface geometry [108]. [7]

4.4 Conclusion

Using a TB model of a toy IV-VI rock salt semiconductor, we identify "chemical knobs" that can be used to tune the level of convergence in the PbTe VB structure to engineer more complex Fermi surfaces. Because all of the VB pockets (L, Σ, Δ, and W) are largely cation-s–anion-p anti-bonding states with varying strengths, the convergence of these bands is primarily dictated by the strength of this s-p coupling. The s-p coupling is influenced by the s-p energy separation and by the hopping parameter describing the interaction, $V_{sp\sigma}$. Decreasing the strength of the s-p coupling by either increasing the energy separation of decreasing the magnitude of $V_{sp\sigma}$ favors convergence (in cases where the VBM is at L). In real materials, $V_{sp\sigma}$ can be reduced, or effectively reduced, by increasing the lattice constant (e.g., through temperature, pressure, or alloying), increasing the s-p splitting through chemical substitutions on the anion or cation site, or introducing chemical substitutions that replace the cation with a cation that introduces unfilled cation-s^0 orbitals at the expense of the filled cation-s^2 orbitals. A secondary approach to tuning convergence in the TB model is to tune the anion-p–anion-p interaction strength, where increasing the interaction strength generally increases convergence (assuming an L VBM).

[7] Note that the transport and zT estimates presented in this chapter are simply meant to provide a *qualitative* comparison of potential transport in theoretical Fermi surfaces that act as perfect spheres, cylinders, or sheets. The goal here is simply to *motivate* the study of these lower-dimensional Fermi surfaces in 3D materials, particularly the IV-VI semiconductor family. More nuanced numerical calculations must be carried out to more accurately estimate the scattering rate of the charge carriers in each type of geometry. Additionally, we assume here that the type of Fermi surface geometry stays constant with increasing carrier concentration, but this is not necessarily the case. If the carrier concentration is increased in a IV-VI compound that has less converged bands (the Fermi surface is spherical/ellipsoidal near the band edge), the Fermi surface will begin to form into tubes, and eventually sheets at higher carrier concentrations. That being, said, these predictions provide a good starting point for understanding how band convergence may influence the thermoelectric transport properties, especially at lower doping concentrations.

Moreover, we calculate TB Fermi surfaces and find that increasing band convergence does not simply introduce additional carrier pockets (increasing N_V), but it leads to more substantial changes to the nature of the Fermi surface. For instance, when the L and Σ pockets are sufficiently converged, the Fermi surface forms twelve interconnected tubes, and when the Δ and W bands are also sufficiently converged, the Fermi surface starts to resemble sheets. The complexity of the Fermi surface increases upon the transition from the 3D to 2D to 1D type Fermi surfaces. This Fermi surface evolution marks a change in the nature of transport, such that the tubes (simplified as cylinders) should have a 2D-like DOS and the sheets should have a 1D-like DOS. We model the thermoelectric transport arising from the different classes of Fermi surfaces using different scattering-time assumptions, and find that the 2D-like (tubes) and 1D-like (sheets) Fermi surface may lead to power factor and zT enhancements over the 3D-like (L-point ellipsoids) Fermi surface if the electron-phonon scattering between points on the tubes and sheets does not completely negate the benefits from the increased Seebeck coefficient and carrier concentration.

GeTe Band Structure Evolution upon Cubic to Rhombohedral Transition

5.1 Introduction

Group-IV chalcogenide semiconductors, particularly PbTe, have been extensively studied as high-performing, mid-temperature thermoelectric materials [28, 29, 35, 38, 73, 75, 91, 121, 129, 130]. Excellent p-type thermoelectric performance in these IV-VI semiconductors—when they are in the cubic rock-salt phase—occurs largely as the result of high valley degeneracy (N_V) from the convergence of the L ($N_V = 4$) and Σ ($N_V = 12$) valence band (VB) pockets at high temperature and/or when strategically alloyed to achieve convergence [28, 29, 35, 38, 91, 92, 131, 132]. While PbTe has historically attracted the most attention of the IV-VI chalcogenide thermoelectrics due to its excellent performance as an n- and p-type thermoelectric, GeTe has gained increasing attention as a Pb-free alternative, and as a result, has seen significant improvements in its performance throughout the past few decades [131].

Among the traditional IV-VI thermoelectric semiconductors, GeTe is unique in that it undergoes a transition from a low-temperature rhombohedral phase ($R3m$) to a high temperature cubic phase ($Fm\bar{3}m$) at $\sim$ 700K [1,2]. The primitive unit cells (2 atoms/cell) of both the cubic and rhombohedral phases of GeTe are shown in Figure 5.1. In the cubic rock salt phase (c-GeTe), the Ge atom is located at the center of the Te coordination octahedron. The transition from the cubic to rhombohedral phase (r-GeTe) is the result of the displacement of the Ge atoms from the center of the octahedron,

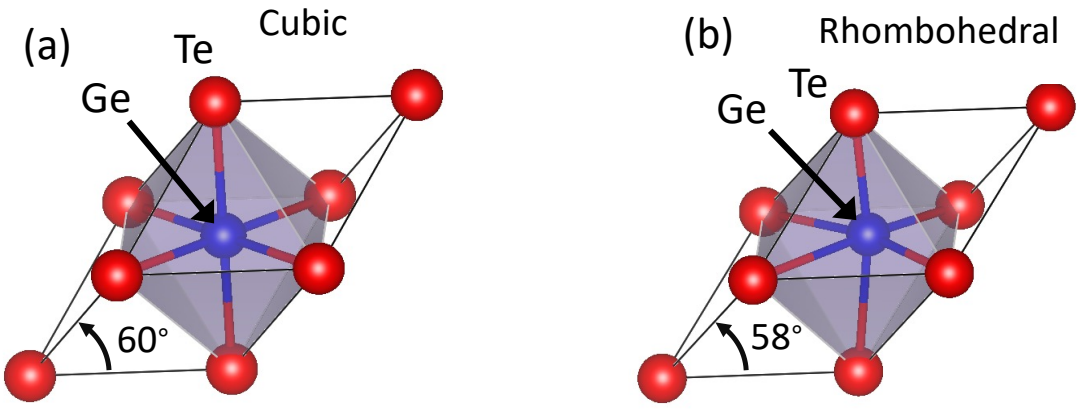

Figure 5.1: Primitive unit cell of GeTe in the cubic rock salt phase and rhombohedral phase, where Te is located at (0, 0, 0) in both cases. (a) In the cubic phase, Ge (blue) is located at (0.5, 0.5, 0.5), and the primitive cell interaxial angle (γ) is 60°. (b) In the rhombohedral phase, the Ge is displaced from the center of the Te (red) octahedron at $(0.5 \pm \delta, 0.5 \pm \delta, 0.5 \pm \delta)$, where $\delta \sim 0.03$, and the interaxial angle is 58°.

moving from the $(0.5, 0.5, 0.5)$ position to $(0.5 \pm \delta, 0.5 \pm \delta, 0.5 \pm \delta)$ position (in the primitive lattice basis), where $\delta \sim 0.03$. It is also marked by a reduction in the primitive unit cell interaxial angle, γ, from $\gamma = 60°$ to $\gamma \sim 58°$ (see Figure 5.1a-b) [92, 129, 131–134]. The rhombohedral phase can also be regarded as a distortion of the conventional cubic unit cell along the [111] direction.

Upon the cubic to rhombohedral phase transformation, the electronic structure of GeTe is significantly altered (see Figure 5.2). The Brillouin zones (BZs) for the rhombohedral and cubic unit cells are shown in Figure 5.2.[1] In the c-GeTe, the VBM is located at the L-point ($N_V = 4$), with a secondary VBM located along the Σ line (ΓK; $N_V = 12$) that is ~ 0.06 eV below the L VBM (Figure 5.2c). There is an additional VB pocket along the Δ (ΓX) direction with $N_V = 6$ that is ~ 0.3 eV below the L VBM and could become important to transport at high doping level and/or when the bands are highly converged [122, 135, 136]. When the GeTe unit cells distorts from c-GeTe to r-GeTe, the L point in c-GeTe ($N_V = 4$) splits into two different $\boldsymbol{k}$-points in r-GeTe, L ($N_V = 3$)

[1] The coordinates of the special points in both the FCC and rhombohedral Bravais lattices are given in Appendix A.

and Z ($N_V = 1$) (Figure 5.2a-b). Moreover, the Σ line in c-GeTe ($N_V = 12$), splits into two distinct directions that each have $N_V = 6$, Σ (ΓP) and η (ΓX), in r-GeTe. The Δ line from c-GeTe maintains its six-fold degeneracy upon the transition to r-GeTe, but the naming convention changes such that it is labeled as the ΓF line in r-GeTe [137]. In contrast to c-GeTe, the VBM of r-GeTe is along the Σ direction, and the next highest VB pockets are the L and Z bands, which are both 0.2 eV below the Σ VBM, with Z being slightly higher (Figure 5.2d).

The differing location of the VBMs in c-GeTe and r-GeTe introduces a new degree-of-freedom for electronic band engineering in GeTe and its alloys: the extent of rhombohedral distortion [94, 129, 131, 133]. Increasing the extent of the rhombohedral distortion increases the Σ VBM relative to the L/Z VBM, but breaks the degeneracy of the (cubic) Σ and L bands. While it is typically believed that any reduction in symmetry from the cubic to rhombohedral phase necessarily reduces N_V because the degeneracy of the both L and Σ bands is broken [39, 92, 130, 138, 139], there may actually be opportunities to achieve higher N_V through slight reductions in the symmetry due to better convergence between the L, Z and Σ bands [129,131,133,140]. Additionally, r-GeTe has lower lattice thermal conductivity due to its larger distribution of bond lengths [131], offering a different source of improved performance in r-GeTe relative to c-GeTe.

Alloying can tune the shape of the GeTe unit cell, and hence, be used for band engineering, by controlling the stereochemical activity of the cation-s lone pair electrons. Because the rhombohedral distortion at low temperature is due to the stereochemical expression of the Ge-s lone pairs [66], the phase transition temperature or the level of distortion (from cubic) at a given temperature can be decreased by alloying on the cation site with a cation that suppresses this lone-pair expression, such as Li, Mn, Cd, Na, Cu, Sb, Bi, Pb, and Sn [39, 92, 93, 122, 130, 131, 133, 135, 136, 141–146, 146]. It is important to note that these substitutions also alter the nature of the chemical interactions in the material, so changes to the band structure with respect to both symmetry and chemistry need to be considered. That being said, cation-site alloying to tune the shape (γ and δ) of GeTe has been shown to successfully enhance thermoelectric performance in several studies by promoting

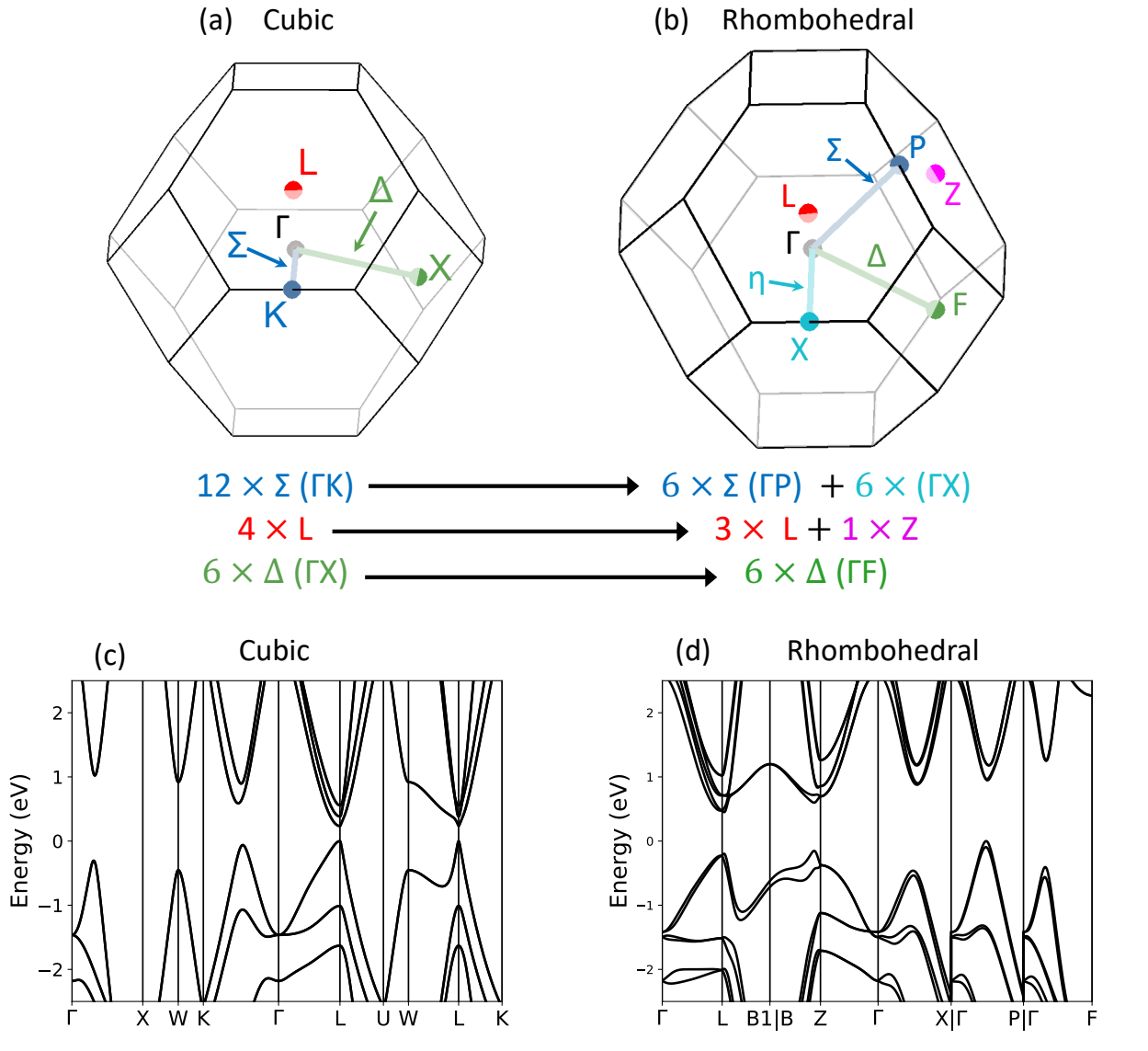

Figure 5.2: Labelled first Brillouin zones (BZs) of the (a) cubic rock salt and (b) rhombohedral phases of GeTe. DFT electronic band structures of (c) c-GeTe and (d) r-GeTe, calculated using the PBE functional with SOC.

band convergence [39, 135, 136, 140, 143, 146].

While differences between the band structures in c-GeTe and r-GeTe are already well-understood [94], the chemical origins of these variations have not been thoroughly explored. Density functional theory (DFT) calculations show that the offset, δ, rather than the interaxial angle, γ, is responsible for the emergence of the Σ VBM in r-GeTe [94]. However, the reduction in γ has a significant impact on the relative energies and convergence of the various local VBMs. Here, we aim to elucidate the chemical origins of changes to the electronic band structure upon the transition from r-GeTe to c-GeTe using a linear combination of atomic orbitals (LCAO), or tight-binding (TB) framework [62,66]–in addition to crystal orbital Hamilton population (COHP) calculations—isolating the effects of modifying γ and δ.

5.2 Trends from Density Functional Theory

Using DFT electronic band structure calculations, we obtain a detailed picture of how both γ and δ influence the L, Z, Σ, η, and Δ bands in GeTe. First, we look at how the band structure (band edges) evolves upon varying γ and δ, as seen in Figure 5.3 (calculated with SOC). From these band structure calculations, it is clear that increasing δ favors the Σ VBM over the Z VBM because it lowers the energy of the Z and L bands relative to the Σ band. On the other hand reducing γ disfavors the Σ VBM over the Z VBM but increases the L VBM relative to the Σ VBM. The relative energies of the VB edges with respect to to δ for $\gamma = 60^\circ$ and $\gamma = 58^\circ$ can be seen in Figure F.1 in Appendix F.

To gain a better sense of how the shape of the unit cell influences the (nominal) value of N_V, heat maps are calculated to show the valley degeneracy for all combinations of γ and δ, such that $0 < \delta < 0.03$ and $57.5^\circ < \gamma < 60^\circ$. These N_V maps were constructed by taking a linear interpolation of a 6 by 7 "grid" of band structure calculations and simply counting the number of VB pockets under a given threshold for $E_{VBM} - E_F$ using the degeneracies of L, Z, Σ, and η given in Figure 5.2. Even though the Z-VBM is actually offset from the true Z-point (when $\delta \neq 0$), we still consider

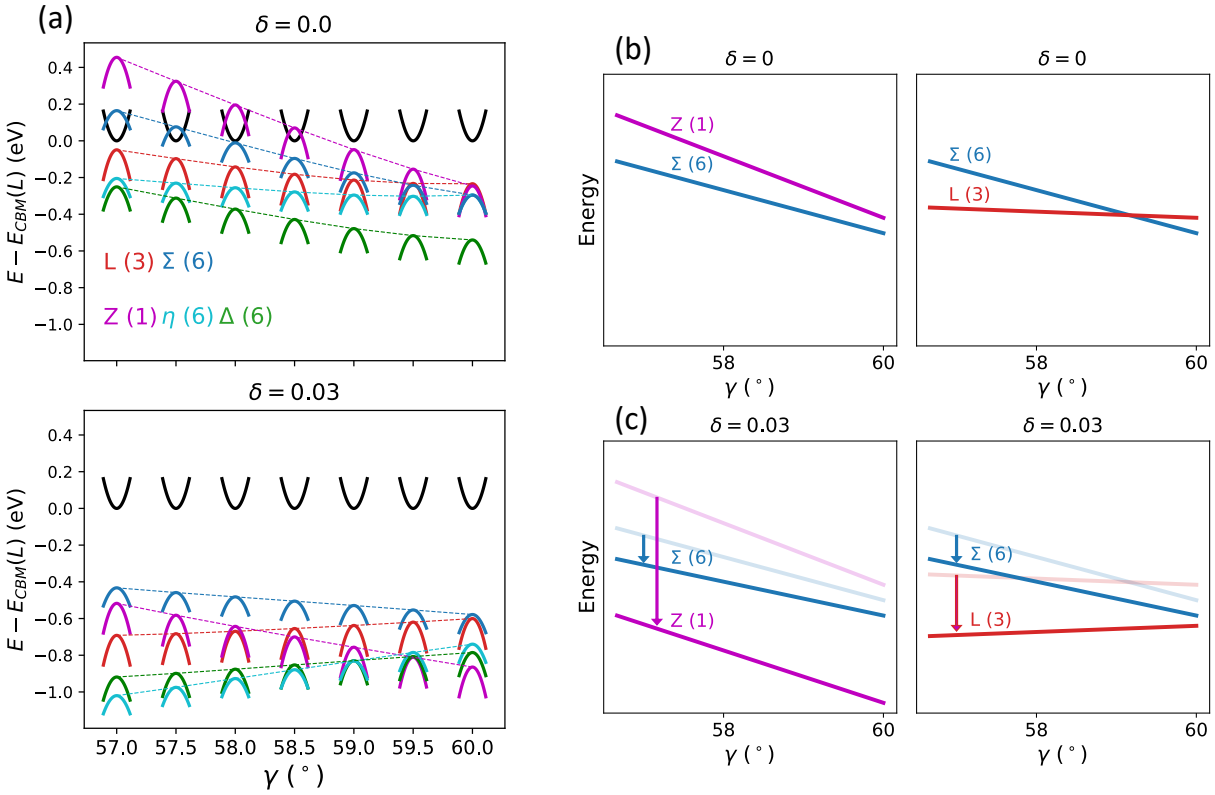

Figure 5.3: (a) Schematic of the valence band (VB) edge energies (L, Z, Σ, η, and Δ) with respect to the L-point CBM (black) as a function of interaxial angle (γ) when the Ge-offset, $\delta = 0$ (top) and $\delta = 0.03$ (bottom). The energies (shown with dashed lines) are calculated from DFT with spin-orbital coupling (SOC). (b)-(c) Qualitative *sketches* of just the L, Z, and Σ, band energies as a function of γ for $\delta = 0$ and 0.03. Increasing the offset from $\delta = 0$ to 0.03 pushes the Z and L bands down in energy relative to the Σ band (for all γ). The values in parentheses are the degeneracies for each specified $\boldsymbol{k}$-point or line.

it to add $N_V = 1$ to the total degeneracy, because it only emerges near the band edge when δ is very close to zero, and the Z-point offset is negligible when δ is nearly zero (see Figure F.2). Based on the N_V heat maps, if we consider the cases where the Fermi energy 0.03 eV or 0.05 eV below the VBM (Figure 5.4), the optimal crystal structure for achieving high N_V is a slightly distorted rhombohedral phase ($\gamma \sim 59.7° - 59.9°$ and $\delta \sim 0.005 - 0.01$). This slightly distorted structure gives a nominal $N_V = 10$ due to convergence between the Σ (6), L (3), and Z (1) bands. In the cubic structure, $N_V = 4$ because only the L band is within the energy threshold. If the shape of the crystal can be tuned such that δ is increased but the deviation of γ from 60° remains small, then a relatively high N_V of 9 can be achieved. In this case, Σ and L are converged, but the increase in δ breaks the convergence of the Z band, which is pushed down in energy with increasing δ. On the other hand, if γ is decreased to less than $\sim 59.7°$, but δ remains very close to 0, then only the Z band will be within the threshold of the VBM, giving a low band degeneracy of $N_V = 1$. This shows that, if feasible, it is better to only increase δ than to only decrease γ.

If we increase the energy threshold for determining N_V (i.e., higher temperature or doping concentration) such that $E_{VBM} - E_F \sim$ 0.07-0.1 eV, then having a cubic *or* slightly distorted rhombohedral structure is adequate for achieving a high $N_V = 16$ because the L, Z, Σ and η pockets would fall within the threshold (Figure 5.4c-d). VB Fermi surfaces for different degrees of rhombohedral distortion and Fermi energies are shown in Figure 5.5. These Fermi surfaces provide insights into Fermi surface complexity beyond the nominal band degeneracy. For instance, while the nominal values of valley degeneracy are the same for the slightly distorted and cubic geometries for a Fermi energy 0.1 eV below the VBM, the Σ pockets are more elongated for the slightly distorted geometry. This elongation may lead to better thermoelectric quality factor due to low-dimensional (2D) type transport and higher carrier pocket anisotropy (higher Fermi surface complexity factor) [34, 45].

Because we cannot necessarily choose any arbitrary combination of γ and δ (γ results from δ [66]), we put the N_V maps from Figure 5.4 in context by considering the “natural" relationship

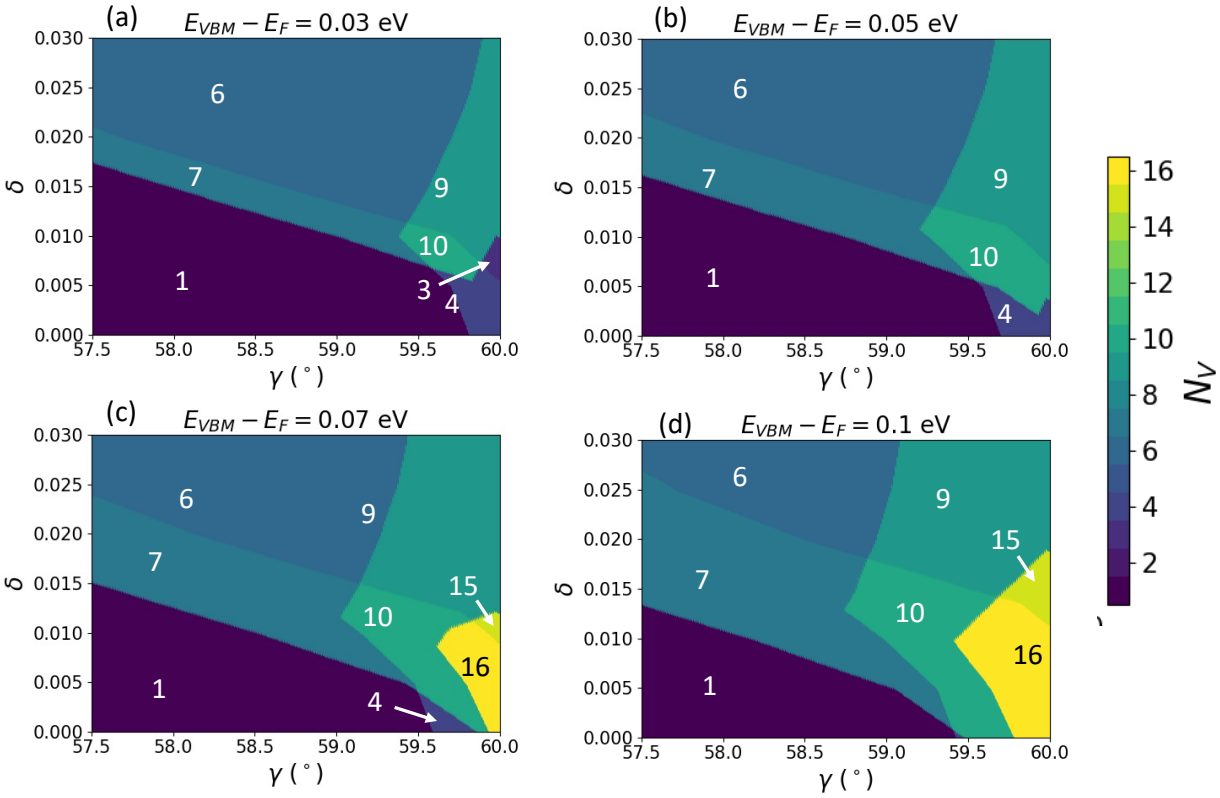

Figure 5.4: 2D heat maps showing the nominal valley degeneracy (N_V) of the valence band using a Fermi energy (E_F) of $E_{VBM} - E_F = 0.03$ eV, (b) $E_{VBM} - E_F = 0.05$ eV, (c) $E_{VBM} - E_F = 0.07$ eV, and (d) $E_{VBM} - E_F = 0.10$ eV. E_{VBM} is the energy of the VBM. The values of nominal N_V are labeled in each region.

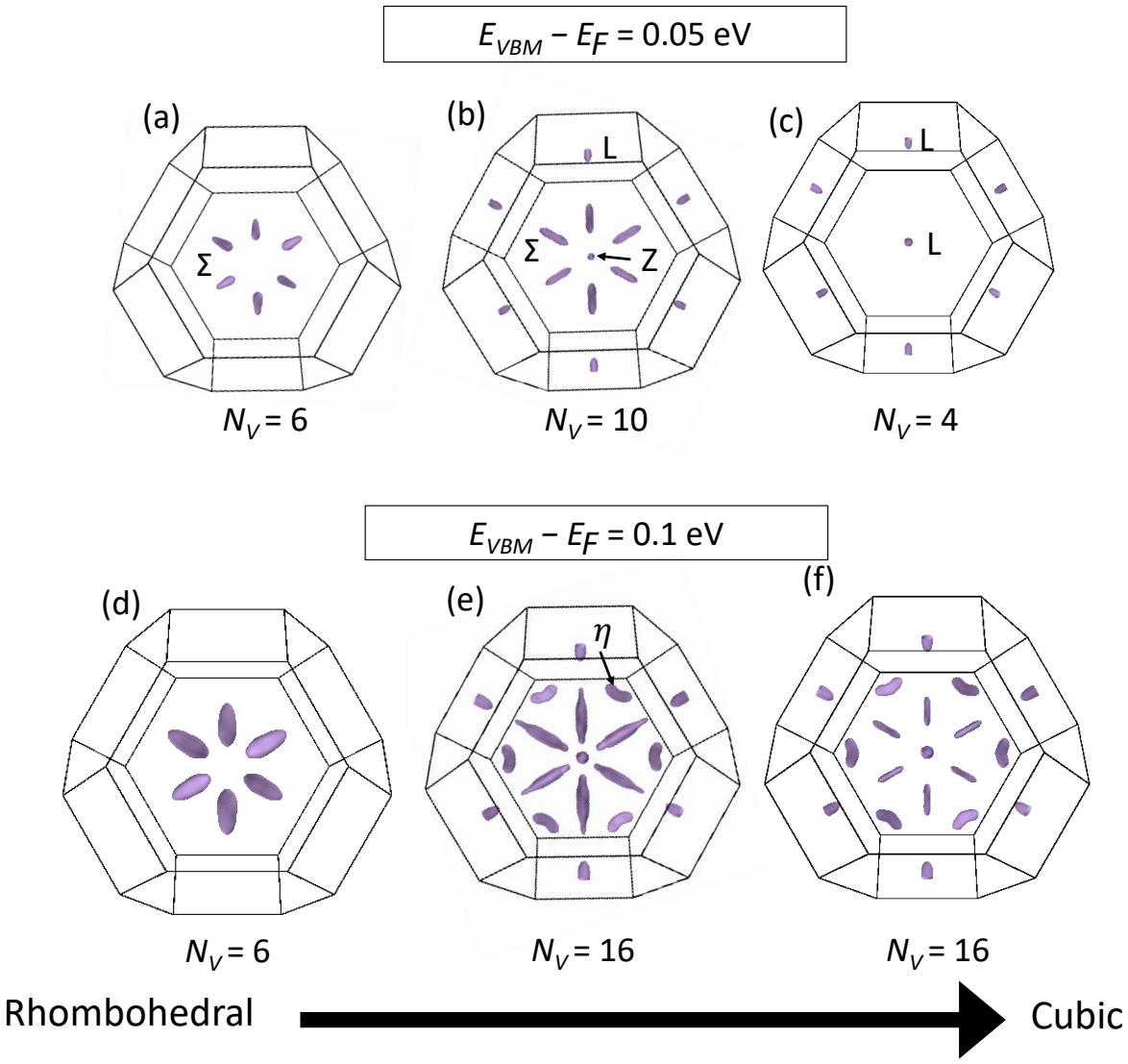

Figure 5.5: Evolution of GeTe valence band Fermi surface upon increase in symmetry from the rhombohedral to cubic structure. (a)-(c) Fermi surfaces calculated 0.05 eV below the VBM for the (a) relaxed r-GeTe, (b) less distorted r-GeTe with $\delta = 0.01$ and $\gamma = 59.7°$, and (c) relaxed c-GeTe. (d)-(f) Fermi surfaces calculated 0.10 eV below the VBM for the (d) relaxed r-GeTe, (e) less distorted r-GeTe with $\delta = 0.01$ and $\gamma = 59.7°$, and (f) relaxed c-GeTe. The nominal values of N_V are given below each Fermi surface.

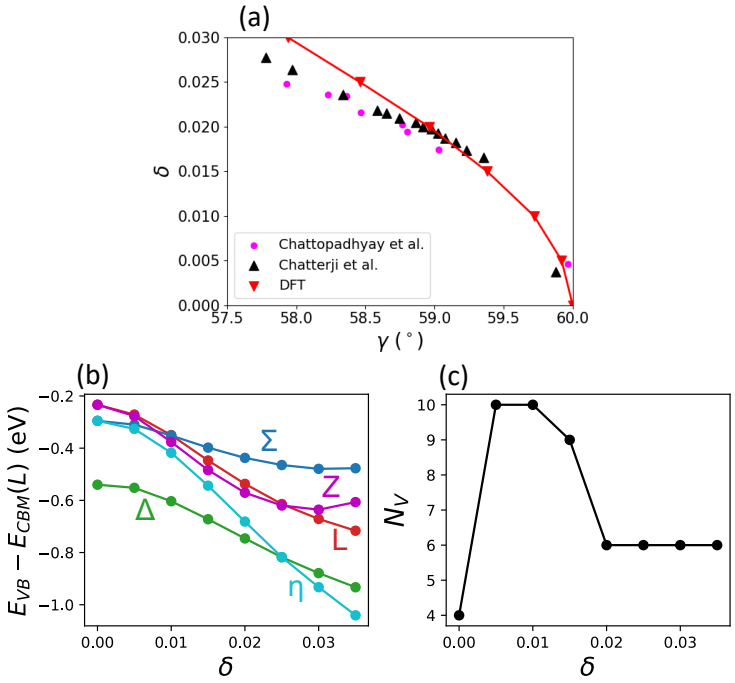

Figure 5.6: (a) Offset (δ) versus interaxial angle (γ) values determined experimentally (magenta circles and black triangles) [1, 2] and from DFT (red inverted triangles). (b) Valence band energies (E_{VB}) of the Σ, L, Z, η and Δ bands along the interpolated DFT γ vs. δ line. The energies are shown relative to the energy of the CBM at the L-point ($E_{CBM}(L)$). (c) Nominal valley degeneracy (N_V) along the DFT γ vs. δ line for a Fermi energy 0.05 eV below the VBM.

between γ and δ. In Figure 5.6a, the values of γ and δ from Refs. 1 and 2 are shown. Additionally, the DFT δ vs. γ path was found by setting an offset value δ and relaxing the unit cell shape to get the corresponding γ and unit cell volume. The DFT relationship between γ and δ is in relatively good agreement with the experimental values. By interpolating along the DFT γ vs. δ line, we calculated the relative VB energies (Σ, L, Z, η, and Δ) and the nominal values of N_V along this natural structure pathway (Figure 5.6b). Clearly, when following this δ vs. γ path, it is possible to access the $N_V = 10$ region at very small rhombohedral distortions, before the distortion becomes large enough to result in the lower $N_V = 6$ type Fermi surface (Figure 5.6c).

5.3 Orbital Chemistry Interpretation

The aim of this section is to explain *why* the VB structure varies the way it does with varying interaxial angle and cation offset using an orbital chemistry framework. Specifically, we use the LCAO, or TB, method to approximate the GeTe wavefunctions as a superposition of atomic-orbital wavefunctions.

5.3.1 Atomic-Orbital Pictures

To understand how the energy of the competing VBMs varies with the primitive cell interaxial angle (γ), we consider the atomic-orbital wavefunction consisting of Ge-s and Te-p orbitals. As discussed in Chapter 3, in cubic rock salt IV-VI semiconductors, the VBMs at L, Σ, Δ, and W can be approximated as cation-s–anion-p anti-bonding wavefunctions, where the s-p bonding strength is greatest at L followed by Σ then Δ and W (which are the same in terms of s-p anti-bonding). We use the s-p VB orbital picture from Chapter 3 to visualize the VB edge atomic-orbital wavefunctions in GeTe. That is, we consider an eigenstate described by a Te-p atomic orbital octahedrally coordinated by six Ge-s atomic orbitals in a net anti-bonding configuration. The angle between the direction of the p-orbital and the vector between the Te-p and Ge-s orbital for a neighbor pair is given by ϕ. The cation-s and anion-p orbitals are in the most anti-bonding configuration when $\phi = 0°$ and in a non-bonding configuration when $\phi = 90°$. When $180° \geq \phi > 90$, the s-p interaction is bonding. We solve for the VB wavefunction pictures (i.e., determine ϕ) by setting up a TB Hamiltonian based on only cation-s–anion-p interactions and solving for the eigenvectors corresponding to the different VBMs. We then define the s-p hopping integral, or interaction strength, at a given $\boldsymbol{k}$-point, V_{sp}, using Equation 5.1 (rewritten below from Chapter 4). Here, $V_{sp\sigma}$ is the $\boldsymbol{k}$-independent s-p interaction strength that depends on the interatomic distance between the orbitals and the chemistry (i.e., more orbital overlap leads to greater $V_{sp\sigma}$) [6, 65]. The index, i, iterates over the six closest neighbors.

$$V_{sp}(\boldsymbol{k}) = V_{sp\sigma} \sum_{i}^{6} \cos\left(\phi_i(\boldsymbol{k})\right) \tag{5.1}$$

Recall from Chapters 3 and 4 that the values of $V_{sp}(\boldsymbol{k})$ at L, Σ, Δ, and W for the IV-VI rock salt compounds are $V_{sp}(\mathrm{L}) = 2\sqrt{3}V_{sp\sigma}$, $V_{sp}(\Sigma) = 2\sqrt{2}V_{sp\sigma}$, and $V_{sp}(\Delta) = V_{sp}(\mathrm{W}) = 2V_{sp\sigma}$ [47]. Here, the hopping parameters for Σ and Δ are calculated at the points, $\Sigma = \frac{\pi}{a}(0,1,1)$ and $\Delta = \frac{\pi}{a}(0,0,1)$, respectively, where a is the lattice constant for the cubic cell. While these are not the true locations of the VB edges (the locations vary with chemistry and composition), these are the exact locations of the Σ and Δ VBMs when there are only nearest-neighbor *s*-*p* and *p*-*p* σ-bonding interactions in a TB model. That is, they are the locations where the *s*-*p* bonding strength is greatest (along those lines) and the *p*-*p* σ-bonding strength is exactly zero. The energy of the VB edge in this *s*-*p* atomic-orbital framework, E_{VB}, would then be given by Equation 5.2.

$$E_{VB}(\boldsymbol{k}) = \frac{1}{2}(E_s + E_p) + \frac{1}{2}\sqrt{(E_p - E_s)^2 + 4V_{sp}(\boldsymbol{k})^2} \tag{5.2}$$

The same *s*-*p* framework used to understand band convergence in IV-VI rock salt materials can be used to explain changes to the band edges with respect to the interaxial angle (when $\delta = 0$). When the primitive cell interaxial angle, γ, is reduced from 60°, the *s*-*p* bonding angles, ϕ, change which changes the overall anti-bonding strength. Atomic orbital sketches of the L and Σ VBM atomic-orbital wavefunctions (eigenstates) can be seen in Figure 5.7a. At L, the Te-*p* orbital is anti-bonding with all six Ge-*s* nearest neighbors, and $\cos\left(\phi_L^c\right) = 1/\sqrt{3}$ for all these neighbors. Near the Σ VBM, the Te-*p* orbital is anti-bonding with four nearest-neighbors (non-bonding with two), and $\cos\left(\phi_c^\Sigma\right) = 1/\sqrt{2}$. When $\gamma < 60°$, each of these eigenstates splits into two distinct eigenstates with different *s*-*p* bonding angles (Figure 5.7b). In the rhombohedral phase ($\gamma < 60$), the *s*-*p* angle for the Z-point (ϕ_Z^r) decreases as γ decreases, and as a result, the anti-bonding strength increases at Z (Figure 5.8). On the other hand, at (rhombohedral) L, the *s*-*p* bonding angle for two of the neighbors (ϕ_{1L}^r) increases, while it slightly decreases for the other four neighbors (ϕ_{2L}^r). The

average *s*-*p* bonding angle for L slightly increases, which leads to a slight decrease in the anti-bonding strength as γ decreases (Figure 5.8). As a result, the energy of Z increases relative to L as γ decreases. The splitting of Σ into Σ and η with changing γ can be explained in a similar manner. As γ decreases from 60°, the *s*-*p* bonding angle in the Σ eigenstate decreases, while the *s*-*p* bonding angle in the η eigenstate increases. Consequently, the Σ VBM becomes more anti-bonding relative to the η VBM, and the Σ VBM increases in energy relative to the L VBM. Both of these trends are consistent with DFT calculations for $\delta = 0$ and $\delta = 0.03$ (Figure 5.3 and F.2).

5.3.2 Crystal Orbital Hamilton Population Calculations

To confirm the anti-bonding behavior of the L, Z, Σ and η bands upon decreasing γ and to understand the changes in bonding upon increasing δ, we analyze $\boldsymbol{k}$-resolved COHP, or projected COHP (pCOHP) values in the highest VB. The $\boldsymbol{k}$-resolved COHP reflects how bonding or anti-bonding the interactions are in a given band at a given $\boldsymbol{k}$-point. Positive COHP values indicate anti-bonding interactions, negative values indicate bonding interactions, and the magnitude indicates the strength of the interaction.

Figure 5.9 shows the Ge-*s*–Te-*p* and Ge-*p*–Te-*p* pCOHPs for the L, Z, Σ, η, and Δ VBMs as a function of γ. When $\delta = 0$, there Ge-*p*–Te-*p* interactions are zero or nearly zero at all γ. Consistent with the predictions from the Ge-*s*–Te-*p* atomic-orbital model described earlier, the Z and Σ VBMs become more anti-bonding as γ decreases, with Z being more anti-bonding than Σ, while L and η become slightly less anti-bonding when γ decreases, with L being more anti-bonding. The Ge-*s*–Te-*p* anti-bonding strength of the Δ VBM, however, is virtually constant for all γ, and is the least anti-bonding of the five VBMs shown in Figure 5.9. This is because the *s*-*p* bonding angle in the Δ VBM eigenstate is $\phi = 0°$ (Figure 3.10), and changing γ does not alter it. When δ is increased to $\delta = 0.03$, breaking the inversion symmetry (Figure 5.9b), the same trends in Ge-*s*–Te-*p* anti-bonding strength are seen: the strength in L and η bands decreases, the strength in Z and Σ bands increases, and the strength in the Δ band is constant with decreasing γ. When δ increases

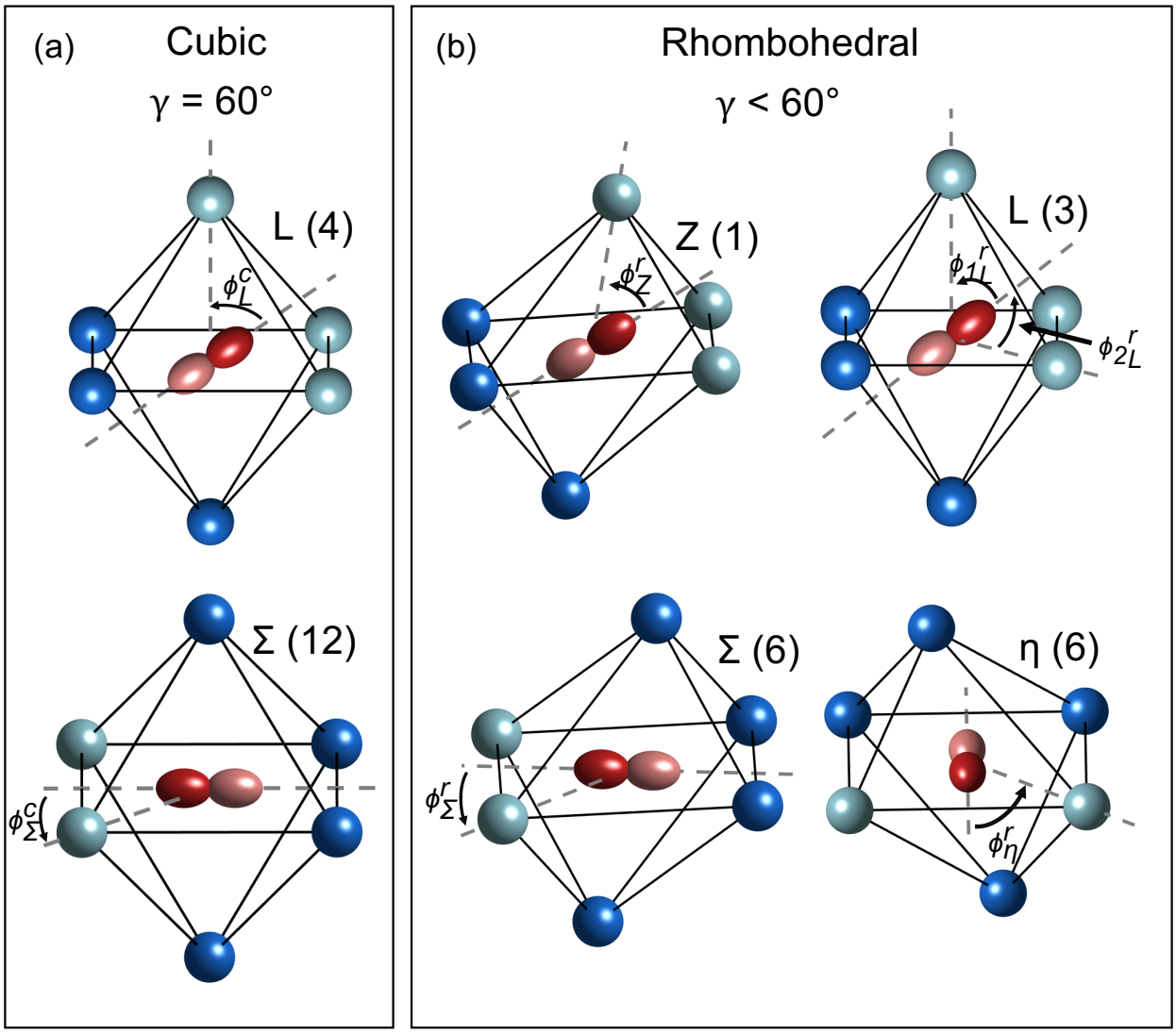

Figure 5.7: Visualizations of simplified tight-binding (TB) wavefunctions at local VBMs in c-GeTe ($\gamma = 60°$) and r-GeTe ($\gamma < 60°$), assuming that only the interaxial angle (γ) varies, while the offset is constant at $\gamma = 0$. (a) For c-GeTe, at the L-point, the Te-p orbital is oriented such that it is anti-bonding with all six neighbors, and the angle between the Te-p orbital and the Ge-s orbitals (ϕ_L^c) is such that $\cos\phi_L^c = 1/\sqrt{3}$. At the Σ maximum, the Te-p orbital is anti-bonding with 4 Ge-s neighbors and non-bonding with 2 Ge-s neighbors. The bonding angle between the Te-p orbital and the 4 anti-bonding Ge-s orbitals (ϕ_Σ^c) is given by $\cos\phi_\Sigma^c = 1/\sqrt{2}$. (b) TB wavefunctions after c-GeTe are distorted through a reduction in γ. The Z-point VBM wavefunction is characterized by a bonding angle (ϕ_Z^r) that is less than ϕ_L^c. The L-point wavefunction is defined by two different bonding angles, a bonding angle ϕ_{1L}^r (2/6 of bonds), where that $\phi_{1L}^r > \phi_L^c$, and an angle, ϕ_{2L}^r (4/6 of bonds), where that $\phi_{2L}^r > \phi_L^c$. The cubic Σ VBM splits into the rhombohedral Σ and η bands, where $\phi_\Sigma^r < \phi_\Sigma^c$ and $\phi_\eta^r > \phi_\Sigma^c$.

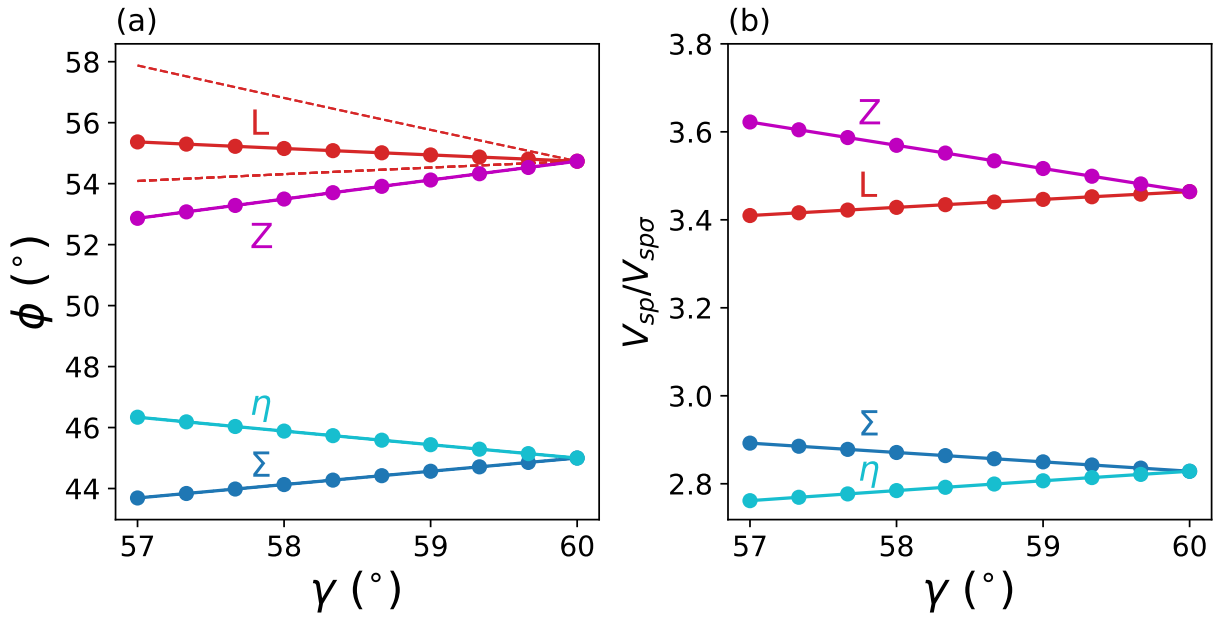

Figure 5.8: Ge-s–Te-p bonding angles ϕ and effective s-p interaction strength, $V_{sp}/V_{sp\sigma}$ (from Equation 5.2), as a function of interaxial angle (γ) and atomic offset (δ). For L and Z, all 6 neighbors are considered, and for Σ and η, the 4 strongly anti-bonding neighbors are considered. (a) ϕ vs. γ for L, Z, η, and Σ. At L, there are two distinct s-p bonding angles (shown in dashed lines), so the average is shown using the red "-o" line. At the L VBM, the average value of ϕ increases with decreasing γ, while at Z, ϕ decreases. At the η VBM, ϕ increases with decreasing γ, while at the Σ VBM, ϕ decreases. (b) Thus, the Z and Σ VBs becomes more anti-bonding as γ decreases, while the L and η bands becomes less anti-bonding.

and γ is constant, the Ge-s–Te-p anti-bonding character of all five VB pockets decreases at all values of γ, and they decrease such that the Z band has less Ge-s–Te-p anti-bonding character than the L and Σ VB pockets.

Furthermore, breaking the inversion symmetry also allows for the Ge-p–Te-p bonding interaction to emerge in the VBMs (Figure 5.9d) [147]. Because this interaction pushes down the energy of the s-p anti-bonding states that comprise the VB edge, it has been described as effectively lowering the energy of the s^2 lone pair, which is the driving force for the rhombohedral distortion GeTe [66,147]. According to the COHP values, The Ge-p–Te-p bonding interaction is strongest in the η VB pocket, followed by the Δ, Z , L and Σ VB pockets. The weaker strength of Ge-p–Te-p bonding in the Σ VB pocket relative to the Z and L VB pockets explains the emergence of the Σ VBM in r-GeTe, as illustrated in Figure 5.10. After adding the Ge-s–Te-p and Ge-p–Te-p COHP contributions of the various VBMs when $\delta = 0.03$, (Figure 5.9f), it can be seen that the Ge–Te interactions are most anti-bonding in the L VBM, followed by Σ, Z, η, and Δ.

The Ge-p–Te-p bonding interactions in the VB edge when $\delta \neq 0$ also give insight into why the Z VBM is offset from the “true" Z-point when inversion symmetry is broken. Regardless of γ, the offset of the Z VBM from the true Z-point emerges when δ reaches a large enough value (see Figure F.2). The offset from the Z-point is due to the emergence of, and increase in Ge-p–Te-p interaction at the Z-point with increasing δ. Figure F.3 (Appendix F) shows the COHP values for the true Z point when $\delta = 0.03$, and it is less net anti-bonding than that in the Z VBM (offset from the true Z-point), which pushes the maximum off the actual Z-point to where the net anti-bonding strength is higher.

The Ge–Te (cation–anion) interactions alone do not fully explain the relative energies of the competing VBMs. For instance, the Ge–Te COHP suggests that the L VBM is the most (net) anti-bonding in r-GeTe, but the VBM is located along Σ rather than at L. The discrepancy between the cation–anion COHP and the actual relative band energies can be accounted for in the Te-p–Te-p next- or second-next-nearest neighbor interactions. The L (Z) and Σ (η) VBMs both have Te-p–Te-

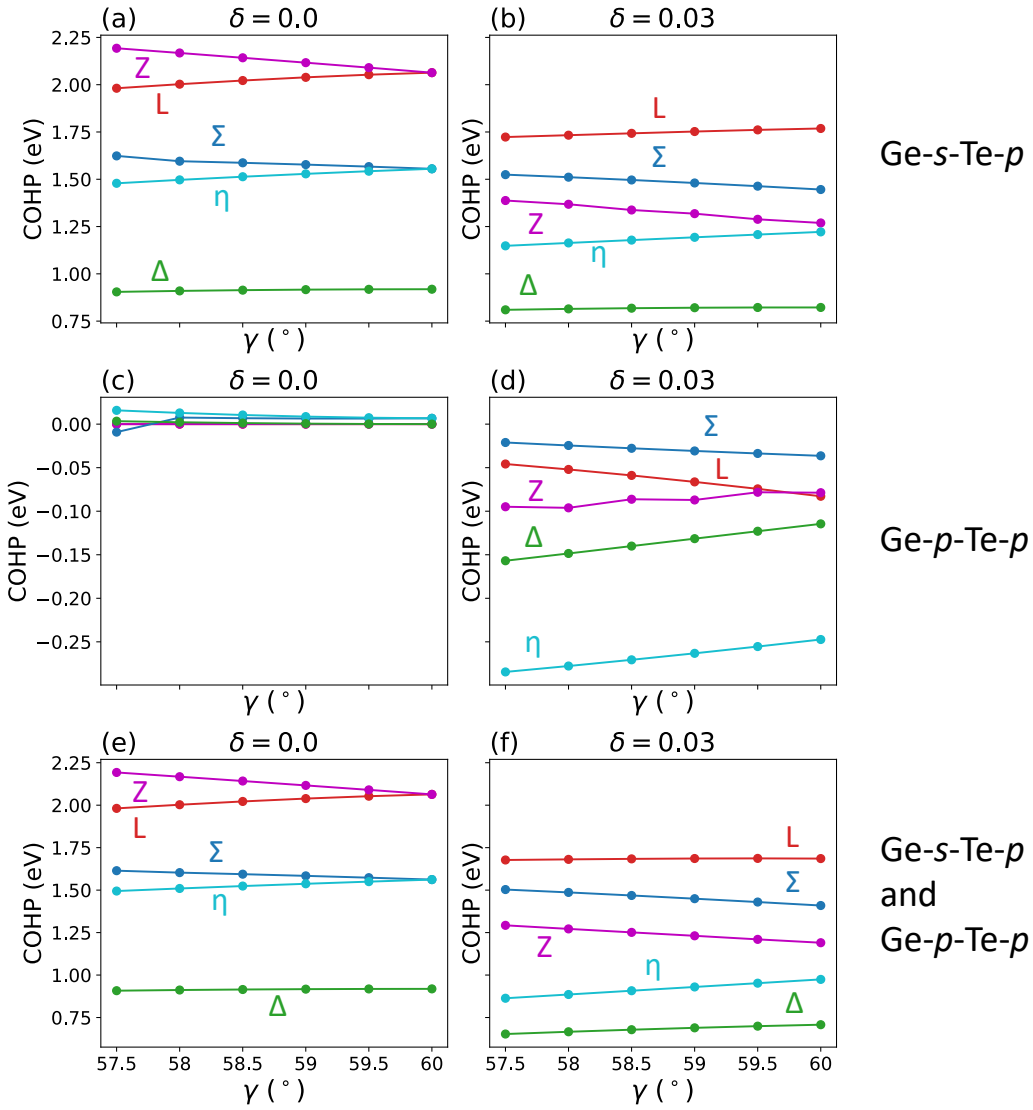

Figure 5.9: ***k***-resolved, band-resolved projected crystal orbital Hamilton population (pCOHP) values versus interaxial angle (γ) in the Z (magenta), L (red), Σ (blue), η (turquoise), and Δ (green) VBMs in GeTe. COHP of Ge-*s*–Te-*p* interaction when (a) $\delta = 0$ and (b) $\delta = 0.03$. COHP of Ge-*p*–Te-*p* interaction when (c) $\delta = 0$ and (d) $\delta = 0.03$. Sum of Ge-*s*–Te-*p* and Ge-*p*–Te-*p* COHP values when (e) $\delta = 0$ and (f) $\delta = 0.03$.

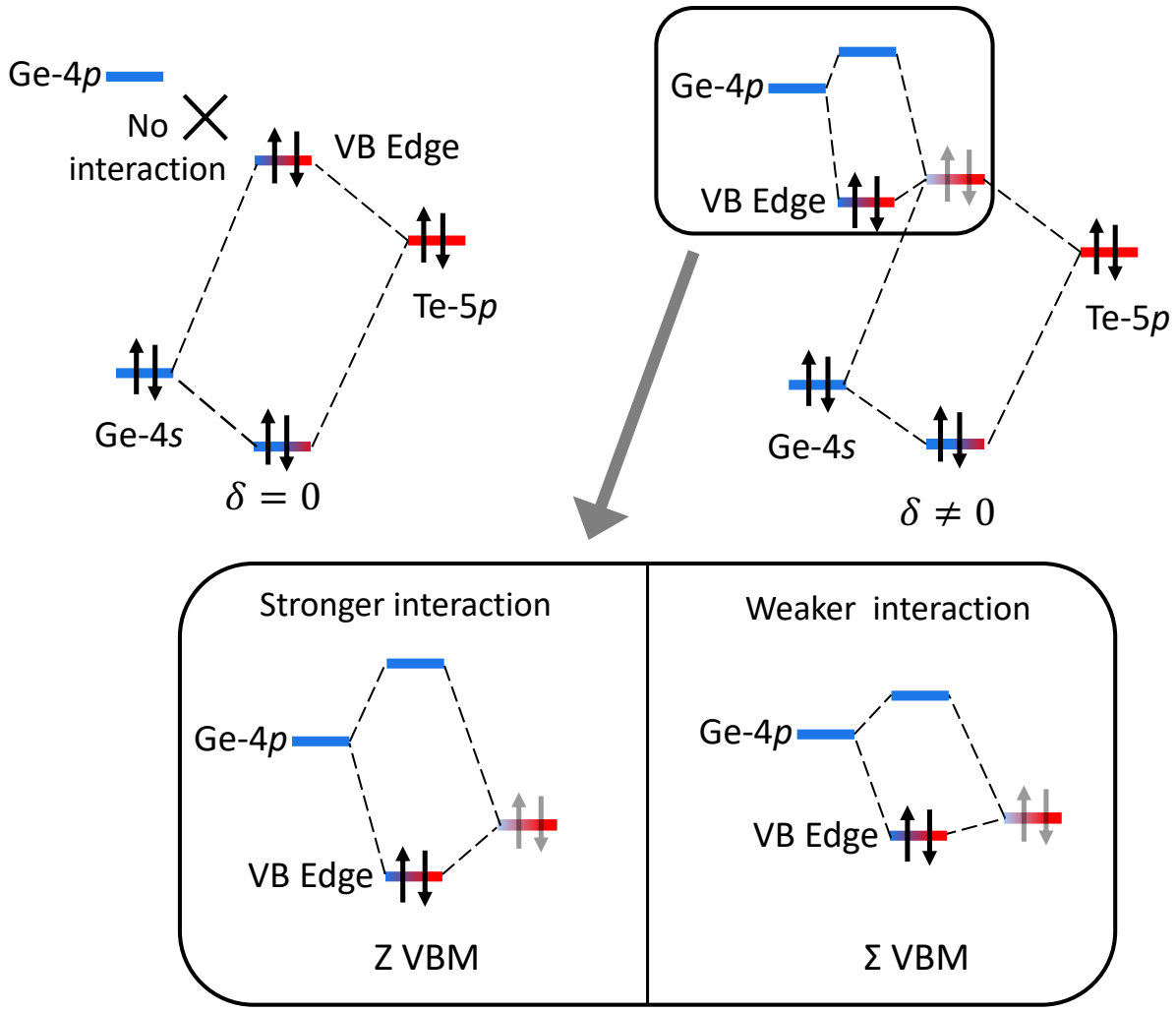

Figure 5.10: Molecular-orbital-like bonding diagrams representing the GeTe valence band (VB) edges, illustrating the reduction in energy of the anti-bonding VB edge and the emergence of the Σ VBM over the Z (or L) VBM when the Ge offset (δ) is greater than zero (inversion symmetry broken). The states near the VB edge are characterized by cation-s–anion-p anti-bonding character. In the rock salt structure ($\delta = 0$), interactions between the anti-bonding VBM and the cation-p states are symmetry forbidden. When inversion symmetry is broken, the s-p anti-bonding strength decreases and the cation-p (Ge-p) states can interact with these anti-bonding states, which lowers their energies. Moreover, the bonding interaction with the Ge-p states is stronger in the Z VB than in the Σ VB, which pushes the energy of the Z VB down more, favoring the Σ VBM in r-GeTe.

p bonding character, but this bonding character is stronger in the L (Z) bands than in the Σ (η) bands (refer to Chapters 3 and 4 for details) [47]. As a result, the L VB is pushed below the Σ VB despite the Ge–Te anti-bonding interactions being stronger in the L band [47].

5.3.3 Tight-Binding Thought Experiments

To gain more insight into how atomic-orbital interactions influence the electronic structure with respect to the unit cell shape, we perform TB thought experiments, where we employ a toy model of GeTe and vary geometry (i.e., δ and γ), the Ge–Te interaction parameters, and SOC strength.[2] The TB parameters for this toy model (unless specified otherwise) are described in Table 5.1. Using this TB approach, we can better understand why increasing δ reduces the energy of the Z VB edge below that of the Σ VBM to ultimately yield a Σ VBM and why the Z VBM is slightly offset from the true Z point. For simplicity, in this section, we start by using a TB model that only includes the Ge–Te interactions. Note that because the Te-p–Te-p interactions are not included, the VBM will not be at Σ, even with larger δ, as the Te-p–Te-p interactions lower the energy of the Σ (and η) bands relative to the L (and Z) bands. Also, the $V_{pp\sigma}$ and $V_{sp\sigma}$ values given represent the interactions that correspond to the *average* Ge–Te distance for the six shortest Ge–Te neighbor pairs. Then the actual values of $V_{pp\sigma}$ and $V_{sp\sigma}$ for the three nearest and three next-nearest neighbors (six nearest neighbors when $\delta = 0$) are set by requiring that $V(d) = V(d_0) \times (d_0/d)^2$, where d is the neighbor distance d_0 is the *average* interatomic distance for the six shortest Ge-Te neighbor pairs. The same type of method is used to define the $V_{pp\sigma,Te}$ parameters when $\gamma \neq 60°$, but using the twelve shortest Te-Te neighbor pairs.

Modifying Geometry and Atomic-Orbital Interactions

The TB model can explain the offsetting of the Z VBM from the true Z point in addition to the decrease in the energy of the Z VB relative to the Σ VB upon an increase in δ. As seen in Figure

[2]Note that this model is not fit to the GeTe band structure from DFT of experiments. It is simply a toy model that *qualitatively* reproduces the valence band structures and trends in its behavior.

Table 5.1: Tight-binding parameters for a toy model of GeTe. The hopping parameters, $V_{sp\sigma}$ and $V_{pp\sigma}$, are defined for the case where $\delta = 0$, and there are six (equivalent) nearest-neighbors. When $\delta \neq 0$, and the six nearest-neighbors split into three nearest-neighbors and three next-nearest neighbors, the hopping parameters are adjusted such that $V(d) = V(d_0) \times (d_0/d)^2$, where d_0 is the average interatomic distance for the six shortest Ge-Te neighbor pairs. The same type of adjustment is made for the Te-p–Te-p interactions when γ is modified.

Parameter	Description	Value (eV)
$V_{sp\sigma}$	Ge-s–Te-p σ-bonding	1.5
$V_{pp\sigma}$	Ge-p–Te-p σ-bonding	4.0
$V_{pp\pi}$	Ge-p–Te-p π-bonding	-(1/8)$V_{pp\sigma}$
$V_{pp\sigma,Te}$	Te-p–Te-p σ-bonding	0.275
$V_{pp\pi,Te}$	Te-p–Te-p π-bonding	0
$E_{Te-p} - E_{Ge-s}$	Ge-s–Te-p on-site energy separation	10.0
$E_{Ge-p} - E_{Te-p}$	Ge-p–Te-p on-site energy separation	3.0

5.11a, which shows the TB band structure (with Ge-s–Te-p and Ge-p–Te-p interactions) around Z and Σ, there is no offset when $\delta = 0$, but as δ increases, the Z VBM moves farther away from Z and it decreases in energy (Figure 5.11a). Notice that the energy of the VB edge at the true Z-point also decreases. By contrast, the Σ VBM shows a minimal decrease in energy when δ increases. The TB model also shows that the Ge-p–Te-p interactions are responsible for the offsetting behavior and the decreases in energy of the Z band. There is no offset when $V_{pp\sigma} = 0$, and the offset from the true Z-point increases as $V_{pp\sigma}$ increases (Figure 5.11b). Additionally, the energy of the Z VBM (and the energy of the VB edge at the true Z-point) decreases relative to the Σ VBM as $V_{pp\sigma}$ increases.

Moreover, a TB model with Ge-p–Te-p interactions but without Ge-s–Te-p interactions emphasizes the role that the Ge-p–Te-p interactions alone play. When there are no Ge-s–Te-p interactions, the Z VBM moves farther away from the true Z-point as δ increases, but the energy of this Z VBM remains constant (Figure 5.11c). That being said, the energy of the band at the true Z-point still decreases with increasing δ. Moreover, when δ is constant and $V_{pp\sigma}$ (and $V_{pp\pi}$) increases in strength, the location and energy of the Z VBM remain unchanged, but the energy of the VB edge at the true Z-point decreases with increasing $V_{pp\sigma}$. Thus, the band maximum between B and Z that results from *only* the Ge-p–Te-p interactions is non-bonding (its energy is constant with $V_{pp\sigma}$), while

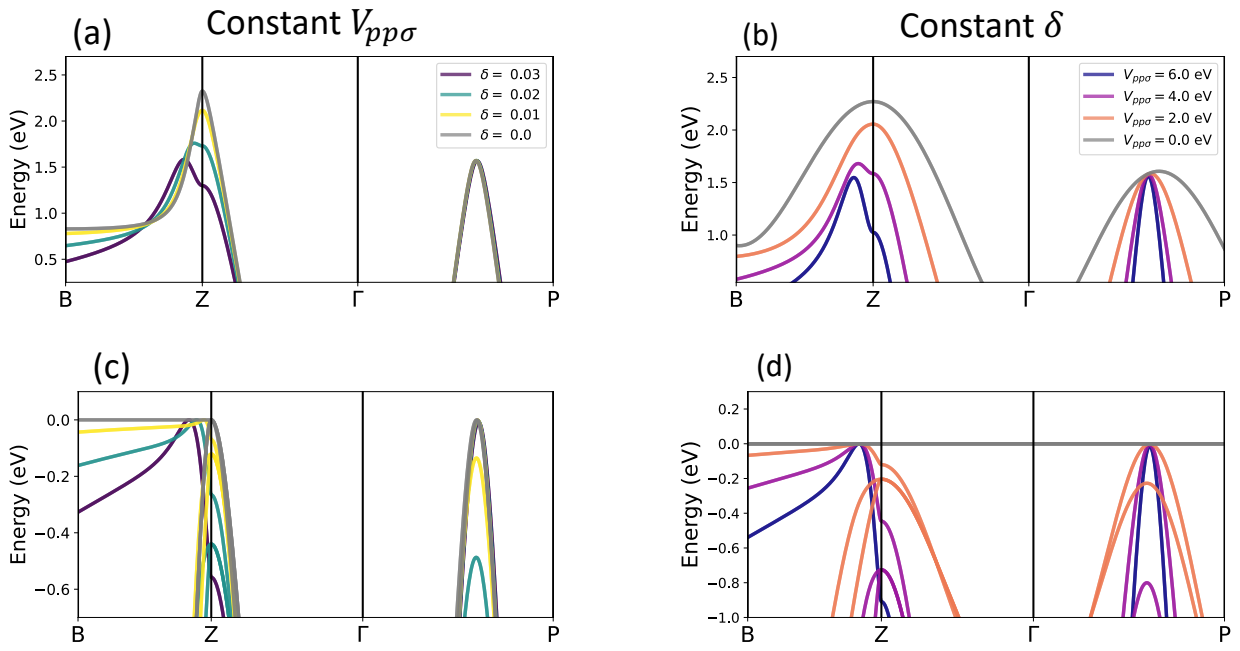

Figure 5.11: TB electronic structure for a toy model of GeTe (interaxial angle set to $\gamma = 58°$) illustrating the origin of the Z-VBM offset from the Z-point and its decrease in energy upon increasing δ. Band structures when (a) $V_{pp\sigma} = 4$ eV, $V_{pp\pi} = -0.5$ eV, $V_{sp\sigma} = 1.5$ eV, and δ varies from 0 to 0.03, (b) $\delta = 0.03$, $V_{sp\sigma} = 1.5$ eV and $V_{pp\sigma}$ varies from 0 to 6 eV ($V_{pp\pi} = -V_{pp\sigma}/8$), (c) $V_{pp\sigma} = 4$ eV, $V_{pp\pi} = -0.5$ eV, $V_{sp\sigma} = 0$ eV and δ varies from 0 to 0.03, and (d) $\delta = 0.03$ $V_{sp\sigma} = 0$ eV and $V_{pp\sigma}$ varies from 0 to 6 eV ($V_{pp\pi} = -V_{pp\sigma}/8$).

the band becomes more bonding away from that point (toward both B and Z). In terms of basic atomic-orbital interactions, the location and energy of the Z VBM results from a trade-off between the Ge-s–Te-p anti-bonding interaction, which favors the VBM at the true Z-point (it reaches a local maximum in strength *at* Z), and the Ge-p–Te-p bonding interaction, which favors a VBM offset from the Z-point, as it pushes the energy of the highest VB down in energy at Z (and between the true Z-point and the offset Z-VBM). Consequently, the Z-VBM is located between the true Z-point and the point (between B and Z) where it *would* be located if there were no Ge-s–Te-p interactions and only Ge-p–Te-p interactions.

As seen in Figure 5.11, the energy of the Σ VB pocket remains virtually constant with respect to changes in δ and Ge-s–Te-p interaction strength. This indicates that the energy of the Σ VB is nearly independent of the Ge-p–Te-p interactions, and hence, more weakly dependent on δ. Thus,

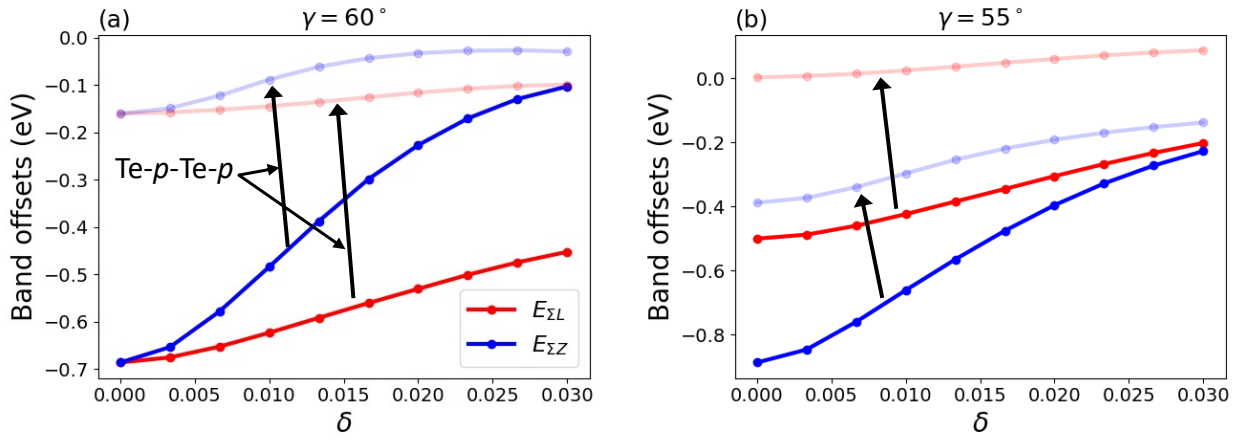

Figure 5.12: Tight-binding (TB) band offsets (calculated without SOC) between the Σ and L bands ($E_{\Sigma L}$, red lines) and between the Σ and Z bands ($E_{\Sigma Z}$, blue lines) as a function of cation offset for the cases where (a) the interaxial angle is given by $\gamma = 60°$, and (b) $\gamma = 55°$. The darker red and blue lines are from calculations that do not include Te-p–Te-p bonding interactions, and the fainter lines are from calculations that include the Te-p–Te-p interactions ($V_{pp\sigma,Te} = 0.275$ eV). The black arrows point to the upward shift in the $E_{\Sigma L}$ and $E_{\Sigma Z}$ lines when the anion-p–anion-p interactions are included. The remaining TB hopping parameters are given by $V_{sp\sigma} = 1.5$ eV, $V_{pp\sigma} = 4.0$ eV, $V_{pp\pi} = -0.5$ eV (see Table 5.1). The cation offset is set to $\delta = 0.03$ for all calculations. Note that These TB offsets just give a *qualitative* description of GeTe and do not give the actual values of the band offsets. For instance, in r-GeTe, the VBM is along ΓP (Σ), not Z or L.

when the inversion symmetry is broken, the Σ band is lowered to a much smaller extent than the Z or L bands are (see Figure 5.10). These offset (δ) effects—in addition to effects from the interaxial angle and anion-p–anion-p interactions— in the TB model are depicted more clearly in Figure 5.12. Both the energy difference between the Σ and Z bands ($E_{\Sigma Z}$) and between the Σ and L bands ($E_{\Sigma L}$) increases with increasing δ. Furthermore, when Te-p–Te-p interactions are incorporated, both the $E_{\Sigma Z}$ and $E_{\Sigma L}$ curves shift upwards, which is consistent with these anion-p interactions pushing the energy of the L and Z bands down more so than the Σ band (see Chapters 3 and 4). Finally, when the primitive cell interaxial angle, γ, is reduced from 60° (Figure 5.12a) to 55° (Figure 5.12b), the $E_{\Sigma Z}$ curves shift down while the $E_{\Sigma L}$ curves shift upward. This behavior is consistent with the Z band becoming more s-p anti-bonding and the L band becoming less s-p anti-bonding relative to the Σ band as γ is reduced.[3]

[3]Note that Figure 5.12 does *not* reproduce the DFT or experimentally calculated values of the band offsets. Rather, it is intended to depict *trends* with respect to structural parameters and chemical interactions.

Effect of Spin-Orbital Coupling

Simple atomic-orbital interactions alone are not sufficient to fully explain the behavior of the VB edges when inversion symmetry is broken, as SOC also plays a role through the Rashba spin-splitting effect [134, 148, 149]. The Rashba effect causes the spin-splitting of single-electron (spin) bands in $\boldsymbol{k}$-space, and in GeTe, it has a particularly pronounced effect around the Z-point. Moreover, it has been shown that increasing the strength of the Rashba effect by alloying Ge with Sn promotes the convergence of the Z and Σ VB edges in r-GeTe, which leads to better thermoelectric performance [134]. Using another toy model of GeTe, we can investigate the effect of SOC on Rashba splitting. From Figure 5.13a, it is clear that while the Z offset exists without SOC, increasing the strength of the SOC makes the offset more pronounced—the energy difference between the band at Z and the maximum *off* Z increases, and the VBM moves farther away from the Z-point. Not only does the enhanced offsetting from SOC increase N_V by converging the Z and Σ VBs, but because the Z VB pocket is not actually on the high-symmetry Z-point, it actually has higher N_V than the degeneracy of the Z-point and leads to a more complex Fermi surface (when converged near the Σ VB in r-GeTe). From Figure 5.13b, it is evident that the anion-p–cation-p interactions are needed for this dramatic offsetting effect to occur. That is, when there are no p-p interactions, we see the typical spin-splitting of the band at Z—the bands shift in different directions in $\boldsymbol{k}$-space [134]—but we do not get the sharp peak off of Z that is observed in the real (DFT) band structure (with and without SOC). This sharp peak only emerges when the p-p interaction is introduced, and it becomes sharper when the strength of the p-p interaction increases.

5.4 Computational Methods

The first-principles DFT calculations to obtain the cubic and rhombohedral GeTe band structure (and corresponding orbital characters) were performed using the Vienna ab initio Simulation Package (VASP), employing projector augmented wave (PAW) pseudopotentials and the PBE exchange-

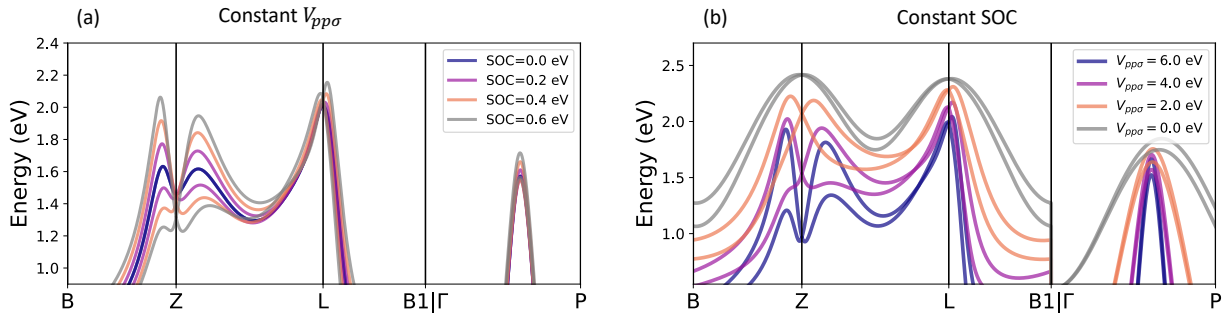

Figure 5.13: Tight-binding (TB) band structure, showing the top of the valence band (VB), in a toy model of r-GeTe ($\delta = 0.03$, $\gamma = 58°$) with (a) varying spin-orbit coupling (SOC) strength and constant $V_{pp\sigma} = 4.0$ eV, and (b) constant SOC = 0.5 eV with varying values of $V_{pp\sigma}$. The other TB parameters are set such that $V_{pp\pi} = -V_{pp\sigma}/8$, $E_{Ge-p} - E_{Te-p} = 3.5$, $V_{sp\sigma} = 1.5$ eV, and $V_{pp\sigma,Te} = V_{pp\pi,Te} = 0$. These TB band structures only give a *qualitative* description of r-GeTe and do not give the actual values of the band offsets. For instance, in r-GeTe, the VBM is along ΓP (Σ), not (slightly off) Z.

correlation functional, derived from the generalized-gradient approximation (GGA). [48–51, 87, 88]. A plane-wave energy cutoff of 450 eV was used for each calculation. The structural degrees of freedom were relaxed (without including SOC), until the forces on atoms were less than 0.01 eV/nm, using a Γ-centered [89] $\boldsymbol{k}$-point mesh of size $13 \times 13 \times 13$. After relaxation, the self-consistent electronic structure calculations were performed using a Γ-centered $\boldsymbol{k}$-point mesh of size $20 \times 20 \times 20$. To find the δ vs γ relationship, the offset (δ) was set manually, and the interaxial angle (γ) was determined by relaxing the unit cell with respect to the unit cell shape, while constraining the atomic positions. The $\boldsymbol{k}$-vector resolved crystal orbital Hamilton population (COHP) calculations were performed using the version 4.0.0 of the LOBSTER software with the pbeVASPFit2015 basis set [52–54, 150].

5.5 Conclusion

The rhombohedral distortion GeTe, marked by a reduction in the primitive lattice interaxial angle (γ) and by the offset (δ) of Ge from the center of the Te-octahedron, creates new degrees-of-freedom for band engineering. While the VBM in c-GeTe is located at the L-point, with the Σ VB less than 0.1 eV below, r-GeTe has a VBM along the Σ symmetry line, with the next lowest VB 0.2 eV lower.

While reducing the symmetry from the cubic to rhombohedral phase is often thought to reduce the valley degeneracy, there may be some cases, particularly when the Fermi energy is closer to the VBM, where a *slight* rhombohedral distortion is beneficial because it brings the Σ band closer to the L band.

Detailed analysis of DFT band structures over a range of γ and δ values shows that δ, the cation offset, is responsible for the emergence of the Σ VBM in r-GeTe. On the other hand, the decrease in γ actually leads to an increase in the Z VB relative to the Σ and L VBs, while the relative energy of the L VB decreases relative to the Σ band. Using an atomic-orbital TB framework and $\boldsymbol{k}$-resolved COHP calculations, we show that changes to the band structure with respect to γ can be explained through changes to the Ge-s–Te-p anti-bonding character in each of the VB pockets. Specifically, the strength of this interaction increases at Z and Σ (more so at Z) and slightly decreases at L and η. Moreover, we show that the emergence of the Σ VBM over the L and Z VBs with increasing δ is due to the presence of Ge-p–Te-p bonding interactions in the various VBM states when inversion symmetry is broken. These bonding interactions remain minimal in the Σ VBM state and are stronger in the L and Z bands.

Finally, we show using COHP and a toy TB model that the offset of the Z VBM from the true Z-point when the inversion symmetry is broken ($\delta \neq 0$) is from a trade-off between the Ge-p–Te-p bonding interactions and Ge-s–Te-p anti-bonding interactions at the Z-point. Moreover, using another toy GeTe model with SOC, we show that SOC enhances this Z-point offsetting effect and increases the energy of the Z VBM relative to the Σ VBM, which explains another technique for enhancing Σ-Z convergence in r-GeTe, where the Σ band is higher in energy than the Z band: enhancing the Rashba effect through stronger SOC.

Future work in this area should focus on better understanding how variations in the Fermi surface (i.e., valley degeneracy and carrier pocket anisotropy) influence the electronic transport at different doping levels using software packages like BoltzTrap2 or AMSET [151, 152]. Moreover, because alloying/doping is typically required to control the geometry, it is necessary to study the

combined effect of changing the chemistry *and* geometry of the material in tandem. Many of the alloying species, such as Mn, Li, Cd, Na, etc., are known to converge the VB pockets in IV-VI semiconductors, so these effects may dominate over or change the nature of the effects of geometry alone.

Engineering Band Degeneracy in Half-Heusler Thermoelectrics

6.1 Introduction

As discussed in Chapter 1, high valley degeneracy can be achieved by having a valence band maximum (VBM) or conduction band minimum (CBM) at a low symmetry point in the Brillouin zone (BZ) of a high symmetry crystal and/or by having multiple band extrema converged within a few k_BT in energy at the same point or different points in the BZ [29,36]. In this chapter, we distinguish between degeneracy imposed by the crystal symmetry, N_{V_k}, and that due to number of degenerate bands at a given $\boldsymbol{k}$-point, the orbital degeneracy (N_{V_o}), such that the total valley degeneracy (for a specified $\boldsymbol{k}$-point) is given by $N_V = N_{V_k} \times N_{V_o}$. For example, there is only one Γ-point ($\boldsymbol{k} = \boldsymbol{0}$) located at the center of the BZ, so if a VBM or CBM were located at the Γ-point, the symmetry-imposed valley degeneracy would be $N_{V_k} = 1$. If this Γ-point VBM or CBM were doubly degenerate, then we would have $N_{V_o} = 2$, giving $N_V = 1 \times 2 = 2$ for the Γ-point contribution. On the other hand, in the BZ of a face centered cubic (FCC) material, there are three symmetrically equivalent X-points (half of an X-point on each of the six square faces), so a VBM or CBM at the X-point

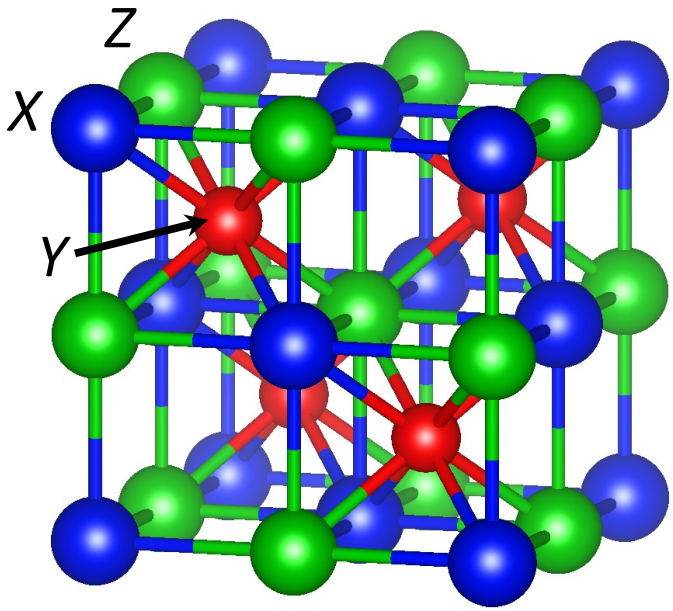

Figure 6.1: The half-Heusler crystal structure (space group #216) is comprised of three crystallographic sites, each forming an FCC sublattice. The X (blue) and Z (green) sites form the octahedrally coordinated rock salt structure with X at the (0, 0, 0) position and Z at the (1/2, 1/2, 1/2) position. The Y-sites (red) at (1/4, 1/4, 1/4) fill half of the rock salt tetrahedral sites, while the other half of the tetrahedral sites are unfilled.

would yield $N_{V_k} = 3$. Recall that convergence of multiple bands at a single $\boldsymbol{k}$-point may not be as beneficial as convergence between band extrema that are farther apart in the BZ [36].

Semiconducting half-Heusler (hH) compounds comprise an important class of thermoelectric materials. [154–160] They exhibit high chemical, mechanical, and temperature stability and are relatively simple to synthesize [157,158,161–164]. The typical hH crystal structure (shown in Figure 6.1) has composition XYZ and belongs to the $F\bar{4}3$m space group (#216). The X-site is typically occupied by the most electropositive species, the Y-site contains a transition metal element, and the Z-site is occupied by a main group element (Sb, Sn, Bi, etc). The Y and Z sites form a polyanionic zinc blende sublattice, $[YZ]^{n-}$, while the X and Z sites form the rock salt lattice (with Y filling half of the rock salt tetrahedral sites) [157,161,165–167]. While the Wyckoff positions of X

and Z are interchangeable with no effect on the properties, interchanging Y with one of the other sites alters the electronic structure [167–169]. Stable, semiconducting compositions form when the valence electron count is balanced using Zintl chemistry [155, 161, 170–173].

All three atomic sites can be alloyed to improve both the electronic and thermal properties of hH thermoelectrics. The valence imbalance from an aliovalent substitution leads to doping, while isoelectronic alloying can lead to altering the band masses and energies as well as scattering [158, 159, 174–181]. Although some 60+ XYZ combinations of transition-metal-based hH compounds are known, their electronic structures can be classified broadly based on the nature of their band extrema (VBMs or CBMs). For example, Dylla *et. al* describe three basic types that can be mapped according to the location of their VBMs in the BZ, which can be at Γ ($N_{V_k} = 1$; $N_{V_o} = 3$), L ($N_{V_k} = 4$; $N_{V_o} = 2$) or W ($N_{V_k} = 6$; $N_{V_o} = 1$). The valence band (VB) edge at Γ is dominated by mainly the X-d orbitals, while the VB edge at L consists of mostly Y-d character. The W-point VB edge also contains mostly Y-d character but has more Z-p contribution than the L-point VB edge in most cases. Thus, there is a natural strategy to alter the energy of the VB edge at L or Γ where one simply changes the group number of the X or Y element: increasing the group number difference between X and Y favors the Γ-point VBM, while the converse favors the L-point and W-point VBMs. Moreover, near the transition between the Γ-point and L-point VBM, the W-point ($N_{V_k} = 6$; $N_{V_o} = 1$) VBM emerges [182]. Here, we discuss the chemical origins of the W-point VBM and show that the energy of the Z-p orbitals plays an important role in the emergence of the W-pocket, such that all three sites must be strategically chosen to engineer this class of hH thermoelectrics.

We see a similar picture for conduction band convergence. For typical transition-metal-based hH thermoelectrics, the CBM is located at the X-point ($N_{V_k} = 3$), and there are two symmetrically distinct bands that could be the CBM depending on the compound, one that is anti-bonding with mostly Y-d character, and one that is non-bonding with predominantly X-d character [68].[1] In

[1]There are exceptions to this X-point CBM and its orbital description in valence-balanced hH semiconductors. Specifically, there are compounds that have low-lying s-orbital states near the CB edge, resulting in a CBM at the

typical hH thermoelectrics, the anti-bonding (Y-d) and non-bonding (X-d) CBMs belong to the X_3 and X_2 symmetry representation of the T_d point group, respectively. Higher CB degeneracy of $N_V \sim 6$ can be achieved by converging these two CBMs, such that $N_{V_o} = 2$. Guo *et. al* report trends dictating CB convergence that are nearly identical to those describing VB convergence (between Γ and L). That is, decreasing the group number difference between X and Y increases the energy of the X_3 CBM relative to the X_2 CBM [188]. Thus, tuning the VBs and CBs is chemically quite simple: adjust the group number of the X and Y elements, with secondary effects from the electronegativity.

Generally, compounds with a VBM at Γ tend to have the X_3 CBM, and those with the L VBM tend to have the X_2 CBM, though there are exceptions to this. MNiSn (M = Ti, Zr, Hf) hH alloys, which are common n-type candidates [175, 189–193] comprise the Γ VBM, X_3 CBM class, [182, 188] while high performing p-type compounds, such as the (V,Nb,Ta)FeSb alloys [31, 194–197], comprise the L VBM, X_2 CBM type [188]. The better p-type performance seen in the latter category can be directly attributed to the higher VB degeneracy from having a VBM located at the L-point rather than at the Γ-point [31, 40, 154, 182, 189, 197, 198]. In this chapter, we use ZrNiSn and NbFeSb as the model systems for the hH compounds with a Γ-point VBM and X_3 CBM and those with an L-point VBM and X_2 CBM, respectively. While we only provide a detailed analysis of ZrNiSn and NbFeSb, the differences in their electronic structures and bonding can be broadly generalized, as NbFeSb better represents compounds with a smaller group number difference between X and Y, and ZrNiSn better represents compounds that have a larger group number difference between X and Y.

While the community understands the VBM and CBM classifications, the orbital character of the band edges is not understood well enough. For instance, there is not a clear understanding of *why* the orbital character at the Γ-point VB edge differs greatly from the VB edge at the L-point and why the Γ-point CB edge character (mostly X-d) differs significantly from the X_3 CB orbital

Γ-point rather than the X-point (e.g., ScPbSb, ScPtBi, LuPtBi, YPdBi, CePdBi, ScNiBi, LuAuSn, etc.). In this class of hH compound, the CB and VB edges may cross at the Γ-point, closing the bandgap (the s-orbitals and d-orbitals do not hybridize at Γ, which allows the bands to cross). These hH compounds may have applications as topological insulators [183–187].

character (mostly Y-d). Additionally, while simple bonding pictures might predict the CB edge to be dominated by the orbitals of the more electropositive X species and the VB edge by the more electronegative Y species [161], this is not the case at each $\boldsymbol{k}$-point. By gaining insight into the chemistry behind the orbital classifications identified in Refs. 182 and 188, we can better understand and develop strategies to engineering more highly converged hH electronic structures with greater thermoelectric performance.

Here, we aim to explain how the VB and CB edges can so dramatically change character as they traverse from Γ to L or from Γ to X. The essential mechanism at play is the avoided crossing, sometimes called a band (or level) anti-crossing [4, 169]. Band anti-crossings occur when two interacting bands that would normally cross each other if they were non-interacting are forbidden to cross. The result is two distinct bands characterized by an admixture of the original (non-interacting) bands [4]. The Γ and L VBMs are the result of an avoided crossing between a band that decreases in energy from Γ to L, with primarily Y-d character at L, and a band with mostly X-d character that increases in energy from Γ to L. A simplified sketch of this avoided crossing along the $\Gamma - \Lambda - \mathrm{L}$ path is depicted in Figure 6.2. The result is a valence band edge with local maxima at Γ and L that are dominated by X-d and Y-d character, respectively.

In general, increasing the energy of the X-d orbitals increases the energy of the blue band in Figure 6.2, and increasing the energy of the Y-d orbitals increases the energy of the red band (more so near L). Therefore, in materials with a greater energy (group number) difference between X and Y (ZrNiSn), the Γ VB pocket is higher compared to the L VB pocket. Conversely, in materials with a smaller group number difference (NbFeSb), the L VB pocket is higher relative to that at Γ. In terms of doping/alloying, these changes to the anti-crossing bands could be accomplished by tuning the weighted average of the group number (or electronegativity) difference between X and Y based on the end-member compounds.

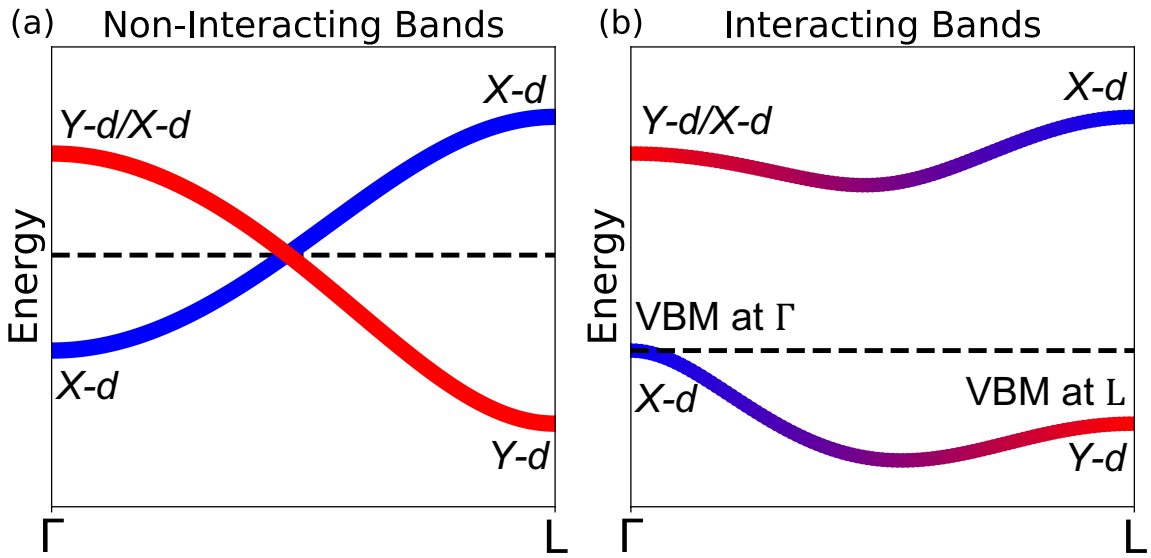

Figure 6.2: Simplified sketch of two bands (each doubly degenerate, yielding four bands total) along the Λ-line in a half-Heusler compound before and after interacting and inducing an avoided crossing. (a) When the bands are non-interacting, one of the bands decreases energy from Γ to L and has orbital character that transitions from being mainly Y-d–X-d at Γ to being mostly Y-d at L. The second band increases in energy from Γ to L and contains mostly X-d character. (b) When the bands interact, an avoided crossing occurs, and the lower band transitions from having X-d character at Γ to Y-d character at L. There are two local VBM, one at Γ with X-d character and one at L with Y-d character. The relative energies of these VBMs can be tuned via substitutions on the X- and Y-sites. The dashed horizontal line in (a) and (b) represents the Fermi energy.

6.2 Avoided Crossings in the Half-Heusler Electronic Structure

The symmetry properties of electronic bands are crucial for understanding band behavior and interactions. Using a group theory, [4, 5, 199] the electronic bands at various $\boldsymbol{k}$-points/paths can be classified based on the irreducible symmetry representations of their corresponding wavefunctions [68], where we can describe the electronic wavefuctions using the linear combination of atomic orbitals (LCAO) approach [63–65, 84]. Bands (or orbitals) that belong to the same symmetry representation at a given point in the BZ can interact, whereas interactions between bands belonging to different representations are forbidden [4, 5]. The first-principles electronic band structures with band symmetry labels and orbital projections along the X-Δ-Γ-Λ-L path for ZrNiSn and NbFeSb can be seen in Figure 6.3 (the orbital character at the band edges is in agreement with that reported in Ref. 182). All the density-functional theory (DFT) calculations presented here are carried out using the Perdew-Burke-Ernzerhof (PBE) [51] functional without including spin-orbital coupling (SOC) effects. The bands labeled as Γ_{15} are triply degenerate states, those labeled as Γ_{12}, X_5, L_3, $\Delta_{3,4}$, or Λ_3 are doubly degenerate states, and those labeled as X_1, X_2, X_3, X_4, L_1, Δ_1, Δ_2, or Λ_1 are singlet states (see Appendix D for more information on group theory band notation).

Often, the bandgap is attributed to Y-d–X-d bonding, leading to band edges dominated by the transition metal d-orbitals. [157, 161, 165, 168, 200–203]. Based on this bonding description, one might expect states near the CB edge to have more X-d character and states near the VB edge to exhibit mostly Y-d orbital character because X is more electropositive. However, a closer look at $\boldsymbol{k}$-point dependence of the atomic orbital compositions (Fig. 6.3) suggests that this simple bonding description does not adequately capture the important features of the band structure, particularly those needed to understand band convergence and degeneracy. For example, it fails to explain why X-d states dominate the VB edge at the Γ-point and why the X_3 CBM exhibits predominantly Y-d character. Therefore, we must take a more nuanced approach to looking at the bonding at different $\boldsymbol{k}$-points in the BZ by considering the role of avoided crossings in the hH band structure [169].

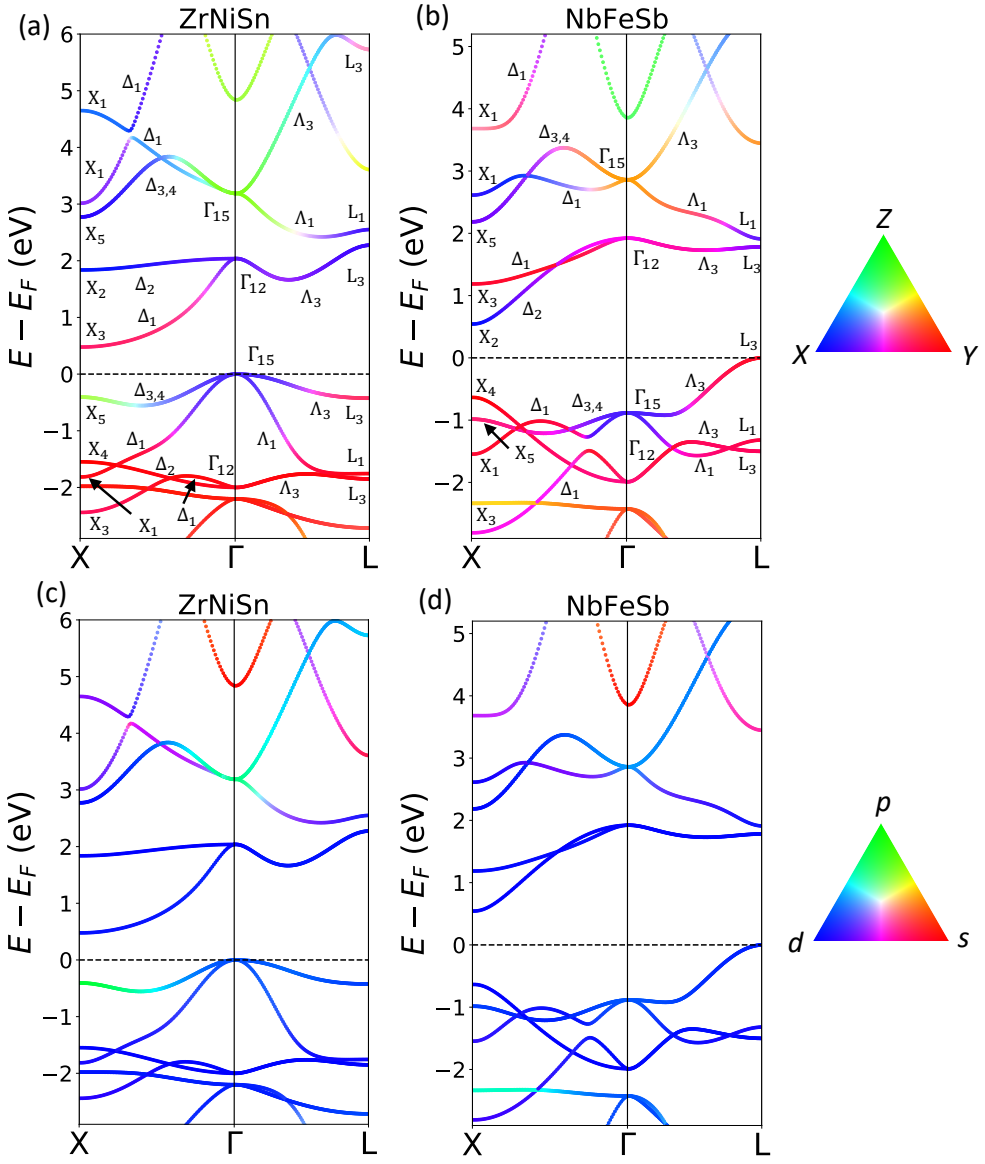

Figure 6.3: DFT-calculated electronic band structure calculations of half-Heusler compounds, ZrNiSn and NbFeSb, showing (a)-(b) the relative contribution of each atomic species (X, Y, Z) and (c)-(d) the relative contribution of each orbital type (s, p, d). The symmetry representations for select bands at the X-, Γ-, and L- points and along the Δ- and Λ-lines are shown. The dashed line indicates the Fermi energy.

6.2.1 Tight-Binding Model of Avoided Crossings

Avoided crossings in band structures occur because the eigenvalues (energies) of two interacting eigenstates (wavefunctions) cannot be equal to each other. When bands belonging to different symmetry representations approach each other in energy, they are able to cross normally, such that there is a $\boldsymbol{k}-$point where the energy of the two bands are equal. On the other hand, bands that belong to the same symmetry representation will interact, and therefore, are forbidden to cross, resulting in two distinct bands that are an admixture of the original wavefunctions. An avoided crossing may result in a band having different orbital character at different $\boldsymbol{k}-$points. Moreover, it can lead to a certain orbital being found in one band at a given $\boldsymbol{k}-$points but in another band at a different $\boldsymbol{k}-$points, rather than belonging to a continuous band.

We employ the tight-binding (TB), or LCAO, [63–66, 84, 204] framework to better understand different ways that avoided crossings can appear in a band structure. As mentioned in Chapter 2, the TB solution for the energy levels in a diatomic molecule can be a useful tool for understanding complex electronic structures [47]. Consider the interaction between two orbitals (1 and 2) that are members of the same symmetry representation. The expressions for the resulting bonding (ε_-) and anti-bonding (ε_+) energy levels are given in Equation 6.1. E_1 and E_2 represent the on-site energies of the atomic orbitals prior to interacting, and V is the tight-binding hopping integral that describes the strength of the interaction between the two orbitals. In order to extend this simple diatomic molecule model to complex crystal structures, we can adjust the on-site energies and hopping (interaction) parameters so that they are *effective* on-site energies (($E_1(\boldsymbol{k})$ and ($E_2(\boldsymbol{k})$) and interaction parameters, or hopping integrals ($V(\boldsymbol{k})$), which are a function of the $\boldsymbol{k}$-vector. [47] That is, we can write Equation 6.1, as a function of $\boldsymbol{k}$, as shown in Equation 6.2, in order to describe more complex electronic dispersions with a simple diatomic molecule TB model.

$$\varepsilon_\pm = \frac{1}{2}(E_1 + E_2) \pm \frac{1}{2}\sqrt{(E_1 - E_2)^2 + 4V^2} \tag{6.1}$$

$$\varepsilon_{\pm}(\boldsymbol{k}) = \frac{1}{2}(E_1(\boldsymbol{k}) + E_2(\boldsymbol{k})) \pm \frac{1}{2}\sqrt{(E_1(\boldsymbol{k}) - E_2(\boldsymbol{k}))^2 + 4V^2(\boldsymbol{k})} \tag{6.2}$$

Simply understanding how the effective hopping integrals varies as a function of $\boldsymbol{k}$ provides insight into how electronic bands behave. For instance, regardless of whether or not avoided crossings are present, $\boldsymbol{k}$-dependent hopping integrals that are strongest at Γ result in bonding bands that run up in energy (increase in energy, becoming less bonding) from Γ and in anti-bonding bands that run down in energy from Γ. Conversely, interactions that are weakest at Γ result in bonding bands that run down in energy from Γ and in anti-bonding bands that run up in energy from Γ [84].

A schematic of a normal band crossing and three illustrative cases of avoided crossings can be seen in Figure 6.4, where the red and blue coloring represent the orbital character of each interacting orbital. In all four cases, the *effective* on-site energy of the red state is decreasing, and the *effective* on-site energy of the blue state is increasing. The increase/decrease of effective on-site energies is due to secondary interactions that are not captured in the $V(\boldsymbol{k})$ term, such as interactions of the orbitals with themselves (their periodic images). Figure 6.4a depicts two non-interacting bands that cross trivially with no change in the character of the bands upon crossing, consistent with a TB hopping integral of $V = 0$. Figure 6.4b represents the case where the TB hopping integral is constant across the $\boldsymbol{k}$-path. Figure 6.4c illustrates an avoided crossing where V is a function of the $\boldsymbol{k}$-vector. In this case, V varies sinusoidally, and is at a maximum at the center of the path where the bands would have crossed. The resulting anti-crossing bands bow outward from each other. Figure 6.4d also represents a case where V varies, but in this example, V increases from left to right. Note that only cases where $V \geq 0$ are shown, but V can be negative as well (the magnitude is what is important in this example).

6.2.2 Avoided Crossings along $\Gamma - \Delta - \mathbf{X}$

The presence of avoided crossings in hH compounds along the Δ symmetry line was introduced by Ogut *et. al* in 1995 in order to explain the formation of the bandgap in these compounds [169].

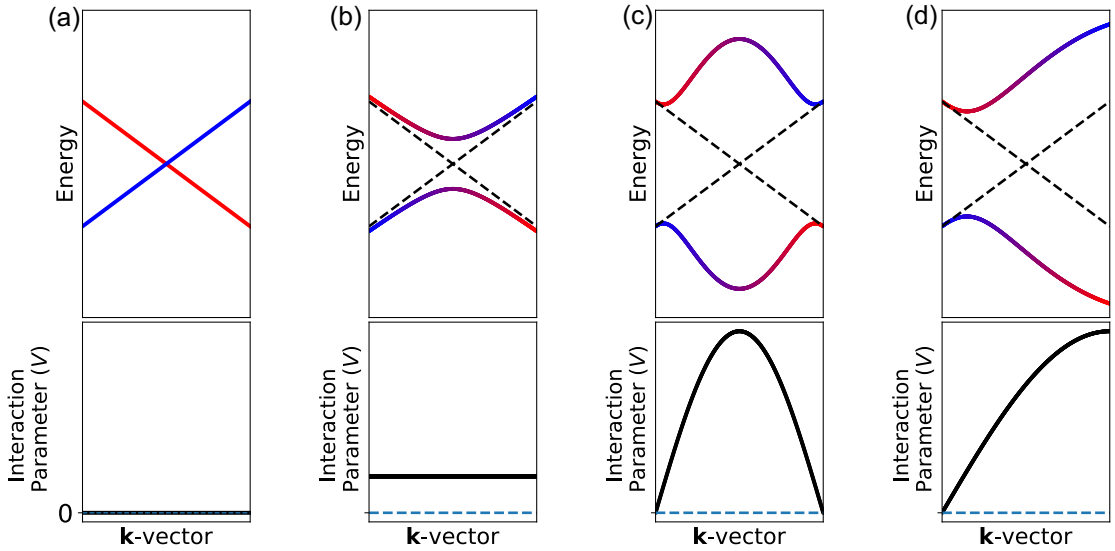

Figure 6.4: Schematic depiction of a normal crossing and three cases of avoided crossings (top) with corresponding sketches of the tight-binding hopping integral, V (bottom). (a) Normal crossing with an interaction of $V = 0$. (b) Avoided crossing when the hopping integral, V, is constant along the entire $\boldsymbol{k}$-path. (c) Avoided crossing where the hopping integral varies sinusoidally, such that $V = 0$ at the far right and left and reaches a maximum at the center of the $\boldsymbol{k}$-path where the bands would have crossed. (d) Avoided crossing when V varies, such that $V = 0$ at the far left and is at a maximum at the far right of the plot. Red and blue coloring is used to depict the character of the bands, and in (b)-(d) top, the dashed lines indicate the behavior of the bands when $V = 0$. In (b)-(d) bottom, the blue horizontal dashed lines are shown at $V = 0$.

Ogut *et al.* identify an avoided crossing between the highest $\Delta_{3,4}$ VB and the lowest energy $\Delta_{3,4}$ CB in ZrNiSn. We can see the signature of this avoided crossing in the complementary character of the two anticrossing $\Delta_{3,4}$ bands (see Figure 6.3a and c). [169] That is, the lower band has mostly Zr-d character at Γ and Sn-p character at X, and the upper band has mostly Sn-p character at Γ and predominantly Zr-d character at X.

We can think of these bands as being the result of an avoided crossing between a "Zr-d band" and a "Sn-p band". That is, if there were no interactions between the two bands, there would simply be an X-d band that increases in energy from Γ to X crossing a Sn-p band that decreases in energy from Γ to X like Figure 6.4a. In fact, we can use $\boldsymbol{k}$-point-resolved, band-resolved crystal orbital Hamilton populations (COHPs) [52, 205] to explain this behavior. While multiple orbital interactions (including interactions between atoms and their periodic images) are needed to fully explain the complex hH electronic structure, we focus on a few important interactions as examples. The COHPs of the $\Delta_{3,4}$ VB and CB for ZrNiSn can be seen in Figure 6.5a,c where positive values of the COHP indicate an anti-bonding interaction, negative values of the COHP indicate a bonding interaction, and the magnitude represents the strength of the interaction. The COHP values show that the "Zr-d band" would run up in energy from Γ to X because of the Zr-d–Ni-p interaction (bonding in the $\Delta_{3,4}$ VB) that is strongest at Γ and decreases to almost zero at X. In other words, this Zr-d–Ni-p interaction pushes the Zr-d states down in energy, such that they are found in the VB edge where the interaction is strongest (at Γ) and in the CB where the interaction is weakest (at X). Additionally, there is an interaction between the Ni-p and Sn-p orbitals (bonding in the VB) that increases in strength from Γ to X. This interaction explains why the Sn-p state would run down in energy from Γ to X. That is, the Sn-p states are pushed down in energy by the Ni-p states at X more so than at Γ, such that the Sn-p states are found in the VB at X but in the CB at Γ.

COHP also explains why the $\Delta_{3,4}$ bands bow out from each other like the avoided crossing depicted in Figure 6.4c. As shown in Figure 6.4c, this type of avoided crossing is the result of a strong interaction between the two states that reaches a peak strength about halfway along the path

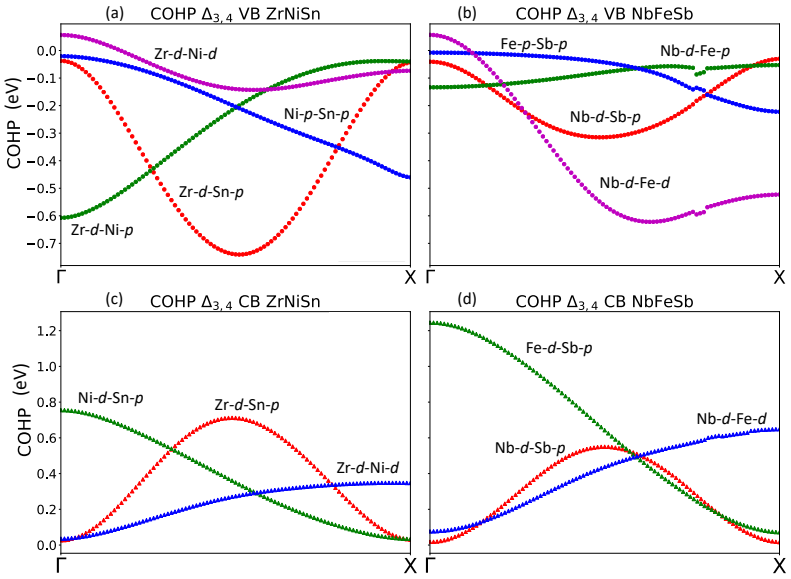

Figure 6.5: $\boldsymbol{k}$-resolved, band-resolved crystal orbital Hamilton (COHP) values in the $\Delta_{3,4}$ (a) valence band (VB) of ZrNiSn, (b) VB of NbFeSb, (c) conduction band (CB) of ZrNiSn, and (d) CB of NbFeSb. In the VB, the green curve represents X-d–Y-p interactions, the red curve represents X-d–Z-p interactions, the purple curve represents X-d–Y-d interactions, and the blue curve represents Y-p–Z-p interactions. In the CB COHP plots, the red curve represents X-d–Z-p interactions, the green curve represents Y-d–Z-p interactions, and the blue curve represents X-d–Y-d interactions.

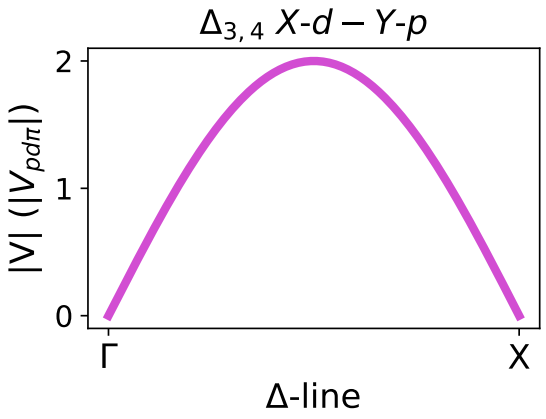

Figure 6.6: Magnitude of X-d-Z-p tight-binding hopping integral in the $\Delta_{3,4}$ bands in a generic half-Heusler compound.

of the avoided crossing [169]. Based on the $\Delta_{3,4}$ VB and CB COHP values (Figure 6.5), the Zr-d–Sn-p and Nb-d–Sb-p interactions both satisfy this condition. This X-d–Z-p interaction is nearly zero at Γ and at X, and it reaches a peak in strength halfway along the Γ − Δ−X line (bonding in the VB and anti-bonding in the CB). The shape of the X-d-Z-p interaction can also be reproduced using an analytical TB model describing a generic hH compound. The $\boldsymbol{k}$-dependent interaction strength, V_{pd}, for this interaction (quantified by the magnitude of the $\boldsymbol{k}$-dependent hopping integral coupling these two orbitals) in the $\Delta_{3,4}$ band is given by the Equation, $|V_{pd}| = 2|V_{pd\pi}\sin(\pi d)|$ (see Figure 6.6), where d varies from 0 at Γ to 1 at X, and $V_{pd\pi}$ is the π-bonding interaction between the d and p orbitals (see Appendix D for details on derivation).

While the avoided crossing between the $\Delta_{3,4}$ bands in ZrNiSn is between a predominantly X-d state that increases in energy from Γ to X and a predominantly Z-p state that decreases in energy from Γ to X, the explanation in NbFeSb is slightly different. In NbFeSb this avoided crossing is better described as one between the X-d state and a Y-d state. As seen in Figure 6.7, the Γ_{15} CB state in NbFeSb is comprised of mostly Fe-d states with a smaller contribution from the Sb-p states. This is the inverse of the case in ZrNiSn, where the Γ_{15} CB contains mostly Sn-p character with some Ni-d character. Moreover, while the highest X_5 VB state in ZrNiSn is described by mostly

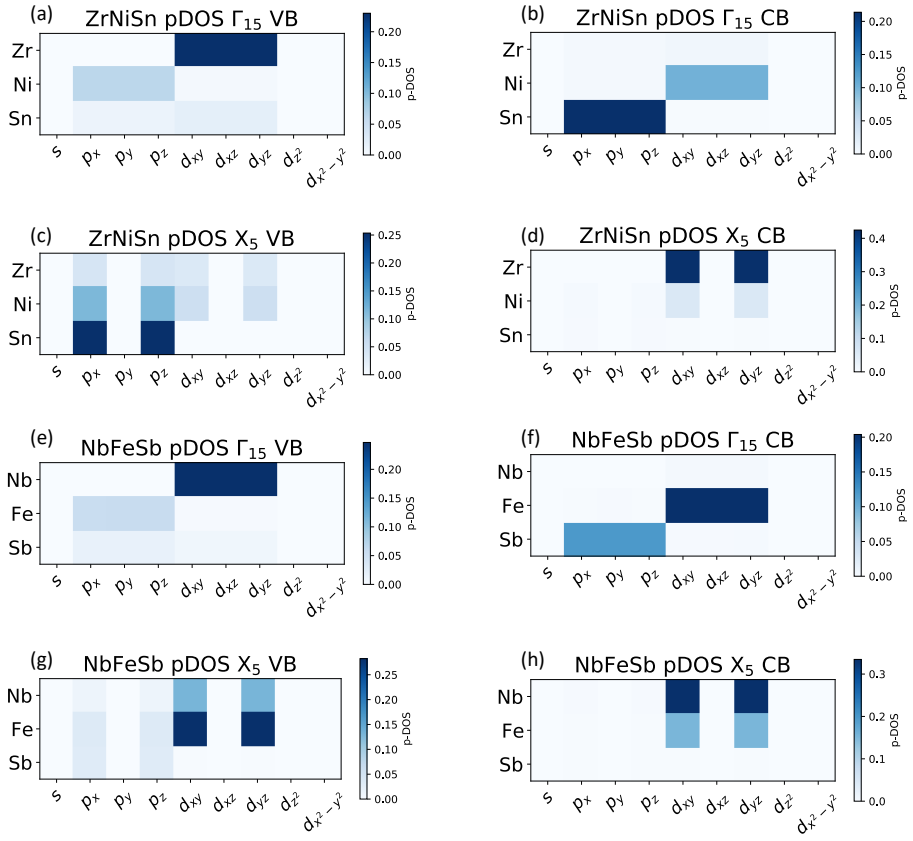

Figure 6.7: Heat maps representing the normalized band-resolved projected density of states (pDOS) of (a) the Γ_{15} valence band (VB), (b) the Γ_{15} conduction band (CB), (c) the X_5 VB, and (d) the X_5 CB in ZrNiSn and of (e) the Γ_{15} VB, (f) the Γ_{15} CB, (g) the X_5 VB, and (h) the X_5 CB in NbFeSb. For the Γ_{15} bands, the pDOS shown is the average of the three triply degenerate bands comprising that state, and for the X_5 bands it is the average of the two doubly degenerate bands. The orbital projections are normalized, such that the sum of the orbital projection for each band at each $\boldsymbol{k}$-point is equal to one.

Sn-*p* character with some Ni-*p* character, in NbFeSb, this state contains mostly Fe-*d* character with a smaller contribution of Nb-*d* orbitals (and even less Sb-*p* and Fe-*p*). This difference in orbital character is also reflected in the COHP values. The *X*-*d*–*Y*-*d* bonding interaction in the VB and the *Y*-*d*–*Z*-*p* and *X*-*d*–*Y*-*d* interactions in the CB are more dominant in NbFeSb than in ZrNiSn (Figure 6.5).

Therefore, the behavior of the $\Delta_{3,4}$ VB in NbFeSb can be better understood by studying the strength of the Nb-*d*–Fe-*d* interaction (Figure 6.5b). At the Γ point, this interaction is very weakly

anti-bonding and becomes more strongly bonding toward X. Overall, the strength increases from Γ toward X, but there is a peak in the strength about midway from Γ to X (closer to X). The bonding interaction decreases the energy of the Fe-*d* orbitals, so the fact that it is stronger at X than at Γ is consistent with Fe-*d* orbitals being found below the bandgap at X (Figure 6.7b) and above the bandgap at Γ (Figure 6.7g). We note that the bonding interaction between the Nb-*d* and Fe-*p* states is also present in the Γ_{15} VB edge, which further pushes the energy of the Nb-*d* states at Γ down relative to their energy at X. While the *X*-*d*–*Y*-*d* interaction is less dominant in ZrNiSn, the Zr-*d*–Ni-*d* interaction is also important for understanding the distribution of Zr-*d* states in ZrNiSn, as the increase in strength of this interaction from Γ to X further (in addition to the Zr-*d*–Ni-*p* interaction) explains the presence of Zr-*d* states in the CBs at X and in the VB edge at Γ. Finally, in contrast to ZrNiSn, the *Y*-*d*–*Z*-*p* interaction in NbFeSb increases the energy of the *Y*-*d*, rather than the *Z*-*p*, orbitals at Γ in NbFeSb. Therefore, the increasing strength of this interaction from X to Γ (Figure 6.5d) further explains the presence of Fe-*d* orbitals in the CB at Γ_{15} (Figure 6.7f) and in the VB at X_5 (Figure 6.7g).

This discrepancy between the orbital character of the highest X_5 VB between the two compounds is consistent with the energy of the Fe-*d* orbitals being greater than that of the Sb-*p* orbitals, while the Ni-*d* orbitals are lower relative to the Sn-*p* orbitals in ZrNiSn. This might be expected from the greater group number difference between *Y* and *Z* in NbFeSb compared to ZrNiSn. Consequently, the Sb-*p* states at X are located deeper into the VBs, and do not appear heavily in the highest X_5 VB, while the Fe-*d* states dominate instead. Furthermore, because Γ_{15} is an anti-bonding state between the *Y*-*d* and *Z*-*p* orbitals, it will have character most closely resembling the higher energy state, which is Sn-*p* in ZrNiSn and Fe-*d* in NbFeSb. In general, increasing the energy of the *Y*-*d* orbitals (decreasing the group number of *Y*) will favor the behavior seen in NbFeSb, while decreasing the energy of the *Y*-*d* orbitals (increasing group number of *Y*) would favor the behavior seen in ZrNiSn.

Qualitative bonding pictures at the Γ-point in ZrNiSn and NbFeSb are depicted in Figure 6.8

to illustrate some of their differences. We show the relevant bonding interactions in two steps: (1) the formation of the zinc blende $[YZ]^{n-}$ polyanion, and (2) the subsequent interactions between $[YZ]^{n-}$ and X^{n+} to form the hH XYZ structure. In both compounds the VB edge is depicted as a bonding state between the X-d state and a hybridized Y-p anti-bonding state. Moreover, we can see that because the relative energy of the Y-d orbitals is greater in NbFeSb, the t_2^* (Γ_{15}) CB state has more Y-d than Z-p character in NbFeSb but more Z-p than Y-d character than ZrNiSn.

6.2.3 Avoided Crossings along $\Gamma - \Lambda - \mathbf{L}$

The band gaps of hH thermoelectric compounds are established by avoided crossings that result in an 18-electron (valence-balanced) valence band. Therefore, in order to understand the origin and orbital character of the VB edges at Γ and L and whether the VBM is at Γ or L, we must study the avoided crossings along the Γ–L path. The symmetry labels for the relevant Γ, Λ, and L bands are given in Figure 6.9. Because the highest energy VB belongs to the Λ_3 symmetry representation, we look at how the states in this Λ_3 VB interact with other Λ_3 bands, specifically the Λ_3 CB and a lower Λ_3 VB (the second-highest Λ_3 VB). While there are multiple Λ_3 avoided crossings, we simplify the analysis to focus on the avoided crossing that directly yields the bandgap. In both ZrNiSn and NbFeSb, the Γ-point VB edge is dominated by the X-d_{t_2} orbitals (Figures 6.9a and c). As seen in Figure 6.9a and c, this X-d_{t_2} character can also be found at the L-point of the Λ_3 CB (in the L_3 band). Therefore, the X-d_{t_2} orbitals in Γ-point VB edge come from an "X-d_{t_2} band" that would run up in energy from Γ to L, like shown in Figure 6.2a (blue curve), if it were not for an avoided crossing. The $\boldsymbol{k}$-resolved, band-resolved COHP (Figure 6.10) explains why this "X-d_{t_2} band" would run up in energy from Γ to L. As seen in Figure 6.10b, in the highest Λ_3 VB (VB upper), there is a Zr-d_{t_2}–Ni-p bonding interaction that is strongest at Γ and decreases toward L. Moreover, as seen in Figure 6.10c, in the Λ_3 CB, there is Zr-d_{t_2}–Ni-d_{t_2} anti-bonding character that increases from Γ (where it is 0 because there is no d_{t2}-orbital character in Γ_{12}) to L. The former interaction pushes the Zr-d_{t_2} orbitals down in energy at Γ, such that they are found in the VB, while the latter

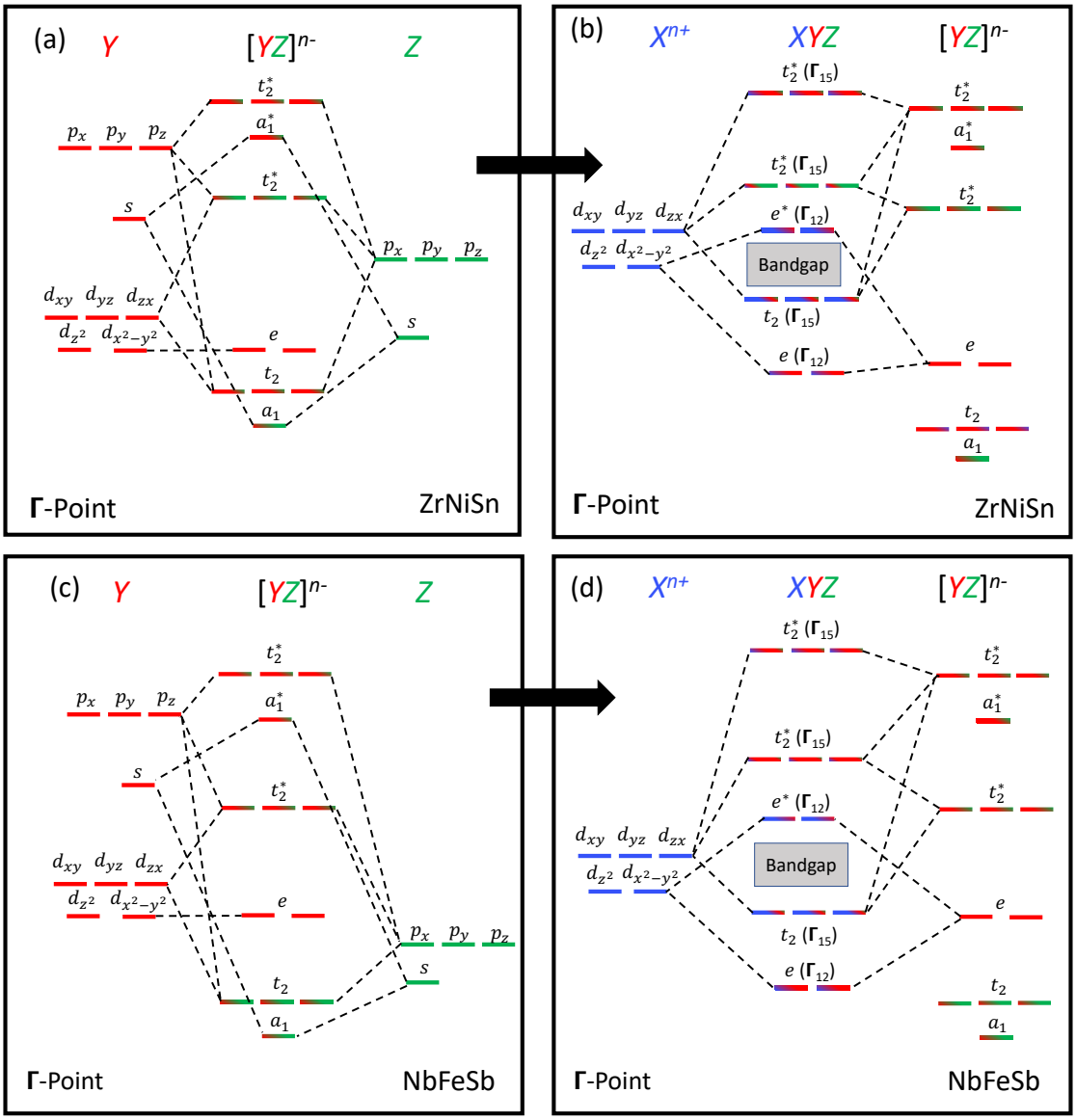

Figure 6.8: Qualitative sketches of the molecular orbital diagrams at the Γ-point representing (a,c) the formation of the $[YZ]^{n-}$ polyanion and (b,d) the formation of the XYZ half-Heusler (hH) structure from $[YZ]^{n-}$ and X^{n+}. The diagrams in (a)-(b) more closely resemble the bonding in ZrNiSn, and those in (c)-(d) most closely resemble NbFeSb. The symmetry representations of the molecular orbitals with respect to the T_d point group are shown, with the corresponding band symmetry labels shown in parentheses. The VB edge at Γ can be described as a bonding state between the triply degenerate X-d orbitals and a Z-p–Y-p anti-bonding state. The relative energies of the atomic and molecular orbitals will vary as the chemistry of the compound changes. Note that the energy scales in each of the four MO sketches are arbitrary.

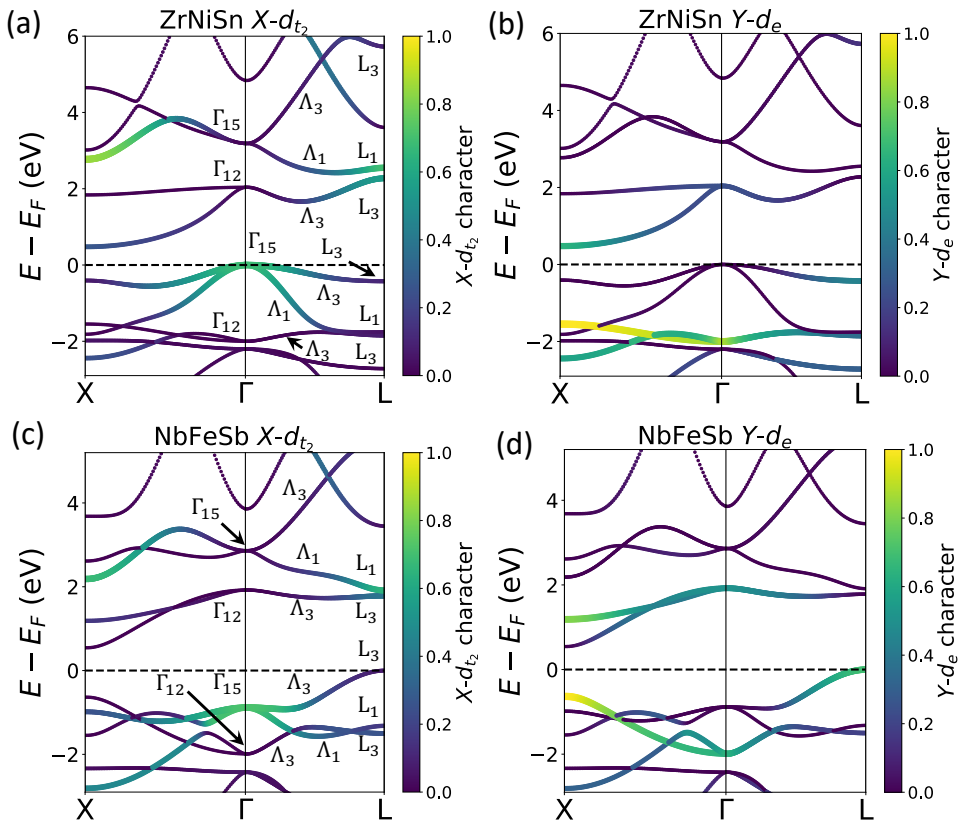

Figure 6.9: Electronic band structures calculated *via* DFT showing the normalized d-orbital contributions of each band at each $\boldsymbol{k}$-point. The thickness of the line represents the contribution from the designated orbitals, and the dashed horizontal line represents the Fermi energy and is at the VB edge for both compounds. We show the contributions of (a) the Zr-d_{t_2} orbitals in ZrNiSn, (b) the Ni-d_e orbitals in ZrNiSn, (c) the Nb-d_{t_2} orbitals in NbFeSb, and (d) the Fe-d_e orbitals in NbFeSb. Symmetry representation labels for various $\Gamma - \Lambda - \mathrm{L}$ bands are shown in (a) and (c) for reference.

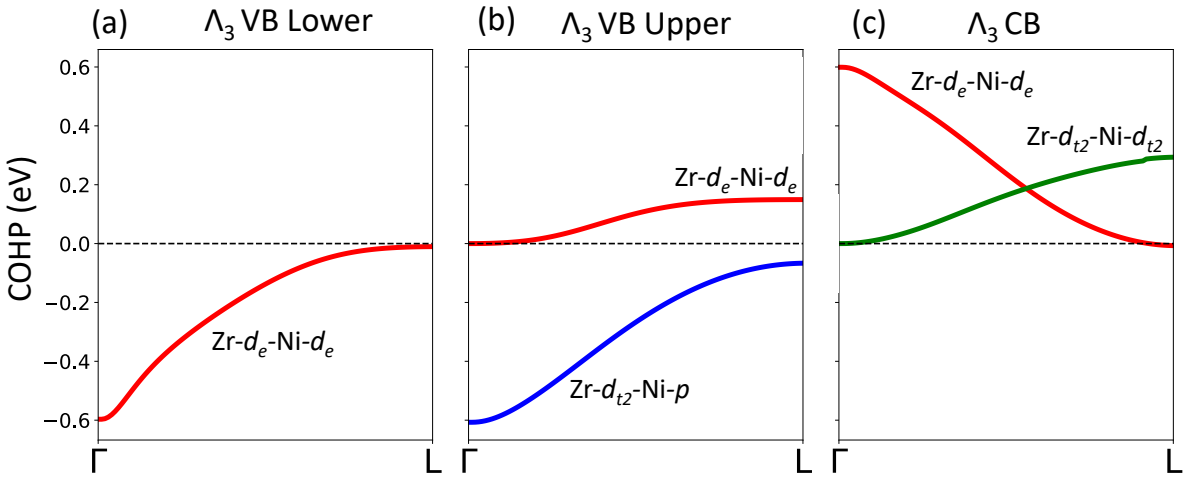

Figure 6.10: ***k***-point-resolved, band-resolved projected COHP values for various interactions in ZrNiSn in (a) the second-highest Λ_3 VB (VB lower), (b) the highest Λ_3 VB (VB upper), and (c) the Λ_3 CB. Negative COHP values correspond to bonding character, while positive COHP values indicate anti-bonding character.

interaction pushes the Zr-d_{t_2} orbitals up in energy at L such that they are found in the CB.

Therefore, in order for there to be a bandgap along the Λ path, there must be an avoided crossing between this "X-d_{t_2} band" and another band that would run down in energy from Γ to L if there were no avoided crossing (red curve in Figure 6.2a). In this case, we can consider an "X-d_e–Y-d_e band" that would run down in energy from Γ to L, starting in the Λ_3 CB. This band would run down from Γ toward L because of X-d_e–Y-d_e anti-bonding interactions that are strongest at Γ and decrease in strength toward L (see Figures 6.10b,c). Because the "X-d_{t_2} band" and "X-d_e–Y-d_e band" belong to the same symmetry representation, Λ_3, they will interact (via X-d_{t_2}–X-d_e, X-d_{t_2}–Y-d_e, etc. interactions) and undergo an avoided crossing like that shown in Figure 6.2b to open up the bandgap.

In both ZrNiSn and NbFeSb, the L-point VBM is dominated by Y-d_e character, which cannot be explained directly from the avoided crossing depicted in Figure 6.2. As seen in Figures 6.9b-d, the Y-d_e orbitals dominate at the Γ-point of the lower Λ_3 VB (the second-highest Λ_3 VB). Therefore, the origin of the Y-d_e states at the L-point VB edge can be explained by a Y-d_e state that would run up in energy from Γ to L if there were no avoided crossings. Again, the ***k***-resolved, band-resolved

COHP explains why this Y-d_e state increases in energy from Γ and ends at the L-point VB edge. As seen in Figure 6.10a, there is a strong Zr-d_e–Ni-d_e bonding interaction in the lower Λ_3 VB that pushes the energy of the Ni-d_e orbitals down in energy. This interaction is strongest at Γ, which is why the energy of this state is lowest at Γ. Clearly, this Y-d_e state does not form a continuous VB in the actual band structure, so there is an avoided crossing between this "Y-d_e band" (that would exist if there were no avoided crossing) and another Λ_3 state that would run down in energy from Γ to L.

6.3 Chemical Origins of X-Point Conduction Bands

For high-performing n-type hH thermoelectrics, it may be beneficial to engineer high valley degeneracy in the CB edge by converging the two competing CBMs at the X-point, such that $N_{V_o} = 2$. The X-point in hH compounds has D_{2d} point group symmetry, and the two competing CBMs in typical hH thermoelectrics have distinct symmetry representations within this point group, either X_2 (NbFeSb) or X_3 (ZrNiSn) [68]. Similar CB behavior is observed in Mg_2Si-Mg_2Sn solid solutions, which also have two competing CBMs at the X-point, and it is found that peak thermoelectric performance is obtained in the solid solution where the two CBs are converged [42, 43]. In the thermoelectric hH compounds studied here, the X_2 band contains entirely X-d character, while the X_3 band has predominantly Y-d character hybridized with X-d and some Z-p character (see Figures 6.3 and 6.11[2]) Furthermore, as discussed in Ref. 68 the X_2 state is expected to be non-bonding, as there are no other available X_2 states from the Y- or Z-species (see Table D.15). On the other hand, X-d_{xy}, Y-d_{z^2}, and Z-p_z all transform like the X_3 representation of the D_{2d} point group, and therefore interact with each other, such that the X_3 CBM is predicted to have anti-bonding character [68].

[2]Note that the heat map in Figure 6.11 is from DFT calculations that define X to be at X = $2\pi(0, 1, 0)$, while the group symmetry analysis is conducted assuming that X = $2\pi(0, 0, 1)$. As a result, the orbital basis must simply rotated, such that $z \rightarrow y$ when going from the group theory analysis to the DFT heat map plots. However, the d_e orbitals always map back onto d_e orbitals and d_{t2} orbitals always back mack onto other d_{t2} orbitals.

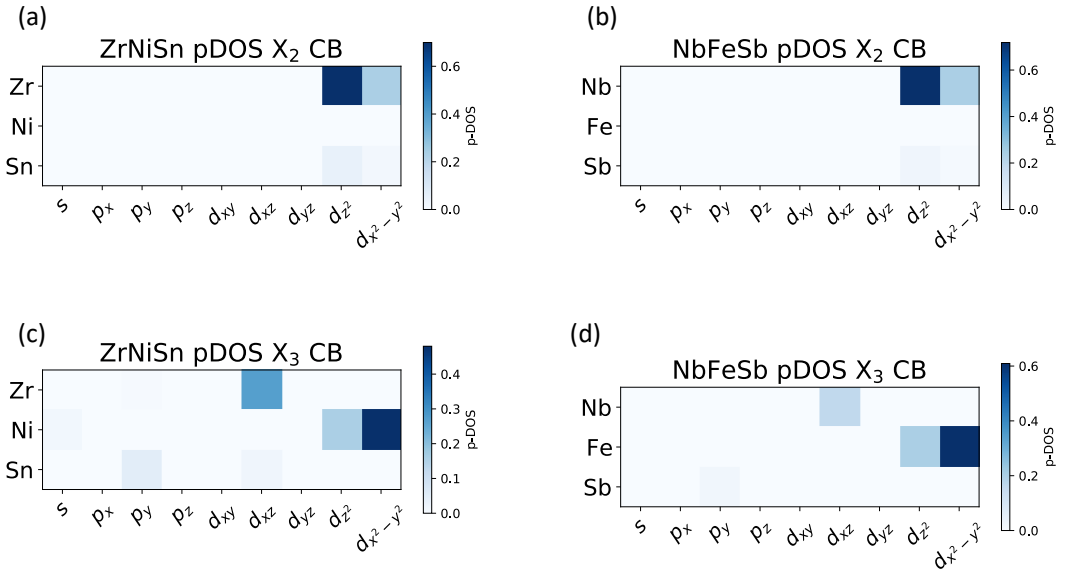

Figure 6.11: Heat maps showing normalized projected density of states (p-DOS) for the X_2 CB in (a) ZrNiSn and (b) NbFeSb and for the X_3 CBs in (c) ZrNiSn and in (d) NbFeSb.

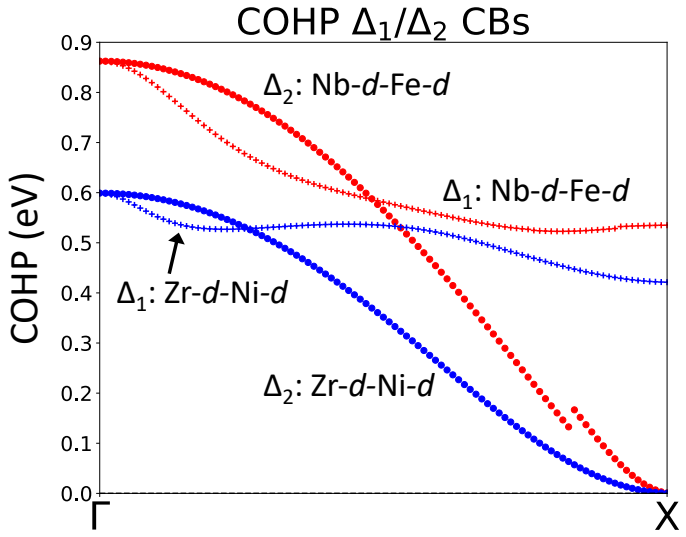

Figure 6.12: ***k***-resolved, band-resolved COHP values for the X-d–Y-d interactions in the $\Gamma_{12}-\Delta_1-X_3$ and $\Gamma_{12}-\Delta_2-X_2$ bands in ZrNiSn and NbFeSb. The red lines correspond to the Nb-d–Fe-d interaction in NbFeSb, and the blue lines correspond to the Zr-d–Ni-d interactions in ZrNiSn. The filled circles denote the Δ_2 band, while the plus (+) symbols represent the Δ_1 band. At Γ, both of the Γ_{12} states are anti-bonding, and at X, the X_3 state is anti-bonding, while the X_2 state is non-bonding.

The COHP values for the $\Gamma_{12}-\Delta_2-X_2$ and the $\Gamma_{12}-\Delta_1-X_3$ bands (Figure 6.12) are consistent with these group theoretical predictions of the bonding character of the competing CBMs, and they also give insight into why the CBM is located at the X-point rather than at the Γ-point. In the Δ_2 band the X-d–Y-d interaction is anti-bonding in the Γ_{12} band and decreases in magnitude along the Δ_2 band to zero in the X_2 band. As a result, the X_2 CB is completely non-bonding, and the Δ_2 CB decreases in energy from Γ to X. Moreover, the COHP values show that the Δ_1 CB is an X-d–Y-d anti-bonding state along the entire band, including the X-point (X_3 band). The anti-bonding character in the Δ_1 CB is stronger at Γ than at X, leading to the Δ_1 CB running down from Γ to X.

The analytical TB model of the generic hH compound can also explain the COHP behavior, and hence, band behavior of the low-lying conduction bands from Γ to X (see Appendix D for more details). In both the Δ_1 and Δ_2 bands, X-d_e–Y-d_e interactions are present, and in the TB model, the strength of the hopping integral in both bands is given by the expression $|V_{dd}| = \frac{8}{3}|V_{pp\pi}\cos(\pi d/2)|$

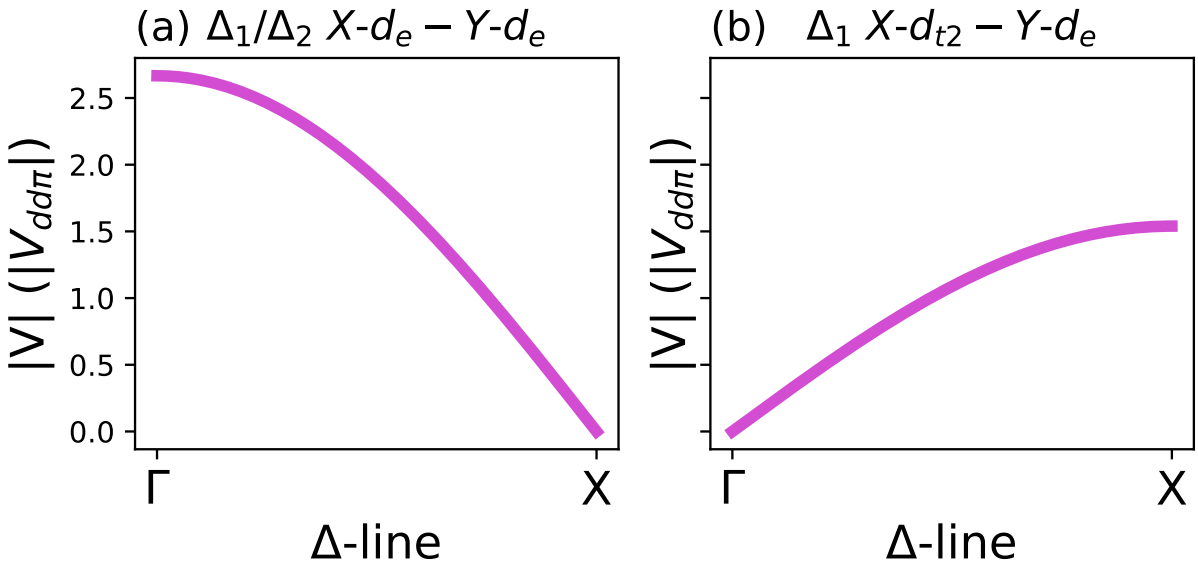

Figure 6.13: Magnitude of tight-binding (TB) hopping integrals $|V|$ for (a) the X-d_e–Y-d_e interactions in the Δ_1 and Δ_2 bands and (b) the X-d_{t2}–Y-d_e interaction in the Δ_1 band.

(Figure 6.13a). Thus, according to TB, this d_e-d_e interaction, which is anti-bonding in the low-lying CBs, reaches a maximum strength at Γ and decreases to zero strength at X. Moreover, in the Δ_1 band, but not the Δ_2 band, there is a d_e–d_{t2} interaction, which is anti-bonding in the Δ_1 CB, given by the TB hopping integral, $|V_{dd}| = \frac{8\sqrt{3}}{9}|V_{dd\pi}\sin(\pi d/2)|$ (Figure 6.13b). Therefore, the strength of this interaction reaches a maximum at X and decreases to zero at Γ, but because the maximum strength of this interaction is weaker than the maximum strength of the d_e-d_e interaction, the overall interaction strength decrease from Γ to X in the Δ_1 band. However, unlike the Δ_2 band, the Δ_1 band does not become non-bonding at X.

While looking at only the X-d–Y-d interactions is sufficient to understand why the CBM is at X, in order to understand the orbital character and relative energies of the competing CBMs, a more detailed approach is required. That is, these interactions do not explain the discontinuity of character between Γ_{12} and X_3 (connected by Δ_1), the dominance of Y-d (Y-d_{z^2}) over X-d (X-d_{xy}) orbitals in X_3, or why, as an anti-bonding state between X-d and Y-d, the X_3 band is not always higher in energy than the non-bonding X_2 band. The discontinuity in the Δ_1 CB is due to avoided

Table 6.1: COHP values (***k***-point and band resolved) for select bands at the X-point in ZrNiSn and NbFeSb. Positive values of COHP indicate anti-bonding interactions, and negative COHP values indicate bonding interactions.

Interaction	Band	ZrNiSn COHP (eV)	NbFeSb COHP (eV)
Y-d_{z^2}–Z-p_z	X_3^{CB}	0.34	0.36
X-d_{xy}–Y-d_{z^2}	X_3^{CB}	0.42	0.54
X-d_{xy}–Y-s	X_3^{VB}	-0.83	-0.73

crossings with other Δ_1 states. Again, we use ***k***-resolved, band-resolved COHP calculations (see Table 6.1) to formulate a qualitative molecular orbital picture (see Figure 6.14) that is consistent with observations in the CB structures. For instance, in addition to the X_3 CB (denoted X_3^{CB} in Table 6.1) having Y-d_{z^2}–X-d_{xy} anti-bonding character, it also exhibits Y-d_{z^2}–Z-p_z anti-bonding character (Figure 6.14a). The Y-d_{z^2}–Z-p_z interaction explains why the Y-d_{z^2} states are pushed up to be near the CB edge rather than in the VB. Additionally, there is a bonding interaction between the X-d_{xy} and Y-s states that pushes the X-d_{xy} states lower into the VB (found in X_3^{VB}, the X_3 band that is located between -2 eV and -3 eV below the VB edge) rather than near the CB edge (Figure 6.14b-c). This bonding character is apparent in the strongly negative COHP value corresponding to this interaction in the X_3^{VB} band (Table 6.1). Note that all of the interactions listed in Table 6.1 for the X-point are symmetry-forbidden at the Γ-point. The TB hopping integrals corresponding to these interactions along the Δ path are described in Appendix D for interested readers (see Table D.19).

The qualitative molecular orbital sketch depicted in Figure 6.14 also explains why compounds like NbFeSb have the X_2 CBM and why compounds like ZrNiSn have the X_3 CBM. When the relative energy difference between the X-d and Y-d orbitals is greater (e.g. ZrNiSn), the anti-bonding b_2^* (X_3) state from Figure 6.14a is lower in energy than the non-bonding X-$d_{x^2-y^2}$ (X_2) state, resulting in the X_3 CBM (Figure 6.14b). On the other hand, when the energy difference between X-d and Y-d is smaller (e.g. NbFeSb), the anti-bonding X_3 from Figure 6.14a is greater in energy than the non-bonding X_2 state, yielding the X_2, X-d dominated CBM (Figure 6.14c). It is then evident how tuning the relative energies of the X-d and Y-d orbitals is an effective method to converge

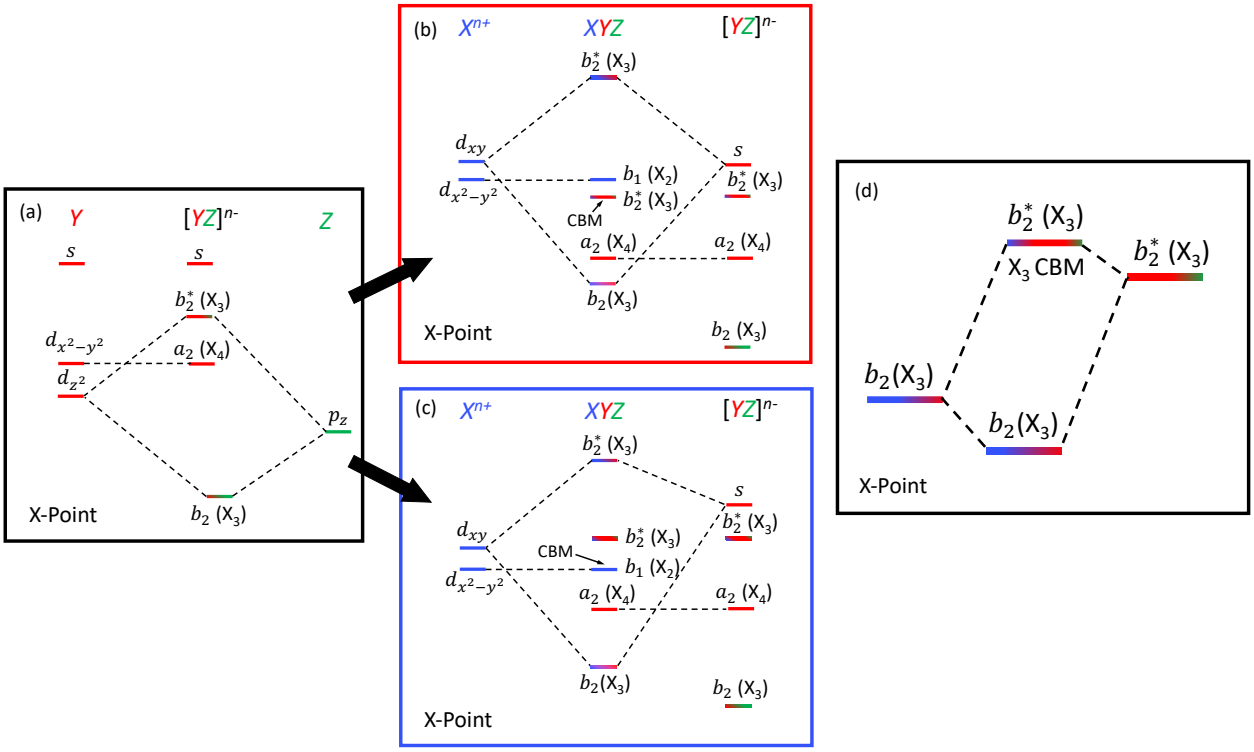

Figure 6.14: Qualitative sketch of molecular orbital diagrams at the X-point that explain the character and relative energies of the competing X_2 and X_3 CBMs. (a) The Y-d_{z^2} orbitals interact with the Z-p_z orbitals to form a bonding and anti-bonding state, while the Y-$d_{x^2-y^2}$ orbitals are non-bonding. (b)-(c) The X-d_{xy} orbitals interact with the Y-s orbitals to form a bonding and anti-bonding state below and above the two competing CBMs, respectively. (b) When there is a greater difference between the relative energies of the X-d and Y-d orbitals, the anti-bonding X_3 state from (a) is the CBM. (c) When there is a smaller difference (NbFeSb) between the relative energies of the X-d and Y-d orbitals, the non-bonding X-$d_{x^2-y^2}$ state (X_2) is the CBM. (d) The X_3 anti-bonding state (from Y-d–Z-p interaction) in (a) interacts with the X_3 bonding states (from X-d–Y-d interaction) from (b) and (c), such that the X_3 CBM has X-d–Y-d anti-bonding character.

the two competing CBMs. Increasing the difference in the energies of the X-d and Y-d orbitals (assuming that the hopping integral/parameter, V, for the X-d–Y-d and Y-d–Z-p interactions is not substantially altered) results in the energy of the X_2 (non-bonding) CB increasing relative to the X_3 (anti-bonding) CB, which leads to an X_3 CBM.

6.4 Chemical Origins of W-Point VBM

Because the W-point has a high valley degeneracy of $N_{V_k} = 6$, understanding how to engineer hH compounds and alloys with contributions from the W-point VBM can allow for the discovery of even better p-type hH thermoelectrics [203]. Although Dylla *et al.* identify only one material that has a distinct (not effectively converged) global VBM at the W-point (NbRhSn), six other compounds where the W-point and L-point are converged within 100 meV are identified. All seven of these W-pocket materials have a group-IV element (Ge, Sn, Pb) occupying the Z-site and a group IX element (Co, Rh, Ir) occupying the Y-site. [182]. As discussed in Ref. 182, the orbital composition of the W-point VBM is typically characterized by a larger Z-p contribution relative to the L- and Γ-point VBMs. That is, as seen in Figure 6.15, while the L- and W- points of the highest VB are both comprised of largely Y-d_e orbital character, there is greater contribution from the Z-p orbitals at W. This suggests that Y-d–Z-p interactions are important for understanding convergence between the L- and W- point VB pockets.

We compare the orbital contributions and COHP values of two W-pocket materials (NbRhSn and NbCoSn) with NbFeSb and ZrNiSn to better understand the origin of the W-pocket. In NbCoSn, the L and W VBMs are effectively converged, while in NbRhSn, the W-point VBM is more prominent. The importance of the Y-d–Z-p interaction is highlighted in the convergence trends plotted in Figure 6.16a-b. As seen in Figure 6.16a, there is a clear correlation between the difference in energy of the W- and L-point VB pockets and the difference in Z-p orbital character between the W- and L-points – as the difference in % Z-p character increases, the relative energy of the W-point VBM increases relative to the L-point VBM. Furthermore, as seen in Figure 6.16b, there is

Table 6.2: COHP values corresponding to the Y-d–Z-p interaction at the L and W VBMs and the energy difference between the L and W VBMs for four different hH compounds.

Compound	COHP (eV) at W	COHP (eV) at L	COHP (eV) (W-L)	E_{VBM}(L) − E_{VBM}(W) (eV)
ZrNiSn	0.52	0.34	0.18	0.08
NbFeSb	0.43	0.24	0.19	0.37
NbRhSn	0.68	0.29	0.39	-0.15
NbCoSn	0.58	0.25	0.33	-0.02

a trend between the difference in the Pauling electronegativity [3, 6] of the Z- and Y- sites and the difference in energy between the two VBMs. As the electronegativity difference increases, the energy of the L-point VBM increases relative to the W-point VBM. NbRhSn represents an extreme case where the Pauling electronegativity of the Z-site species is less than the that of the Y-site species, which explains why it has a distinct W-point VBM. The COHP values describing to the Y-d–Z-p interaction also highlight the importance of this interaction in the emergence of the W-point VBM (see Table 6.2). The compounds that contain W-point VB pockets near the Fermi energy (NbCoSn and NbRhSn) both have stronger relative COHP values at the W-point.

The W- and L-point VBMs begin emerging concurrently (with respect to the Γ-point VBM) because they are both dominated by Y-d_e orbital character. That is, when the energy of the Y-d states relative to the X-d states is high enough for the L VBM to approach and exceed the energy of the Γ VBM, the energy of the W-point VB pocket can also begin to approach the VB edge. In fact, based on the sixteen hH DFT calculations presented in this work, the trend relating the group number difference between the Y- and X- sites and the energy offset between the Γ- and W-point VBMs closely resembles the trend describing the offsets between the Γ and L VB pockets (see Figure 6.16c). Both the L- and W-point VB pockets begin emerging when the $Y - X$ group number difference is four or five.

Thus, we can also explain why all of the W-pocket compounds identified in Ref. 182 contain *both* a Y-site species from group IX and a Z-site species from group IV. Because a group number difference (Y-X) of four to five marks the point at which the L- and W-point VBMs emerge with

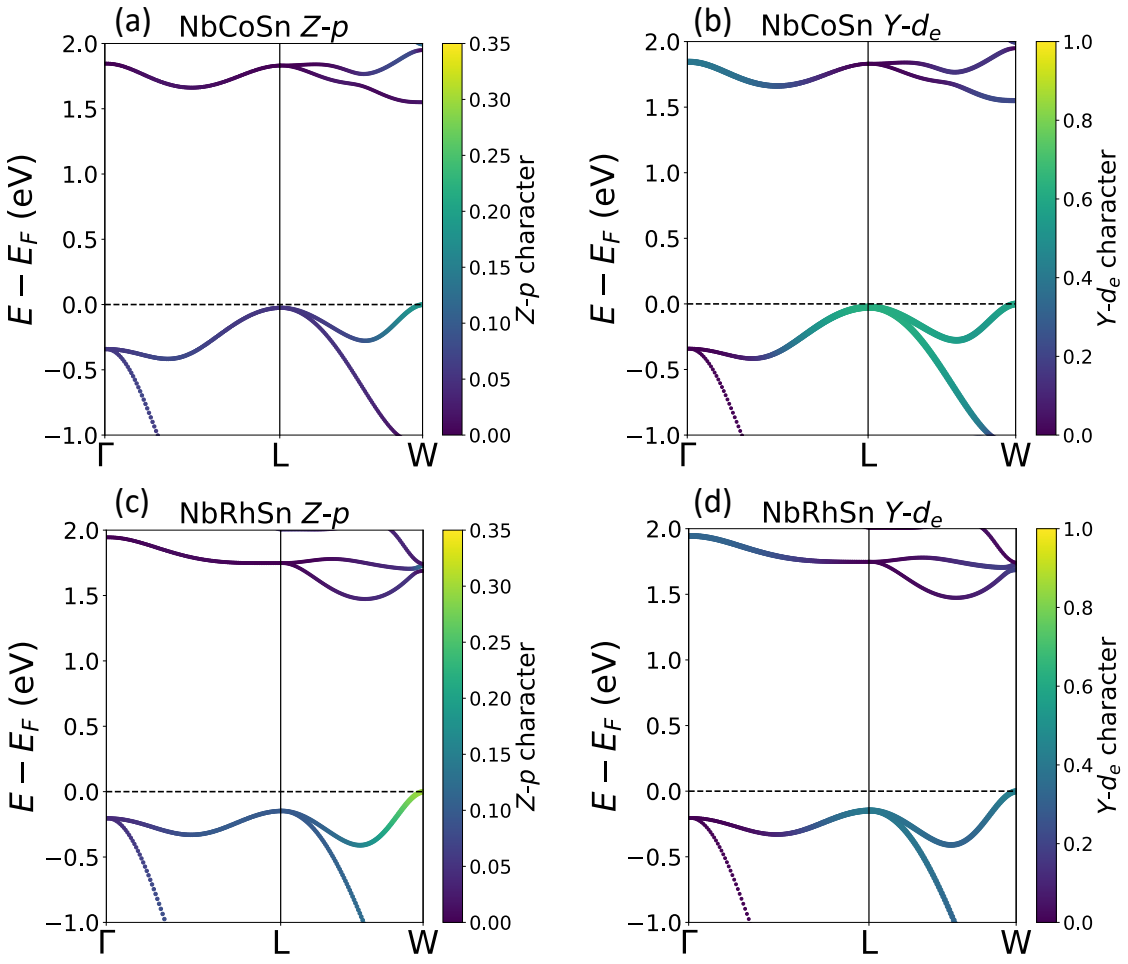

Figure 6.15: Electronic band structures calculated *via* DFT for two hH compounds, NbRhSn and NbCoSn, with VBMs at the W-point. The color and line thickness represents the normalized contribution of the (a) Sn-p orbitals in NbCoSn, (b) Co-d_e orbitals in NbCoSn, (c) Sn-p orbitals in NhRhSn, and (d) Rh-d_e orbitals in NbRhSn.

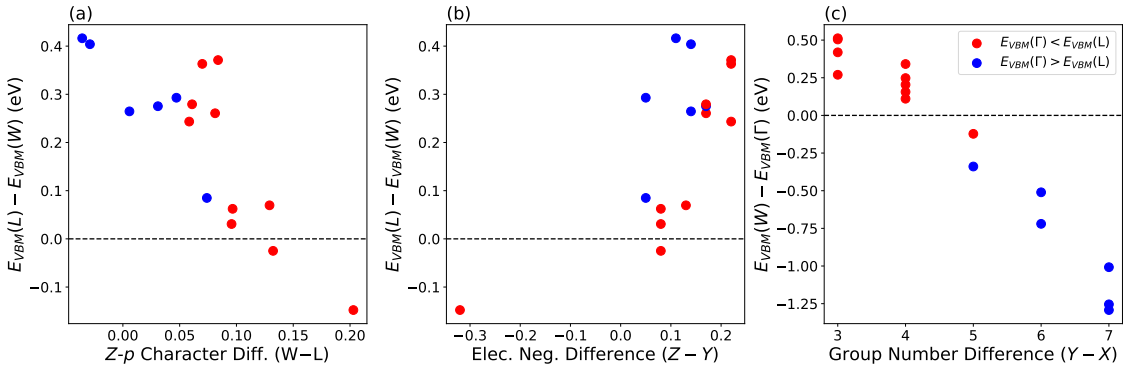

Figure 6.16: (a) Scatter plot showing how the energy difference between the L and W VBMs (E_{VBM}(L) − E_{VBM}(W)) varies with the difference in the normalized Z-p orbital contribution between the L and W valence band edges. (b) Plot showing E_{VBM}(L) − E_{VBM}(W) versus the Pauling electronegativity difference between the Y- and Z-site species [3]. (c) Plot of $E_{VBM}(W) - E_{VBM}(\Gamma)$ versus the difference in group number between Y and X. The blue points correspond to compounds that have a VBM at the Γ-point, and the red points correspond to compounds that have a VBM at the L- or W-points.

respect to the Γ-point VB edge [182], when the group number difference is five or higher, the Γ-point VBM is favored, and when the group number difference is four or less, the L and W VBMs are favored. Given that hH semiconductors must have a valence electron count of 18, the restriction of having a group number difference between X and Y of three or four effectively limits the hH candidates to those containing Y-site elements from groups VIII (Fe, Ru, Os) or IX (Co, Rh, Ir) and Z-site elements from group IV (Ge, Sn, Pb) or group V (As, Sb, Bi). Of these possible Y/Z combinations, the one that favors the lowest electronegativity difference between the Y- and Z-sites (to increase the energy W-point VB pocket relative to that of the L-point VB pocket) is a group-IX Y-site and group-IV Z-site.

6.5 Tuning Band Edge Energies via Alloying

Assuming that the electronic band structures of substitutional alloys can be approximated as linear interpolations of the end-member band structures, [32, 33, 42, 182, 188, 206, 207] the chemistry and electronic structures of the end-member cases can be used as starting points to develop and understand alloying strategies for high valley degeneracy. In fact, Guo *et. al* show that this concept

works in hH compounds [188]. Therefore, understanding the trends in the band-edge energies of end-member compounds can help us understand/predict alloy behavior in terms of band degeneracy.

The origin of the VB convergence trends of end-member compounds (non-alloys) outlined in Ref. 182 and of the CB convergence trends discussed in Ref. 188 can be understood through the simple TB model of a diatomic molecule. It can be shown that increasing the on-site energy of either atomic orbital state (E_1 or E_2) will result in the increase of both the bonding and anti-bonding energy levels determined by Equation 6.1. Furthermore, it can be shown that the increase is greater for the molecular orbital state that is closer in energy to the on-site energy that was changed [153]. That is, modifying the on-site energy of the higher-energy atomic orbital has a greater impact on the anti-bonding state, and moving the on-site energy of the lower-energy atomic orbital has a greater impact on the bonding state. Therefore, the Γ-point VBM and X_2 CBM, which have mostly X-d character are most sensitive to the on-site energy of the X-d orbitals, and the L-point VBM and X_3 CBM which have mostly Y-d character, are most sensitive to the energy of the Y-d orbitals. In general, as the group number of the X/Y species increases, the on-site energy decreases [63], so increasing the group number difference between X and Y increases the relative energy of the X-d orbitals relative to the Y-d orbitals, which raises the relative energy of the Γ-point VB edge relative to the L-point VB edge and the energy of the X_2 CB relative to that of the X_3 CB. There is also a secondary effect from Pauling electronegativity [182, 188], as the electronegativity of an element correlates to the on-site energy of its orbitals (and the group number).

It is important to note that the aforementioned relationship between the orbital energies and molecular orbital energies assumes that the strength of the hopping parameter/integral, V, is not altered (upon the chemical substitution) in such a way that it counteracts the effect of the atomic orbital energy changes. The magnitude of the hopping parameter (interatomic matrix element) depends on the interatomic distance, which can be be tuned through physical and chemical manipulations. The strength of V scales inversely with the interatomic distance which can be modified via strain, temperature or alloying. Moreover, the interatomic matrix elements for d-orbitals in

transition-metal-based compounds (describing the interactions between two d-orbitals or between d-orbitals and s- or p- orbitals) increases with a value known as the d-state radius [63]. Because substitutions that alter the atomic energies generally have at least some affect on the strength of the interatomic matrix element, we may see cases where behavior deviates from what is expected based only tuning the on-site energy terms.

Aliovalent alloying (substitutions) on the X- and Y- sites that change the *average* group number difference can be used to consistently tune the convergence of the L and Γ VB edges [182] and of the competing X_2 and X_3 CBMs [188], but the predicted effect of isovalent substitutions on the X and Y sites (based on end-member compounds) is generally less straightforward with regards to the energy of the X-d and Y-d atomic orbitals. Based solely on the atomic orbital energies, we would expect isoelectronic substitutions that increase the electronegativity of X or decrease the electronegativity of Y to increase the energy of the L VB edge relative to that of the Γ VB edge and to increase the energy of the X_3 CB relative to the energy of the X_2 CB. However, there are instances where these trends do not hold, possibly because of changes in the hopping parameters (interatomic matrix elements), V, that counteract the expected modifications in the band structure. In fact, this is a possible reason why the group number is a stronger predictor than the Pauling electronegativity [182, 188, 208].

Specifically, there are cases where isoelectronic substitutions on the Y-site with more electronegative species increase the energy of the X_3 band relative to the X_2 band and where isoelectronic substitutions on the X-site with more electronegative species increase the energy of the Γ VB relative to the L VB. For instance, the value of $E(X_3) - E(X_2)$ is greater in NbRhSn than in NbCoSn, despite the Pauling electronegativity of Rh being greater than that of Co. This behavior may be attributed to the fact that the d-state radius in Rh is greater than in Co [63], so the anti-bonding Y-d–Z-p and X-d–Y-d interactions, which increase the energy of the X_3 band, are stronger. Additionally, the value of $E_{VBM}(L) - E_{VBM}(\Gamma)$ is greater in NbCoSn than in VCoSn, which is the opposite of what is expected based on the electronegativity of X. A possible explanation is greater

overlap between the Nb-d orbitals and the Co-p orbitals compared to the overlap between the V-d and Co-p orbitals (Nb-d has a greater d-state radius), which pushes the energy of the Γ VB down in energy more in NbCoSn than in VCoSn. That being said, despite some exceptions, the overall trend still holds that as the electronegativity difference between X and Y increases, the Γ VB increases relative to the L VB and the X_2 CB increases relative to the X_3 CB [135, 182, 208].

Because the strategies for CB and VB convergence require similar chemical manipulations, especially in terms of the group number differences, we expect the relative energies of the competing VBMs (at Γ and L) and competing CBMs to be correlated. In fact, as seen in Figure 6.17, $E_{VBM}(\Gamma) - E_{VBM}(\mathrm{L})$ decreases with increasing $E(\mathrm{X_3}) - E(\mathrm{X_2})$ based on a sample of sixteen DFT calculations of hH electronic structures.[3] We observe that hH compounds with $E_{VBM}(\mathrm{L}) < E_{VBM}(\Gamma)$ tend to possess the X_3 (Y-d) CBM, while compounds with $E_{VBM}(\mathrm{L}) > E_{VBM}(\Gamma)$ tend to have the X_2 (X-d) CBM. We also note that the W-pocket materials appear when $E(X_3) - E(X_2)$ is greater than -0.5 eV, suggesting that compounds where the CBMs are near convergence or where the X_2 CB is lower are more likely to have the W-pocket bear the VB edge (e.g., NbCoSn).

The strategy for enhancing VB degeneracy through the introduction of W-pockets near the band edge requires tuning the chemistry of all three sites. The strategy for achieving convergence between the W and Γ VBMs is analogous to that for achieving convergence between the L and Γ VBMs due to the similar chemistry of the VB edge at L and W (both dominated by Y-d orbitals). That is, the energy of the W-pocket relative to that of the Γ-pocket can be increased by reducing the difference in group number (or electronegativity) between the X- and Y-sites, which then concurrently raises energy of the L-pocket relative to the Γ-pocket. However, because the W-point has a stronger dependence on Y-d–Z-p bonding than the L-point does, it is necessary to tune the electronegativity difference between the Y and Z sites to converge the L- and W- pockets. Increasing the energy of the Z-p orbitals relative to that of the Y-d orbitals would increase the energy of the W VBM relative to that of the L VBM. In practice, this can be achieved via substitutions on the Y- and/or Z-sites that reduce the electronegativity difference between Y and Z. We note that it may also be

[3] This same trend is reported in a larger sample size in Ref. 208.

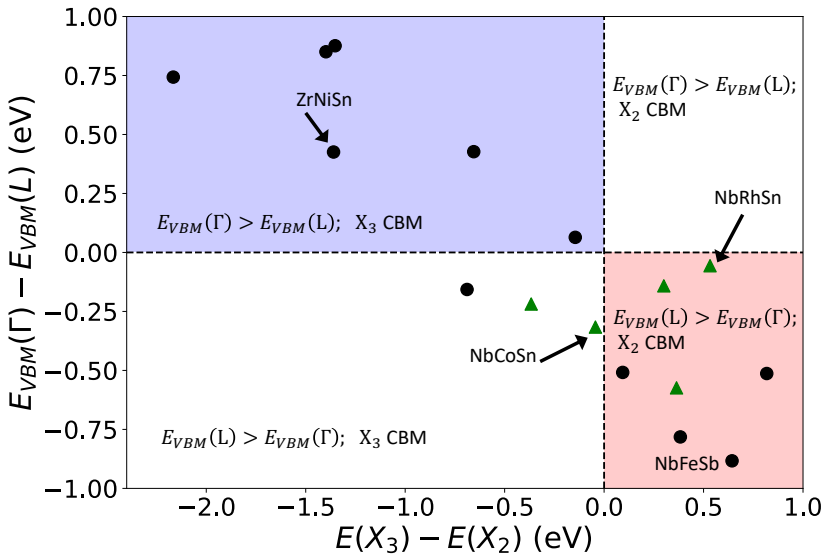

Figure 6.17: Plot of $E_{VBM}(\Gamma) - E_{VBM}(\mathrm{L})$ versus $E(X_3) - E(X_2)$ (calculated from DFT-PBE) for sixteen different half-Heusler compounds. Four different quadrants are defined according to the $E_{VBM}(\Gamma) - E_{VBM}(\mathrm{L}) = 0$ and $E(\mathrm{X_3}) - E(\mathrm{X_2}) = 0$. $E_{VBM}(\Gamma) - E_{VBM}(\mathrm{L})$ generally decreases with $E(X_3) - E(X_2)$. The blue region is comprised of compounds where the X-d orbitals dominate the higher energy VB (Γ) and the higher energy CB ($\mathrm{X_2}$), and the red region is comprised of compounds where the Y-d orbitals dominate the higher energy VB (L) and the higher energy CB ($\mathrm{X_3}$). Materials with W-pockets at or near (within 100 meV of) the VB edge are denoted with green triangles.

important to consider how the hopping parameter, V, may change upon substitutions.

6.6 Computational Methods

The first-principles DFT calculations were performed using the Vienna ab initio Simulation Package (VASP) and employing projector augmented wave (PAW) pseudopotentials and the PBE exchange-correlation functional. [48–51, 87, 88]. Spin-orbit coupling effects were not included in the electronic structure calculations. A plane-wave cutoff energy of 500 eV was used for each calculation. The structural degrees of freedom were relaxed using a Γ-centered [89] $\boldsymbol{k}$-point mesh of size $11 \times 11 \times 11$, until the forces on the atoms was less than 0.01 eV/nm. The electronic structure calculations were performed using a Γ-centered $\boldsymbol{k}$-point mesh of size $15 \times 15 \times 15$. The $\boldsymbol{k}$-vector resolved COHP calculations were performed using the version 4.0.0 of the LOBSTER software. [52–54, 150, 209]

6.7 Conclusions

Band engineering to achieve high valley degeneracy is a promising method for achieving high thermoelectric performance in both n-type and p-type half-Heusler thermoelectrics. Though there are dozens of hH thermoelectric candidates, they can be classified into three categories based on the location of the VBM (L, Γ, and W) and two categories based on the nature of the X-point CBM (X_2 or X_3). Consequently, there are routes to improve the performance of both the n- and p-type compounds by increasing N_V. For the p-type materials, this can be accomplished by engineering materials with low symmetry VBMs (W or L) and/or by converging multiple VB pockets. Likewise, the CB degeneracy, and hence, n-type performance, can be enhanced by converging the competing X-d-dominated and Y-d-dominated CBs at the X-point.

In prior studies, high-throughput DFT studies have shown that the competing VBMs (at L and Γ) and competing CBMs can be converged by simply adjusting the chemistry of the X- and Y-sites. The key to understanding the origin of these chemical trends is observing that the Γ_{15} VB

edge and the X_2 CB consists of mostly X-d character, while the L_3 VB edge and X_3 CB have mostly Y-d orbital character. Therefore, substitutions on the X- and Y-sites that decrease the (average) difference in group number between X and Y increase the energy of the L VBM relative to the Γ VBM and increase the energy of the X_3 CB relative to the X_2 CB, giving the basis for potential alloying strategies. While previous bonding descriptions have failed to explain the origin of these trends, in this work, we use avoided crossings and molecular orbital pictures informed by group theory and COHP calculations to explain the origin, orbital character, and relative energy of these transport edges, using ZrNiSn and NbFeSb as example cases.

Finally, we investigate the origin of the W-point VB edge and describe techniques to move this high degeneracy pocket higher in energy toward the VB edge. The W-point VBM can be described as a Y-d–Z-p anti-bonding state, and in general, increasing the energy contribution of Z-p orbitals in the VB edge increases the energy of the W-point VBM relative to that of the L-point VBM. Moreover, the strategy for converging the W- and Γ-pockets is the same as that for converging the L- and Γ- pockets. Not only do these findings explain why hH compounds with Y-site elements from group IX and Z-site elements from group IV exhibit W-pocket VBs, but it also suggests another alloying strategy that can further enhance VB convergence: tuning the relative electronegativity of the Y- and Z- sites or tuning the strength of the Y-d–Z-p interaction.

Broadly speaking, the work presented in this Chapter shows that recognizing various types of avoided crossings is crucial to understanding and engineering complex electronic structures for a variety of semiconductor-based applications. Future work in this area should focus on validating these alloying strategies *via* experimental data and first-principles calculations of disordered alloy systems containing aliovalent and isovalent substitutions.

Importance of Mg-Sb Interactions in Achieving High Conduction Band Degeneracy in Mg_3Sb_2

This chapter is largely reproduced with permission from M. K. Brod, S. Anand, and G. J. Snyder. *Materials Today Physics*, 31, 100959 (2023) [113].

7.1 Introduction

Recently, Mg_3Sb_2 has gained significant attention as a highly promising new n-type thermoelectric material for low- and moderate-temperature applications, competitive with state-of-the-art Bi_2Te_3 [210–213]. Zintl-phase Mg_3Sb_2 is a low-cost, non-toxic thermoelectric material comprised of Earth-abundant materials [210, 212, 214, 215]. It crystallizes in the layered $CaAl_2Si_2$-type structure (space group: #164; $P\bar{3}m1$) (see Figure 7.1), and it contains two unique types of Mg-sites, Mg(1) and Mg(2), distinguished by their coordination environment [213, 216]. Mg(1) is octahedrally coordinated by Sb atoms, while the Mg(2) is tetrahedrally coordinated by Sb atoms (Figure 7.1b,c) [217]. The competitive n-type performance of Mg_3Sb_2-based thermoelectrics is largely attributed to its relatively high conduction band (CB) degeneracy and low lattice thermal conductivity, κ_L. The high valley degeneracy is due to the conduction band minimum (CBM) being located at a low-symmetry point (U^*) inside the ΓALM plane of the BZ (see Table A.3 in Appendix A), which exhibits six-fold degeneracy ($N_V = 6$) [205, 212, 218]. The relatively low lattice thermal conductivity in $Mg_3(Bi,Sb)_2$ is the result of high anharmonicity caused by weak interlayer bonding and

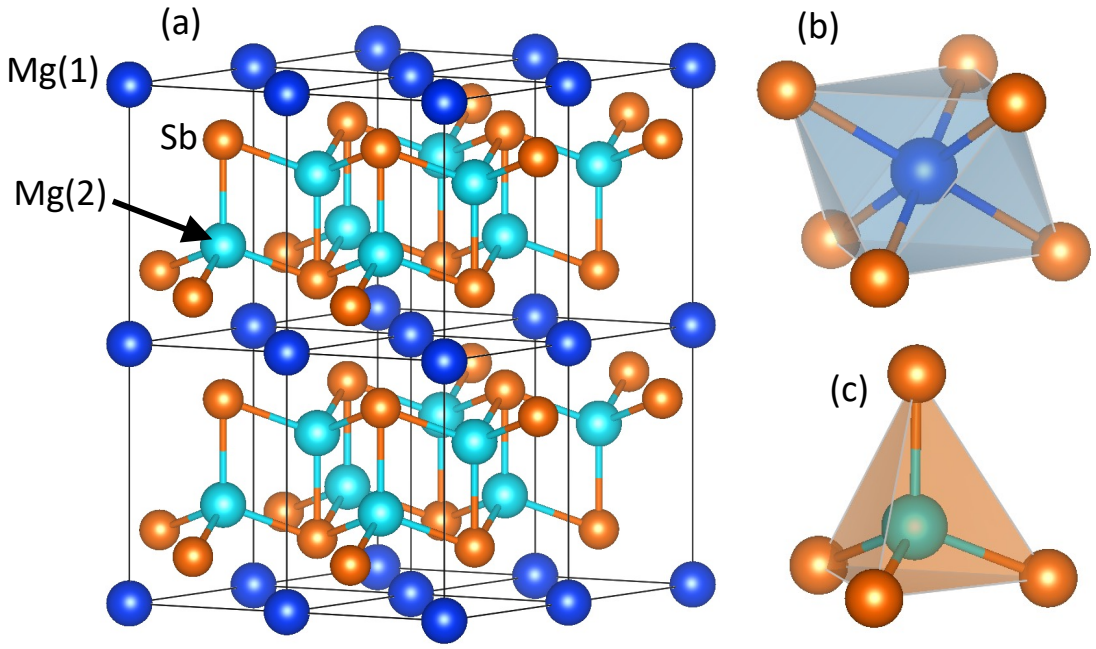

Figure 7.1: (a) Crystal structure of Mg_3Sb_2. The blue and turquoise atoms represent Mg and the orange atoms represent Sb. (b) The Mg(1) site (dark blue) is octahedrally coordinated by Sb, while (c) Mg(2) (turquoise) is tetrahedrally coordinated by Sb.

asymmetric anion lone-pair electrons [219, 220].

By contrast, p-type Mg_3Sb_2 exhibits poorer thermoelectric performance than its n-type counterpart because the valence band maximum (VBM) is located at the high-symmetry Γ-point, giving it lower valley degeneracy ($N_V = 1$) [210, 212, 215, 221–223]. The VB edge is dominated by Sb-p states (with Sb-s states deeper into the VB) [206, 218, 224, 225], so the high-symmetry Γ-point VBM in Mg_3Sb_2 is the result of Sb-p–Sb-p interactions, which are most anti-bonding at Γ and become less anti-bonding (or more bonding) away from Γ. In fact, this Γ-point VBM is quite typical in semiconductors that have VB states that are dominated by p-orbital-like states [62, 66]. Because the anion-p rather than cation-states dominate the behavior of the VBs in $CaAl_2Si_2$-type Zintl compounds, the Γ-point VBM is consistently present in this class of layered compounds, regardless of the CBM location [206, 218]. However, the chemistry of the CBM, which is the focus of the present work, is less straightforward.

It is known that alloying Mg_3Sb_2 with Mg_3Bi_2 can enhance n-type transport by increasing the electron mobility (lowering m_I^*) [32, 131, 210, 211, 226]. The change in electron mobility upon Bi substitution can be attributed to an increase curvature around the electron transport edge at U* [32, 131]. Increasing the Bi content also decreases the band gap energy, which reduces the optimal thermoelectric operating temperature [32, 227]. On the other hand, substituting Sb with As increases the band gap energy but is detrimental to the electron mobility [23, 225].

In order to better understand the low-symmetry CBM and the effects of alloying on electronic transport, it is helpful to look at the chemical origins of the U* CBM. The states near the CB edge exhibit mostly Mg-s character (with Mg-p contributions higher in the CB) [205,210,224,225,228,229]. Thus, the behavior of the CB edge should be largely influenced by the Mg-s orbitals and their interactions with neighboring orbitals. In prior works, the high-degeneracy U* CBM has been attributed to Mg(1)-s–Mg(2)-s bonding interactions in the CB [205, 224]. However, as discussed later in this chapter, trends in the electronic structures of Mg_3X_2 (X = Bi, Sb, As) cannot entirely be explained through Mg(1)-s–Mg(2)-s interactions alone (though these interactions may explain carrier pocket anisotropy).

Here, we aim to elucidate the chemical origins of the low-symmetry U* CBM by considering Mg–Sb interactions. We show that the Mg-s–Sb-p interactions play a critical role in the presence of the low-symmetry CBM and are consistent with observed trends in the CB structure upon anion-site substitutions. We show that the states surrounding the CB edge have Mg-s–Sb-p anti-bonding character that reaches a minimum near U* (Figure 7.2). Increasing the strength of this interaction increase the curvature around the CB edge, which should lead to an increase in electron mobility. Prior studies overlooked the importance of the Mg-s–Sb-p interactions because the orbital and bonding contributions from Sb-p at the U*–point are minimal [205, 224] (Figure 7.2). That being said, the importance of Mg-s–Sb-p anti-bonding is evident through trends in the electronic structures (e.g., the increase in mobility when Sb is replaced with Bi), in the $\boldsymbol{k}$-dependent orbital contributions, and $\boldsymbol{k}$-resolved crystal orbital Hamilton population (COHP) calculations [52, 53, 230].

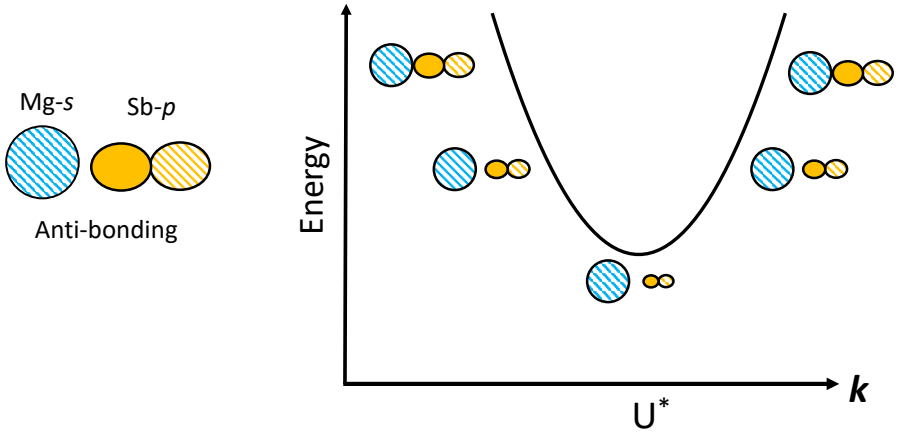

Figure 7.2: Illustration of how Mg-s–Sb-p anti-bonding interactions yield the low-symmetry CBM at U* in Mg_3Sb_2. In this sketch, the relative size of the Sb-p orbitals qualitatively represents the relative contribution of the Sb-p orbitals relative to the Mg-s orbitals and corresponds to the strength of the Mg-s–Sb-p anti-bonding interactions. Mg-s–Sb-p anti-bonding interactions are weaker near U* and becomes stronger away from U*, leading to a minimum (or local minimum) at U*.

Cation substitutions also influence n-type transport behavior. For instance, when Mg(1) is replaced with a more electropositive species (Ca, Yb, Sr, Ba, etc.) the CB Fermi surface becomes more anisotropic, while substitution with a more electronegative species (Be) decreases anisotropy [205]. Higher Fermi surface anisotropy may be beneficial to thermoelectric performance, though it could also have the detrimental effect of reducing carrier mobility [34, 46, 224, 231]. In this chapter, we explain how these changes in the CB edge upon cation substitution are due to changes or disruptions in cation-s–anion-p interactions.

7.2 Background: Orbital Chemistry Framework

Here, we describe a chemical framework based on the tight-binding (TB) model that can be used to interpret density functional theory (DFT) results and understand how different orbital interactions influence the location of the CBM, the electron mobility, and the band gap energy in Mg_3X_2 (X =Bi, Sb, As). In this section, we use TB band structures of toy models for crystalline semiconductors to explain (1) how to determine the orbital interactions responsible for a given VBM or CBM and

(2) how the shape of band edge can be modified using chemical manipulations. Details on the TB model can be found Chapter 2.

7.2.1 Two-Orbital, Two-Band Model

As an example, consider a toy model of a binary FCC rock salt compound, MX, where only nearest-neighbor M-s–X-s interactions are relevant. The energies of the M-s and X-s orbital before interacting, the on-site energies, are given by E_{M-s} and E_{X-s}. The interaction strength between the two s-orbitals is given by the magnitude of the hopping integral which is a function of $\boldsymbol{k}$ for a periodic crystal. For this system, the interaction strength reaches a maximum at the Γ-point and a minimum at the L-point. Along the Γ-L path, the interaction is given by the expression, $V_{MX}(l) = 6V_{ss\sigma}\cos(\pi l/2)$, where l varies from 0 at Γ to 1 at L. The $\boldsymbol{k}$-dependent $\cos(\pi l/2)$ term is derived using the methods in Ref. 65, and $V_{ss\sigma}$ is a constant that describes the interaction strength between two s-orbitals that are in their most bonding state (i.e., two completely in-phase s-orbitals). Analogous constants of the form $V_{ll'm}$ exist for different types of orbital interactions (see Chapter 2 for more detail).

As discussed in Chapter 2, the electronic structure for this toy system, shown in Figure 7.3a, can be calculated using Equation 2.24, and the band energies depend on both a local and non-local term. The local term is related to the on-site energies of the orbitals weighted by their contributions, and the non-local term is determined by the strength of the interactions between the orbitals. The orbital character/contribution of a given orbital to a given band is given by $|c_\alpha^n|^2$, where α labels the orbital and n is the band index (see Equation 2.29). These values are shown in Figure 7.3b-c for the toy model. The $|c_\alpha^n|^2$ values describe the $\boldsymbol{k}$-resolved, band-resolved partial density of states (pDOS) for atomic orbital α. The non-local term is described by the crystal orbital Hamilton population (COHP) [52], where positive COHP values indicate anti-bonding character, while negative COHP values indicate bonding character. Here, we consider $\boldsymbol{k}$-resolved COHP values [230], which describe the interaction strength at a specific $\boldsymbol{k}$-point in a specific band. The magnitude of the COHP values

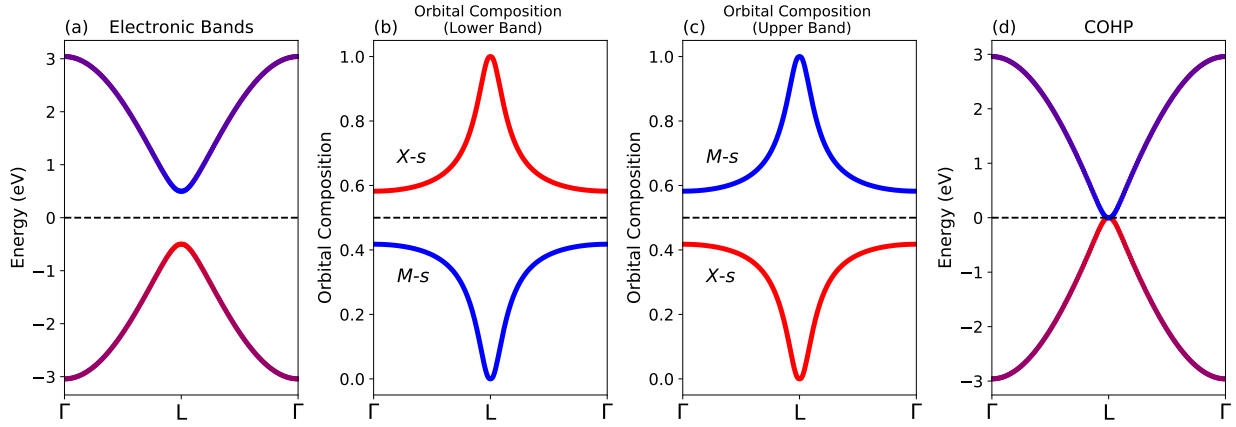

Figure 7.3: Electronic bands, orbital compositions, and crystal orbital Hamilton population (COHP) values for a two-orbital tight-binding (TB) model serve as guides to interpret orbital contributions and COHP values calculated from DFT. (a) TB band structure where the color of the bands represents the relative contributions from the M-s (blue) and X-s (red) orbitals. (b) TB orbital contributions of M-s (blue) and X-s orbital (red) to the lower band. (c) Orbital contributions in the upper band. (d) The non-local term (COHP) reaches a maximum in magnitude at Γ and is zero at L. These plots are based on a TB model of an FCC rock salt structure comprising M-s and X-s orbitals with an hopping parameter given by $V_{MX}(l) = 6V_{ss\sigma}\cos(\pi l/2)$, where $l = 0$ at Γ and $l = 1$ at L and $V_{ss\sigma} = -1/2$. The on-site energies are defined such that $(E_{M-s} + E_{X-s})/2 = 0$ and $E_{M-s} - E_{X-s} = 1$.

corresponds to (but is not necessarily equal to) the magnitude of $V_{MX}(\boldsymbol{k})$ and reaches a maximum at Γ and a minimum at L (Figure 7.3d).

The $\boldsymbol{k}$-resolved orbital contributions (pDOS) and COHP values from the toy model described here (Figure 7.3) can be used as an initial reference for interpreting the chemical origins of a CBM (or VBM) from first-principles DFT calculations. In this simple two-band model, the higher-energy band would correspond to the CB edge near U* in Mg_3Sb_2. Therefore, in order to show that the Mg-s–Sb-p anti-bonding interactions are responsible for the U* CBM within this two-band framework, we must show that the Mg-s contribution reaches a local maximum, and the Sb-p contribution reaches a local minimum at U*. Moreover, we must show that the Mg-s–Sb-p COHP values are positive (anti-bonding) and reach a local minimum around U*.

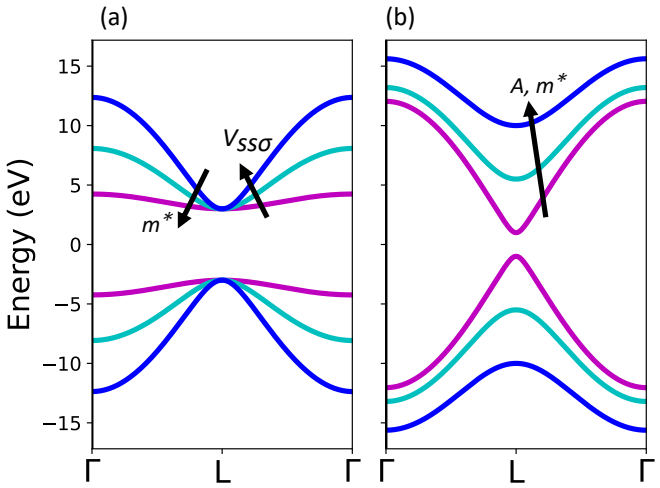

Figure 7.4: The two-band tight-binding (TB) electronic band structure for a toy FCC crystal consisting of M-s and X-s orbitals shows that both increasing the s-orbital interaction strength and decreasing the energy difference between orbitals decrease the effective mass of the carriers. (a) Bands calculated with $A = \frac{1}{2}(E_{M,s} - E_{X,s}) = 3.0$ eV and $V_{ss\sigma}$ = -0.5 eV (magenta), -1.25 eV (green), and -2.0 eV (blue). (b) Bands calculated with $V_{ss\sigma} = -2.0$ eV and A =1.0 eV (magenta), 5.5 eV (green), and 10.0 eV (blue).

7.2.2 Tuning Band Edge Curvature

After identifying the orbital interactions responsible for the CBM or VBM in a material, the TB model can also be used to identify strategies to tune the shape of the band edge and optimize transport properties (e.g., decrease the inertial effective mass). Here, we focus specifically on how the band curvature and carrier mobility can be increased by tuning atomic orbital energies and orbital overlap (interaction) strengths.

Consider the same MX toy model described in the previous section. We define a parameter A, given by $A = \frac{1}{2}(E_{M-s} - E_{X-s})$, to describe the energy separation between the two atomic orbitals. Band structures for this toy model are calculated with various values for $V_{ss\sigma}$ (constant A) and various values of A (constant $V_{ss\sigma}$), as seen in Figure 7.4. The band width and curvature increases with increasing s–s interaction strength, described by $V_{ss\sigma}$, and with decreasing A, resulting in a lower m_I^* [66].

The results of this simple example can be generalized to explain some chemical trends in more

complex electronic structures. When describing bands that result largely from an interaction between two orbitals, increasing the ($\boldsymbol{k}$-independent) strength of the orbital interaction (i.e., the magnitude of $V_{ss\sigma}$, $V_{sp\sigma}$, $V_{pp\sigma}$, $V_{pp\pi}$, etc.) and decreasing A increase the curvature around the band edge and reduce the band effective mass. Thus, if the goal is to increase band curvature (and carrier mobility) it is beneficial to reduce the energy difference between the interacting orbitals through substitutions/alloying and increase the magnitude of the $\boldsymbol{k}$-independent portion of hopping parameter, V. Note that reducing the on-site energy difference can also decrease the band gap energy which may be detrimental to thermoelectric performance by inducing bipolar effects if not optimized for temperature.

7.3 First-Principles DFT Calculations

7.3.1 Conduction Band Location and Curvature

To evaluate the relative importance of the various bonding interactions in the CB structure of Mg_3Sb_2, we study the shape of the U* band in the three Mg_3X_2 (X = As, Sb, Bi) compounds in the $P\bar{3}m1$ space group using first-principles DFT calculations with the Perdew-Burke-Ernzerhof (PBE) functional. [51]. We focus on the CB structure in the ΓALM plane because it captures the critical points for understanding n-type transport (Figure 7.5). The 2D band energy heat maps in the ΓALM plane for the three compounds are shown in Figure 7.5a-c. In all three compounds, there is a CB minimum in the ΓALM plane a six-fold degenerate U* point, where the exact location of U* varies slightly based on the compound and composition (coordinates given in Appendix E). In Mg_3As_2 and Mg_3Bi_2, the additional CB pocket at Γ emerges, implying a potential increase N_V when Mg_3Sb_2 is alloyed with these compounds from the convergence between the U* and Γ bands [23, 205, 227].

Additionally, we plot the CBs along the LM, L*M* and A*U paths (see Figure 7.5d) and estimate the inertial effective masses [18,56] along the latter two directions to better visualize the curvature of

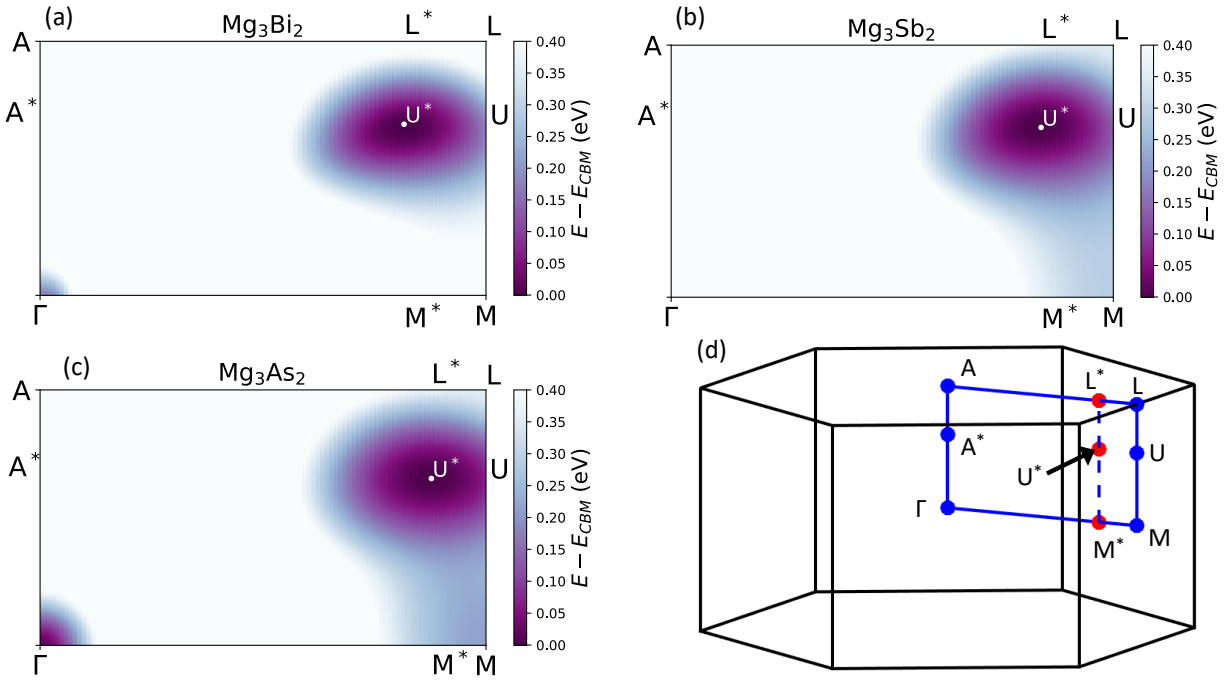

Figure 7.5: 2D heat maps of the of the conduction bands (CBs) in the ΓALM plane for an energy window of 0 eV to 0.4 eV above the CBM for (a) Mg_3Bi_2, (b) Mg_3Sb_2, and (c) Mg_3As_2. (d) Diagram of the first BZ for the hexagonal Bravais lattice with special points in the ΓALM plane labeled.

the CB edge around U* (see Figure 7.6). We include the band structures of Mg_3SbBi and Mg_3AsSb to better understand the potential effects of alloying. That is, these compounds represent cases where we have 50% alloying on the anion-site. Recall that the exact coordinates of L*, M*, A* and U vary slightly with composition, and the length along each of the three paths shown follows the trend Mg_3As_2 > Mg_3AsSb > Mg_3Sb_2 >Mg_3SbBi > Mg_3Bi_2.[1] The CB effective mass along each of the two specified directions was calculated using the expression in Equation 7.1, [67] where the term, $\frac{\partial^2 E}{\partial k^2}$, was determined numerically by fitting a parabolic function around the U* point (see Table E.1 in Appendix E). The effective mass along each of the two directions is greatest for Mg_3As_2 and smallest for Mg_3Bi_2, showing that the curvature of the CB edge around U* in Mg_3X_2 increases as X moves down the Pnictogen group from As to Sb to Bi. This increase in curvature coincides with an increase in the $\Gamma \rightarrow$U* band gap energy. Moreover, the curvatures for Mg_3SbBi and Mg_3AsSb are intermediate between those of the end-member cases, validating that we can *approximate* the properties of alloy systems as interpolations of their end-member compounds. Note that the PBE-GGA functional significantly underestimates the band gap energy (the band gap energy of Mg_3Sb_2 is ∼0.6 eV [210, 227]) but is acceptable for simply comparing the shape of the CB edge [211], and the higher CB edge curvature in Mg_3Bi_2 is consistent with previous reports that find that alloying Mg_3Sb_2 with Mg_3Bi_2 lowers the (inertial) effective mass of the CB edge [32, 212, 227]. Additionally, the band curvatures for Mg_3SbBi and Mg_3AsSb falls between that of their end-member compounds.

$$m^* = \hbar^2 \left(\frac{\partial^2 E}{\partial k^2} \right)^{-1} \tag{7.1}$$

Because carrier pocket anisotropy may be beneficial to thermoelectric performance [34], it is worth noting that the chemistry of the anion-site can change the level of carrier pocket anisotropy in the CB Fermi surface. If the Fermi energy is close enough to the band edge that only parabolic

[1] Note that this trend in BZ path-lengths actually favors higher curvature in Mg_3Bi_2 and lower curvature in Mg_3As_2 when all other parameters (A- and V-type parameters from the TB framework) are held constant. Therefore, in order to ensure that the composition/chemistry of the compounds, and not the path lengths, are responsible for the curvature, the curvature was calculated assuming constant path lengths across compounds, and the same trends in curvature were found, indicating that the chemistry and not the unit cell size alone is responsible for the curvature trends.

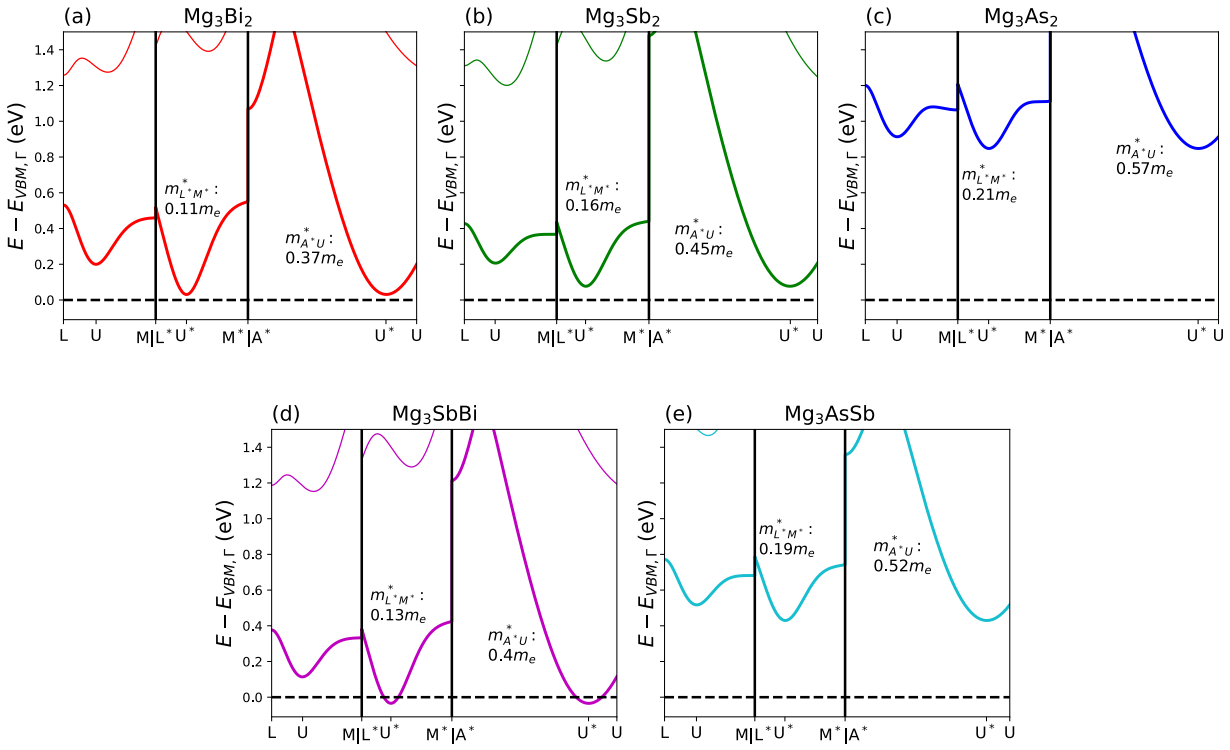

Figure 7.6: DFT-calculated conduction bands along the LM, L*M* and A*U paths for (a) Mg_3Bi_2, (b) Mg_3Sb_2, (c) Mg_3As_2, (d) Mg_3SbBi, and (e) Mg_3AsSb. The inertial effective masses (calculated from band curvature) for the L*M* and A*U directions are given. The lowest CB is marked with a thicker line width. The horizontal dashed line represents the energy of the VBM at Γ.

effects are relevant (i.e., the Fermi surface is approximately ellipsoidal), then the level of anisotropy could be compared via the ratios of the intertial effective masses along the ΓA ($m^*_{L^*M^*}$) to those along ΓM ($m^*_{A^*U}$) directions. Based on the intertial effective masses, Mg_3As_2 would be the most isotropic and Mg_3Bi_2 would be the most anisotropic [131]. However, it is not sufficient to assume that the bands always behave parabolically. In $Ae$$Mg_2X_2$-based compounds that possess the U* CB pocket, anisotropy from non-parabolic effects arises when the M and U* bands align, causing the U* pocket to stretch toward M in a non-parabolic manner [205, 223]. As seen in Figure 7.5, the Fermi surface in Mg_3As_2 stretches toward M more so than Mg_3Sb_2, while in Mg_3Bi_2 it stretches less toward M, suggesting that alloying on the Sb-site with As may be more beneficial for promoting carrier pocket anisotropy, while substituting with Bi may be detrimental. More detailed transport calculations should be conducted to better understand the trade-off between anisotropy and inertial effective mass.

These trends in the curvature and effective mass near the U* band edge are not consistent with the hypothesis claiming that the Mg(1)–Mg(2) interactions are mainly responsible for the U* CBM. In general, we expect the interaction strength between two orbitals to decrease as the interatomic spacing between the atoms increases and as the difference in the on-site energies of the atomic orbitals increases [6, 63, 64, 226]. Because the Mg(1)-Mg(2) interatomic spacing increases as we move down the Pnictogen group from As to Bi [23, 213, 223, 225], we expect the strength of the Mg(1)-s–Mg(2)-s interactions to be weakest in Mg_3Bi_2 and strongest in Mg_3Sb_2. Therefore, if the Mg(1)–Mg(2) interactions were the primary source of the U* CBM, then the dispersion would be greatest (m^*_I lowest) in Mg_3As_2 and smallest (m^*_I highest) in Mg_3Bi_2. However, the opposite trend is observed, motivating the study of additional interactions as possible sources of the low-symmetry CBM. In a previous study, it was shown that as the Mg(1)–Mg(2) distance increases and interaction strength decreases with increasing Bi content, the band curvature and carrier mobility increase [226]. It was also shown that increasing the Mg(1)–Mg(2) distance through strain (without substitution Sb with Bi) slightly increases carrier mobility but that adding Bi significantly enhances this effect [226]. This study not only suggests that Mg(1)–Mg(2) interactions are not consistent

with trends in the CB curvature, but it also suggests that the anion-orbitals play an important role in the shape of the U* CB pocket.

The Mg–Sb interactions may explain the trends in curvature and mobility, and we expect the CB to contain Mg–Sb anti-bonding states because the Mg states that dominate the CB edge are higher in energy than the Sb orbitals. Based on the atomic orbital on-site energies, we expect the Mg–X interactions to be strongest in Mg_3Bi_2 and weakest in Mg_3As_2 because the energy of the X-site orbitals increases relative to those of the Mg atoms as we move down the Pnictogen group from As to Bi [63, 226]. Therefore, we investigate the Mg-s–X-p interactions as a potential source of the low-symmetry U* CBM using $\boldsymbol{k}$-resolved pDOS and COHP calculations.

7.3.2 Orbital Character and COHP Values

We examine components of both the local and non-local contributions to the energy eigenvalues (see Equation 2.37 and Figure 7.3) around the U* CBM to study the importance of the Mg–Mg versus Mg–Sb interactions. Computationally, the contribution of different orbitals to the local term can be determined by the relative orbital contributions (Figures 7.7-7.8), and the non-local, or interaction, term can be calculated via COHP (Figure 7.9) [52–54, 150, 205].

The normalized relative orbital contributions (pDOS) along the LM, L*M* and A*U paths (see Figure 7.7) are consistent with Mg-s–X-p anti-bonding interactions leading to the U* CBM. Note that the sharp minimum and maximum in Figures 7.7b and c, respectively, along A*U are due to a band crossing that occurs at that point and are not bonding features. The greatest orbital contribution to the U* band comes from the Mg-s orbitals with more contribution from Mg(1) than Mg(2), and the total Mg contribution reaches a maximum near U* (Figure 7.7a-b). Additionally, the X-p contribution reaches a minimum near U* (Figure 7.7c). These orbital characters are consistent with the orbital characters of the toy model depicted in Figure 7.3c, where the red curve corresponds to X-p and the blue curve corresponds to Mg(1)-s. Moreover, the relative contribution of the X-p orbitals is greatest in Mg_3Bi_2 and smallest in Mg_3As_2, which is corresponds to the Mg-s–X-p

interactions being strongest in Mg_3Bi_2.

In light of Figure 7.3, which is based on a two-band (two orbital) model, we also look at the ratios between the Mg(1)-s and X-p contributions and between the Mg(1)-s and Mg(2)-s contributions as a proxies for the bond strength around the CB edge (Figure 7.8). Based on the two-band TB model, as the bond strength between two orbitals increases, the ratio of the orbitals to the total contribution of those two orbitals approaches 1/2, and as the interaction becomes weaker, the ratio of the dominating orbital to the total approaches one (Figure 7.3b-c). Given this framework and the orbital ratios depicted in Figure 7.8, the strength of the Mg(1)-s–X-p anti-bonding interaction is weakest around U*, and the overall strength of this interaction is greatest in Mg_3Bi_2 and weakest in Mg_3As_2. Furthermore, the orbital ratios suggest that the strength of the Mg(1)-s–Mg(2)-s interaction generally increases from L to M and from L* to M* while reaching a smaller peak near U*.

Moreover, we employ $\boldsymbol{k}$-resolved, band-resolved (values for the lowest CB) projected COHP (pCOHP) calculations in order to verify the nature of the orbital interactions (Figure 7.9). Here, we focus mainly on the interactions involving the Mg(1)-s orbitals, as they provide the greatest contribution to the CB edge character (Figure 7.7a). Again, the sharp peaks along the A*U path (closer to A*) are due to a band crossing and are not bonding features. The Mg(1)-s–Mg(2)-s interactions in the lowest CB are bonding (COHP < 0), while the Mg(1)-s–Sb-p interactions are anti-bonding (COHP > 0). While there are small peaks in the strength of the Mg(1)-s–Mg(2)-s interactions of Mg_3Sb_2 and Mg_3Bi_2 near U* along the L*M* path, this peak is not seen in Mg_3As_2. The Mg(1)-Mg(2) interaction generally increases in strength from L* to M* and from L to M, and there is not a clear peak near U along the LM path for any of the compounds. The general increase in the strength of the Mg(1)-s–Mg(2)-s bonding interaction from L/L* to M/M* (which is partially counteracted by a general increase in Mg(1)-s–Sb-p anti-bonding strength) may also explain why the anisotropy from the CB carrier pocket stretching (non-parabolically) toward M is largest in Mg_3As_2 and smallest in Mg_3Bi_2. The Mg(1)-s–Mg(2)-s interaction, which is strongest in Mg_3As_2

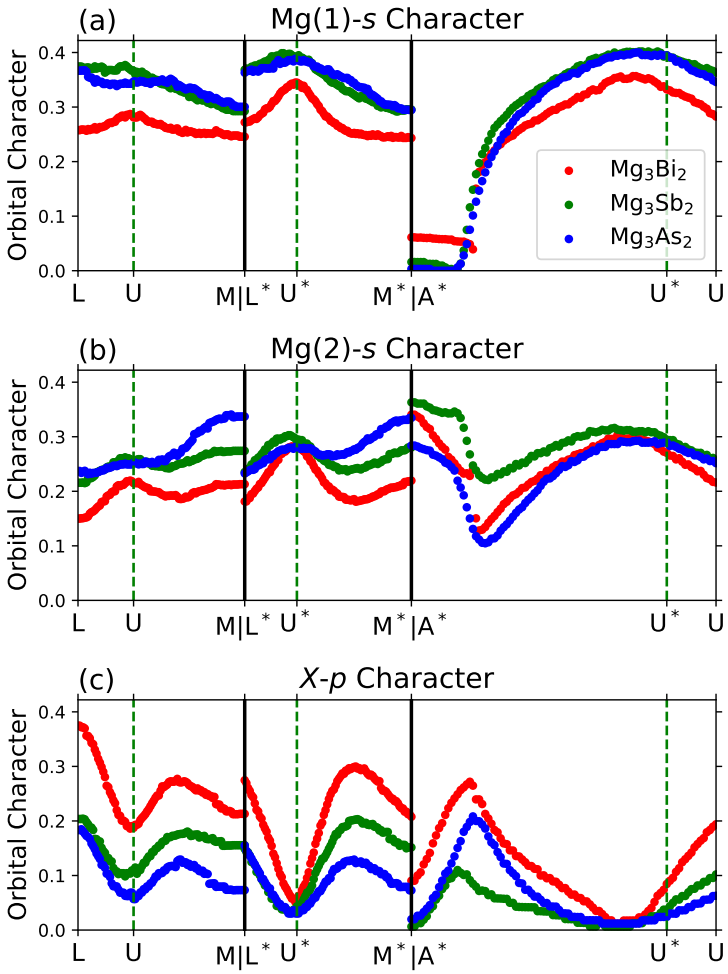

Figure 7.7: Normalized values of DFT orbital contributions, or projected density of states (pDOS), to the lowest conduction band (CB) of the (a) octahedrally coordinated Mg(1)-s, (b) tetrahedrally coordinated Mg(2)-s, (c) and X-p orbitals for the three Mg_3X_2 (X = Bi, Sb, As) compounds. The green dashed vertical lines represent the location of the CB energy minimums for Mg_3Sb_2 along each path. Red, green, and blue curves correspond to Mg_3Bi_2, Mg_3Sb_2, and Mg_3As_2, respectively.

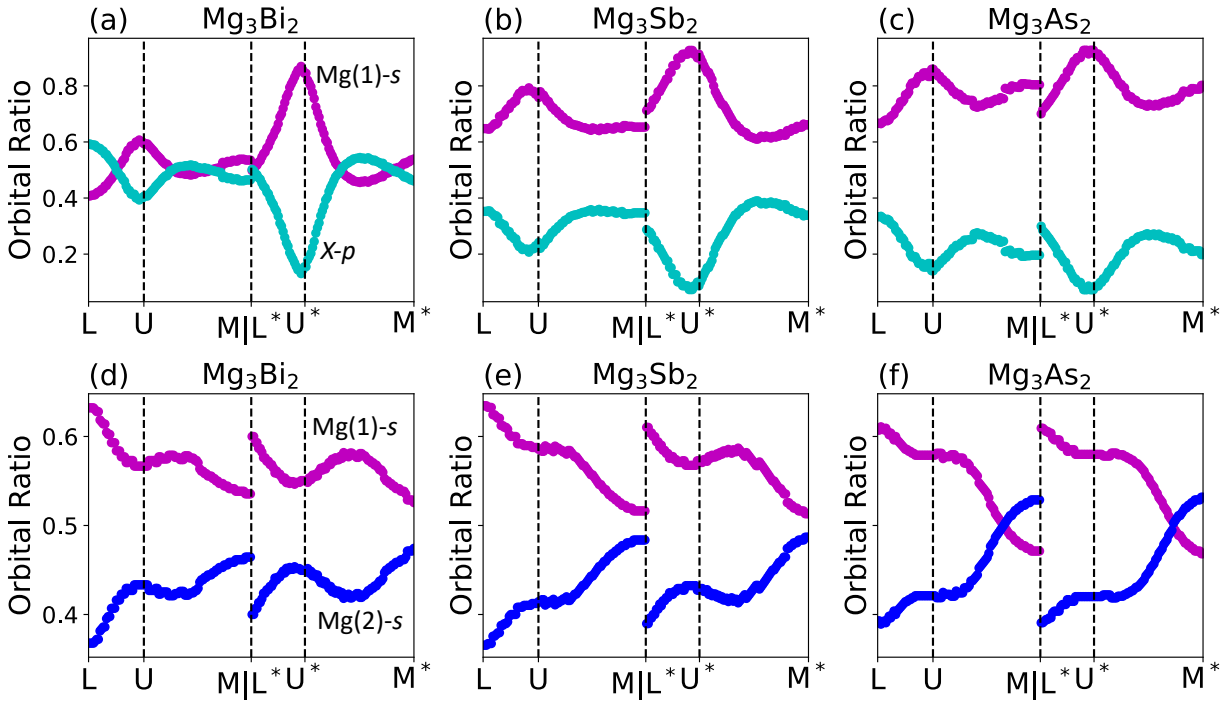

Figure 7.8: (a)-(c) Ratios of the Mg(1)-s and X-p orbital contributions, or projected density of states (pDOS), in the lowest conduction band (CB) to the sum of the Mg(1)-s and X-p contributions in the lowest CB for Mg_3Bi_2, Mg_3Sb_2, and Mg_3As_2. (d)-(f) Ratios of the Mg(1)-s and Mg(2)-s orbital contributions to the sum of the Mg(1)-s and Mg(2)-s contributions for Mg_3Bi_2, Mg_3Sb_2, and Mg_3As_2.

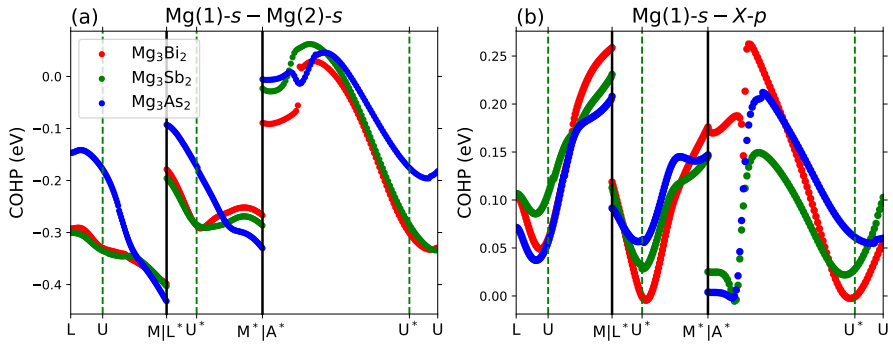

Figure 7.9: $\boldsymbol{k}$-resolved, band-resolved crystal orbital Hamilton population (COHP) values for the lowest conduction band (CB) corresponding to the (a) Mg(1)-s–Mg(2)-s and (b) Mg(1)-s–X-p interactions in Mg_3X_2 (X = Bi, Sb, As). Red, green, and blue lines correspond to Mg_3Bi_2, Mg_3Sb_2, and Mg_3As_2, respectively. The green dashed vertical lines represent the location of the minimums of the CB edge along each path for Mg_3Sb_2.

and weakest in Mg_3Bi_2 (due to the interatomic distances), pushes the energy of the M-point CB pocket down, which promotes band alignment between the U* and M bands, and hence, anisotropy.

In contrast to the Mg(1)-s–Mg(2)-s interactions, the shape of the Mg(1)-s–X-p COHP coincides well with the shape of the CB near the U* for all three compounds along all three $\boldsymbol{k}$-paths shown. The COHP values indicate that there is a local minimum in anti-bonding strength near U*, which results in the CB energy increasing away from the U*-point and a minimum at U*. While the higher values the Mg-s orbital character and Mg(1)-s–Mg(2)-s COHP strength and lower values of the Sb-p orbital character and Mg-s–Sb-p COHP are signatures of Mg-s–Sb-p interactions contributing to the U* CBM, they are also the reason that these interactions have been overlooked in the past [205,224]. Thus, in general, when trying to understand the chemical origins of a band extrema at a specific point, it is often important to examine how the orbital character and interactions vary around that point and not only examine that specific point.

Similar results are observed when we replace Mg(1) with Be [113]. In the three $BeMg_2X_2$ (X = Bi, Sb, As) compounds, there is an analogous minimum in the ΓALM plane at a low-symmetry U* point. The lowest CB is dominated by Be-s and Mg-s orbitals, with a greater contribution from the Be-s orbitals. The DFT and COHP calculations are consistent Be-s–X-p interactions (analogous

Table 7.1: Tight-binding (TB) hopping parameters for a toy compound based on Mg_3Sb_2. .

Parameter	Bond Type	Number of Neighbors	Value (eV)
Mg(1)-*s*-Sb-p	σ	6	1.4
Mg(2)-*s*–Sb-p (short)	σ	3	2.0
Mg(2)-*s*–Sb-p (long)	σ	1	1.8
Mg(1)-*s*–Sb-s	σ	6	-0.8
Mg(2)-*s*–Sb-s (short)	σ	3	-1.3
Mg(2)-*s*–Sb-s (long)	σ	1	-1.0
X-*p*–Sb-*p*	σ	3	1.0
X-*p*–Sb-*p*	π	3	-0.1
$E_{Mg-s} - E_{Sb-p}$	N/A	N/A	3.0
$E_{Mg-s} - E_{Sb-s}$	N/A	N/A	10.0

to the Mg(1)-*s*–*X*-*p* interactions) being largely responsible for the low-symmetry CBM.

7.4 Tight-Binding Conduction Band Structure

Using a simple TB model based on the Mg_3X_2 structure, we can show that Mg-*s*–*X*-*p* interactions are sufficient to explain the local minimum at U*, and we can qualitatively reproduce the trends in band curvature seen in Mg_3X_2 compounds. The TB model used here describes a toy compound that is based on the Mg_3X_2 structure, where the TB parameters (Table 7.1) are approximated based on the parameters outlined in Ref. 63 (then adjusted to achieve a more realistic CB shape). The TB results presented here are intended for the sake of *qualitatively* understanding the shape of the CB edge and chemical trends in its behavior and are not meant to reproduce the full band structure of Mg_3Sb_2.

The 2D energy heat map for the CB edge in the ΓALM plane (calculated using a TB model with only Mg-*s*–*X*-*p*, *X*-*p*–*X*-*p*, and Mg-*s*–*X*-*s* interactions) can be seen in Figure 7.10a. This TB model predicts a CBM at U*. The corresponding Mg-*s*–Sb-*p* COHP values for the lowest CB in the ΓALM plane, calculated using Equation 2.38, are given in Figure 7.10b. Based on these TB COHP values, the Mg-*s*–*X*-*p* interactions are anti-bonding and reach a local minimum near U*. If only Mg-*s*–*X*-*p*

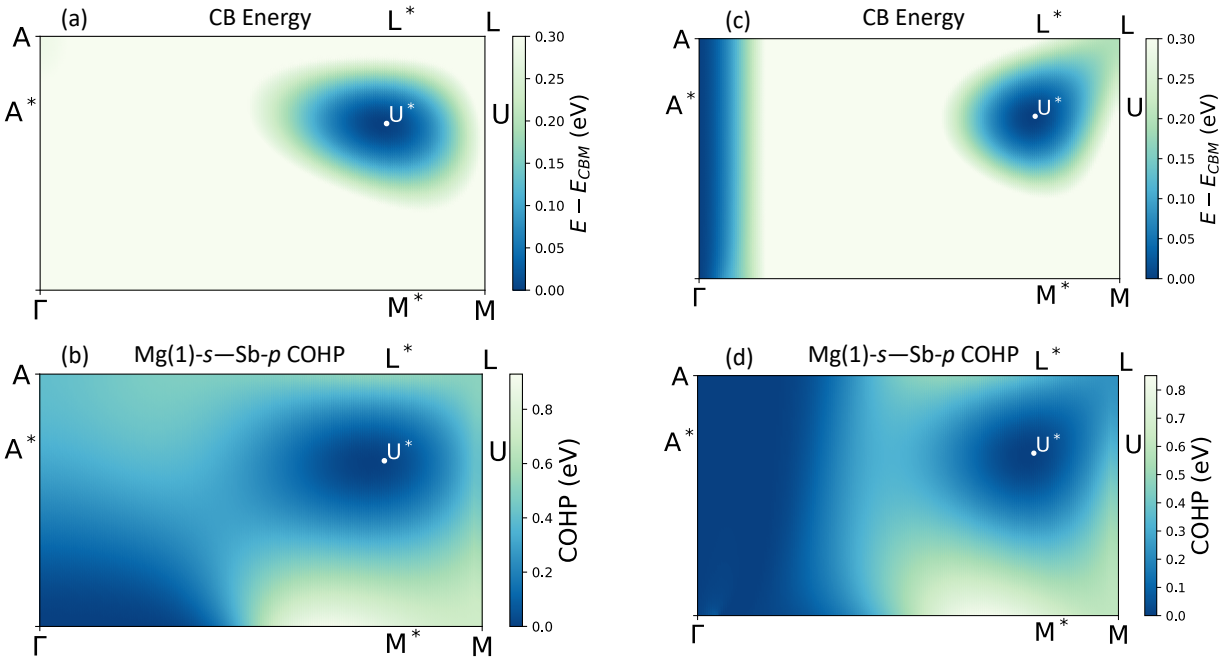

Figure 7.10: Tight-binding (TB) conduction band (CB) structure and (projected) crystal orbital Hamilton population (COHP) values between Mg(1)-s and Sb-p. (a) 2D CB energy heat map (energy variations over a range of 0.0-3.0 eV above the CBM are shown) and (b) TB Mg(1)-s–X-p COHP values of the lowest CB in the ΓALM plane (positive COHP values indicate anti-bonding interactions), calculated using a Mg_3X_2-based TB model that considers only Mg-s–X-p, X-p–X-p, and Mg-s–X-s interactions. (c) 2D CB energy heat map and (d) Mg(1)-s–X-p pCOHP heat map calculated using only Mg-s–X-p interactions.

interactions are considered, there is still a local CBM at U*—corresponding to a local minimum in Mg-s–X-p anti-bonding character—but the minimum along LM is at the L-point (rather than U), and there is a large CB pocket that emerges along the ΓA line (7.10c-d). Despite the fact that the model with only s-p interactions reproduces the CB edge less accurately, it shows that these interactions are crucial in obtaining the U* minimum, as this general feature is maintained when only these interactions are present.

Using this TB model, we can also reproduce the trend in band curvature observed when X changes from As to Bi in Mg_3X_2. This change is modeled by simply changing the energy difference between the Mg-s orbitals and the X-p orbitals in our toy TB model based on Mg_3X_2. As mentioned before, the difference between these on-site energies is greatest in Mg_3As_2 and smallest in Mg_3Bi_2

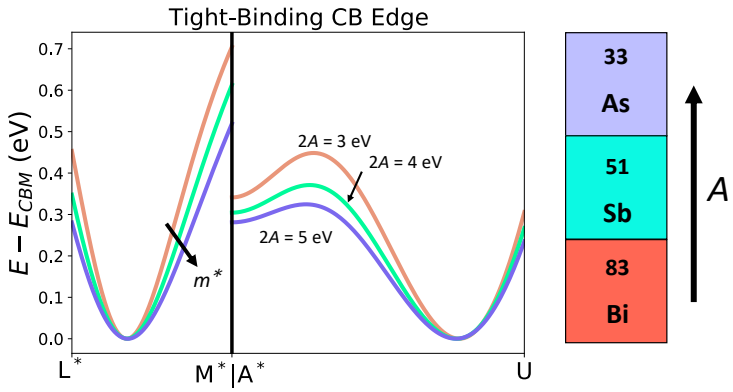

Figure 7.11: Tight-binding (TB) electronic band structure of the lowest-energy conduction band (CB) in a toy compound based on Mg_3X_2 upon varying the difference on on-site energies between the Mg-s and X-p orbitals ($2A$). The effective mass describing the CB edge increases (curvature decreases) as the on-site energy difference increases from 3 eV to 5 eV, which *qualitatively* reflects how the value of $A = \frac{1}{2}(E_{Mg-s} - E_{X-p})$ increases from Bi to As when moving up the Pnictogen group.

[63]. As seen in Figure 7.11, as the on-site energy difference increases from 3.0 eV (the value used to produce Figure 7.10) to 5.0 eV, the dispersion and curvature of the bands near the U* CBM decreases, resulting in increasing values of effective mass along each of the two directions shown. Note that for this thought experiment, we keep the TB hopping parameters constant, but in reality these values would change with chemistry.

7.5 Influence of Cation on Conduction Band Behavior

Because the CBM edge in the Mg_3X_2 compounds is comprised of mainly Mg-s orbitals, cation substitutions can greatly influence the behavior of the U* CB pocket, and changes to the CB structure with respect to cation substitutions can be explained by considering disruptions to the Mg-s–Sb-p anti-bonding interaction. In $Ae$$Mg_2Sb_2$ compounds (Ae = Be, Mg, Ca, Sr, Ba, Yb) where the Ae site is fully occupied by a more electropositive species (Ca, Sr, Ba, Yb), the CBM is located at the M-point ($N_V = 3$) rather than at the U* point. [205,218,228,232] Sun *et al.* find that the Fermi surface pockets of Mg_3Sb_2 alloyed with Ca, Yb, Sr, and Ba on the Mg(1)-site exhibits greater anisotropy, while the electron Fermi surface of Mg_3Sb_2 alloyed with Be is less anisotropic.

As mentioned earlier, the anisotropy of the electron Fermi surface is due to the carrier pocket stretching (non-parabolically) toward the M-point [205, 223]. Thus, assuming that the electronic structure of a solid-solution mixture can be approximated via an interpolation of the electronic structures of its end-members, [32, 33, 42, 182, 206, 207] this trend in anisotropy is expected based on the M-point CBMs in AeMg$_2$Sb$_2$ (Ae = Ca, Sr, Ba, Yb). That is, we can imagine the interpolation between a CB with a minimum at U* and a minimum at M as a band that stretches between U* and M, and the more of the M-CBM compound present, the more that the CB pocket will stretch toward M, and vice-versa. Moreover, Wood *et al.* show experimentally that substituting Yb on the Mg(1) site is detrimental to thermoelectric performance because it decreases the electron weighted mobility [224]. Similarly, Imasato *et al.* report that La-doping on the cation site also decreases the electron mobility [231].

Substitutions on the Mg(1)-site modify the orbital character of the band edge which alters the Mg(1)-s–Sb-p interactions that contribute to the U* CBM. To better understand the influence of these substitutions, we study the CB behavior and corresponding orbital contributions of the end-member compounds for two representative cases: BeMg$_2$Sb$_2$ and CaMg$_2$Sb$_2$ (see Figure 7.12). Because BeMg$_2$Sb$_2$ exhibits the U* CB pocket and CaMg$_2$Sb$_2$ does not (it has an M-point CBM) (Figure 7.12a-b) [205, 218], the interactions near the CB edge in BeMg$_2$Sb$_2$ should be more similar to those in Mg$_3$Sb$_2$ than the interactions near the CB edge of CaMg$_2$Sb$_2$. The level of similarity (or dissimilarity) between band structures is reflected in the orbital composition of the lowest CB near the band edge. The lowest CB in BeMg$_2$Sb$_2$ is dominated by Be-s and Mg-s orbitals, with a greater contribution from the Be-s orbitals (see Figure 7.12c). There is also a substantial contribution from the Sb-p orbitals, which reaches a minimum near U*. On the other hand, as seen in Figure 7.12d, the lowest CB in CaMg$_2$Sb$_2$ is dominated by states more closely resembling Ca-d with some Mg-s character and very little Ca-s and Sb-p character. Similar Ae-d dominated orbital character is seen in the lowest CB of SrMg$_2$Sb$_2$ and BaMg$_2$Sb$_2$, which have the same M-point CBM [113]. Clearly, the orbital character of the CB edge in BeMg$_2$Sb$_2$, dominated by Ae-s and Sb-p character, is more similar to that in Mg$_3$Sb$_2$ than CaMg$_2$Sb$_2$ is. Cation-site substitutions that remove the s-orbitals

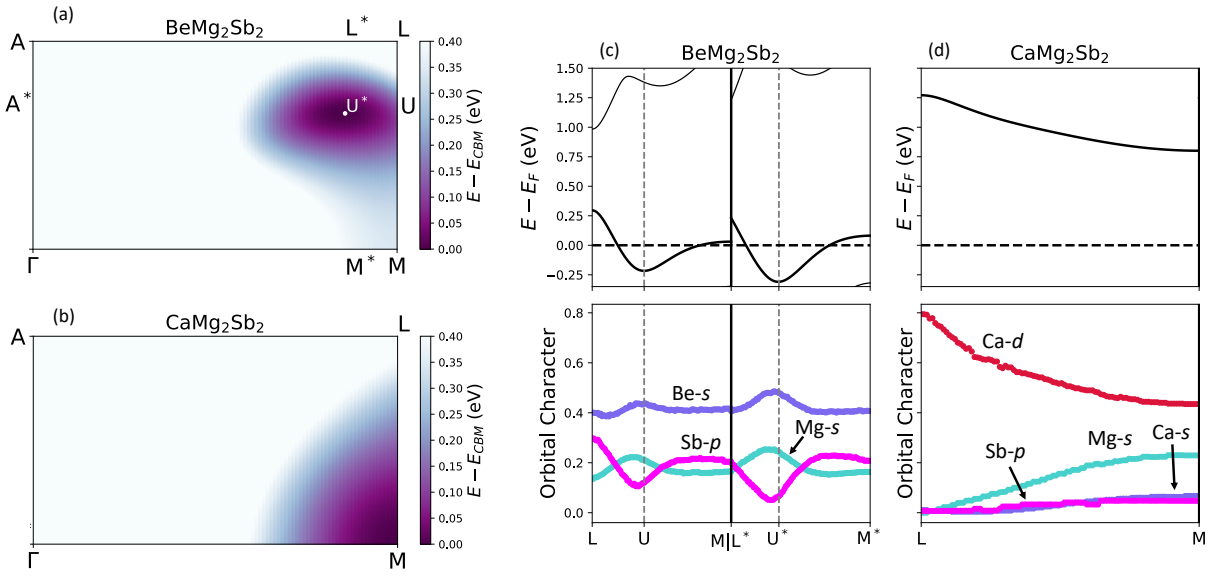

Figure 7.12: 2D energy heat maps of the lowest conduction band (CB) in (a) $BeMg_2Sb_2$ and (b) $CaMg_2Sb_2$ in the ΓALM plane showing an energy window of 0 eV to 0.4 eV above the conduction band minimum. (c) Energy (top) and orbital contributions (bottom) of the U* band from the Be-*s*, Mg-*s*, and Sb-*p* orbitals in $BeMg_2Sb_2$. (d) Energy (top) and orbital contributions (bottom) of the lowest CB from the Ca-*s*, Mg-*s*, Ca-*d*, and Sb-*p* orbitals in $CaMg_2Sb_2$. In the top panels of (c) and (d), the dashed horizontal lines denote the Fermi energy.

near the CB edge disrupt the cation-*s*–anion-*p* interactions, and therefore, stretch the CB Fermi surface toward M. On the other hand, cation-site substitutions that retain the *Ae*-*s* character are less disruptive and (as in $BeMg_2Sb_2$) may disfavor the stretching of the carrier pocket toward M [205]. The lower anisotropy upon Be-alloying may be due to a lower energy separation between the Be-*s* states and Sb-*p* states than between the Mg-*s* and Sb-*p* states, leading to stronger anti-bonding near M/M*, which disfavors U*–M band alignment.

7.6 Computational Methods

The first-principles DFT calculations were performed with the Vienna ab initio Simulation Package (VASP) and employing projector augmented wave (PAW) pseudopotentials and the PBE functional derived from a gradient-generalized approximation (GGA). [48–51, 87, 88] without including spin-

orbit coupling effects. All calculations were performed using a plane-wave energy cutoff of 500 eV. The structural degrees of freedom were relaxed until the forces on the atoms were less than 0.01 eV/nm using a Γ-centered $\boldsymbol{k}$-point mesh [89] with KPPRA$\sim$ 4000 (KPPRA = K-Point Per Reciprocal Atom). The electronic structure calculations were performed using a Γ-centered $\boldsymbol{k}$-point with KPPRA$\sim$ 8000. The $\boldsymbol{k}$-resolved pDOS values (Figure 7.7) were normalized such that at each $\boldsymbol{k}$-point, in each band, the sum of all the atomic-orbital contributions (from VASP) are equal to one. The $\boldsymbol{k}$-vector resolved COHP calculations were performed using the version 4.0.0 of the LOBSTER software, using the pbeVASPFit2015 basis set [52–54, 150, 230].

7.7 Conclusion

The excellent n-type performance of Mg_3Sb_2 is due to the fact that the CBM is located at the low-symmetry U* point in the BZ, which has a high valley degeneracy of $N_V = 6$ and relatively light m_I^*. In this chapter, we explore the chemical origins of the low-symmetry CBM in light of changes to the CB edge structure upon substitutions on the anion (and cation) site. While previous studies attribute the U* CBM to bonding interactions between the Mg(1) and Mg(2) orbitals, these interactions cannot fully explain the increase in mobility when Mg_3Sb_2 is alloyed with Bi on the Sb-site.

We show that that Mg-s–Sb-p anti-bonding interactions are consistent with the U* CBM and can explain mobility trends with respect to alloying on the Sb-site (with Bi or As). Based on DFT and COHP calculations, there is Mg-s–Sb-p anti-bonding character near the CB edge, which reaches a minimum in strength at U*. Increasing the strength of this interaction (e.g., substituting Sb with Bi) leads to an increase in band curvature around the CBM. Additionally, a TB model based on Mg_3Sb_2 qualitatively reproduces the U* CBM and highlights the importance of the Mg-s–Sb-p interactions. Furthermore, substitutions on the octahedrally coordinated Mg(1) site alter the behavior of the CB edge due to changes or disruptions to the Mg-s–Sb-p anti-bonding interactions. When Mg(1) is replaced by Be, the Ae-s–Sb-p (Ae = Be, Mg) interactions are still present near

the CB edge, so the U* CBM is maintained. On the other hand, when Mg(1) is replaced with more electropositive, isovalent species, such as Ca, Ba, or Sr, *Ae*-s states near the U* CB edge are replaced with states more closely resembling *Ae*-*d* orbitals, so the CBM moves toward the M-point.

Conclusion and Future Perspectives

Because the transport properties of thermoelectric materials depend greatly on their electronic band dispersions, band engineering in $\boldsymbol{k}$-space has proven highly effective in optimizing thermoelectric performance across a wide range of thermoelectric materials. Specifically, it is considered beneficial to have thermoelectric materials with *complex* Fermi surfaces, characterized by high valley degeneracy and carrier-pocket anisotropy. In this thesis, we investigated the orbital chemistry of and chemical trends in the complex electronic structures of a variety of thermoelectric semiconductors in order to better understand and predict band engineering strategies. A number of methods were employed to elucidate the chemistry of electronic structures, such as tight-binding (TB), density functional theory (DFT), crystal orbital Hamilton populations (COHP), and group theory.

We first explored the orbital chemistry of the valence bands in IV-VI semiconductors, like rock-salt PbTe. We developed a TB framework—including numerical, analytical, and visual descriptions—to understand important features in the valence bands of PbTe and applied this framework to explain the origins of high valley degeneracy and band convergence in PbTe. The TB model shows that the strength of cation-s–anion-p interactions are the primary determinants of Fermi surface complexity, with anion-p–anion-p interactions being of secondary importance, as the valence band maxima are primarily cation-s–anion-p anti-bonding states with mostly anion-p character. The anion-p–cation-p interactions are not particularly important in predicting trends in convergence—the valence band edges are non-bonding or nearly non-bonding with respect to these interactions—but they are important in explaining the locations of the different valence band pockets. Furthermore, we showed using TB that higher convergence in PbTe (and IV-VI rock salt semiconductors in generally) may

lead to changes to the Fermi surface complexity beyond a nominal increase in valley degeneracy. It may also lead to more fundamental changes to the nature of the Fermi surface, specifically the dimensionality of transport.

We then extended this IV-VI semiconductor framework to understand the chemical origins of changes in the valence band structure of GeTe upon the cubic to rhombohedral transformation, marked by a reduction in the primitive-cell interaxial angle and the offset of the Ge-atom from the center of the Te-octahedron. As GeTe transforms from its cubic to rhombohedral phase, the VBM goes from being located at the L-point (with the Σ band slightly lower) to being along the Σ-line. DFT calculations over a range of interaxial angles and offsets show that Fermi surface complexity is greatest when GeTe is in its cubic phase or *slightly* distorted. Also, using DFT, it is shown that the Ge-offset is primarily responsible for the Σ VBM in the rhombohedral phase, though the interaxial angle influences the relative energies of other valence band pockets. Using TB and COHP calculations, it is shown that changes with respect to the interaxial angle can be explained through changes to the *s*-*p* anti-bonding character at the various VBMs, while changes with respect to Ge-offset are largely due to the emergence of cation-*p*–anion-*p* bonding character (in tandem with a reduction in cation-*s*–anion-*p* anti-bonding character) in the valence band edges when inversion symmetry is broken.

Next, we investigated the chemistry of both the conduction and valence band edges in transition-metal-based half-Heusler thermoelectrics. There are three possible locations where the VBM can be located and two competing (potential) CBMs at the same $\boldsymbol{k}$-point, providing possible routes to enhance band convergence and achieve higher valley degeneracy for both n-type and p-type versions of these compounds. While the chemical trends dictating band convergence in half-Heuslers were fairly well-understood, the origins of these trends were not as well-understood because there is significant variation in the orbital character along the band edges. The discontinuity in orbital character renders simple molecular-orbital-like diagrams (representing only the Γ-point) insufficient for fully understanding the chemical make-up of the band edges. We explained the chemical ori-

gins of the band edges using $\boldsymbol{k}$-dependent bonding diagrams and showed that recognizing avoided crossings across the band gap are crucial for understanding the $\boldsymbol{k}$-dependent chemical contributions of the band edges. We employed band-resolved, $\boldsymbol{k}$-resolved COHP calculations in conjunction with group-theory and TB analysis to explain these avoided crossings and their implications for alloying strategies.

Finally, we explored the chemical origins of high conduction band degeneracy in Zintl-phase Mg_3Sb_2. $Mg_3(Sb, Bi)_2$ alloys are very high-performing mid-low temperature thermoelectrics due to the CBM being located at a low-symmetry, six-fold degenerate point in the Brillouin zone. While prior studies have suggested that Mg-s–Mg-s interactions are responsible for the low-symmetry CBM, we showed that this explanation cannot fully explain trends in electron mobility with respect to alloying. We proposed an alternative explanation that focuses on the importance of the cation-s–anion-p interactions. We show using DFT, COHP, and TB that these interactions can, in fact, explain the existence of the highly-degenerate CBM, in addition to explaining mobility trends with respect to alloying.

There are numerous possible topics for future investigation related to this dissertation. While this thesis focused primarily on Fermi surface complexity and high valley degeneracy, the orbital-chemistry approach to understanding electronic dispersions can be applied to a variety of different band structure features and associated properties, such as band gap energy, band inversion, carrier mobility, and deformation potential (see Equation 2.16) [68]. Additionally, applying codes that numerically (rather than analytically) predict transport properties, such as BoltzTrap2 [151] or AMSET [152], to TB band structures could provide new and unique types of insight into how different orbital interactions influence transport properties. Finally, predictions of how alloying will influence the band structure Fermi surface for all the material families discussed in this thesis can be explored using super-cell DFT calculations (e.g., special quasi-random structures).

References

[1] Tapan Chatterji, C. M.N. Kumar, and Urszula D. Wdowik. Anomalous temperature-induced volume contraction in GeTe. *Physical Review B*, 91(5):1–8, 2015.

[2] T. Chattopadhyay, J. X. Boucherle, and H. G. von Schnering. Neutron diffraction study on the structural phase transition in gete. *Journal of Physics C: Solid State Physics*, 20(10):1431–1440, 1987.

[3] A.L. Allred. Electronegativity values from thermochemical data. *Journal Inorg. Nucl. Chemistry*, 17(3):215–221, 1961.

[4] M.S. Dresselhaus, G. Dresselhaus, and A. Jorio. *Group Theory: Application to the Physics of Condensed Matter*. Springer Berlin Heidelberg, 2007.

[5] F.A. Cotton. *Chemical Applications of Group Theory*. Wiley India, 2003.

[6] G.S. Rohrer. *Structure and Bonding in Crystalline Materials*. Cambridge University Press, 2001.

[7] Lon E. Bell. Cooling, heating, generating power, and recovering waste heat with thermoelectric systems. *Science*, 321(5895):1457–1461, 2008.

[8] G Jeffrey Snyder and Eric S Toberer. Complex thermoelectric materials. *Nature Materials*, 7(2):105–114, 2008.

[9] D.M. Rowe. Applications of nuclear-powered thermoelectric generators in space. *Applied Energy*, 40(4):241–271, 1991.

[10] James P. Male. *Defect engineering for more reliable and efficient PbTe-based thermoelectric materials*. PhD thesis, Northwesern University, Evanston, Illinois, 2022.

[11] D.M. Rowe. *Thermoelectrics Handbook: Macro to Nano*. CRC Press, Boca Raton, 2006.

[12] Robert Freer and Anthony V. Powell. Realising the potential of thermoelectric technology: a roadmap. *Journal of Materials Chemistry A*, 8:441–463, 2020.

[13] B. Orr, A. Akbarzadeh, M. Mochizuki, and R. Singh. A review of car waste heat recovery systems utilising thermoelectric generators and heat pipes. *Applied Thermal Engineering*, 101:490–495, 2016.

[14] Shiho Kim, Soonseo Park, SunKook Kim, and Seok-Ho Rhi. A Thermoelectric Generator Using Engine Coolant for Light-Duty Internal Combustion Engine-Powered Vehicles. *Journal of Electronic Materials*, 40(5):812–816, 2011.

[15] G. Jeffrey Snyder, Saniya LeBlanc, Doug Crane, Herschel Pangborn, Chris E. Forest, Alex Rattner, Leah Borgsmiller, and Shashank Priya. Distributed and localized cooling with thermoelectrics. *Joule*, 5(4):748–751, 2021.

[16] Diana Enescu and Elena Otilia Virjoghe. A review on thermoelectric cooling parameters and performance. *Renewable and Sustainable Energy Reviews*, 38:903–916, 2014.

[17] Jun Mao, Gang Chen, and Zhifeng Ren. Thermoelectric cooling materials. *Nature Materials*, 20(4):454–461, 2021.

[18] Alex Zevalkink, David M. Smiadak, Jeff L. Blackburn, Andrew J Ferguson, Michael L. Chabinyc, Olivier Delaire, Jian Wang, Kirill Kovnir, Joshua Martin, Laura T. Schelhas, Taylor D. Sparks, Stephen D. Kang, Maxwell T. Dylla, G. Jeffrey Snyder, Brenden R. Ortiz, and Eric S. Toberer. A practical field guide to thermoelectrics: Fundamentals, synthesis, and characterization. *Applied Physical Review*, 5(2):021303, 2018.

[19] Xinyue Zhang, Zhonglin Bu, Xuemin Shi, Zhiwei Chen, Siqi Lin, Bing Shan, Maxwell Wood, Alemayouh H. Snyder, Lidong Chen, G. Jeffrey Snyder, and Yanzhong Pei. Electronic quality factor for thermoelectrics. *Science Advances*, 6(46):6–11, 2020.

[20] Wuyang Ren, Xin Shi, Zhiming Wang, and Zhifeng Ren. Crystallographic design for half-heuslers with low lattice thermal conductivity. *Materials Today Physics*, 25:100704, 2022.

[21] Manoj K Jana and Kanishka Biswas. Crystalline Solids with Intrinsically Low Lattice Thermal Conductivity for Thermoelectric Energy Conversion. *ACS Energy Letters*, 3(6):1315–1324, 2018.

[22] Di Wu, Li-Dong Zhao, Xiao Tong, Wei Li, Lijun Wu, Qing Tan, Yanling Pei, Li Huang, Jing-Feng Li, Yimei Zhu, et al. Superior thermoelectric performance in pbte–pbs pseudo-binary: extremely low thermal conductivity and modulated carrier concentration. *Energy & Environmental Science*, 8(7):2056–2068, 2015.

[23] Kazuki Imasato, Shashwat Anand, Ramya Gurunathan, and G. Jeffrey Snyder. The effect of Mg3As2 alloying on the thermoelectric properties of n-type Mg3(Sb, Bi)2. *Dalton Transactions*, 50(27):9376–9382, 2021.

[24] Riley Hanus, Matthias T. Agne, Alexander J. E. Rettie, Zhiwei Chen, Gangjian Tan, Duck Young Chung, Mercouri G. Kanatzidis, Yanzhong Pei, Peter W. Voorhees, and G. Jeffrey Snyder. Lattice softening significantly reduces thermal conductivity and leads to high thermoelectric efficiency. *Advanced Materials*, 31(21):1900108, 2019.

[25] Yee Kan Koh, C. J. Vineis, S. D. Calawa, M. P. Walsh, and David G. Cahill. Lattice thermal conductivity of nanostructured thermoelectric materials based on pbte. *Applied Physics Letters*, 94(15):153101, 2009.

[26] J. C. Caylor, K. Coonley, J. Stuart, T. Colpitts, and R. Venkatasubramanian. Enhanced thermoelectric performance in pbte-based superlattice structures from reduction of lattice thermal conductivity. *Applied Physics Letters*, 87(2):023105, 2005.

[27] Jiaqing He, Steven N. Girard, Mercouri G. Kanatzidis, and Vinayak P. Dravid. Microstructure-lattice thermal conductivity correlation in nanostructured pbte0.7s0.3 thermoelectric materials. *Advanced Functional Materials*, 20(5):764–772, 2010.

[28] Yanzhong Pei, Aaron D. LaLonde, Nicholas A. Heinz, and G. Jeffrey Snyder. High thermoelectric figure of merit in PbTe alloys demonstrated in PbTe-CdTe. *Advanced Energy Materials*, 2(6):670–675, 2012.

[29] Yanzhong Pei, Xiaoya Shi, Aaron Lalonde, Heng Wang, Lidong Chen, and G. Jeffrey Snyder. Convergence of electronic bands for high performance bulk thermoelectrics. *Nature*, 473(7345):66–69, 2011.

[30] Hong Zhu, Wenhao Sun, Rickard Armiento, Predrag Lazic, and Gerbrand Ceder. Band structure engineering through orbital interaction for enhanced thermoelectric power factor. *Applied Physics Letters*, 104(8):1–5, 2014.

[31] Chenguang Fu, Tiejun Zhu, Yintu Liu, Hanhui Xie, and Xinbing Zhao. Band engineering of high performance p-type fenbsb based half-heusler thermoelectric materials for figure of merit zt > 1. *Energy Environ. Science*, 8:216–220, 2015.

[32] Kazuki Imasato, Stephen Dongmin Kang, Saneyuki Ohno, and G. Jeffrey Snyder. Band engineering in Mg_3Sb_2 by alloying with Mg3Bi2 for enhanced thermoelectric performance. *Materials Horizons*, 5:59–64, 2018.

[33] Hyun-Sik Kim, Nicholas A. Heinz, Zachary M. Gibbs, Yinglu Tang, Stephen D. Kang, and G. Jeffrey Snyder. High thermoelectric performance in $(Bi_{0.25}Sb_{0.75})_2Te_3$ due to band convergence and improved by carrier concentration control. *Materials Today*, 20(8):452–459, 2017.

[34] Zachary M. Gibbs, Francesco Ricci, Guodong Li, Hong Zhu, Kristin Persson, Gerbrand Ceder, Geoffroy Hautier, Anubhav Jain, and G. Jeffrey Snyder. Effective mass and Fermi surface complexity factor from ab initio band structure calculations. *Npj Computational Materials*, 3(1):1–6, 2017.

[35] Yanzhong Pei, Heng Wang, and G. J. Snyder. Band Engineering of Thermoelectric Materials. *Advanced Materials*, 24(46):6125–6135, 2012.

[36] Junsoo Park, Maxwell Dylla, Yi Xia, Max Wood, G Jeffrey Snyder, and Anubhav Jain. When band convergence is not beneficial for thermoelectrics. *Nature Communications*, 12(1):3425, 2021.

[37] Jinfeng Dong, Yilin Jiang, Yandong Sun, Jue Liu, Jun Pei, Wei Li, Xian Yi Tan, Lei Hu, Ning Jia, Ben Xu, Qian Li, Jing-Feng Li, Qingyu Yan, and Mercouri G Kanatzidis. Discordant Distortion in Cubic GeMnTe2 and High Thermoelectric Properties of GeMnTe2-xSbTe. *Journal of the American Chemical Society*, 2023.

[38] Gangjian Tan, Li Dong Zhao, Fengyuan Shi, Jeff W. Doak, Shih Han Lo, Hui Sun, Chris Wolverton, Vinayak P. Dravid, Ctirad Uher, and Mercouri G. Kanatzidis. High thermoelectric performance of p-type SnTe via a synergistic band engineering and nanostructuring approach. *Journal of the American Chemical Society*, 136(19):7006–7017, 2014.

[39] Zheng Zheng, Xianli Su, Rigui Deng, Constantinos Stoumpos, Hongyao Xie, Wei Liu, Yonggao Yan, Shiqiang Hao, Ctirad Uher, Chris Wolverton, Mercouri G Kanatzidis, and Xinfeng Tang. Rhombohedral to Cubic Conversion of GeTe via MnTe Alloying Leads to Ultralow Thermal Conductivity, Electronic Band Convergence, and High Thermoelectric Performance. *Journal of the American Chemical Society*, 140(7):2673–2686, 2018.

[40] Hangtian Zhu, Ran He, Jun Mao, Qing Zhu, Chunhua Li, Jifeng Sun, Wuyang Ren, Yumei Wang, Zihang Liu, Zhongjia Tang, Andrei Sotnikov, Zhiming Wang, David Broido, David J Singh, Gang Chen, Kornelius Nielsch, and Zhifeng Ren. Discovery of ZrCoBi based half Heuslers with high thermoelectric conversion efficiency. *Nature Communications*, 9(1):2497, 2018.

[41] Ian T. Witting, Francesco Ricci, Thomas C. Chasapis, Geoffroy Hautier, and G. Jeffrey Snyder. The Thermoelectric Properties of n-Type Bismuth Telluride: Bismuth Selenide Alloys $Bi_2Te_{3-x}Se_x$. *Research*, 2020.

[42] J. J. Pulikkotil, D. J. Singh, S. Auluck, M. Saravanan, D. K. Misra, A. Dhar, and R. C. Budhani. Doping and temperature dependence of thermoelectric properties in Mg_2(Si,Sn). *Physical Review B*, 86(15):1–8, 2012.

[43] V. K. Zaitsev, M. I. Fedorov, E. A. Gurieva, I. S. Eremin, P. P. Konstantinov, A. Yu Samunin, and M. V. Vedernikov. Highly effective Mg2 Si1-x Snx thermoelectrics. *Physical Review B*, 74(4):2–6, 2006.

[44] Yinglu Tang, Zachary M Gibbs, Luis A Agapito, Guodong Li, Hyun-Sik Kim, Marco Buongiorno Nardelli, Stefano Curtarolo, and G Jeffrey Snyder. Convergence of multi-valley bands as the electronic origin of high thermoelectric performance in CoSb3 skutterudites. *Nature Materials*, 14(12):1223–1228, 2015.

[45] David Parker, Xin Chen, and David J. Singh. High Three-Dimensional Thermoelectric Performance from Low-Dimensional Bands. *Physical Review Letters*, 110(14):146601, 2013.

[46] Xin Chen, David Parker, and David J. Singh. Importance of non-parabolic band effects in the thermoelectric properties of semiconductors. *Science Rep.*, 3:3168, 2013.

[47] Madison K. Brod and G. Jeffrey Snyder. Orbital chemistry of high valence band convergence and low-dimensional topology in PbTe. *Journal of Materials Chemistry A*, 9:12119–12139, 2021.

[48] Georg Kresse and Jürgen Furthmüller. Efficiency of ab-initio total energy calculations for metals and semiconductors using a plane-wave basis set. *Computational Materials Science*, 6(1):15–50, 1996.

[49] G. Kresse. Ab initio molecular dynamics for liquid metals. *Journal of Non-Crystalline Solids*, 192:222–229, 1995.

[50] Georg Kresse and Jürgen Furthmüller. Efficient iterative schemes for ab initio total-energy calculations using a plane-wave basis set. *Physical Review B*, 54(16):11169, 1996.

[51] John P Perdew, Kieron Burke, and Matthias Ernzerhof. Generalized gradient approximation made simple. *Physical Review Letters*, 77(18):3865, 1996.

[52] Richard Dronskowski and Peter E. Blöchl. Crystal orbital hamilton populations (COHP). Energy-resolved visualization of chemical bonding in solids based on density-functional calculations. *Journal of Physical Chemistry*, 97(33):8617–8624, 1993.

[53] Stefan Maintz, Volker L Deringer, Andrei L Tchougréeff, and Richard Dronskowski. Analytic projection from plane-wave and paw wavefunctions and application to chemical-bonding analysis in solids. *Journal Computational Chemistry*, 34(29):2557—2567, 2013.

[54] Stefan Maintz, Volker L. Deringer, Andrei L. Tchougréeff, and Richard Dronskowski. LOBSTER: A tool to extract chemical bonding from plane-wave based DFT. *Journal Computational Chemistry*, 37(11):1030–1035, 2016.

[55] Madison K Brod, Michael Y Toriyama, and G Jeffrey Snyder. Orbital chemistry that leads to high valley degeneracy in pbte. *Chemistry of Materials*, 32(22):9771–9779, 2020.

[56] Andrew F. May and Gerald Jeffrey Snyder. *Introduction to modeling thermoelectric transport at high temperatures*, pages 11–1–11–18. CRC Press, 2017.

[57] Stephen Dongmin Kang. *Charge Transport Analysis Using the Seebeck Coefficient-Conductivity Relation*. PhD thesis, California Institute of Technology, Pasadena, California, 2018.

[58] Stephen Dongmin Kang and G. Jeffrey Snyder. Charge-transport model for conducting polymers. *Nature Materials*, 16(2):252–257, 2017.

[59] J. Bardeen and W. Shockley. Deformation potentials and mobilities in non-polar crystals. *Physical Review*, 80:72–80, 1950.

[60] Conyers Herring and Erich Vogt. Transport and deformation-potential theory for many-valley semiconductors with anisotropic scattering. *Physical Review*, 101:944–961, 1956.

[61] P. Rhodes and Edmund Clifton Stoner. Fermi-dirac functions of integral order. *Proceedings of the Royal Society of London. Series A. Mathematical and Physical Sciences*, 204(1078):396–405, 1950.

[62] Roald Hoffmann. How chemistry and physics meet in the solid state. *Angew. Chemistry, Int. Ed. Engl.*, 26(9):846–878, 1987.

[63] Walter A. Harrison. *Electronic Structure and the Properties of Solids: The Physics of the Chemical Bond*. Dover Books on Physics. Dover Publications, 1989.

[64] Walter A. Harrison. Tight-binding theory of molecules and solids. *Pure Applied Chemistry*, 61(12):2161–2169, 1989.

[65] J. C. Slater and G. F. Koster. Simplified LCAO method for the periodic potential problem. *Physical Review*, 94(6):1498–1524, 1954.

[66] Wolfgang G. Zeier, Alex Zevalkink, Zachary M. Gibbs, Geoffroy Hautier, Mercouri G. Kanatzidis, and G. Jeffrey Snyder. Thinking Like a Chemist: Intuition in Thermoelectric Materials. *Angewandte Chemie International Edition*, 55(24):6826–6841, 2016.

[67] N.W. Ashcroft and N.D. Mermin. *Solid State Physics*. Saunders College, Philadelphia, 1976.

[68] Jiawei Zhou, Hangtian Zhu, Te Huan Liu, Qichen Song, Ran He, Jun Mao, Zihang Liu, Wuyang Ren, Bolin Liao, David J Singh, Zhifeng Ren, and Gang Chen. Large thermoelectric power factor from crystal symmetry-protected non-bonding orbital in half-Heuslers. *Nature Communications*, 9(1):1–9, 2018.

[69] Maxwell Thomas Dylla, Stephen Dongmin Kang, and G. Jeffrey Snyder. Effect of Two-Dimensional Crystal Orbitals on Fermi Surfaces and Electron Transport in Three-Dimensional Perovskite Oxides. *Angewandte Chemie - International Edition*, 58(17):5503–5512, 2019.

[70] Li Dong Zhao, Vinayak P. Dravid, and Mercouri G. Kanatzidis. The panoscopic approach to high performance thermoelectrics. *Energy and Environmental Science*, 7(1):251–268, 2014.

[71] L. D. Zhao, H. J. Wu, S. Q. Hao, C. I. Wu, X. Y. Zhou, K. Biswas, J. Q. He, T. P. Hogan, C. Uher, C. Wolverton, V. P. Dravid, and M. G. Kanatzidis. All-scale hierarchical thermoelectrics: Mgte in pbte facilitates valence band convergence and suppresses bipolar thermal transport for high performance. *Energy and Environmental Science*, 6:3346–3355, 2013.

[72] Yanzhong Pei, Aaron Lalonde, Shiho Iwanaga, and G. Jeffrey Snyder. High thermoelectric figure of merit in heavy hole dominated PbTe. *Energy and Environmental Science*, 4(6):2085–2089, 2011.

[73] Yanzhong Pei, Aaron D. LaLonde, Nicholas A. Heinz, Xiaoya Shi, Shiho Iwanaga, Heng Wang, Lidong Chen, and G. Jeffrey Snyder. Stabilizing the optimal carrier concentration for high thermoelectric efficiency. *Advanced Materials*, 23(47):5674–5678, 2011.

[74] Aaron D. LaLonde, Yanzhong Pei, Heng Wang, and G. Jeffrey Snyder. Lead telluride alloy thermoelectrics. *Materials Today*, 14(11):526 – 532, 2011.

[75] Yanzhong Pei, Heng Wang, Zachary M Gibbs, Aaron D LaLonde, and G Jeffrey Snyder. Thermopower enhancement in Pb1xMnxTe alloys and its effect on thermoelectric efficiency. *NPG Asia Materials*, 4(9):e28–e28, 2012.

[76] Yu. I. Ravich, B. A. Efimova, and I. A. Smirnov. *Semiconducting Lead Chalcogenides*, volume 5 of *Monographs in Semiconductor Physics*, chapter Band Structure and Scattering Mechanisms (Theory and Conclusions from Experimental Data), pages 263–322. Springer, Boston, MA, 1970.

[77] Zachary M. Gibbs, Hyoungchul Kim, Heng Wang, Robert L. White, Fivos Drymiotis, Massoud Kaviany, and G. Jeffrey Snyder. Temperature dependent band gap in PbX (X = S, Se, Te). *Applied Physics Letters*, 103(26), 2013.

[78] Ransell D'Souza, Jiang Cao, José D. Querales-Flores, Stephen Fahy, and Ivana Savić. Electron-phonon scattering and thermoelectric transport in *p*-type pbte from first principles. *Physical Review B*, 102:115204, 2020.

[79] A. J. Crocker and L. M. Rogers. Interpretation of the Hall coefficient, electrical resistivity and Seebeck coefficient of p-type lead telluride. *British Journal Applied Physics*, 18(5):563–573, 1967.

[80] David J. Singh. Doping-dependent thermopower of PbTe from Boltzmann transport calculations. *Physical Review B*, 81:195217, 2010.

[81] José D. Querales-Flores, Jiang Cao, Stephen Fahy, and Ivana Savić. Temperature effects on the electronic band structure of pbte from first principles. *Physical Review Materials*, 3:055405, 2019.

[82] H. Sitter, K. Lischka, and H. Heinrich. Structure of the second valence band in pbte. *Physical Review B*, 16:680–687, 1977.

[83] R. N. Tauber, A. A. MacHonis, and I. B. Cadoff. Thermal and optical energy gaps in PbTe. *Journal of Applied Physics*, 37(13):4855–4860, 1966.

[84] Roald Hoffmann. How Chemistry and Physics Meet in the Solid State. *Angew. Chemistry Int. Ed. Engl.*, 26(9):846–878, 1987.

[85] Haowei Peng, Jung Hwan Song, M. G. Kanatzidis, and Arthur J. Freeman. Electronic structure and transport properties of doped PbSe. *Physical Review B: Condensed Matter Physics*, 84(12):1–13, 2011.

[86] Su Huai Wei and Alex Zunger. Electronic and structural anomalies in lead chalcogenides. *Physical Review B: Condensed Matter*, 55(20):13605–13610, 1997.

[87] Peter E Blöchl. Projector augmented-wave method. *Physical Review B*, 50(24):17953, 1994.

[88] Georg Kresse and Daniel Joubert. From ultrasoft pseudopotentials to the projector augmented-wave method. *Physical Review B*, 59(3):1758, 1999.

[89] Hendrik J Monkhorst and James D Pack. Special points for Brillouin-zone integrations. *Physical Review B*, 13(12):5188, 1976.

[90] Michael Y. Toriyama, Madison K. Brod, Lídia C. Gomes, Ferdaushi A. Bipasha, Badih A. Assaf, Elif Ertekin, and G. Jeffrey Snyder. Tuning valley degeneracy with band inversion. *Journal of Materials Chemistry A*, 10:1588–1595, 2022.

[91] Gangjian Tan, Wolfgang G. Zeier, Fengyuan Shi, Pengli Wang, G. Jeffery Snyder, Vinayak P. Dravid, and Mercouri G. Kanatzidis. High Thermoelectric Performance SnTe-In2Te3 Solid Solutions Enabled by Resonant Levels and Strong Vacancy Phonon Scattering. *Chemistry of Materials*, 27(22):7801–7811, 2015.

[92] Suresh Perumal, Pavithra Bellare, U. Sandhya Shenoy, Umesh V. Waghmare, and Kanishka Biswas. Low Thermal Conductivity and High Thermoelectric Performance in Sb and Bi Codoped GeTe: Complementary Effect of Band Convergence and Nanostructuring. *Chemistry of Materials*, 29(24):10426–10435, 2017.

[93] Jinfeng Dong, Fu Hua Sun, Huaichao Tang, Jun Pei, Hua Lu Zhuang, Hai Hua Hu, Bo Ping Zhang, Yu Pan, and Jing Feng Li. Medium-temperature thermoelectric GeTe: Vacancy suppression and band structure engineering leading to high performance. *Energy Environ. Sci.*, 12(4):1396–1403, 2019.

[94] Tianyu Wang, Chun Zhang, Jia-Yue Yang, and Linhua Liu. Engineering the electronic band structure and thermoelectric performance of GeTe via lattice structure manipulation from first-principles. *Physical Chemistry Chemical Physics*, 23:23576–23585, 2021.

[95] Ananya Banik, U Sandhya Shenoy, Shashwat Anand, Umesh V Waghmare, and Kanishka Biswas. Mg Alloying in SnTe Facilitates Valence Band Convergence and Optimizes Thermoelectric Properties. *Chemistry of Materials*, 27(2):581–587, 2015.

[96] Zachary M Gibbs, Aaron LaLonde, and G Jeffrey Snyder. Optical band gap and the burstein–moss effect in iodine doped PbTe using diffuse reflectance infrared fourier transform spectroscopy. *New Journal of Physics*, 15(7):075020, 2013.

[97] Priyanka Jood, James P Male, Shashwat Anand, Yoshitaka Matsushita, Yoshiki Takagiwa, Mercouri G Kanatzidis, G Jeffrey Snyder, and Michihiro Ohta. Na Doping in PbTe: Solubility, Band Convergence, Phase Boundary Mapping, and Thermoelectric Properties. *Journal of the American Chemical Society*, 142(36):15464–15475, 2020.

[98] L M Rogers and A J Crocker. Transport properties of the $Cd_xPb_{1-x}Te$ Alloy System. *Journal of Physics D: Applied Physics*, 4(7):1006–1015, 1971.

[99] A. Crocker and L. Rogers. Valence Band Structure of PbTe. *Journal de Physique Colloques*, 29(C4):C4–129–C4–132, 1968.

[100] J.J. Harris and B.K. Ridley. Room temperature transport properties of p-type PbTe. *Journal of Physics and Chemistry of Solids*, 33(7):1455 – 1464, 1972.

[101] Daniel I. Bilc, Geoffroy Hautier, David Waroquiers, Gian-Marco Rignanese, and Philippe Ghosez. Low-dimensional transport and large thermoelectric power factors in bulk semiconductors by band engineering of highly directional electronic states. *Physical Review Letters*, 114:136601, 2015.

[102] Raseong Kim, Supriyo Datta, and Mark S. Lundstrom. Influence of dimensionality on thermoelectric device performance. *Journal of Applied Physics*, 105(3):034506, 2009.

[103] L. D. Hicks and M. S. Dresselhaus. Thermoelectric figure of merit of a one-dimensional conductor. *Physical Review B*, 47:16631–16634, 1993.

[104] M.S. Dresselhaus, G. Chen, M.Y. Tang, R.G. Yang, H. Lee, D.Z. Wang, Z.F. Ren, J.-P. Fleurial, and P. Gogna. New directions for low-dimensional thermoelectric materials. *Advanced Materials*, 19(8):1043–1053, 2007.

[105] Joseph P. Heremans, Mildred S. Dresselhaus, Lon E. Bell, and Donald T. Morelli. When thermoelectrics reached the nanoscale. *Nature Nanotechnology*, 8(7):471 – 473, 2013.

[106] Jane E. Cornett and Oded Rabin. Thermoelectric figure of merit calculations for semiconducting nanowires. *Applied Physics Letters*, 98(18):182104, 2011.

[107] Jane E. Cornett and Oded Rabin. Universal scaling relations for the thermoelectric power factor of semiconducting nanostructures. *Physical Review B*, 84:205410, 2011.

[108] Junsoo Park, Yi Xia, Vidvuds Ozoliņš, and Anubhav Jain. Optimal band structure for thermoelectrics with realistic scattering and bands. *npj Computational Materials*, 7(1):43, 2021.

[109] Kerstin Hummer, Andreas Grüneis, and Georg Kresse. Structural and electronic properties of lead chalcogenides from first principles. *Physical Review B - Condensed Matter and Materials Physics*, 75(19):1–9, 2007.

[110] Anuj Goyal, Prashun Gorai, Eric S. Toberer, and Vladan Stevanović. First-principles calculation of intrinsic defect chemistry and self-doping in PbTe. *npj Computational Materials*, 3(1):1–9, 2017.

[111] Matteo Cagnoni, Daniel Führen, and Matthias Wuttig. Thermoelectric Performance of IV–VI Compounds with Octahedral-Like Coordination: A Chemical-Bonding Perspective. *Advanced Materials*, 30(33), 2018.

[112] Jonathan M. Skelton, Stephen C. Parker, Atsushi Togo, Isao Tanaka, and Aron Walsh. Thermal physics of the lead chalcogenides pbs, pbse, and pbte from first principles. *Physical Review B*, 89:205203, 2014.

[113] Madison K. Brod, Shashwat Anand, and G. Jeffrey Snyder. The Importance of Mg–Sb Interactions in Achieving High Conduction Band Degeneracy in Mg3Sb2 for High n-Type Thermoelectric Performance. *Materials Today Physics*, 31:100959, 2023.

[114] Xing Gao and Murray S. Daw. Investigation of band inversion in (pb,sn)te alloys using ab initio calculations. *Physical Review B*, 77:033103, 2008.

[115] Na Wang, Damien West, Junwei Liu, Jia Li, Qimin Yan, Bing Lin Gu, S. B. Zhang, and Wenhui Duan. Microscopic origin of the p -type conductivity of the topological crystalline insulator SnTe and the effect of Pb alloying. *Physical Review B - Condensed Matter and Materials Physics*, 89(4):1–6, 2014.

[116] Zhen-Yu Ye, Hui-Xiong Deng, Hui-Zhen Wu, Shu-Shen Li, Su-Huai Wei, and Jun-Wei Luo. The origin of electronic band structure anomaly in topological crystalline insulator group-IV tellurides. *npj Computational Materials*, 1(1):15001, 2015.

[117] Jim Phillips. *Bonds and bands in semiconductors*. Elsevier, 2012.

[118] Martin Jansen. Effects of relativistic motion of electrons on the chemistry of gold and platinum. *Solid State Sciences*, 7(12):1464–1474, 2005. Special issue in honour of C.N.R. Rao.

[119] Pablo Aguado-Puente, Stephen Fahy, and Myrta Grüning. *gw* study of pressure-induced topological insulator transition in group-iv tellurides. *Physical Review Research*, 2:043105, 2020.

[120] Raza Moshwan, Lei Yang, Jin Zou, and Zhi-Gang Chen. Eco-Friendly SnTe Thermoelectric Materials: Progress and Future Challenges. *Advanced Functional Materials*, 27(43):1703278, 2017.

[121] Suresh Perumal, Subhajit Roychowdhury, and Kanishka Biswas. High performance thermoelectric materials and devices based on GeTe. *Journal of Materials Chemistry C*, 4(32):7520–7536, 2016.

[122] Ming Liu, Jianbo Zhu, Bo Cui, Fengkai Guo, Zihang Liu, Yuke Zhu, Muchun Guo, Yuxin Sun, Qian Zhang, Yongsheng Zhang, Wei Cai, and Jiehe Sui. High-performance lead-free cubic gete-based thermoelectric alloy. *Cell Reports Physical Science*, 3(6):100902, 2022.

[123] M. O. Nestoklon, R. Benchamekh, and P. Voisin. Virtual crystal description of III-V semiconductor alloys in the tight binding approach. *Journal of Physics Condensed Matter*, 28(30):11–16, 2016.

[124] L. Bellaiche, S. H. Wei, and Alex Zunger. Band gaps of GaPN and GaAsN alloys. *Applied Physics Letters*, 70(26):3558–3560, 1997.

[125] L. Bellaiche and David Vanderbilt. Virtual crystal approximation revisited: Application to dielectric and piezoelectric properties of perovskites. *Physical Review B - Condensed Matter and Materials Physics*, 61(12):7877–7882, 2000.

[126] Jesús Jiménez Arias, Daniel Suescun Díaz, and Diego A. Rasero Causil. Tight-binding study of the structure of the electronic energy band of the quaternary solid solutions series CuIn1xAlxTe2. *European Physical Journal B*, 92(5), 2019.

[127] Vahid Askarpour and Jesse Maassen. First-principles analysis of intravalley and intervalley electron-phonon scattering in thermoelectric materials. *Physical Review B*, 107:045203, Jan 2023.

[128] Stephen Dongmin Kang and G. Jeffrey Snyder. Transport property analysis method for thermoelectric materials: Material quality factor and the effective mass model. *arXiv*, pages 1–5, 2017.

[129] Min Hong, Jin Zou, and Zhi Gang Chen. Thermoelectric GeTe with Diverse Degrees of Freedom Having Secured Superhigh Performance. *Advanced Materials*, 31(14):1–23, 2019.

[130] Zhe Guo, Gang Wu, Xiaojian Tan, Ruoyu Wang, Zongwei Zhang, Guangjie Wu, Qiang Zhang, Jiehua Wu, Guo-Qiang Liu, and Jun Jiang. Enhanced thermoelectric performance in gete by synergy of midgap state and band convergence. *Advanced Functional Materials*, page 2212421, 2022.

[131] Juan Li, Shuai Zhang, Boyi Wang, Shichao Liu, Luo Yue, Guiwu Lu, and Shuqi Zheng. Designing high-performance n-type Mg_3Sb_2-based thermoelectric materials through forming solid solutions and biaxial strain. *Journal of Materials Chemistry A*, 6:20454–20462, 2018.

[132] Meng Li, Qiang Sun, Sheng Duo Xu, Min Hong, Wan Yu Lyu, Ji Xing Liu, Yuan Wang, Matthew Dargusch, Jin Zou, and Zhi Gang Chen. Optimizing Electronic Quality Factor toward High-Performance $Ge_{1xy}Ta_xSb_yTe$ Thermoelectrics: The Role of Transition Metal Doping. *Advanced Materials*, 33(40):1–8, 2021.

[133] Juan Li, Xinyue Zhang, Xiao Wang, Zhonglin Bu, Liangtao Zheng, Binqiang Zhou, Fen Xiong, Yue Chen, and Yanzhong Pei. High-Performance GeTe Thermoelectrics in Both Rhombohedral and Cubic Phases. *Journal of the American Chemical Society*, 140(47):16190–16197, 2018.

[134] Min Hong, Wanyu Lyv, Meng Li, Shengduo Xu, Qiang Sun, Jin Zou, and Zhi Gang Chen. Rashba Effect Maximizes Thermoelectric Performance of GeTe Derivatives. *Joule*, 4(9):2030–2043, 2020.

[135] F. Guo, M. Liu, J. Zhu, Z. Liu, Y. Zhu, M. Guo, X. Dong, Q. Zhang, Y. Zhang, W. Cai, and J. Sui. Suppressing lone-pair expression endows room-temperature cubic structure and high thermoelectric performance in GeTe-based materials. *Materials Today Physics*, 27:100780, 2022.

[136] Sichen Duan, Wenhua Xue, Honghao Yao, Xinyu Wang, Chen Wang, Shan Li, Zongwei Zhang, Li Yin, Xin Bao, Lihong Huang, Xiaodong Wang, Chen Chen, Jiehe Sui, Yue Chen, Jun Mao, Feng Cao, Yumei Wang, and Qian Zhang. Achieving High Thermoelectric Performance by NaSbTe2 Alloying in GeTe for Simultaneous Suppression of Ge Vacancies and Band Tailoring. *Advanced Energy Materials*, 12(3):1–8, 2022.

[137] Wahyu Setyawan and Stefano Curtarolo. High-throughput electronic band structure calculations: Challenges and tools. *Computational Materials Science*, 49(2):299–312, 2010.

[138] Meng Li, Min Hong, Xiao Tang, Qiang Sun, Wan-Yu Lyu, Sheng-Duo Xu, Liang-Zhi Kou, Matthew Dargusch, Jin Zou, and Zhi-Gang Chen. Crystal symmetry induced structure and bonding manipulation boosting thermoelectric performance of GeTe. *Nano Energy*, 73:104740, 2020.

[139] Juan Li, Zhiwei Chen, Xinyue Zhang, Yongxing Sun, Jiong Yang, and Yanzhong Pei. Electronic origin of the high thermoelectric performance of GeTe among the p-type group IV monotellurides. *NPG Asia Materials*, 9(3), 2017.

[140] Xinyue Zhang, Zhonglin Bu, Siqi Lin, Zhiwei Chen, Wen Li, and Yanzhong Pei. GeTe Thermoelectrics. *Joule*, 4(5):986–1003, 2020.

[141] J.N Bierly, L Muldawer, and O Beckman. The continuous rhombohedral-gubic transformation in gete-snte alloys. *Acta Metallurgica*, 11(5):447–454, 1963.

[142] Z. Bu, W. Li, J. Li, X. Zhang, J. Mao, Y. Chen, and Y. Pei. Dilute Cu2Te-alloying enables extraordinary performance of r-GeTe thermoelectrics. *Materials Today Physics*, 9:100096, 2019.

[143] Juan Li, Qing Hu, Shan He, Xiaobo Tan, Qian Deng, Yan Zhong, Fujie Zhang, and Ran Ang. Enhancing near-room-temperature gete thermoelectrics through in/pb co-doping. *ACS Applied Materials & Interfaces*, 13(31):37273–37279, 2021. PMID: 34319070.

[144] J. C. Woolley and P. Nikolic. Some properties of GeTe-PbTe alloys. *Journal of The Electrochemical Society*, 112(1):82, 1965.

[145] Jesse M. Adamczyk, Ferdaushi A. Bipasha, Grace Ann Rome, Kamil Ciesielski, Elif Ertekin, and Eric S. Toberer. Symmetry breaking in ge1xmnxte and the impact on thermoelectric transport. *Journal of Materials Chemistry A*, 10:16468–16477, 2022.

[146] Zhonglin Bu, Zhiwei Chen, Xinyue Zhang, Siqi Lin, Jianjun Mao, Wen Li, Yue Chen, and Yanzhong Pei. Near-room-temperature rhombohedral ge1-xpbxte thermoelectrics. *Materials Today Physics*, 15:100260, 2020.

[147] Aron Walsh, David J. Payne, Russell G. Egdell, and Graeme W. Watson. Stereochemistry of post-transition metal oxides: revision of the classical lone pair model. *Chemical Society Reviews*, 40:4455–4463, 2011.

[148] Aamir Shafique and Young Han Shin. Thermoelectric and phonon transport properties of two-dimensional IV-VI compounds. *Scientific Reports*, 7(1):1–10, 2017.

[149] Domenico Di Sante, Paolo Barone, Riccardo Bertacco, and Silvia Picozzi. Electric control of the giant rashba effect in bulk gete. *Advanced Materials*, 25(4):509–513, 2013.

[150] Volker L Deringer, Andrei L Tchougréeff, and Richard Dronskowski. Crystal Orbital Hamilton Population (COHP) Analysis As Projected from Plane-Wave Basis Sets. *Journal of Physical Chemistry A*, 115(21):5461–5466, 2011.

[151] Georg K.H. Madsen, Jesús Carrete, and Matthieu J. Verstraete. Boltztrap2, a program for interpolating band structures and calculating semi-classical transport coefficients. *Computer Physics Communications*, 231:140–145, 2018.

[152] Alex M Ganose, Junsoo Park, Alireza Faghaninia, Rachel Woods-Robinson, Kristin A Persson, and Anubhav Jain. Efficient calculation of carrier scattering rates from first principles. *Nature Communications*, 12(1):2222, 2021.

[153] Madison K Brod, Shashwat Anand, and G Jeffrey Snyder. The importance of avoided crossings in understanding high valley degeneracy in half-heusler thermoelectric semiconductors. *Advanced Electronic Materials*, 8(4):2101367, 2022.

[154] Hangtian Zhu, Jun Mao, Yuwei Li, Jifeng Sun, Yumei Wang, Qing Zhu, Guannan Li, Qichen Song, Jiawei Zhou, Yuhao Fu, Ran He, Tian Tong, Zihang Liu, Wuyang Ren, Li You, Zhiming Wang, Jun Luo, Andrei Sotnikov, Jiming Bao, Kornelius Nielsch, Gang Chen, David J Singh, and Zhifeng Ren. Discovery of TaFeSb-based half-Heuslers with high thermoelectric performance. *Nature Commuications*, 10(1):270, 2019.

[155] Shashwat Anand, Kaiyang Xia, Vinay I. Hegde, Umut Aydemir, Vancho Kocevski, Tiejun Zhu, Chris Wolverton, and G. Jeffrey Snyder. A valence balanced rule for discovery of 18-electron half-Heuslers with defects. *Energy and Environmental Science*, 11(6):1480–1488, 2018.

[156] F G Aliev, V V Kozyrkov, V V Moshchalkov, R V Scolozdra, and K Durczewski. Narrow band in the intermetallic compounds MNiSn (M=Ti, Zr, Hf). *Zeitschrift für Physik B Condensed Matter*, 80(3):353–357, 1990.

[157] Tanja Graf, Claudia Felser, and Stuart S.P. Parkin. Simple rules for the understanding of Heusler compounds. *Progress in Solid State Chemistry*, 39(1):1–50, 2011.

[158] JosephR. Sootsman, DuckYoung Chung, and MercouriG. Kanatzidis. New and old concepts in thermoelectric materials. *Angewandte Chemie International Edition*, 48(46):8616–8639, 2009.

[159] Lihong Huang, Qinyong Zhang, Bo Yuan, Xiang Lai, Xiao Yan, and Zhifeng Ren. Recent progress in half-heusler thermoelectric materials. *Materials Research Bulletin*, 76:107–112, 2016.

[160] S Joseph Poon, Di Wu, Song Zhu, Wenjie Xie, Terry M Tritt, Peter Thomas, and Rama Venkatasubramanian. Half-Heusler phases and nanocomposites as emerging high-ZT thermoelectric materials. *Journal of Materials Research*, 26(22):2795–2802, 2011.

[161] Wolfgang G. Zeier, Jennifer Schmitt, Geoffroy Hautier, Umut Aydemir, Zachary M. Gibbs, Claudia Felser, and G. Jeffrey Snyder. Engineering half-Heusler thermoelectric materials using Zintl chemistry. *Nature Reviews Materials*, 1(6):16032, 2016.

[162] M.M. Al Malki, Q. Qiu, T. Zhu, G.J. Snyder, and D.C. Dunand. Creep behavior and postcreep thermoelectric performance of the n-type half-Heusler alloy Hf0.3Zr0.7NiSn0.98Sb0.02. *Materials Today Physics*, 9:100134, 2019.

[163] Lihong Huang, Ran He, Shuo Chen, Hao Zhang, Keshab Dahal, Haiqing Zhou, Hui Wang, Qinyong Zhang, and Zhifeng Ren. A new n-type half-Heusler thermoelectric material NbCoSb. *Materials Research Bulletin*, 70:773–778, 2015.

[164] Shashwat Anand, Kaiyang Xia, Tiejun Zhu, Chris Wolverton, and Gerald Jeffrey Snyder. Temperature dependent n-type self doping in nominally 19-electron half-heusler thermoelectric materials. *Advanced Energy Materials*, 8(30):1801409, 2018.

[165] Jan Willem G. Bos and Ruth A. Downie. Half-Heusler thermoelectrics: A complex class of materials. *Journal of Physics: Condensed Matter*, 26(43), 2014.

[166] Alexander Page, P. F.P. Poudeu, and Ctirad Uher. A first-principles approach to half-Heusler thermoelectrics: Accelerated prediction and understanding of material properties. *Journal Materiomics*, 2(2):104–113, 2016.

[167] P. Larson, S. D. Mahanti, and M. G. Kanatzidis. Structural stability of Ni-containing half-Heusler compounds. *Physical Review B*, 62(19):12754–12762, 2000.

[168] B. R. K. Nanda and I. Dasgupta. Electronic structure and magnetism in half-Heusler compounds. *Journal of Physics: Condensed Matter*, 15(43):7307–7323, 2003.

[169] Serdar Öğüt and Karin M. Rabe. Band gap and stability in the ternary intermetallic compounds nisnm (m=ti,zr,hf): A first-principles study. *Physical Review B*, 51:10443–10453, 1995.

[170] Susan Mary Kauzlarich. *Chemistry, structure, and bonding of Zintl phases and ions*. VCH Publishers, 1996.

[171] Eric S Toberer, Andrew F May, and G Jeffrey Snyder. Zintl Chemistry for Designing High Efficiency Thermoelectric Materials. *Chemistry of Materials*, 22(3):624–634, 2010.

[172] Reinhard Nesper. The zintl-klemm concept – a historical survey. *Z Anorg Allg Chem*, 640(14):2639–2648, 2014.

[173] Alex Zevalkink, Wolfgang G Zeier, Ethan Cheng, Jeffrey Snyder, Jean-Pierre Fleurial, and Sabah Bux. Nonstoichiometry in the Zintl Phase Yb1δZn2Sb2 as a Route to Thermoelectric Optimization. *Chemistry of Materials*, 26(19):5710–5717, 2014.

[174] Slade R. Culp, J. W. Simonson, S. Joseph Poon, V. Ponnambalam, J. Edwards, and Terry M. Tritt. (zr,hf)co(sb,sn) half-heusler phases as high-temperature (>700°c) p-type thermoelectric materials. *Applied Physics Letters*, 93(2):022105, 2008.

[175] Slade R. Culp, S. Joseph Poon, Nicoleta Hickman, Terry M. Tritt, and J. Blumm. Effect of substitutions on the thermoelectric figure of merit of half-Heusler phases at 800°C. *Applied Physics Letters*, 88(4):1–3, 2006.

[176] Shuo Chen, Kevin C. Lukas, Weishu Liu, Cyril P. Opeil, Gang Chen, and Zhifeng Ren. Effect of Hf concentration on thermoelectric properties of nanostructured n-type half-heusler materials HfxZr1-xNiSn 0.99Sb0.01. *Advanced Energy Materials*, 3(9):1210–1214, 2013.

[177] Bo Yuan, Bo Wang, Lihong Huang, Xiaobo Lei, Lidong Zhao, Chao Wang, and Qinyong Zhang. Effects of Sb Substitution by Sn on the Thermoelectric Properties of ZrCoSb. *Journal of Electronic Materials*, 46(5):3076–3082, 2017.

[178] Kenta Kawano, Ken Kurosaki, Takeyuki Sekimoto, Hiroaki Muta, and Shinsuke Yamanaka. Effect of sn doping on the thermoelectric properties of ernisb-based p-type half-heusler compound. *Applied Physics Letters*, 91(6):062115, 2007.

[179] Nathan J Takas, Pranati Sahoo, Dinesh Misra, Hongfang Zhao, Nathaniel L Henderson, Kevin Stokes, and Pierre F P Poudeu. Effects of Ir Substitution and Processing Conditions on Thermoelectric Performance of p-Type Zr0.5Hf0.5Co1xIrxSb0.99Sn0.01 Half-Heusler Alloys. *Journal Electron. Materials*, 40(5):662–669, 2011.

[180] Yuanfeng Liu and Pierre F.P. Poudeu. Thermoelectric properties of Ge doped n-type TixZr1-xNiSn0.975Ge0.025 half-Heusler alloys. *Journal of Materials Chemistry A*, 3(23):12507–12514, 2015.

[181] Shashwat Anand, Max Wood, Yi Xia, Chris Wolverton, and G Jeffrey Snyder. Double half-heuslers. *Joule*, 3(5):1226–1238, 2019.

[182] Maxwell T. Dylla, Alexander Dunn, Shashwat Anand, Anubhav Jain, and G. Jeffrey Snyder. Machine Learning Chemical Guidelines for Engineering Electronic Structures in Half-Heusler Thermoelectric Materials. *Research*, 2020:1–8, 2020.

[183] Stanislav Chadov, Xiaoliang Qi, Jürgen Kübler, Gerhard H. Fecher, Claudia Felser, and Shou Cheng Zhang. Tunable multifunctional topological insulators in ternary Heusler compounds. *Nature Materials*, 9(7):541–545, 2010.

[184] F. Casper, T. Graf, S. Chadov, B. Balke, and C. Felser. Half-Heusler compounds: Novel materials for energy and spintronic applications. *Semicond Sci Technol*, 27(6), 2012.

[185] Guangqian Ding, G. Y. Gao, Li Yu, Yun Ni, and KaiLun Yao. Thermoelectric properties of half-Heusler topological insulators MPtBi (M=Sc, Y, La) induced by strain. *Journal of Applied Physics*, 119(2):025105, 2016.

[186] Kulwinder Kaur, Shobhna Dhiman, and Ranjan Kumar. Emergence of thermoelectricity in half heusler topological semimetals with strain. *Physics Letters A*, 381(4):339–343, 2017.

[187] Hsin Lin, L Andrew Wray, Yuqi Xia, Suyang Xu, Shuang Jia, Robert J Cava, Arun Bansil, and M Zahid Hasan. Half-Heusler ternary compounds as new multifunctional experimental platforms for topological quantum phenomena. *Nature Materials*, 9(7):546–549, 2010.

[188] Shuping Guo, Shashwat Anand, Madison K. Brod, Yongsheng Zhang, and G. Jeffrey Snyder. Conduction band engineering of half-heusler thermoelectrics using orbital chemistry. *Journal of Materials Chemistry A*, 10:3051–3057, 2022.

[189] Chenguang Fu, Tiejun Zhu, Yanzhong Pei, Hanhui Xie, Heng Wang, G. Jeffrey Snyder, Yong Liu, Yintu Liu, and Xinbing Zhao. High band degeneracy contributes to high thermoelectric performance in p-type Half-Heusler compounds. *Advanced Energy Materials*, 4(18), 2014.

[190] Cui Yu, Tie-Jun Zhu, Rui-Zhi Shi, Yun Zhang, Xin-Bing Zhao, and Jian He. High-performance half-heusler thermoelectric materials hf1x zrxnisn1ysby prepared by levitation melting and spark plasma sintering. *Acta Materialia*, 57(9):2757–2764, 2009.

[191] S. Populoh, M.H. Aguirre, O.C. Brunko, K. Galazka, Y. Lu, and A. Weidenkaff. High figure of merit in (Ti,Zr,Hf)NiSn half-Heusler alloys. *Scripta Materialia*, 66(12):1073–1076, 2012.

[192] Appala Naidu Gandi and Udo Schwingenschlögl. Electron dominated thermoelectric response in MNiSn (M: Ti, Zr, Hf) half-Heusler alloys. *Physics Chemistry Chemistry Physics*, 18:14017–14022, 2016.

[193] Shuo Chen and Zhifeng Ren. Recent progress of half-Heusler for moderate temperature thermoelectric applications. *Materials Today*, 16(10):387–395, 2013.

[194] Yu Stadnyk, A Horyn, V Sechovsky, L Romaka, Ya Mudryk, J Tobola, T Stopa, S Kaprzyk, and A Kolomiets. Crystal structure , electrical transport properties and electronic structure of the $VFe_{1x}Cu_xSb$ solid solution. *Journal of Alloys and Compounds*, 402:30–35, 2005.

[195] D. P. Young, P. Khalifah, R. J. Cava, and A. P. Ramirez. Thermoelectric properties of pure and doped FeMSb (M=V,Nb). *Journal Applied Physics*, 87(1):317–321, 2000.

[196] L. Jodin, J. Tobola, P. Pecheur, H. Scherrer, and S. Kaprzyk. Effect of substitutions and defects in half-heusler fevsb studied by electron transport measurements and kkr-cpa electronic structure calculations. *Physical Review B*, 70:184207, 2004.

[197] Chenguang Fu, Shengqiang Bai, Yintu Liu, Yunshan Tang, Lidong Chen, Xinbing Zhao, and Tiejun Zhu. Realizing high figure of merit in heavy-band p-type half-Heusler thermoelectric materials. *Nature Communications*, 6:4–10, 2015.

[198] K. Kutorasinski, J. Tobola, and S. Kaprzyk. Application of Boltzmann transport theory to disordered thermoelectric materials: Ti(Fe,Co,Ni)Sb half-Heusler alloys. *Physica Status Solidi (A) Applications and Materials Science*, 211(6):1229–1234, 2014.

[199] John J Quinn and Kyong-su Yi. *Solid State Physics : Principles and Modern Applications*. Springer, 2018.

[200] R. A. de Groot, F. M. Mueller, P. G. van Engen, and K. H. J. Buschow. New class of materials: Half-metallic ferromagnets. *Physical Review Letters*, 50:2024–2027, 1983.

[201] Hem Chandra Kandpal, Claudia Felser, and Ram Seshadri. Covalent bonding and the nature of band gaps in some half-Heusler compounds. *Journal of Physics D: Applied Physics*, 39(5):776–785, 2006.

[202] I. Galanakis, P. H. Dederichs, and N. Papanikolaou. Origin and properties of the gap in the half-ferromagnetic Heusler alloys. *Physical Review B*, 66(13):1–10, 2002.

[203] Sandip Bhattacharya and Georg K.H. Madsen. A novel p-type half-Heusler from high-throughput transport and defect calculations. *Journal of Materials Chemistry C*, 4(47):11261–11268, 2016.

[204] Galen K. Straub and Walter A. Harrison. Self-consistent tight-binding theory of elasticity in ionic solids. *Physical Review B*, 39(14):10325–10330, 1989.

[205] Xin Sun, Xin Li, Jiong Yang, Jinyang Xi, Ryky Nelson, Christina Ertural, Richard Dronskowski, Weishu Liu, Gerald J. Snyder, David J Singh, and Wenqing Zhang. Achieving band convergence by tuning the bonding ionicity in n-type Mg_3Sb_2. *Journal Computational Chemistry*, 40(18):1693–1700, 2019.

[206] Jiawei Zhang, Lirong Song, Georg K H Madsen, Karl F F Fischer, Wenqing Zhang, Xun Shi, and Bo B Iversen. Designing high-performance layered thermoelectric materials through orbital engineering. *Nature Communications*, 7(1):10892, 2016.

[207] Max Wood, Umut Aydemir, Saneyuki Ohno, and G. Jeffrey Snyder. Observation of valence band crossing: the thermoelectric properties of $CaZn_2Sb_2$–$CaMg_2Sb_2$ solid solution. *Journal of Materials Chemistry A*, 6:9437–9444, 2018.

[208] Madison K Brod, Shuping Guo, Yongsheng Zhang, and G Jeffrey Snyder. Explaining the electronic band structure of half-heusler thermoelectric semiconductors for engineering high valley degeneracy. *MRS Bulletin*, 47(6):573–583, 2022.

[209] C.F. Bunge, J. A. Barrientos, and A.V. Bunge. Roothaan-Hartree-Fock Ground-State Atomic Wave Functions: Slater-Type Orbital Expansions and Expectation Values for Z = 2-54. *Atomic Data and Nuclear Data Tables*, 53(1):113–162, 1993.

[210] Jiawei Zhang, Lirong Song, Steffen Hindborg Pedersen, Hao Yin, Le Thanh Hung, and Bo Brummerstedt Iversen. Discovery of high-performance low-cost n-type Mg_3Sb_2-based thermoelectric materials with multi-valley conduction bands. *Nature Communications*, 8:1–8, 2017.

[211] Jiawei Zhang, Lirong Song, and Bo Brummerstedt Iversen. Insights into the design of thermoelectric Mg_3Sb_2 and its analogs by combining theory and experiment. *Npj Computational Materials*, 5(1):1–17, 2019.

[212] Hiromasa Tamaki, Hiroki K. Sato, and Tsutomu Kanno. Isotropic Conduction Network and Defect Chemistry in Mg3+δSb2-Based Layered Zintl Compounds with High Thermoelectric Performance. *Advanced Materials*, 28(46):10182–10187, 2016.

[213] Airan Li, Chenguang Fu, Xinbing Zhao, and Tiejun Zhu. High-Performance Mg_3Sb_2-xBix Thermoelectrics: Progress and Perspective . *Research*, 2020:1–22, 2020.

[214] Cathie L. Condron, Susan M. Kauzlarich, Franck Gascoin, and G. Jeffrey Snyder. Thermoelectric properties and microstructure of Mg_3Sb_2. *Journal Solid State Chemistry*, 179(8):2252–2257, 2006.

[215] A. Bhardwaj, A. Rajput, A. K. Shukla, J. J. Pulikkotil, A. K. Srivastava, A. Dhar, Govind Gupta, S. Auluck, D. K. Misra, and R. C. Budhani. Mg_3Sb_2-based Zintl compound: A non-toxic, inexpensive and abundant thermoelectric material for power generation. *RSC Advances*, 3(22):8504–8516, 2013.

[216] Jiawei Zhang, Lirong Song, Mattia Sist, Kasper Tolborg, and Bo Brummerstedt Iversen. Chemical bonding origin of the unexpected isotropic physical properties in thermoelectric Mg 3 Sb 2 and related materials. *Nature Communications*, 9(1):1–10, 2018.

[217] Mario Calderón-Cueva, Wanyue Peng, Samantha M. Clarke, Jingxuan Ding, Benjamin L. Brugman, Gill Levental, Ashiwini Balodhi, Megan Rylko, Olivier Delaire, James P.S. Walsh, Susannah M. Dorfman, and Alexandra Zevalkink. Anisotropic Structural Collapse of $Mg_3Sb_2$and Mg3Bi2at High Pressure. *Chemistry of Materials*, 33(2):567–573, 2021.

[218] Jifeng Sun and David J. Singh. Thermoelectric properties of AMg2X2, AZn2Sb2 (A = Ca, Sr, Ba; X = Sb, Bi), and Ba2ZnX2 (X = Sb, Bi) Zintl compounds. *Journal of Materials Chemistry A*, 5(18):8499–8509, 2017.

[219] Wanyue Peng, Guido Petretto, Gian-Marco Rignanese, Geoffroy Hautier, and Alexandra Zevalkink. An unlikely route to low lattice thermal conductivity: Small atoms in a simple layered structure. *Joule*, 2(9):1879–1893, 2018.

[220] Y. Zhu, J. Liu, B. Wei, S. Xu, Y. Song, X. Wang, T.-L. Xia, J. Chen, G.J. Snyder, and J. Hong. Giant phonon anharmonicity driven by the asymmetric lone pairs in Mg_3Bi_2. *Materials Today. Physics*, 27:100791, 2022.

[221] A. Bhardwaj and D. K. Misra. Enhancing thermoelectric properties of a p-type Mg3Sb 2-based Zintl phase compound by Pb substitution in the anionic framework. *RSC Advances*, 4(65):34552–34560, 2014.

[222] A. Bhardwaj, N. S. Chauhan, and D. K. Misra. Significantly enhanced thermoelectric figure of merit of p-type Mg_3Sb_2-based Zintl phase compounds via nanostructuring and employing high energy mechanical milling coupled with spark plasma sintering. *Journal of Materials Chemistry A*, 3(20):10777–10786, 2015.

[223] Jiawei Zhang and Bo Brummerstedt Iversen. Fermi surface complexity, effective mass, and conduction band alignment in n-type thermoelectric mg_3sb_2–xbix from first principles calculations. *Journal Applied Physics*, 126(8):085104, 2019.

[224] Max Wood, Kazuki Imasato, Shashwat Anand, Jiong Yang, and G. Jeffrey Snyder. The importance of the Mg-Mg interaction in Mg_3Sb_2-Mg_3Bi_2 shown through cation site alloying. *Journal of Materials Chemistry A*, 8(4):2033–2038, 2020.

[225] Y. Imai and A. Watanabe. Electronic structures of Mg3Pn2 (Pn=N, P As, Sb and Bi) and Ca3N2 calculated by a first-principle pseudopotential method. *Journal Materials Science*, 41(8):2435–2441, 2006.

[226] Zhijia Han, Zhigang Gui, Y B Zhu, Peng Qin, Bo-Ping Zhang, Wenqing Zhang, Li Huang, and Weishu Liu. The Electronic Transport Channel Protection and Tuning in Real Space to Boost the Thermoelectric Performance of $Mg_{3+\delta}Sb_{2+y}Bi_y$ near Room Temperature. *Research*, 2020:1672051, 2020.

[227] Kazuki Imasato, Stephen Dongmin Kang, and G. Jeffrey Snyder. Exceptional thermoelectric performance in $Mg_3Sb_{0.6}Bi_{1.4}$ for low-grade waste heat recovery. *Energy and Environmental Science*, 12(3):965–971, 2019.

[228] David J. Singh and David Parker. Electronic and transport properties of zintl phase AeMg2Pn2, Ae = Ca,Sr,Ba, Pn = As,Sb,Bi in relation to Mg_3Sb_2. *Journal Applied Physics*, 114(14):143703, 2013.

[229] D. W. Zhou, J. S. Liu, S. H. Xu, and P. Peng. Thermal stability and elastic properties of $Mg_3Sb_2$and Mg3Bi2 phases from first-principles calculations. *Physica B: Condensed Matter*, 405(13):2863–2868, 2010.

[230] Ryky Nelson, Christina Ertural, Janine George, Volker L. Deringer, Geoffroy Hautier, and Richard Dronskowski. Lobster: Local orbital projections, atomic charges, and chemical-bonding analysis from projector-augmented-wave-based density-functional theory. *Journal Computational Chemistry*, 41(21):1931–1940, 2020.

[231] Kazuki Imasato, Max Wood, Jimmy Jiahong Kuo, and G. Jeffrey Snyder. Improved stability and high thermoelectric performance through cation site doping in n-type La-doped Mg3Sb1.5Bi0.5. *Journal of Materials Chemistry A*, 6(41):19941–19946, 2018.

[232] Ting Zhou, Zhenzhen Feng, Jun Mao, Jing Jiang, Hangtian Zhu, David J Singh, Chao Wang, and Zhifeng Ren. Thermoelectric Properties of Zintl Phase YbMg2Sb2. *Chemistry of Materials*, 32(2):776–784, 2020.

[233] H.J. Goldsmid. *Introduction to Thermoelectricity.* Springer Series in Materials Science. Springer Berlin Heidelberg, 2009.

[234] Yu. I. Ravich, B. A. Efimova, and I. A. Smirnov. *Semiconducting Lead Chalcogenides*, volume 5 of *Monographs in Semiconductor Physics*, chapter Thermoelectric and Thermal Properties, pages 149–220. Springer, Boston, MA, 1970.

[235] V. I. Fistul. *Heavily Doped Semiconductors.* Monographs in Semiconductor Physics ; 1. Springer US, New York, NY, 1st ed. 1969. edition.

[236] J. M. Ziman. *Electrons and Phonons: The Theory of Transport Phenomena in Solids.* International series of monographs on physics. OUP Oxford, 2001.

[237] Xufeng Wang, Vahid Askarpour, Jesse Maassen, and Mark Lundstrom. On the calculation of Lorenz numbers for complex thermoelectric materials. *Journal of Applied Physics*, 123(5):055104, 2018.

Appendices

Brillouin Zone Special Points

Here, special points in the first Brillouin zones (BZs) of face-centered cubic (FCC), rhombohedral, and hexagonal Bravais lattices are given in terms of the primitive lattice basis vectors. The conventions for the labels BZ labels follow those described in Ref. 137.[1] When using these points to calculate Bloch phase factors of the form, $e^{i\boldsymbol{k}\cdot\boldsymbol{r}}$, the $\boldsymbol{k}$-points must first be multiplied by a factor of 2π.

In general, the real-space lattice vectors are given by $\boldsymbol{a}$, $\boldsymbol{b}$, and $\boldsymbol{c}$, and the reciprocal-space lattice vectors are denoted by $\boldsymbol{a}^*$, $\boldsymbol{b}^*$, and $\boldsymbol{c}^*$.

A.1 Face-Centered Cubic

Given that the FCC lattice constant is given by a, the conventional lattice vectors for the FCC lattice are given by:

- $\boldsymbol{a} = (a, 0, 0)$
- $\boldsymbol{b} = (0, a, 0)$
- $\boldsymbol{c} = (0, 0, a)$.

The primitive lattice vectors for the FCC lattice are given by:

- $\boldsymbol{a} = (0, a/2, a/2)$
- $\boldsymbol{b} = (a/2, 0, a/2)$
- $\boldsymbol{c} = (a/2, a/2, 0)$.

[1] See Ref. 137 for labeled Brillouin zone diagrams.

Table A.1: Special points in the face-centered cubic Bravais lattice first Brillouin zone in reciprocal lattice coordinates.

Label	$\times\boldsymbol{a}^*$	$\times\boldsymbol{b}^*$	$\times\boldsymbol{c}^*$
Γ	0	0	0
K	3/8	3/8	3/4
L	1/2	1/2	1/2
U	5/8	1/4	5/8
W	1/2	1/4	3/4
X	1/2	0	1/2

A.2 Rhombohedral

Given that the lattice constants for the rhombohedral lattice are given by a and γ, where γ is the primitive-cell interaxial angle (see Chapter 5), the lattice vectors are as follows:

- $\boldsymbol{a} = (a\cos(\gamma/2), -a\sin(\gamma/2), 0)$
- $\boldsymbol{b} = (a\cos(\gamma/2), a\sin(\gamma/2), 0)$
- $\boldsymbol{c} = (a\cos(\gamma)/\cos(\gamma/2), 0, a\sqrt{1-\cos^2(\gamma)/\cos^2(\gamma/2)}$.

Table A.2: Special points in the first Brillouin zone of the rhombohedral Bravais lattice in reciprocal lattice coordinates, where $\eta = (1+4\cos\gamma)/(2+4\cos\gamma)$, and $\nu = 3/4 - \eta/2$.

Label	$\times\boldsymbol{a}^*$	$\times\boldsymbol{b}^*$	$\times\boldsymbol{c}^*$
Γ	0	0	0
B	η	1/2	1 - η
B1	1/2	1 - η	$\eta - 1$
F	1/2	1/2	0
L	1/2	0	0
P	η	ν	ν
X	ν	0	$-\nu$
Z	1/2	1/2	1/2

A.3 Hexagonal

The lattice vectors for the hexagonal lattice are given as follows:

- $\boldsymbol{a} = (a/2, -a\sqrt{3}/2, 0)$

- $\boldsymbol{b} = (a/2, a\sqrt{3}/2, 0)$
- $\boldsymbol{c} = (0, 0, c)$.

Table A.3: Special points in the hexagonal Bravais lattice first Brillouin zone in reciprocal lattice coordinates.

Label	$\times\boldsymbol{a}^*$	$\times\boldsymbol{b}^*$	$\times\boldsymbol{c}^*$
Γ	0	0	0
A	0	0	1/2
H	1/3	1/3	1/2
K	1/3	1/3	0
L	1/2	0	1/2
M	1/2	0	0

PbTe Hamiltonian

The analytical tight-binding solutions for rock salt PbTe without spin-orbit coupling were determined by solving for the eigenvalues of the Hamiltonian given in Equation B.1, using the Slater-Koster matrix elements [65]. The Hamiltonian, $\hat{H}$, is an Hermitian matrix, so $H_{ij} = \bar{H}_{ji}$, where $\bar{H}_{ji}$ is the complex-conjugate of H_{ji}. The 8-dimensional TB basis is Pb-6s, Pb-6p_x, Pb-6p_y, Pb-6p_z, Te-5s, Te-5p_x, Te-5p$_y$, Te-5p_z. This Hamiltonian can be generalized for any IV-VI rock salt compound, where Pb represents the anion and Te represents the cation. The k-point must be in their Cartesian form to use the following equations.

$$\hat{\boldsymbol{H}} = \begin{pmatrix} H_{11} & H_{12} & \cdots & H_{18} \\ H_{21} & H_{22} & \cdots & H_{28} \\ \vdots & \vdots & \ddots & \vdots \\ H_{81} & H_{82} & \cdots & H_{88} \end{pmatrix} \tag{B.1}$$

We do not provide the expressions for every Hamiltonian element, but representative examples of Hamiltonian elements are given below in Equations B.2-B.9. E_{b-a} represents the on-site energy terms, where a denotes the orbital (s or p) and b denotes the element (Pb or Te). The overlap parameters of the form, $V_{\alpha\beta m}$, where α and β represent the two orbitals (s or p) and m represents the type of bonding (σ or π). When there is an element label in the subscript, the overlap parameter represents the interaction between the next-nearest neighbors for that element (Pb or Te). When there is no element referenced in the subscript, then the parameter represents a nearest neighbor interaction between Pb and Te. However, $V_{sp\sigma 1}$ and $V_{sp\sigma 2}$ are used here to distinguish between the two different nearest neighbor s–p interactions. $V_{sp\sigma 1}$ denotes the interaction between the Pb-s and Te-p orbitals, and $V_{sp\sigma 2}$ denotes the interaction parameter between the Te-s and Pb-p orbitals.

$$\begin{aligned} H_{11} = E_{Pb-s} + 2V_{ss\sigma,Pb}[&\cos(k_x a/2 + k_y/2) + \cos(k_x a/2 - k_y a/2) + \\ &\cos(k_y a/2 + k_z a/2) + \cos(k_y a/2 - k_z a/2) + \\ &\cos(k_x a/2 + k_z a/2) + \cos(k_x a/2 - k_z a/2)] \end{aligned} \tag{B.2}$$

$$H_{12} = -\frac{2i}{\sqrt{2}} V_{sp\sigma,Pb}[\sin(k_x a/2 + k_y a/2) + \sin(k_x a/2 - k_y a/2) + \sin(k_x a/2 + k_z a/2) + \sin(k_x a/2 - k_z a/2)] \quad \text{(B.3)}$$

$$H_{23} = (V_{pp\sigma,Pb} - V_{pp\pi,Pb})[\cos(k_x a/2 + k_y a/2) - \cos(k_x a/2 - k_y a/2)] \quad \text{(B.4)}$$

$$H_{15} = 2V_{ss\sigma}[\cos(k_x a/2) + \cos(k_y a/2) + \cos(k_z a/2)] \quad \text{(B.5)}$$

$$H_{16} = -2iV_{sp\sigma 1} \sin(k_x a/2) \quad \text{(B.6)}$$

$$H_{25} = -2iV_{sp\sigma 2} \sin(k_x a/2) \quad \text{(B.7)}$$

$$H_{26} = 2V_{pp\sigma} \cos(k_x a/2) + 2V_{pp\pi}[\cos(k_y a/2) + \cos(k_z a/2)] \quad \text{(B.8)}$$

$$H_{77} = E_{Te-p} + (V_{pp\sigma,Te} + V_{pp\pi,Te})[\cos(k_x a/2 + k_y a/2) + \cos(k_x a/2 - k_y a/2) + \cos(k_y a/2 + k_z a/2) + \cos(k_y a/2 - k_z a/2)] + 2V_{pp\pi,Te}[\cos(k_x a/2 + k_z a/2) + \cos(k_x a/2 - k_z a/2)] \quad \text{(B.9)}$$

1D-, 2D-, and 3D-Like Transport in IV-VI Rock Salt Semiconductors

Here, we consider a transport model developed using the Boltzmann transport equation (BTE) [56, 58, 67, 128, 233–236] to model thermoelectric transport IV-VI semiconductors—like PbTe— to understand how it changes as the valence bands become more highly converged. The spherical 3D Fermi surface pockets have a degeneracy of 4, and the Fermi-surface cylinders for the 2D case have a degeneracy of 12 , radius $|\boldsymbol{k}|$, and length $l_{2D} = 2\pi/a$, where a is the lattice parameter. For a cylinder oriented along the z-axis, $\boldsymbol{k}^2 = k_x^2 + k_y^2$, with analogous expressions for all three directions. In PbTe, the 1D Fermi surface can be described as sheets with thickness $2|\boldsymbol{k}|$, a square cross-section characterized by a side length of $l_{1D} = 2\sqrt{2}\pi/a$, and degeneracy of 6. For a sheet aligned in the x-y plane, $|\boldsymbol{k}| = |k_z|$, with analogues in all three directions.

C.1 Density of States

The expressions for the DOS in each type of Fermi surface (distinguished by the dimensionality of transport), $g_{mD}(\varepsilon)$ $(m = 1, 2, 3)$, where $\varepsilon = E/k_BT$, and E is the energy below the VBM, are given in Equations C.1-C.3. These DOS expressions account for all 4 spheres, 12 cylinders, and 6 sheets.

$$g_{1D}(\varepsilon) = \frac{12(2m_b^*)^{1/2}}{a^2\pi\hbar}(k_BT)^{-1/2}\varepsilon^{-1/2} \tag{C.1}$$

$$g_{2D}(\varepsilon) = \frac{12m_b^*}{a\pi\hbar^2} \tag{C.2}$$

$$g_{3D}(\varepsilon) = \frac{2(2m_b^*)^{3/2}}{\pi^2\hbar^3}(k_BT)^{1/2}\varepsilon^{1/2} \tag{C.3}$$

The above expressions for the DOS can be used to give the hole concentrations per unit cell in each dimension, as given in Equations 4.11-4.13.

C.2 Electrical Conductivity

In general, the electrical conductivity is given in Equation C.4 [45, 58, 67]

$$\sigma(T) = \int \frac{e^2}{3}\tau(E)v^2(E)g(E)\left(-\frac{df}{dE}\right)dE, \tag{C.4}$$

where $v(E)$ is the carrier velocity at a given energy and can be broken down into its directional tensor components. For instance, the x-component of the velocity, can be found by taking the partial derivative of energy with respect k_x.

$$v_x = \frac{1}{\hbar}\frac{\partial E}{\partial k_x} = \frac{\hbar k_x}{m^{*2}} \tag{C.5}$$

In the 1D topology case $v_x^2(E) = 2E/m_I^*$, in 2D $v_x^2(E) = E/m_I^*$, and in 3D $v_x^2(E) = 2E/3m_I^*$, where $v_x(E)$ is the velocity component along the x-direction. For a cubic material, $v_x = v_y = v_z$. The expression for $v(E)$ is the same regardless of the type of geometry because for the 1D case, $v^2(E) = v_x^2(E)$, in 2D $v^2(E) = 2v_x^2(E)$, and in 3D $v^2(E) = 3v_x^2(E)$, yielding $v^2(E) = 2E/m_I^*$ for all three geometries [58].

In this model, we assume a DOS dependent scattering rate which would come from an energy-independent matrix element in Fermi's golden rule as used in analytic theories of deformation potential or acoustic phonon scattering [58]. The DOS dependence gives an energy-dependent scattering time, τ, given by $\tau = \tau_0\varepsilon^r$, where r depends on the assumptions made in the scattering-time model used. τ_0 is a constant that is given by $\tau_0 = \frac{\mu_0 m_I^*}{e}$, where m_I^* is the intertial effective mass [18]. For the constant scattering time approximation (τ independent of energy), the scattering exponent is given as $r = 0$. If we assume acoustic-phonon scattering, the value of r is $-1/2, 0$, or $1/2$ for the 3D, 2D, and 1D cases, respectively. The value of r for acoustic-phonon scattering is chosen such that the energy dependence of τ is inversely related to the energy dependence of g ($\tau \propto 1/g$). If a constant scattering time approximation is used, $r = 0$ for all Fermi surface geometries.

The term $\frac{e^2}{3}\tau(E)v^2(E)g(E)$ in Equation C.4 can be combined to the single term $\sigma_E(E)$, which is the electrical conductivity transport function [58]. That is, we can write the electrical conductivity as $\sigma = \int \sigma_E(E)\left(-\frac{df}{dE}\right)dE$. Furthermore, $\sigma_E(E)$ can be written in terms of a transport coefficient, σ_{E_0}, through the expression, $\sigma_E(E) = \sigma_{E_0}\varepsilon^s$, where $s = 1/2 + r, 1 + r$, or $3/2 + r$ for the 1D, 2D, and 3D cases, respectively, and the form of σ_{E_0} varies with the dimensionality of the band, as seen in the following set of equations.

$$\sigma_{E_0,1D} = \frac{8e\left(2m_e k_B T\right)^{1/2}}{a^2\pi\hbar}\mu_0\left(\frac{m_b^*}{m_e}\right)^{1/2} \tag{C.6}$$

$$\sigma_{E_0,2D} = \frac{8em_e k_B T}{\pi a\hbar^2}\mu_0\left(\frac{m_b^*}{m_e}\right) \tag{C.7}$$

$$\sigma_{E_0,3D} = \frac{4e\left(2m_e k_B T\right)^{3/2}}{3\pi^2\hbar^3}\mu_0\left(\frac{m_b^*}{m_e}\right)^{3/2} \tag{C.8}$$

Because we assume $N_V = 4$ for the 3D pockets at L in PbTe, we can rewrite equation C.8 in terms of m^*_{DOS}, where $m^*_{DOS} = m^*_b 4^{2/3}$.

$$\sigma_{E_0,3D} = \frac{e\left(2m_e k_B T\right)^{3/2}}{3\pi^2\hbar^3}\mu_0\left(\frac{m^*_{DOS}}{m_e}\right)^{3/2} \tag{C.9}$$

In Equation C.9, the term, $\mu_0\left(\frac{m^*_{DOS}}{m_e}\right)^{3/2}$, is the weighted mobility, μ_w, for the 3D effective mass model. [18, 58, 128] Therefore, we can rewrite $\sigma_{E_0,3D}$ in terms of μ_w.

$$\sigma_{E_0,3D} = \frac{e\left(2m_e k_B T\right)^{3/2}}{3\pi^2\hbar^3}\mu_w \tag{C.10}$$

It is instructive to rewrite Equations C.6-C.8 in terms of the hole concentration (see Equations 4.11-4.13 in Chapter 4). The reduced Fermi level (E_F), or reduced chemical potential (μ), is given by $\eta = E_F/k_B T$.

$$\sigma_{E_0,1D} = \frac{2}{3}\frac{p_{1D} e\mu_0}{F_{-\frac{1}{2}}(\eta)} \tag{C.11}$$

$$\sigma_{E_0,2D} = \frac{2}{3}\frac{p_{2D} e\mu_0}{F_0(\eta)} \tag{C.12}$$

$$\sigma_{E_0,3D} = \frac{2}{3}\frac{p_{3D} e\mu_0}{F_{\frac{1}{2}}(\eta)} \tag{C.13}$$

Using Equation C.4 along with Equations C.11-C.13, the electrical conductivity for each case can be expressed as follows.

$$\sigma_{1D} = \frac{2p_{1D} e\mu_0}{3}\left(r + \frac{1}{2}\right)\frac{F_{r-\frac{1}{2}}(\eta)}{F_{-\frac{1}{2}}(\eta)} \tag{C.14}$$

$$\sigma_{2D} = \frac{2p_{2D} e\mu_0}{3}\left(r + 1\right)\frac{F_r(\eta)}{F_0(\eta)} \tag{C.15}$$

$$\sigma_{3D} = \frac{2p_{3D} e\mu_0}{3}\left(r + \frac{3}{2}\right)\frac{F_{r+\frac{1}{2}}(\eta)}{F_{\frac{1}{2}}(\eta)} \tag{C.16}$$

If we use the acoustic-phonon approximation for scattering time, these equations can be simplified, as shown below.

$$\sigma_{1D} = \frac{2p_{1D}e\mu_0}{3}\frac{F_0(\eta)}{F_{-\frac{1}{2}}(\eta)} \tag{C.17}$$

$$\sigma_{2D} = \frac{2p_{2D}e\mu_0}{3} \tag{C.18}$$

$$\sigma_{3D} = \frac{2p_{3D}e\mu_0}{3}\frac{F_0(\eta)}{F_{\frac{1}{2}}(\eta)} \tag{C.19}$$

Using the constant scattering time approximation ($r = 0$), it is evident from the conductivity expressions that, only 1/3 of the charge carriers contribute to the electrical conductivity for the 1D-like bands, 2/3 contribute to the conductivity in the 2D-like bands, and all of the charge carriers contribute to the conductivity in the 3D-like bands. That is, we can write the electrical conductivity for these three cases as $\sigma_{1D} = (1/3)p_{1D}e\mu_0$, $\sigma_{2D} = (2/3)p_{2D}e\mu_0$, and $\sigma_{3D} = p_{3D}e\mu_0$.

C.3 Seebeck Coefficient

The general expression for the Seebeck coefficient, α, is expressed in Equation C.20.

$$\alpha(T) = \left(\frac{k_B}{e}\right)\frac{\int \sigma(\varepsilon)\left(-\frac{df}{d\varepsilon}\right)(\varepsilon - \eta)d\varepsilon}{\int \sigma(\varepsilon)\left(-\frac{df}{d\varepsilon}\right)d\varepsilon} \tag{C.20}$$

This expression can be reduced to Equations C.21-C.23 for the 1D-3D bands.

$$\alpha_{1D} = \left(\frac{k_B}{e}\right)\left[\frac{\left(r+\frac{3}{2}\right)F_{r+\frac{1}{2}}(\eta)}{\left(r+\frac{1}{2}\right)F_{r-\frac{1}{2}}(\eta)} - \eta\right] \tag{C.21}$$

$$\alpha_{2D} = \left(\frac{k_B}{e}\right)\left[\frac{(r+2)F_{r+1}(\eta)}{(r+1)F_r(\eta)} - \eta\right] \tag{C.22}$$

$$\alpha_{3D} = \left(\frac{k_B}{e}\right)\left[\frac{\left(r+\frac{5}{2}\right)F_{r+\frac{3}{2}}(\eta)}{\left(r+\frac{3}{2}\right)F_{r+\frac{1}{2}}(\eta)} - \eta\right] \tag{C.23}$$

When the acoustic-phonon scattering approximation is used, these expressions reduce to that found in in Equation 4.8 for all three dimensionalities.

C.4 Lorenz number

The electronic component of the lattice thermal conductivity can be expressed as $\kappa_e = L\sigma T$, where L is the Lorenz number, given in by $L = \frac{\kappa_0}{\sigma T} - \alpha^2$. The expression for κ_0 is given in Equation C.24. [235, 237]

$$\kappa_0(T) = T\left(\frac{k_B}{e}\right)^2 \int (\varepsilon - \eta)^2 \sigma(\varepsilon) \left(-\frac{df}{d\varepsilon}\right) d\varepsilon \tag{C.24}$$

Therefore, the Lorentz factor can be written in the forms shown in Equation C.25-C.27.

$$L_{1D} = \left(\frac{k_B}{e}\right)^2 \frac{\left(r+\frac{5}{2}\right)\left(r+\frac{1}{2}\right) F_{r+\frac{3}{2}}(\eta) F_{r-\frac{1}{2}}(\eta) - \left(r+\frac{3}{2}\right)^2 F^2_{r+\frac{1}{2}}(\eta)}{\left(r+\frac{1}{2}\right)^2 F^2_{r-\frac{1}{2}}(\eta)} \tag{C.25}$$

$$L_{2D} = \left(\frac{k_B}{e}\right)^2 \frac{(r+3)(r+1) F_{r+2}(\eta) F_r(\eta) - (r+2)^2 F^2_{r+1}(\eta)}{(r+1)^2 F^2_r(\eta)} \tag{C.26}$$

$$L_{3D} = \left(\frac{k_B}{e}\right)^2 \frac{\left(r+\frac{7}{2}\right)\left(r+\frac{3}{2}\right) F_{r+\frac{5}{2}}(\eta) F_{r+\frac{1}{2}}(\eta) - \left(r+\frac{5}{2}\right)^2 F^2_{r+\frac{3}{2}}(\eta)}{\left(r+\frac{3}{2}\right)^2 F^2_{r+\frac{1}{2}}(\eta)} \tag{C.27}$$

If we use the acoustic-phonon scattering approximation, all three of the above expressions reduce to the equation for L given in Equation 4.9.

C.5 Quality Factor and Figure of Merit

In general, the zT for this effective-mass model in all three cases can be calculated using Equations C.28-C.30.

$$zT_{1D}(\eta, B) = \frac{\alpha^2(\eta)}{\frac{(k_B/e)^2}{(r+1/2)B_{1D}F_{r-\frac{1}{2}}(\eta)} + L(\eta)} \tag{C.28}$$

$$zT_{2D}(\eta, B) = \frac{\alpha^2(\eta)}{\frac{(k_B/e)^2}{(r+1)B_{2D}F_r(\eta)} + L(\eta)} \tag{C.29}$$

$$zT_{3D}(\eta, B) = \frac{\alpha^2(\eta)}{\frac{(k_B/e)^2}{(r+3/2)B_{3D}F_{r+\frac{1}{2}}(\eta)} + L(\eta)} \tag{C.30}$$

The quality factor, B, is defined in terms of σ_{E_0} in Equation C.31 [18, 58]. For each topology, the quality factory is calculated from the corresponding σ_{E_0}.

$$B = \left(\frac{k_B}{e}\right)^2 \frac{\sigma_{E_0} T}{\kappa_L} \tag{C.31}$$

For the acoustic-phonon scattering assumption used in here and in Chapter 4, the *expressions* for zT as a function of η are identical for the 1D-, 2D-, and 3D-type bands, and given in Equation 4.10.

Additional Half-Heusler Data and Analysis

D.1 Group Theory Analysis in Half-Heusler Compounds

D.1.1 Introduction: Group Theory Description of Crystal Orbitals

Group theory is a powerful tool for understanding the orbital interactions responsible for the electronic structure of half-Heusler (hH) compounds. In this section, we use the methods outlined in Refs. 4 and 5 to analyze and characterize the hH electronic structure using group theory. Zhou *et al.* have also described the hH electronic structure using similar group theory approaches in order to understand bonding at the L-, X- and Γ-points [68]. By classifying orbitals at various $\boldsymbol{k}$-points or along high-symmetry lines in the Brillouin zone (BZ) by their symmetry representations, we can determine which orbital interactions are allowed or forbidden by symmetry and which bands may undergo avoided crossings with each other. When determining the symmetry representations of atomic orbitals in a crystal, it is necessary to determine both the symmetry representation of the atomic orbitals themselves and the representation of the sub-lattice sites they occupy. Thus, in general, we can express the total representation (Γ^{tot}) of an atomic orbital on a certain crystallographic site as the direct product of the representation of the single atomic orbitals (Γ^{orb}) and of the atomic site ($\Gamma^{\text{a.s.}}$): $\Gamma^{\text{tot}} = \Gamma^{\text{orb}} \otimes \Gamma^{\text{a.s}}$ [4, 5]. In order to determine the symmetry representation of atomic orbitals, it is useful to represent them as polynomials that exhibit the same symmetry transformation properties. These equivalencies for s, p, and d orbitals are given as follows:

- $s \rightarrow x^2 + y^2 + z^2$
- $p_x \rightarrow x$; $p_y \rightarrow y$; $p_z \rightarrow z$
- $d_{xy} \rightarrow xy$; $d_{xz} \rightarrow xz$; $d_{yz} \rightarrow yz$
- $d_{x^2-y^2} \rightarrow x^2 - y^2$; $d_{z^2} \rightarrow 2z^2 - x^2 - y^2$

Here, we look at the symmetry representations at the Γ-point, X-point, and L-point and along the Δ and Λ symmetry lines. The point group symmetries of the Γ-point, X-point, and L-point in the half-Heusler structure (space group #216) are T_d ($\bar{4}3m$), D_{2d} ($\bar{4}2m$), and C_{3v} ($3m$), respectively. The point group symmetries of the Δ and Λ symmetry lines are C_{2v} ($mm2$) and C_{3v}, respectively. [68] The character tables for these point groups are given in Tables D.1-D.5 [4,5]. The first column contains the labels for the irreducible representations with the corresponding band label(s) in parentheses. The naming convention for the irreducible representations is such that A and B represent the one-dimensional representations, E corresponds to a two-dimensional representations, and T denotes three-dimensional representations. The dimensionality of the representation corresponds to the degeneracy of the molecular orbitals or bands belonging to that representation. The A_1 representation is always the identity representation, so the direct product of the A_1 representation with another representation, Γ, yields Γ. Note that we use Γ to denote a generic symmetry representation (not to be confused with the zone center $\boldsymbol{k}-$point, which is also denoted as Γ).

The character tables are useful tools for categorizing different atomic orbitals and bands by their symmetry representation in different parts of the BZ. The first row contains the symmetry classes and number of symmetry elements contained in the class, and the last two columns contain the linear and quadratic polynomial basis functions for each irreducible representation [4, 68]. These basis functions correspond to the atomic orbitals that belong to that representation and are derived assuming that the orbital is located at the origin of the point group. The entries in the table are the characters, χ, of each symmetry class for each representation [4,5].

Table D.1: Character table for the T_d point group. [4,5]

	E	$8C_3$	$3C_2$	$6S_4$	$6\sigma_d$	Linear	Quadratic
A_1 (Γ_1)	1	1	1	1	1		$x^2+y^2+z^2$
A_2 (Γ_2)	1	1	1	-1	-1		
E (Γ_{12})	2	-1	2	0	0		$x^2-y^2, 2z^2-x^2-y^2$
T_1 (Γ_{25})	3	0	-1	1	-1		
T_2 (Γ_{15})	3	0	-1	-1	1	x, y, z	xy, xz, yz

Table D.2: Character table for the D_{2d} point group. [4,5]

	E	$2S_4$	$C_2(z)$	$2C_2'$	$2\sigma_d$	Linear	Quadratic
A_1 (X_1)	1	1	1	1	1		x^2+y^2, z^2
A_2 (X_4)	1	1	1	-1	-1		
B_1 (X_2)	1	-1	1	1	-1		x^2-y^2
B_2 (X_3)	1	-1	1	-1	1	z	xy
E (X_5)	2	0	-2	0	0	x, y	xz, yz

Table D.3: Character table for the C_{3v} point group in the standard setting (axis of 3-fold rotation parallel to the z-axis). [4, 5]

	E	$2C_3(z)$	$3\sigma_v$	Linear	Quadratic
A_1	1	1	1	z	x^2+y^2, z^2
A_2	1	1	-1		
E	2	-1	0	x, y	x^2-y^2, xy, xz, yz

Table D.4: Character table for the C_{2v} point group in the standard setting (vertical mirrors in the xz and yz planes). [4, 5]

	E	$C_2(z)$	$\sigma_v(xz)$	$\sigma_v(yz)$	Linear	Quadratic
A_1	1	1	1	1	z	x^2, y^2, z^2
A_2	1	1	-1	-1		xy
B_1	1	-1	1	-1	x	xz
B_2	1	-1	-1	1	y	yz

Because the group operations in standard setting of the C_{2v} and C_{3v} point groups do not coincide with point group settings required to describe the Δ-line and Λ-line (including the L-point), respectively, in the BZ for space group #216, we re-derive the basis functions for the character tables of the C_{2v} and C_{3v} so that they are compatible with the symmetry of the X- and L-points of the hH crystal structure (Tables D.5 and D.6). That is, for the Δ-line, $\boldsymbol{k_\Delta} = (0, 0, 2d\pi/a)$, where d varies from 0 at Γ to 1 at X, the mirrors should coincide with the (110) and $(1\bar{1}0)$ ($x+y$ and $x-y$) planes, and the axis of the 4-fold rotoreflection (or rotoinversion) should be parallel to the z-axis. Furthermore, for the Λ-line, $\boldsymbol{k_\Lambda} = (\pi l/a, \pi l/a, \pi l/a)$, where l varies from 0 at Γ to 1 at L, the 3-fold rotation axis is parallel to the [111] direction and the mirrors coincide with the $(1\bar{1}0)$, $(10\bar{1})$, and $(01\bar{1})$ planes (they go through the cube edges). Note that when we use the appropriate setting for the C_{2v} point group, we must combine the B_1 and B_2 (Δ_3 and Δ_4) representations into a 2D representation, $B_{1,2}$ ($\Delta_{3,4}$), in order to represent the symmetry properties of the x, y, xz, and yz basis functions.

Table D.5: Character table for the C_{2v} point group describing the $\boldsymbol{k_X} = (0, 0, 2\pi/a)$ point in the BZ for the hH crystal structure.

	E	$C_2(z)$	$\sigma_d(x+y)$	$\sigma_d(x-y)$	Linear	Quadratic
A_1 (Δ_1)	1	1	1	1	z	x^2+y^2, z^2, xy
A_2 (Δ_2)	1	1	-1	-1		x^2-y^2
$B_{1,2}$ ($\Delta_{3,4}$)	2	-2	0	0	x, y	xz, yz

Table D.6: Character table for the C_{3v} point group describing the $\boldsymbol{k_L} = (\pi/a,\ \pi/a,\ \pi/a)$ point and $\boldsymbol{k_\Lambda} = (\pi l/a,\ \pi l/a,\ \pi l/a)$ line in the BZ for the hH crystal structure.

	E	$2C_3(z)$	$3\sigma_v$	Linear	Quadratic
A_1 (L_1, Λ_1)	1	1	1	$x+y+z$	$x^2+y^2+z^2$, $xy+xz+yz$
A_2 (L_2, Λ_2)	1	1	-1		
E (L_3, Λ_3)	2	-1	0	$2z-x-y, x-y$	$2z^2-x^2-y^2, x^2-y^2$, $2xy-xz-yz, xz-yz$

D.1.2 Finding Basis Functions using the Projection Operator

The linear and quadratic basis functions (given in the character tables), and hence, atomic orbitals belonging to each representation can be determined using the projection operator, [4,5] $\hat{P}^n$, where n labels the irreducible representation. The projection operator for an irreducible representation, n, is given by Equation D.1. In this expression, l_n, is the dimension of the irreducible representation, R is the symmetry operation, h is the number of symmetry elements in the point group (also known as the order of the group), $\chi_n(R)$ is the character of the symmetry operation for the irreducible representation, n, and $\hat{\mathbf{R}}$ is the symmetry operator. If we apply $\hat{P}^n$ to some arbitrary vector or trial function, it will either return zero or a vector/function (either the same as or different from the trial function) that transforms like the irreducible representation denoted by n [4, 5]. The resulting non-zero vector is a basis function of that irreducible representation. Moreover, any linear combination of basis functions yields another valid function that transforms like that representation. To determine the linear basis terms, we use the trial functions, x, y, and z, and to determine the quadratic basis terms, we use the trial functions, xy, xz, yz, x^2, y^2, and z^2. In order to aid in the mathematical analysis, we can define three separate vector spaces with bases, $\{x, y, z\}$, $\{x^2, y^2, z^2\}$, and $\{xy, xz, yz\}$, defined in Equations D.2–D.4. Additionally, we can make use of the fact that $\hat{P}^n |\phi_1 + \phi_2\rangle = \hat{P}^n |\phi_1\rangle + \hat{P}^n |\phi_2\rangle$, for arbitrary functions ϕ_1 and ϕ_2.

$$\hat{P}^n = \frac{l_n}{h} \sum_R \chi_n(R) * \hat{\mathbf{R}} \tag{D.1}$$

$$|x\rangle = \begin{bmatrix}1\\0\\0\end{bmatrix}; \quad |y\rangle = \begin{bmatrix}0\\1\\0\end{bmatrix}; \quad |z\rangle = \begin{bmatrix}0\\0\\1\end{bmatrix} \tag{D.2}$$

$$|x^2\rangle = \begin{bmatrix}1\\0\\0\end{bmatrix}; \quad |y^2\rangle = \begin{bmatrix}0\\1\\0\end{bmatrix}; \quad |z^z\rangle = \begin{bmatrix}0\\0\\1\end{bmatrix} \tag{D.3}$$

$$|xy\rangle = \begin{bmatrix}1\\0\\0\end{bmatrix}; \quad |xz\rangle = \begin{bmatrix}0\\1\\0\end{bmatrix}; \quad |yz\rangle = \begin{bmatrix}0\\0\\1\end{bmatrix} \tag{D.4}$$

As an example, we look at the projection operator for the B_2 representation of the D_{2d} point group. First, we apply the eight symmetry operations of the D_{2d} point group to our trial functions. The results of these transformations on the individual linear and quadratic trial functions are summarized in Table D.7. Next, we multiply the result of each transformation by the character of its respective group elements within the B_2 representation of the D_{2d} point group and take the sum of all the resulting functions. The outcomes of this procedure are given in Table D.8. Note, that we assume that the axis of rotation of the S_4 operations is parallel to the z-axis. Additionally, the $C_2(x)$ and $C_2(y)$ operations belong to the C_2' class referred to in the D_{2d} character table (Table D.2). For each of the different three X-points, the point group basis vectors must be rotated accordingly. For example, for $\boldsymbol{k_X} = (0, 2\pi/a, 0)$, the axis of rotation is parallel to the y-axis.

Table D.7: Transformations of linear and quadratic functions under D_{2d} point group operations.

	E	$S_4(-\pi/2)$	$S_4(+\pi/2)$	$C_2(x)$	$C_2(y)$	$C_2(z)$	$\sigma_d(x+y)$	$\sigma_d(x-y)$
x	x	$-y$	y	x	$-x$	$-x$	$-y$	y
y	y	x	$-x$	$-y$	y	$-y$	$-x$	x
z	z	$-z$	$-z$	$-z$	$-z$	z	z	z
xy	xy	$-xy$	$-xy$	$-xy$	$-xy$	xy	xy	xy
xz	xz	yz	$-yz$	$-xz$	xz	$-xz$	$-yz$	yz
yz	yz	$-xz$	xz	yz	$-yz$	$-yz$	$-xz$	xz
x^2	x^2	y^2	y^2	x^2	x^2	x^2	y^2	y^2
y^2	y^2	x^2	x^2	y^2	y^2	y^2	x^2	x^2
z^2	z^2	z^2	z^2	z^2	z^2	z^2	z^2	z^2

Table D.8: Transformations of linear and quadratic functions under D_{2d} point group operations multiplied by the characters of the group element within the B_2 irreducible representation of the D_{2d} point group with the sum/h ($h = 8$) given in the last column.

	E	$S_4(-\pi/2)$	$S_4(+\pi/2)$	$C_2(x)$	$C_2(y)$	$C_2(z)$	$\sigma_d(x+y)$	$\sigma_d(x-y)$	Sum/h
x	x	y	$-y$	$-x$	x	$-x$	$-y$	y	0
y	y	$-x$	x	y	$-y$	$-y$	$-x$	x	0
z	z	z	z	z	z	z	z	z	z
xy	xy	xy	xy	xy	xy	xy	xy	xy	xy
xz	xz	$-yz$	yz	xz	$-xz$	$-xz$	$-yz$	yz	0
yz	yz	xz	$-xz$	$-yz$	yz	$-yz$	$-xz$	xz	0
x^2	x^2	$-y^2$	$-y^2$	$-x^2$	$-x^2$	x^2	y^2	y^2	0
y^2	y^2	$-x^2$	$-x^2$	$-y^2$	$-y^2$	y^2	x^2	x^2	0
z^2	z^2	$-z^2$	$-z^2$	$-z^2$	$-z^2$	z^2	z^2	z^2	0

Thus, it can be shown that the only linear term that is returned after applying the projection operation to each of the linear trial functions is z and that the only quadratic term returned after

applying the projection operation to each of the quadratic trial functions is xy. That is, $\hat{P}^n|z\rangle = z$, and $\hat{P}^n|xy\rangle = xy$. Therefore, the linear and quadratic basis functions for the B_2 irreducible representation of the D_{2d} point group are z and xy, respectively, and hence, the orbitals (at the point group origin) belonging to this irreducible representation are the p_z and d_{xy} orbitals.

As another example, we repeat the same procedure for the B_1 representation. The transformations multiplied by the corresponding characters of the B_1 irreducible representation of the D_{2d} point group along with the sums for each trial function are given in Table D.9. The only non-zero result of the projection operator on our nine trial functions are $\hat{P}^n|x^2\rangle = \frac{1}{2}(x^2 - y^2)$ and $\hat{P}^n|y^2\rangle = \frac{1}{2}(y^2 - x^2)$. If we choose the trial function $x^2 - y^2$, we get $\hat{P}^n|x^2 - y^2\rangle = x^2 - y^2$. Therefore, we have shown that $x^2 - y^2$ is a basis function for the B_1 representation of the D_{2d} point group and that the $d_{x^2-y^2}$ orbital belongs to this representation. Additionally, because all of the characters corresponding to the A_1 representation are one, it is simple to show (sum over the rows of Table D.7) that the basis functions for the A_1 (X_1) representation are $x^2 + y^2$ and z^2. Linear combinations of these basis functions include $x^2 + y^2 + z^2$ and $2z^2 - x^2 - y^2$, showing that s and d_{z^2} belong to this representation (if centered at the origin of the point group).

Table D.9: Transformations of linear and quadratic trial functions under D_{2d} point group operations multiplied by the characters of the group element within the B_1 irreducible representation of the D_{2d} point group with the sum/h ($h = 8$) given in the last column.

	E	$S_4(-\pi/2)$	$S_4(+\pi/2)$	$C_2(x)$	$C_2(y)$	$C_2(z)$	$\sigma_d(x+y)$	$\sigma_d(x-y)$	Sum/h
x	x	y	$-y$	x	$-x$	$-x$	y	$-y$	0
y	y	$-x$	x	y	$-y$	y	x	$-x$	0
z	z	z	z	$-z$	$-z$	z	$-z$	$-z$	0
xy	xy	xy	xy	$-xy$	$-xy$	xy	$-xy$	$-xy$	0
xz	xz	$-yz$	yz	$-xz$	xz	$-xz$	yz	$-yz$	0
yz	yz	xz	$-xz$	yz	$-yz$	$-yz$	xz	$-xz$	0
x^2	x^2	$-y^2$	$-y^2$	x^2	x^2	x^2	$-y^2$	$-y^2$	$\frac{1}{2}(x^2 - y^2)$
y^2	y^2	$-x^2$	$-x^2$	y^2	y^2	y^2	$-x^2$	$-x^2$	$\frac{1}{2}(y^2 - x^2)$
z^2	z^2	$-z^2$	$-z^2$	z^2	z^2	z^2	$-z^2$	$-z^2$	0

An analogous procedure is used to determine the basis functions for the C_{3v} point group, representing the symmetry of the Λ–line and L–point. Here, we use the point group operations describing the little group along $\Lambda = \frac{\pi}{a}(l, l, l)$ and at $\mathrm{L} = \frac{\pi}{a}(1, 1, 1)$. The results of each symmetry operation in the C_{3v} point group on the linear and quadratic trial functions are summarized in Table D.10. By simply summing over the rows in Table D.10, it is straightforward to see that the basis functions for the A_1 (Λ_1, L_1) representation are $x + y + z$, $x^2 + y^2 + z^2$, $x + y + z$, and $xy + xz + yz$, as given in Table D.6.

Table D.10: Transformations of linear and quadratic trial functions under C_{3v} point group operations.

	E	C_3^1	C_3^2	$\sigma_v(x)$	$\sigma_v(y)$	$\sigma_v(z)$
x	x	y	z	x	z	y
y	y	z	x	z	y	x
z	z	x	y	y	x	z
xy	xy	yz	xz	xz	yz	xy
xz	xz	xy	yz	xy	xz	yz
yz	yz	xz	xy	yz	xy	xz
x^2	x^2	y^2	z^2	x^2	z^2	y^2
y^2	y^2	z^2	x^2	z^2	y^2	x^2
z^2	z^2	x^2	y^2	y^2	x^2	z^2

Following the same procedure as before, the basis functions (orbitals) for the A_2 (L_2, Λ_2) and E (L_3, Λ_3) can be determined by multiplying the results of the group operators on each trial function (Table D.10) by the corresponding characters (Table D.6), as described by Equation D.1. The results of this procedure are summarized in Tables D.11 and D.12. Note than for the E representation, $l_n = 2$ in Equation D.1 because it is a 2D irreducible representation.

Table D.11: Transformations of linear and quadratic trial functions under C_{3v} point group operations multiplied by the character of the group element within the A_2 irreducible representation.

	E	C_3^1	C_3^2	$\sigma_v(x)$	$\sigma_v(y)$	$\sigma_v(z)$	sum/h
x	x	y	z	$-x$	$-z$	$-y$	0
y	y	z	x	$-z$	$-y$	$-x$	0
z	z	x	y	$-y$	$-x$	$-z$	0
xy	xy	yz	xz	$-xz$	$-yz$	$-xy$	0
xz	xz	xy	yz	$-xy$	$-xz$	$-yz$	0
yz	yz	xz	xy	$-yz$	$-xy$	$-xz$	0
x^2	x^2	y^2	z^2	$-x^2$	$-z^2$	$-y^2$	0
y^2	y^2	z^2	x^2	$-z^2$	$-y^2$	$-x^2$	0
z^2	z^2	x^2	y^2	$-y^2$	$-x^2$	$-z^2$	0

Table D.12: Transformations of linear and quadratic trial functions under C_{3v} point group operations multiplied by the character of the group element within the E irreducible representation.

	E	C_3^1	C_3^2	$\sigma_v(x)$	$\sigma_v(y)$	$\sigma_v(z)$	$2\times(\text{sum}/h)$
x	$2x$	$-y$	$-z$	0	0	0	$\frac{1}{3}(2x-y-z)$
y	$2y$	$-z$	$-x$	0	0	0	$\frac{1}{3}(2y-z-x)$
z	$2z$	$-x$	$-y$	0	0	0	$\frac{1}{3}(2z-x-y)$
xy	$2xy$	$-yz$	$-xz$	0	0	0	$\frac{1}{3}(2xy-xz-yz)$
xz	$2xz$	$-xy$	$-yz$	0	0	0	$\frac{1}{3}(2xz-xy-yz)$
yz	$2yz$	$-xz$	$-xy$	0	0	0	$\frac{1}{3}(2yz-xy-xz)$
x^2	$2x^2$	$-y^2$	$-z^2$	0	0	0	$\frac{1}{3}(2x^2-y^2-z^2)$
y^2	$2y^2$	$-z^2$	$-x^2$	0	0	0	$\frac{1}{3}(2y^2-x^2-z^2)$
z^2	$2z^2$	$-x^2$	$-y^2$	0	0	0	$\frac{1}{3}(2z^2-x^2-y^2)$

Clearly, there are no valid linear or quadratic basis functions corresponding to s, p, or d orbitals that belong to the A_2 representation of the C_{3v} point group, while there are multiple choices of basis sets for the E representation. There is no unique choice for the linear and quadratic basis functions of the E representation, so we only seek two linearly independent basis functions for each of the three vector spaces (Equations D.2)–D.4). For example, looking at the $\{x, y, z\}$ space, the results of the operations performed in Table D.12 are $\boldsymbol{v_1} = 2|x\rangle - |y\rangle - |z\rangle$, $\boldsymbol{v_2} = 2|y\rangle - |x\rangle - |z\rangle$, and $\boldsymbol{v_3} = 2|z\rangle - |x\rangle - |y\rangle$. These three vectors are not linearly independent. For instance, $\boldsymbol{v_1} + \boldsymbol{v_2} = -\boldsymbol{v_3}$. If we take $\boldsymbol{v_3}$ to be one basis function, the second one can be found by simply adding $2\boldsymbol{v_1}$ to $\boldsymbol{v_3}$, which gives $3|x\rangle - 3|y\rangle \sim |x\rangle - |y\rangle$. Therefore, $(2z-x-y,\ x-y)$ is a suitable linear basis set for the E representation of the C_{3v} point group along Λ and at L. By performing an analogous procedure for the functions in the $\{x^2, y^2, z^2\}$ and $\{xy, xz, yz\}$ spaces, it can be shown that $(2xy - xz - yz,\ xz - yz)$ and $(2z^2 - x^2 - y^2,\ x^2 - y^2)$ are suitable choices for the quadratic basis functions.

D.1.3 Sub-lattice Symmetry Representations

After the irreducible representations of the atomic orbitals centered at the point group origin are determined, the representations of the unique sub-lattice sites, X (0, 0, 0), Y (1/4, 1/4, 1/4), and Z (1/2, 1/2, 1/2), must also be derived to determine the full representation of each orbital occupying each sublattice. [4,68] Consider an element at position, i, in the unit cell with coordinates $\boldsymbol{r_i}$. If we apply an arbitrary point group operation, $\hat{\boldsymbol{R}}$, to $\boldsymbol{r_i}$, we obtain $\hat{\boldsymbol{R}} \cdot \boldsymbol{r_i} = \boldsymbol{r_{j,t}}$, where $\boldsymbol{r_{j,t}} = \boldsymbol{r_j} + \boldsymbol{t}$. The index, j, denotes a sub-lattice site within *initial* unit cell, and the vector, $\boldsymbol{t}$ defines the translation vector between the new position and $\boldsymbol{r_j}$. The character for a given lattice site for a point group operation, $\hat{\boldsymbol{R}}$, is given by $\chi_k^i(R) = \delta_{R,r_i,r_j} P_k^i$, where $\delta_{R,r_i,r_j} = 1$ if the group operation, $\hat{\boldsymbol{R}}$, maps the coordinates of site i onto an equivalent lattice site in the same or neighboring unit cell (i.e. a site that is an integer number of lattice translations away from the initial site) and $\delta_{R,r_i,r_i} = 0$ otherwise. [4] P_k^i is the phase factor, defined as $P_k^i = e^{i\boldsymbol{k}\cdot\boldsymbol{t}}$. That is, for a given $\boldsymbol{k}$-point, if $i = j$, the character of the lattice is simply given by the phase factor corresponding to the translation (at the Γ-point, all values of P_Γ^i are equal to one). However, because each site in the hH compounds is occupied by a

different element, we can take the simpler approach, as it can be shown that $\delta_{R,r_i,r_j} = 1$ for every point group operation $\hat{\boldsymbol{R}}$. Therefore, for the hH crystal structure, $\chi^i_k(R) = P^i_k = e^{i\boldsymbol{k}\cdot\boldsymbol{t}}$.

We will illustrate this procedure by determining the representation of the Y-site at the X-point in the BZ. Using the Cartesian basis for the direct and reciprocal lattice vectors, we define the Y-site as $\boldsymbol{r_Y} = (\frac{a}{4}, \frac{a}{4}, \frac{a}{4})$ and the X-point with $\boldsymbol{k_X} = (0, 0, 2\pi/a)$, where a is the lattice constant. The lattice vectors for an fcc lattice given in a Cartesian basis are $\boldsymbol{a_1} = (\frac{a}{2}, \frac{a}{2}, 0)$, $\boldsymbol{a_2} = (\frac{a}{2}, 0, \frac{a}{2})$, and $\boldsymbol{a_3} = (0, \frac{a}{2}, \frac{a}{2})$. Because the point group symmetry of the X-point is D_{2d}, we apply each group operation of this point group to $\boldsymbol{r_Y}$ and determine the corresponding translation vector, $\boldsymbol{t}$ and translation phase factor, P^Y_X. The results of this analysis are summarized in Table D.13. For this example, we only give the result of a representative group element for each class.

Table D.13: Transformations of Y-site Cartesian coordinates for representative group elements of each class in the D_{2d} point group along with the corresponding translation vectors and phase factors.

	E	$S_4(-\pi/2)$	$C_2(x)$	$C_2(z)$	$\sigma_d(x+y)$
$\boldsymbol{r_{j,t}}$	$(\frac{a}{4}, \frac{a}{4}, \frac{a}{4})$	$(-\frac{a}{4}, \frac{a}{4}, -\frac{a}{4})$	$(\frac{a}{4}, -\frac{a}{4}, -\frac{a}{4})$	$(-\frac{a}{4}, -\frac{a}{4}, \frac{a}{4})$	$(-\frac{a}{4}, -\frac{a}{4}, \frac{a}{4})$
$\boldsymbol{t}$	$(0, 0, 0)$	$(-\frac{a}{2}, 0, -\frac{a}{2})$	$(0, -\frac{a}{2}, -\frac{a}{2})$	$(-\frac{a}{2}, -\frac{a}{2}, 0)$	$(-\frac{a}{2}, -\frac{a}{2}, 0)$
$\boldsymbol{k_X} \cdot \boldsymbol{t}$	0	$-\pi$	$-\pi$	0	0
P^Y_X	1	-1	-1	1	1

Comparing the phase factor of each symmetry class to the character table for the D_{2d} point group (Table D.2), it is clear that the Y-site in the hH structure belongs to the B_2 representation at the X-point (also shown in Ref. 68). It can be shown that for the Γ-point (T_d), L-point (C_{3v}), Δ-line (C_{2v}) and Λ-line (C_{3v}), all three sites (X, Y, and Z) all belong to the A_1, or identity, representation. Furthermore, the X- and Z-sites at the X-point also belong to the A_1 representation. Therefore, the Y-site at the X-point is the only sub-lattice/$\boldsymbol{k}$-point combination (considered here) where the atomic orbitals on that site do not belong to the symmetry representation of the atomic orbitals themselves. In order to determine the symmetry representation of each orbital on the Y-site at the X-point, we take the direct product of the atomic orbital representation and the site representation. A simple way to determine the direct product of two representations is to simply take the product of the characters. That is, the character of the total representation for an orbital on a lattice site, corresponding to a point group element, R, is given by $\chi^{\text{total}}(R) = \chi^{\text{orb}}(R) \times \chi^{\text{a.s.}}(R)$. For instance, if we want to determine the representation of the $d_{x^2-y^2}$ orbitals on the Y-site at X, we multiply the characters of the B_1 representation and the B_2 representation, as shown in Table D.14.

Table D.14: Multiplication of characters from the B_1 and B_2 representations of the D_{2d} point group.

	E	$2S_4$	$C_2(z)$	$2C_2'$	$2\sigma_d$
B_1 (X_2)	1	-1	1	1	-1
B_2 (X_3)	1	-1	1	-1	1
$B_1 \otimes B_2$	1	1	1	-1	-1

Comparing the last row of Table D.14 to the rows of Table D.2, we can see that the direct product of the B_1 and B_2 representations is the A_2 representation. Repeating this analysis for the remaining orbitals, we can determine remaining representations. The representations for all three crystallographic sites at the X-point are given in Table D.14. These results are in agreement with those given in Ref. 68

Table D.15: Symmetry representations of atomic orbitals at the X-Point (D_{2d}).

Site	s	p_x	p_y	p_z	d_{xy}	d_{yz}	d_{xz}	d_{z^2}	$d_{x^2-y^2}$
X	A_1	E	E	B_2	B_2	E	E	A_1	B_1
Y	B_2	E	E	A_1	A_1	E	E	B_2	A_2
Z	A_1	E	E	B_2	B_2	E	E	A_1	B_1

D.2 Electronic Structure Calculations

Contents of this section are reproduced with permission from the Supporting Information in M. K. Brod, S. Anand, and G. J. Snyder. *Advanced Electronic Materials*, 8(4), 2101367 (2022) [153]. Copyright 2022 by Wiley-VCH GmbH.

The values given in Tables D.16-D.18, have been calculated using DFT+PBE without spin-orbit coupling.

Table D.16: Energy offset of the L and W VBMs, the difference in normalized Z-p orbital character between the W and L points, and the Pauling electronegativity difference between the Y- and Z-species [3, 6].

Compound	E_{VBM}(L) − E_{VBM}(W) (eV)	Z-p Character (W - L)	Elec. Neg. Diff. (Z-Y)
NbCoSb	0.26	0.08	0.17
NbCoSn	-0.02	0.13	0.08
NbFeSb	0.37	0.08	0.22
NbFeSn	0.07	0.13	0.13
NbRhSn	-0.15	0.20	-0.32
ScNiBi	0.42	-0.04	0.11
ScNiSb	0.40	-0.03	0.14
TaCoSn	0.06	0.10	0.08
TaFeSb	0.36	0.07	0.22
TiCoSb	0.28	0.03	0.17
TiNiSn	0.29	0.05	0.05
VCoSn	0.03	0.10	0.08
VFeSb	0.24	0.06	0.22
YNiSb	0.26	0.01	0.14
ZrCoSb	0.28	0.06	0.17
ZrNiSn	0.08	0.07	0.05

Table D.17: Energy offset of the W and Γ VBMs and the group number (GN) difference between the X and Y sites.

Compound	GN Diff. $(Y - X)$	$E_{VBM}(\Gamma) - E_{VBM}(\mathrm{W})$ (eV)
NbCoSb	4	-0.25
NbCoSn	4	-0.34
NbFeSb	3	-0.51
NbFeSn	3	-0.50
NbRhSn	4	-0.20
ScNiBi	7	1.29
ScNiSb	7	1.25
TaCoSn	4	-0.16
TaFeSb	3	-0.42
TiCoSb	5	0.34
TiNiSn	6	0.72
VCoSn	4	-0.11
VFeSb	3	-0.27
YNiSb	7	1.01
ZrCoSb	5	0.12
ZrNiSn	6	0.51

Table D.18: Group number (GN) and Pauling electronegativity difference between the Y and X species and the energy offset of the Γ and L VBMs and of the X_3 and X_2 CBMs.

Compound	GN Diff. $(Y-X)$	Elec. Neg. Diff. $(Y-X)$	$E_{VBM}(\Gamma) - E_{VBM}(\mathrm{L})$ (eV)	$E(\mathrm{X}_3) - E(\mathrm{X}_2)$ (eV)
NbCoSb	4	0.28	-0.51	0.09
NbCoSn	4	0.28	-0.32	-0.04
NbFeSb	3	0.23	-0.88	0.64
NbFeSn	3	0.23	-0.57	0.36
NbRhSn	4	0.68	-0.06	0.53
ScNiBi	7	0.55	0.88	-1.35
ScNiSb	7	0.55	0.85	-1.40
TaCoSn	4	0.38	-0.22	-0.37
TaFeSb	3	0.33	-0.78	0.38
TiCoSb	5	0.34	0.06	-0.14
TiNiSn	6	0.37	0.43	-0.66
VCoSn	4	0.25	-0.14	0.30
VFeSb	3	0.20	-0.51	0.82
YNiSb	7	0.69	0.74	-2.17
ZrCoSb	5	0.55	-0.16	-0.69
ZrNiSn	6	0.58	0.43	-1.36

D.3 Half-Heusler Tight-Binding Interactions

In this section, we derive some of the $\boldsymbol{k}$-dependent tight-binding (TB) hopping integrals—as defined by the TB solution for the energy levels in a diatomic molecule (Equation 2.22)— in transition-metal based half-Heusler (hH) compounds. For all of the d–d-type orbital interactions, we assume $V_{dd\delta} \sim 0$, and therefore only consider the $dd\pi$ and $dd\sigma$ interactions [63, 169]. The values of the $V_{sd\sigma}$, $V_{pd\sigma}$, $V_{pd\pi}$, $V_{dd\sigma}$, and $V_{dd\pi}$, interaction parameters can be approximated using the values in Harrison's solid state table for ZrNiSn [63]. For the $\Gamma - \Delta - \mathrm{X}$ path in the first Brillouin zone, we define the parameter, d, to describe the distance along the path at a point $\boldsymbol{k}_{\boldsymbol{\Delta}} = (0,\, 0,\, 2\pi d)$. At Γ, $d = 0$, and at the X-point, $d = 1$.

D.3.1 X-d–Z-p Interaction along $\Delta_{3,4}$ Bands

The TB interaction strength between the X-d and Z-p orbitals along the $\Gamma_{15} - \Delta_{3,4} - \mathrm{X}_5$ bands can be determined by finding the TB matrix element between the X-d_{xz} and Z-p_x orbitals, defined as $H_{xz,x}$. It can be shown that the matrix elements $H_{yz,x}$ and $H_{xz,y}$ are always equal to zero and that $H_{xz,x} = H_{yz,y}$. Moreover, assuming that $\boldsymbol{k}_{\boldsymbol{\Delta}}$ is parallel to the z-axis, it can be shown that $H_{xy,y} = H_{xy,x} = H_{xy,z} = 0$.

Using the approach outlined by Slater and Koster [65], the matrix elements, $H_{xz,x}$ and $H_{yz,y}$ can be written as follows:

$$H_{xz,x} = H_{yz,y} = -2iV_{pd\pi,XZ}[\sin(k_x a/2) + \sin(k_y a/2) + \sin(k_z a/2)]. \tag{D.5}$$

In Equation D.5, $V_{pd\pi,XZ}$ denotes the hopping integral between the X-d and Z-p orbitals, and a is the lattice constant of the compound. However, we can simplify this matrix element along the $\Delta = 2\pi(0,0,d)$ direction to $H_{xz,x} = H_{yz,y} = -2iV_{pd\pi,XZ}\sin(d\pi)$. Therefore, using the reduced TB basis set, {X-d_{xz}, X-d_{yz}, Z-p_x, Z-p_y}, we can write the Hamiltonian, $\hat{\boldsymbol{H}}_{\boldsymbol{X_d,Z_p}}$, describing the X-$d$–Z-$p$ interaction along $\Gamma_{15} - \Delta_{3,4} - X_5$ as follows (Equation D.6):

$$\hat{\boldsymbol{H}}_{\boldsymbol{X_d,Z_p}} = \begin{bmatrix} E_{X-d} & 0 & H_{xz,x} & 0 \\ 0 & E_{X-d} & 0 & H_{xz,x} \\ H^*_{xz,x} & 0 & E_{Z-p} & 0 \\ 0 & H^*_{xz,x} & 0 & E_{Z-p} \end{bmatrix} \tag{D.6}$$

In the above equation, $H^*_{xz,x}$ and $H^*_{yz,y}$ denote the complex conjugate of $H_{xz,x}$ and $H_{yz,y}$, respectively. The eigenvalues of the Hamiltonian defined in Equation D.6 are given below in Equation D.7. Both the positive (+) and minus (-) solutions are doubly degenerate, giving a total of four eigenvalues.

$$E_{X_d,Z_p} = \frac{1}{2}(E_{X-d} + E_{Z-p}) \pm \frac{1}{2}\sqrt{(E_{X-d} - E_{Z-p})^2 + 16V^2_{pd\pi,XZ}\sin^2(d\pi)} \tag{D.7}$$

Comparing Equation D.7 to Equation 2.22, we can define the effective diatomic hopping integral as

$$V(d) = 2V_{pd\pi,XZ}\sin(d\pi). \tag{D.8}$$

D.3.2 X-d–Y-d Interaction along Δ_1 and Δ_2 Bands

In order to understand the behavior of the Δ_1 CB, we must consider the interactions between the X-d_{z^2} and the Y-d_{z^2} orbitals and the interactions between the X-d_{xy} and the Y-d_{z^2} orbitals along the Δ path, as both of these interactions are allowed by symmetry (see Table D.5). Along the Δ_2 path, we need only consider the interaction between the X-$d_{x^2-y^2}$ and Y-$d_{x^2-y^2}$ orbitals.

The Hamiltonian matrix element describing the interaction between the X-d_{z^2} and Y-d_{z^2} orbitals or between the X-$d_{x^2-y^2}$ and Y-$d_{x^2-y^2}$ orbitals is given by the expression,

$$H_{z^2,z^2} = \frac{2}{3}V_{dd\pi,XY}(e^{-ia(k_x+k_y+k_z)/4} + e^{-ia(-k_x-k_y+k_z)/4} + e^{-ia(k_x-k_y-k_z)/4} + e^{-ia(-k_x+k_y-k_z)/4}). \tag{D.9}$$

Therefore, the Hamiltonian describing either the X-d_{z^2}–Y-d_{z^2} interactions or the X-$d_{x^2-y^2}$–Y-$d_{x^2-y^2}$ interactions along Δ is given in Equation D.10.

$$\hat{\boldsymbol{H}}_{\boldsymbol{X_{d_e}},\boldsymbol{Y_{d_e}}} = \begin{bmatrix} E_{X-d} & \frac{8}{3}V_{dd\pi,XY}\cos(\pi d/2) \\ \frac{8}{3}V_{dd\pi,XY}\cos(\pi d/2) & E_{Y-d} \end{bmatrix} \tag{D.10}$$

The eigenvalues of this Hamiltonian are given in Equation D.11.

$$E_{X_{d_e},Y_{d_e}} = \frac{1}{2}(E_{X-d}+E_{Y-d}) \pm \frac{1}{2}\sqrt{(E_{X-d}-E_{Y-d})^2 + 4[(8/3)V_{dd\pi,XY}\cos(\pi d/2)]^2} \tag{D.11}$$

Therefore, the effective hopping integral between the X-$d_{x^2-y^2}$ and Y-$d_{x^2-y^2}$ orbitals (Δ_2) and between the X-$d_{z^2}{}_2$ and Y-d_{z^2} orbitals (Δ_1) is

$$V(d) = \frac{8}{3}V_{dd\pi,XY}\cos(\pi d/2). \tag{D.12}$$

The Hamiltonian describing the interaction between the Y-d_{z^2} and the X-d_{xy} orbitals, is given by Equation D.13.

$$\hat{\boldsymbol{H}}_{\boldsymbol{X_{d_{xy}}},\boldsymbol{Y_{d_{z^2}}}} = \begin{bmatrix} E_{X-d} & -\frac{8\sqrt{3}}{9}iV_{dd\pi,XY}\sin(\pi d/2) \\ \frac{8\sqrt{3}}{9}iV_{dd\pi,XY}\sin(\pi d/2) & E_{Y-d} \end{bmatrix} \tag{D.13}$$

The Hamiltonian describing the Y-d_{xy}–X-d_{z^2} interaction is analogous to that given in Equation D.13, with X replaced by Y and Y replaced by X. It is straightforward to see that the corresponding eigenvalues for both cases are given by Equation D.23.

$$E_{X_{d_{xy}},Y_{d_{z^2}}} = \frac{1}{2}(E_{X-d}+E_{Y-d}) \pm \frac{1}{2}\sqrt{(E_{X-d}-E_{Y-d})^2 + 4[\frac{8\sqrt{3}}{9}V_{dd\pi,XY}\sin(\pi d/2)]^2} \tag{D.14}$$

Thus, the effective hopping integral for the X-d_{xy}–Y-d_{z^2} (and X-d_{z^2}–Y-d_{xy}) interactions along Δ is

$$V(d) = \frac{8\sqrt{3}}{9}V_{dd\pi,XY}\sin(\pi d/2). \tag{D.15}$$

D.3.3 X-d_{z^2}–Z-s Interaction along Δ_1 Bands

The Hamiltonian element describing the interaction between the X-d_{z^2} and Z-s orbitals along Δ_1 is given by the two-center integral, $H_{z^2,s} = 2V_{sd\sigma,XZ}(\cos(\pi d)-1)$. Thus, the corresponding Hamiltonian is given by Equation D.16 below.

$$\hat{\boldsymbol{H}}_{\boldsymbol{X_{d_{z^2}},Z_s}} = \begin{bmatrix} E_{X-d} & 2V_{sd\sigma,XZ}(\cos(\pi d)-1) \\ 2V_{sd\sigma,XZ}(\cos(\pi d)-1) & E_{Z-s} \end{bmatrix} \tag{D.16}$$

The two eigenvalues of this Hamiltonian are given below.

$$E_{X_{d_{z^2}},Z_s} = \frac{1}{2}(E_{X-d}+E_{Z-s}) \pm \frac{1}{2}\sqrt{(E_{X-d}-E_{Z-s})^2 + 4[2V_{sd\sigma,XZ}(\cos(\pi d)-1)]^2} \tag{D.17}$$

Hence, the effective TB hopping integral describing the Δ_1 X-d_{z^2}–Z-s interaction can be expressed by Equation D.18.

$$V(d) = 2V_{sd\sigma,XZ}(\cos(\pi d)-1) \tag{D.18}$$

D.3.4 X-d_{xy}–Y-s Interaction along Δ_1 Bands

The Hamiltonian element describing the interaction between the X-d_{xy} and Y-s orbital along Δ is $H_{xy,s} = -\frac{4i\sqrt{3}}{3}V_{sd\sigma,XY}\sin(\pi d/2)$, and hence, the Hamiltonian can be written as follows:

$$\hat{\boldsymbol{H}}_{\boldsymbol{X_{d_{xy}},Y_s}} = \begin{bmatrix} E_{X-d} & -\frac{4i\sqrt{3}}{3}V_{sd\sigma,XY}\sin(\pi d/2) \\ \frac{4i\sqrt{3}}{3}V_{sd\sigma,XY}\sin(\pi d/2) & E_{Y-s} \end{bmatrix} \tag{D.19}$$

The two eigenvalues of Equation D.19 are

$$E_{X_{d_{xy}},Y_s} = \frac{1}{2}(E_{X-d}+E_{Y-s}) \pm \frac{1}{2}\sqrt{(E_{X-d}-E_{Y-s})^2 + 4[\frac{4\sqrt{3}}{3}V_{sd\sigma,XY}\sin(\pi d/2)]^2}. \tag{D.20}$$

Therefore, we can write the effective TB hopping integral for the X-d_{xy}–Y-s interaction.

$$V(d) = \frac{4\sqrt{3}}{3}V_{sd\sigma,XY}\sin(\pi d/2) \tag{D.21}$$

D.3.5 Y-d_{z^2}–Z-p_z Interaction along Δ_1 Bands

Next, we look at the Y-d_{z^2}–Z-p_z interactions that contribute to the Δ_1 bands. The Hamiltonian element describing this interaction is given by $H_{z^2,z} = -\frac{8i}{3}V_{pd\pi,YZ}\sin(\pi d/2)$. We can then write the corresponding Hamiltonian.

$$\hat{\boldsymbol{H}}_{\boldsymbol{Y_{d_{z^2}},Z_{pz}}} = \begin{bmatrix} E_{Y-d} & -\frac{8i}{3}V_{pd\pi,YZ}\sin(\pi d/2) \\ \frac{8i}{3}V_{pd\pi,YZ}\sin(\pi d/2) & E_{Z-p} \end{bmatrix} \tag{D.22}$$

The associated eigenvalues are given as follows:

$$E_{Y_{d_{z^2}},Z_{p_z}} = \frac{1}{2}(E_{Y-d} + E_{Z-p}) \pm \frac{1}{2}\sqrt{(E_{Y-d} - E_{Z-p})^2 + 4[\frac{8}{3}V_{pd\pi,YZ}\sin(\pi d/2)]^2}. \tag{D.23}$$

Hence, the effective hopping integral for the Y-d_{z^2}–Z-p_z interaction contributing to the Δ_1 bands can be written as

$$V(d) = \frac{8}{3}V_{pd\pi,YZ}\sin(\pi d/2). \tag{D.24}$$

D.3.6 Summary of Interactions

Table D.19: Summary of effective $\boldsymbol{k}$-dependent tight-binding hopping integrals $V(d)$.

Band Symmetry	Interaction	Equation	Trend in Strength
$\Delta_{3,4}$	X-d–Z-p	D.8	0 at Γ and X, maximum halfway between Γ and X
Δ_1/Δ_2	X-d_e–Y-d_e	D.12	Decreases from Γ to X
Δ_1	X-d_{xy}–Y-d_{z^2}	D.15	Increases from Γ to X
Δ_1	X-d_{z^2}–Y-d_{xy}	D.15	Increases from Γ to X
Δ_1	X-d_{z^2}–Z-s	D.18	Increases from Γ to X
Δ_1	X-d_{xy}–Y-s	D.21	Increases from Γ to X
Δ_1	Y-d_{z^2}–Y-p_z	D.24	Increases from Γ to X

Additional Information for Mg_3Sb_2 Analysis

E.1 Calculating Effective Mass from Band Curvature

This appendix provides supplemental information to Chapter 7, which discusses the importance of Mg–Sb interactions in high conduction band degeneracy in Mg_3Sb_2.

The second derivative of energy with respect to $\boldsymbol{k}$ is determined by finding the value of $2a$ for the parabolic fits ($E - E_{VBM} = ak_l^2 + bk_l + c$) for each material along the L*M* and A*U paths. These values are given in Table E.1. We use k_l to denote the distance in $\boldsymbol{k}$-space along the specified path.

Table E.1: Value of $2a$ ($\partial^2 E/\partial k^2$) for the parabolic fits ($E - E_F = ak_l^2 + bk_l + c$) along the L*M* path and A*U path.

	L*M* Path	A*U Path
Compound	$\partial^2 E/\partial k^2$ (eV·Å^2)	$\partial^2 E/\partial k^2$ (eV·Å^2)
Mg_3Bi_2	70	21
Mg_3Sb_2	48	17
Mg_3As_2	37	13
Mg_3SbBi	58	19
Mg_3AsSb	40	14
$BeMg_2Bi_2$	92	19
$BeMg_2Sb_2$	62	14
$BeMg_2As_2$	34	11

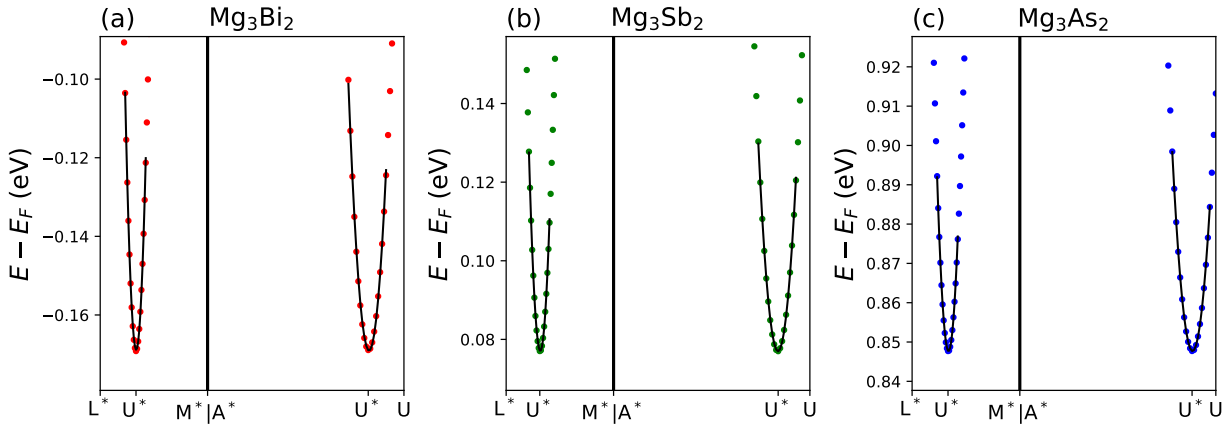

Figure E.1: Parabolic fit (solid black curve) of the U* conduction band edge (colored dots) used to calculate the effective mass along the L*M* direction and the A*U directions for (a) Mg_3Bi_2, (b) Mg_3Sb_2, (c) Mg_3As_2.

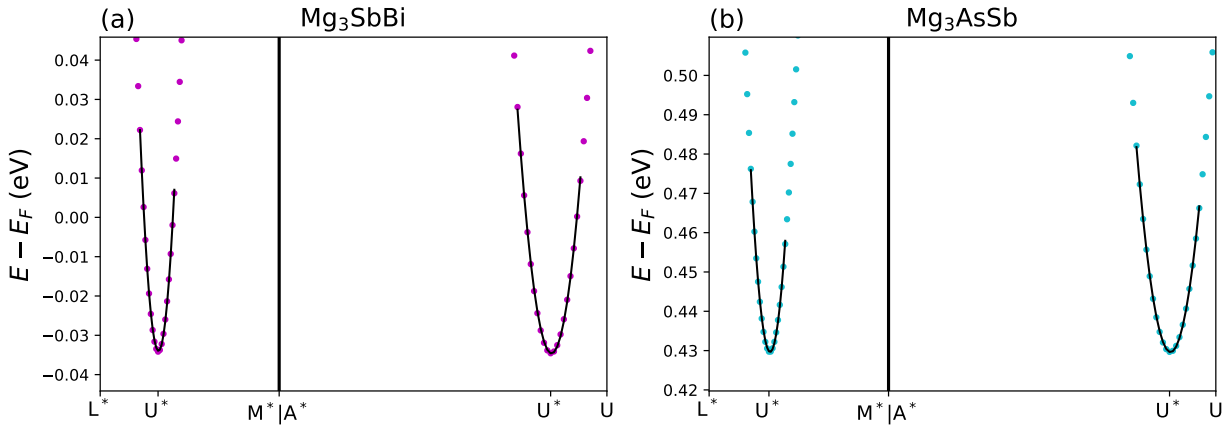

Figure E.2: Parabolic fit (solid black curve) of the U* conduction band edge (colored dots) used to calculate the effective mass along the L*M* direction and the A*U directions for (a) Mg_3SbBi and (b) Mg_3AsSb.

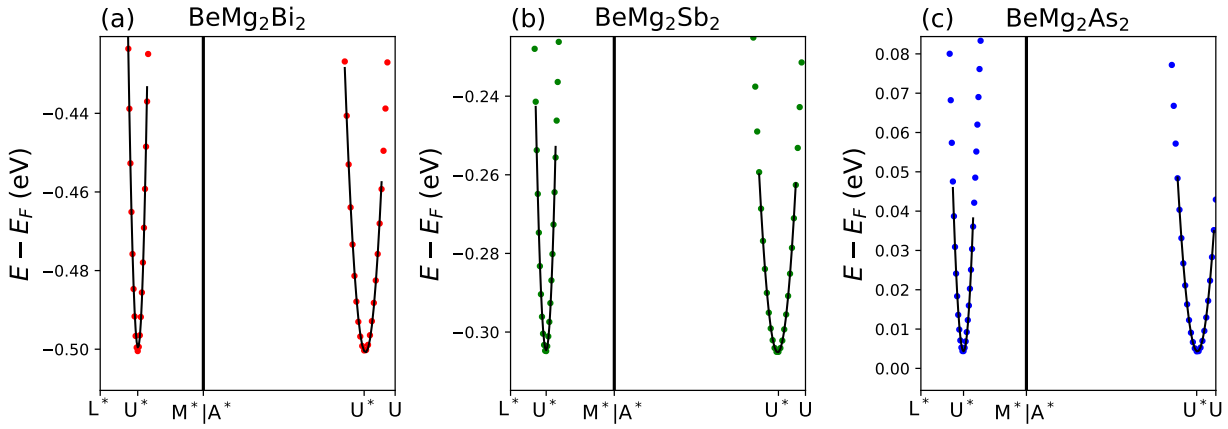

Figure E.3: Parabolic fit (solid black curve) of the U* conduction band edge (colored dots) used to calculate the effective mass along the L*M* direction and the A*U directions for (a) $BeMg_2Bi_2$, (b) $BeMg_2Sb_2$, (c) $BeMg_2As_2$.

E.2 Location of U* for $AeMg_2X_2$ (Ae = Mg, Be; X = Bi, Sb, As)

The locations of the local conduction band minimums inside the ΓALM plane (at the U*-point) are listed below (rounded to two decimal places), where the coordinates are given in the reciprocal lattice basis.

- Mg_3Bi_2: (0, 0.41, 0.33)
- Mg_3Sb_2: (0, 0.42, 0.34)
- Mg_3As_2: (0, 0.44, 0.33)
- Mg_3AsSb: (0, 0.43, 0.33)
- Mg_3SbBi: (0, 0.41, 0.34)
- $BeMg_2Bi_2$: (0, 0.42, 0.32)
- $BeMg_2Sb_2$: (0, 0.43, 0.33)
- $BeMg_2As_2$: (0, 0.45, 0.30)

E.3 Density Functional Theory Structural Parameters

Table E.2: Lattice constants for AeMg$_2X_2$ (Ae =Be, Mg; X =As, Sb, Bi) calculated using DFT-PBE (no SOC).

Compound	a (Å)	c (Å)
$BeMg_2As_2$	4.15	6.45
$BeMg_2Sb_2$	4.41	7.04
$BeMg_2Bi_2$	4.52	7.28
Mg_3As_2	4.29	6.76
Mg_3Sb_2	4.60	7.28
Mg_3Bi_2	4.71	7.46
Mg_3AsSb	4.45	7.03
Mg_3SbBi	4.65	7.38

Table E.3: Bond lengths in Mg_3X_2 calculated using DFT-PBE (no SOC).

Bond	Bond length (Å) Mg_3Bi_2	Bond length (Å) Mg_3Sb_2	Bond length (Å) Mg_3As_2
Mg(1)–X	3.18	3.12	2.93
Mg(2)–X (short)	2.95	2.85	2.63
Mg(2)–X (long)	3.04	2.96	2.78
Mg(1)–Mg(2)	3.90	3.77	3.47
Mg(2)–Mg(2)	3.31	3.28	3.13

Table E.4: Bond lengths in Mg_3SbBi and Mg_3AsSb calculated using DFT-PBE (no SOC).

Bond	Bond length (Å) Mg_3SbBi	Bond length (Å) Mg_3AsSb
Mg(1)–X	3.16 (Bi), 3.13 (Sb)	3.03 (Sb), 3.03 (As)
Mg(2)–X (short)	2.91 (Bi), 2.88 (Sb)	2.80 (Sb), 2.67 (As)
Mg(2)–X (long)	3.05 (Bi), 2.95 (Sb)	3.04 (Sb), 2.71 (As)
Mg(1)–Mg(2)	3.78, 3.89	3.51, 3.74
Mg(2)–Mg(2)	3.29	3.21

Table E.5: Bond lengths in $BeMg_2X_2$ calculated using DFT-PBE (no SOC).

Bond	Bond length (Å) $BeMg_2Bi_2$	Bond length (Å) $BeMg_2Sb_2$	Bond length (Å) $BeMg_2As_2$
Be–X	2.95	2.90	2.73
Mg–X (short)	2.95	2.83	2.58
Mg–X (long)	3.13	3.03	2.86
Be–Mg	3.80	3.65	3.31
Mg–Mg	3.14	3.12	3.05

Supplemental GeTe Data

The plots in this Appendix provide supplemental data to Chapter 5, which describes the chemical origins of the valence band structure in GeTe in the rhombohedral and cubic phases.

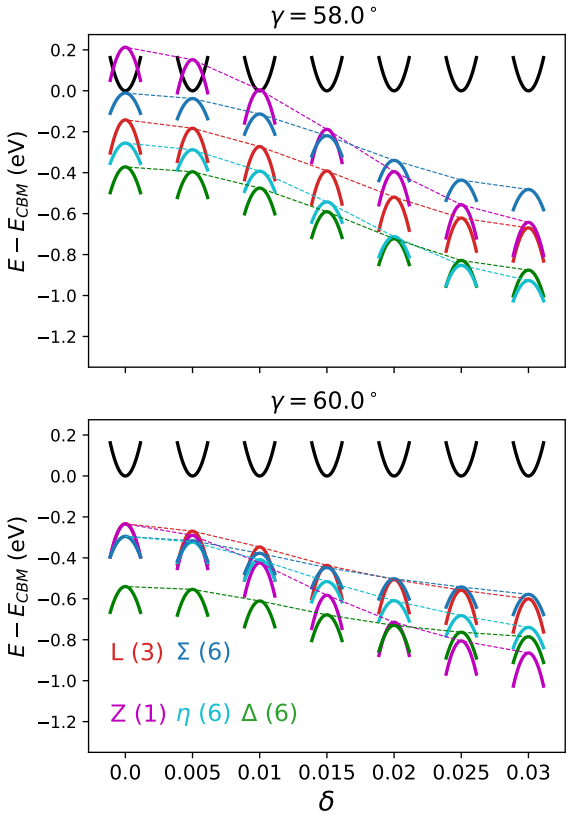

Figure F.1: Schematic of the valence band (VB) edge energies (L, Z, Σ, η, and Δ) with respect to the L-point CBM (shown in black) as a function of the Ge offset, δ, when the primitive-cell interaxial angle is constant at $\gamma = 58°$ (top) and $\gamma = 60°$ (bottom). The band edge energies (shown with dashed lines) are calculated from density functional theory (DFT) using the Perdew–Burke-Ernzerhof (PBE) functional and spin-orbital coupling (SOC).

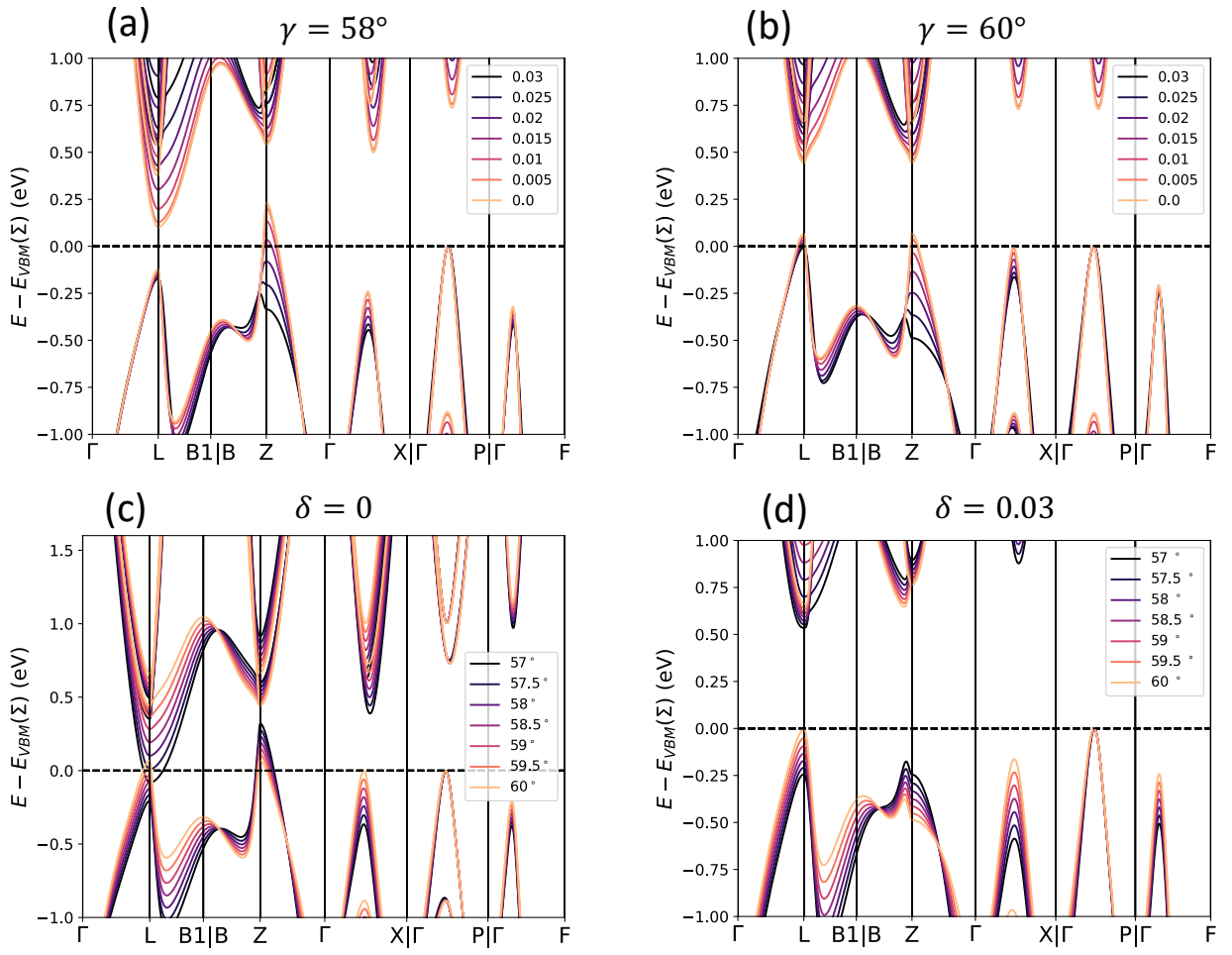

Figure F.2: DFT-calculated electronic band structure of GeTe (no SOC) with varying values of atomic offset, δ, and interaxial angle, γ. (a) GeTe band structure calculated with $\gamma = 58°$ and varying δ, (b) $\gamma = 60°$ and varying δ, (c) $\delta = 0.0$ and varying γ, and (d) $\delta = 0.03$ with varying γ. The energy is set such that the Σ VBM is at 0 eV.

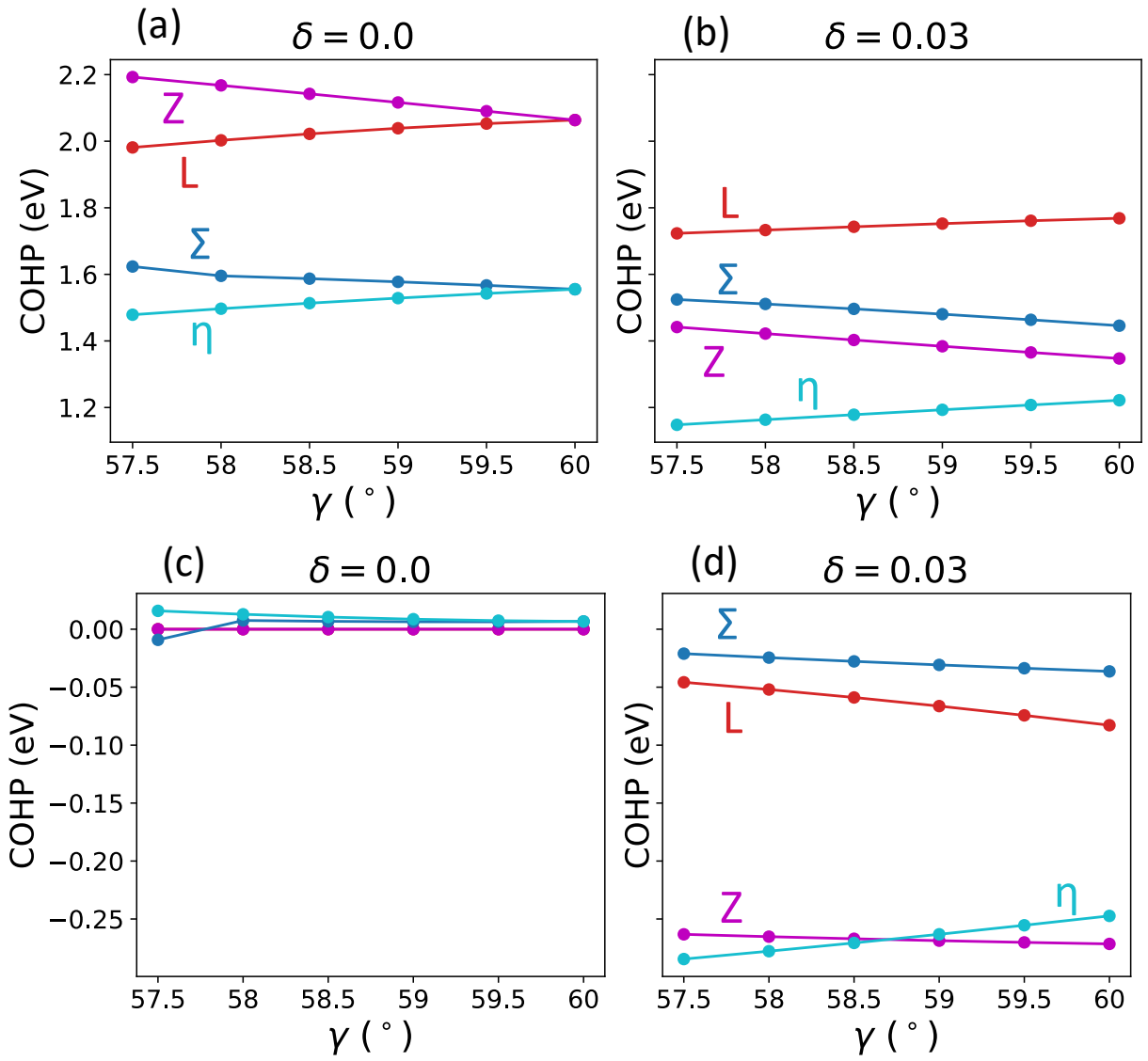

Figure F.3: ***k***-resolved, band-resolved projected crystal orbital Hamilton population (pCOHP) values vs. interaxial angle γ in the Z (magenta), L (red), Σ (blue), and η (turquoise) VBMs in GeTe. For the Z band, the COHP values are always calculated at the *true* Z-point, even when it is not where the maximum near (or on) Z occurs. COHP of Ge-s–Te-p interaction when (a) $\delta = 0$ and (b) $\delta = 0.03$. COHP of Ge-p–Te-p interaction when (c) $\delta = 0$ and (d) $\delta = 0.03$.

Vita

Lead author publications

1. **Madison K. Brod**, Shashwat Anand, and G. Jeffrey Snyder. The importance of Mg–Sb interactions in achieving high conduction band degeneracy in Mg_3Sb_2 for high n-type thermoelectric performance. *Materials Today Physics*, 31:100959, 2023.

2. **Madison K. Brod**, Shuping Guo, Yongsheng Zhang, and G. Jeffrey Snyder. Explaining the electronic band structure of half-Heusler thermoelectric semiconductors for engineering high valley degeneracy. *MRS Bulletin*, 47(6):573–583, 2022.

3. **Madison K. Brod**, Shashwat Anand, and G. Jeffrey Snyder. The importance of avoided crossings in understanding high valley degeneracy in half-Heusler thermoelectric semiconductors. *Advanced Electronic Materials*, 8(4):2101367, 2022.

4. **Madison K. Brod** and G. Jeffrey Snyder. Orbital chemistry of high valence band convergence and low-dimensional topology in PbTe. *Journal of Materials Chemistry A*, 9:12119–12139, 2021.

5. **Madison K. Brod**, Michael Y. Toriyama, and G. Jeffrey Snyder. Orbital chemistry that leads to high valley degeneracy in PbTe. *Chemistry of Materials*, 32(22):9771–9779, 2020.

Contributing author publications

1. Airan Li, **Madison K. Brod**, Yuechu Wang, Kejun Hu, Pengfei Nan, Shen Han, Ziheng Gao, Xinbing Zhao, Binghui Ge, Chenguang Fu, Shashwat Anand, G. Jeffrey Snyder and Tie-Jun Zhu. Opening the Bandgap of Metallic Half-Heuslers via the Introduction of d-d Orbital Interactions. Submitted, 2023.

2. V.K. Ranganayakulu, Te-Hsien Wang, Cheng-Lung Chen, Angus Huang, Ma-Hsuan Ma, Chun-Min Wu, Wei-Han Tsai, Tsu-Lien Hung, Min-Nan Ou, Horng-Tay Jeng, Chih-Hao Lee, Kuei-Hsien Chen, Wen-Hsien Li, **Madison K. Brod**, G. Jeffrey Snyder, and Yang-Yuan Chen. Ultrahigh zT from the low-dimensional Fermi surface nesting in GeTe. Submitted, 2023.

3. Michael Y. Toriyama, **Madison K. Brod**, Lídia C. Gomes, Ferdaushi A. Bipasha, Badih A. Assaf, Elif Ertekin, and G. Jeffrey Snyder. Tuning valley degeneracy with band inversion. *Journal of Materials Chemistry A*, 10:1588–1595, 2022.

4. Michael Toriyama, **Madison K. Brod**, and G. Jeffrey Snyder. Chemical interpretation of charged point defects in semiconductors: A case study of Mg2Si. *ChemNanoMat*, 8:e202200222, 2022.

5. Shuping Guo, Shashwat Anand, **Madison K. Brod**, Yongsheng Zhang, and G. Jeffrey Snyder. Conduction Band Engineering of Half-Heusler Thermoelectrics Using Orbital Chemistry. *Journal of Materials Chemistry A*, 10(6):3051-3057, 2022.

6. Michael Y. Toriyama, Alex M. Ganose, Maxwell Dylla, Shashwat Anand, Junsoo Park, **Madison K. Brod**, Jason M. Munro, Kristin A. Persson, Anubhav Jain, and G. Jeffrey Snyder. How to analyse a density of states. *Materials Today Electronics*, 1:100002, 2022.

7. Zhou Zhang, Yifan Zhu, Jialin Ji, Jianxin Zhang, Huifang Luo, Chenguang Fu, Qianqian Li, **Madison Brod**, G. Jeffrey Snyder, Yubo Zhang, Jiong Yang, and Wenqing Zhang. Ag rearrangement induced metal-insulator phase transition in thermoelectric MgAgSb. *Materials Today Physics*, 25:100702, 2022.

8. Xuemei Zhang, Zhongyi Wang, Bo Zou, **Madison K. Brod**, Jianbo Zhu, Tiantian Jia, Guodong Tang, G. Jeffrey Snyder, and Yongsheng Zhang. Band Engineering SnTe via Trivalent Substitutions for Enhanced Thermoelectric Performance. *Chemistry of Materials*, 33(24):9624-9637, 2021.

9. Tingting Deng, Tong Xing, **Madison K. Brod**, Ye Sheng, Pengfei Qiu, Igor Veremchuk, Qingfeng Song, Tian-Ran Wei, Jiong Yang, G. Jeffrey Snyder. Discovery of high-performance thermoelectric copper chalcogenide using modified diffusion-couple high-throughput synthesis and automated histogram analysis technique. *Energy and Environmental Science*, 13(9):3041-3053, 2020.